

**INTEGRATION OF OBSERVATIONS AND MODELS  
FOR AN IMPROVED UNDERSTANDING OF  
MARINE ECOSYSTEM DYNAMICS**

by

Angela M. Kuhn

Submitted in partial fulfilment of the requirements  
for the degree of Doctor of Philosophy

at

Dalhousie University

Halifax, Nova Scotia

September 2017

Para mis padres y hermanos, en especial, para mi “sistita” Ingrid.

*“Battle within battle must be continually recurring with varying success.”*

Charles Darwin

# TABLE OF CONTENTS

LIST OF TABLES .....	vii
LIST OF FIGURES.....	viii
ABSTRACT.....	xi
LIST OF ABBREVIATIONS AND SYMBOLS USED.....	xii
ACKNOWLEDGEMENTS .....	xv
CHAPTER 1: INTRODUCTION .....	1
1.1 OBJECTIVES.....	4
1.2 CASE STUDIES AND RESEARCH QUESTIONS .....	4
1.2.1 Subpolar North Atlantic open waters .....	4
1.2.2 Northwest North Atlantic Continental Shelf.....	5
1.2.3 Gulf of Aqaba, Red Sea.....	6
1.3 ASSIMILATIVE FRAMEWORK .....	6
1.4 THESIS OUTLINE .....	8
CHAPTER 2: MODEL INVESTIGATIONS OF THE NORTH ATLANTIC SPRING BLOOM INITIATION.....	10
2.1 INTRODUCTION.....	10
2.2 METHODS.....	14
2.2.1 Data Sets.....	14
2.2.2 Base Model Description .....	17
2.2.3 Cost Function Design .....	20
2.2.4 Base Model Sensitivity.....	22
2.2.5 Spring Bloom Initiation Metrics .....	23
2.2.6 Experimental Simulations .....	27
2.3 OPTIMIZED SIMULATION RESULTS .....	27
2.3.1 Plankton Annual Cycles .....	27
2.3.2 Optimal Parameter Values .....	30
2.3.3 Model Sensitivity to Variables .....	35
2.4 EXPERIMENTAL SIMULATIONS .....	38
2.4.1 Experiment I: Zooplankton Response to a Shoaling Mixed Layer .....	38
2.4.2 Experiment II: System Response in the Absence of Mixed Layer Fluctuations...	41
2.4.3 Experiment III: Effects of Zooplankton Dilution and Concentration .....	44
2.5 DISCUSSION.....	50
2.5.1 Is the Optimized Model Consistent with the Critical-Depth Hypothesis? .....	50
2.5.2 Is the Optimized Model Consistent with the Dilution-Recoupling Hypothesis? ..	54
2.5.3 Limitations .....	56

2.6 CONCLUSION .....	60
----------------------	----

CHAPTER 3: EVALUATING ECOSYSTEM MODEL COMPLEXITY IN  
THE NORTHWEST NORTH ATLANTIC, PART I:  
SURROGATE-BASED OPTIMIZATION.....

3.1 INTRODUCTION.....	62
3.2 STUDY AREA: THE NORTHWEST NORTH ATLANTIC.....	66
3.3 MODEL DESCRIPTIONS .....	66
3.3.1 Physical Configuration.....	66
3.3.2 Ecosystem Models.....	67
3.3.3 Surrogate Model.....	69
3.4 OPTIMIZATION PROCEDURE AND SENSITIVITY ANALYSIS .....	72
3.4.1 Observational Datasets for Calibration .....	75
3.4.2 Sensitivity Analysis.....	77
3.4.3 Optimization Experiments.....	83
3.5 RESULTS.....	87
3.5.1 Single vs. Multiple Observed Variables.....	89
3.5.2 Single vs. Multiple Locations.....	90
3.5.2.1 <i>Spatial Patterns in Parameters</i> .....	92
3.5.2.2 <i>Model Portability</i> .....	92
3.5.3 Number of Optimized Parameters.....	95
3.5.4 Fluxes .....	98
3.6 DISCUSSION.....	99
3.6.1 Surrogates and Surrogate-Based Optimization .....	99
3.6.2 Deciding on a Complexity Level.....	101
3.6.3 Uncertainties.....	104
3.7 CONCLUSION .....	108

CHAPTER 4: EVALUATING ECOSYSTEM COMPLEXITY IN  
THE NORTHWEST NORTH ATLANTIC, PART II: SURFACE  
CHLOROPHYLL, PRIMARY PRODUCTION AND ECOSYSTEM DYNAMICS.....

4.1 INTRODUCTION.....	111
4.2 OCEANOGRAPHIC CHARACTERISTICS AND SUB-REGIONS IN THE NORTHWEST NORTH ATLANTIC .....	114
4.3 OBSERVATIONAL DATASETS .....	116
4.4 MODEL DESCRIPTION.....	118
4.4.1 Physical Model.....	118
4.4.2 Biogeochemical Models.....	120
4.5 RESULTS.....	121
4.5.1 Surface Chlorophyll Seasonal Variability.....	121
4.5.2 Surface Chlorophyll Spatial Patterns .....	127

4.5.3 Primary Production .....	128
4.5.4 Standing Stocks .....	130
4.5.5 Phytoplankton Specific Growth and Loss Rates .....	132
4.5.6 Ecosystem Fluxes .....	134
4.5.7 Effect of Multiple Grazers on Nutrients .....	137
4.6 DISCUSSION .....	140
4.6.1 Spring Bloom Bottom-Up Drivers .....	141
4.6.2 Summer Minima Top-Down Drivers .....	144
4.6.3 Magnitude Differences in Primary Production .....	146
4.6.4 Role of Temperature .....	147
4.6.5 Succession of Small and Large Phytoplankton in M3 .....	149
4.6.6 Simple vs. Complex Models .....	150
4.7 CONCLUSIONS .....	153
CHAPTER 5: HETEROTROPHIC AND AUTOTROPHIC N <sub>2</sub> FIXATION IN A BIOGEOCHEMICAL MODEL OF THE GULF OF AQABA (ISRAEL), RED SEA ...	156
5.1 INTRODUCTION .....	156
5.2 STUDY AREA: THE GULF OF AQABA .....	160
5.3 METHODS .....	162
5.3.1 Observations .....	163
5.3.2 Model Descriptions .....	164
5.3.3 Model Parameters .....	167
5.3.3.1 Cost Function Design .....	167
5.3.3.2 Optimized Parameters .....	169
5.3.3.3 Diazotrophs Parameters .....	171
5.4 RESULTS .....	173
5.4.1 Observed NO <sub>3</sub> and PO <sub>4</sub> Patterns .....	173
5.4.2 Model Results .....	176
5.4.2.1 Sensitivity to Physical Nudging .....	176
5.4.2.2 Optimized Model Without N <sub>2</sub> Fixation .....	177
5.4.2.3 Effects of N <sub>2</sub> Fixation on NO <sub>3</sub> and PO <sub>4</sub> .....	179
5.4.2.4 Effects of N <sub>2</sub> Fixation on Chlorophyll and O <sub>2</sub> .....	183
5.4.2.5 Long-term validation .....	185
5.4.2.6 Primary Production and N <sub>2</sub> Fixation Rates .....	187
5.5 DISCUSSION .....	189
5.5.1 Is N <sub>2</sub> Fixation Relevant in the Gulf of Aqaba? .....	189
5.5.2 How does N <sub>2</sub> Fixation Contribute to Primary Production? .....	192
5.5.3 Are Different Diazotrophic Groups Important? .....	193
5.5.4 Limitations and uncertainties .....	197
5.6 CONCLUSIONS .....	199

CHAPTER 6: CONCLUSIONS.....	201
6.1 INSIGHTS INTO ECOSYSTEM MODELLING PHILOSOPHY .....	202
6.2 INSIGHTS INTO MARINE ECOLOGY .....	205
6.3 SUMMARY .....	208
BIBLIOGRAPHY.....	210
APPENDIX A .....	231
APPENDIX B .....	234
APPENDIX C .....	235
APPENDIX D .....	248
APPENDIX E.....	250
APPENDIX F .....	251
APPENDIX G .....	252
APPENDIX I.....	253
APPENDIX J .....	259

## LIST OF TABLES

Table 2.1:	Ecosystem model parameters and symbols used in the Subpolar North Atlantic NPZD model .....	25
Table 2.2:	Optimal parameters, cost, and root-mean-square values resulting from individual and joint optimizations of the Subpolar North Atlantic NPZD model .....	31
Table 2.3:	Spring bloom metrics estimated using satellite-based biomass, and simulated surface phytoplankton cycles in the Subpolar North Atlantic. ....	35
Table 2.4:	Brief description of idealized experiments configuration and conclusions .....	37
Table 3.1:	Correlation between satellite chlorophyll and surface in situ chlorophyll in the northwest North Atlantic .....	73
Table 3.2:	List of one-dimensional model locations used in the optimization experiments, and corresponding nitrate and chlorophyll averages.....	74
Table 3.3:	A priori model parameter estimates and ranges .....	78
Table 3.4:	Summary of optimization experiments .....	86
Table 4.1:	Metrics comparing satellite-based and simulated surface chlorophyll annual cycles in the northwest North Atlantic .....	126
Table 5.1:	Summary of model versions characteristics and assumptions .....	166
Table 5.2:	Parameters used in the Gulf of Aqaba base biogeochemical model..	168
Table 5.3:	Diazotrophs parameters and re-calibrated non-fixing phytoplankton parameters .....	170
Table 5.4:	Model validation using non-assimilated observations .....	186

## LIST OF FIGURES

Figure 2.1:	Satellite-based mean annual surface chlorophyll concentration in the Subpolar North Atlantic, location of study bins, and optimized model results .....	15
Figure 2.2:	Comparison between satellite-based phytoplankton biomass and daily averaged simulated phytoplankton .....	28
Figure 2.3:	Phytoplankton inventory net accumulation rates estimated from observations and model results.....	30
Figure 2.4:	Principal component analysis of optimized parameters .....	33
Figure 2.5:	Sensitivity of simulated surface phytoplankton biomass and inventory accumulation rate to halving and doubling optimal parameter values .....	34
Figure 2.6:	Phytoplankton sensitivity to small perturbations in physical and biological variables .....	36
Figure 2.7::	Relative contribution of the accumulation of zooplankton biomass due to a shoaling mixed layer over changes in zooplankton biomass due to assimilated grazing .....	40
Figure 2.8:	Results of Experiment II, showing simulated annual cycles using different constant mixed layer depths .....	43
Figure 2.9:	Results of Experiment III, showing simulated annual cycles using different winter mixed layer depths as a proxy to impose different winter dilution levels to zooplankton .....	47
Figure 2.10:	Results of Experiment III, showing changes in the date of bloom initiation resulting from experiments using different winter mixed layer depths .....	49
Figure 2.11:	Vertically integrated phytoplankton growth minus vertically integrated phytoplankton losses, critical depth, and mixed layer depth .....	52
Figure 2.12:	Phytoplankton growth and loss (grazing, mortality, respiration) rates, vertically integrated over the model domain .....	55
Figure 3.1:	Map of the northwest North Atlantic study area and sampling locations along transects of the Atlantic Zone Monitoring Program .....	67
Figure 3.2:	Schematics of the ecosystem models used in the northwest North Atlantic case study .....	68
Figure 3.3:	Two-dimensional histograms showing the performance of the	

	model surrogates with respect to surface chlorophyll.....	71
Figure 3.4:	Surrogate-target chlorophyll biases at two locations .....	72
Figure 3.5:	Information used in the design of the cost function.....	76
Figure 3.6:	Parameter sensitivities for the northwest North Atlantic biogeochemical models.....	82
Figure 3.7:	Final cost metrics of the optimization experiments .....	88
Figure 3.8:	Mean surface satellite and in situ chlorophyll compared to optimized results of experiment E4 .....	89
Figure 3.9:	Analysis of spatial patterns in optimal parameters for individual locations .....	91
Figure 3.10:	Results of the model geographical portability experiments.....	92
Figure 3.11:	Example of surface chlorophyll in the model portability experiments .....	95
Figure 3.12:	Diagrams depicting trophic model structures obtained by different optimization experiments.....	97
Figure 3.13:	Vertically integrated phytoplankton growth and loss fluxes .....	99
Figure 4.1:	Northwest North Atlantic major ocean circulation characteristics and model domain sub-regions .....	115
Figure 4.2:	Regressions of in situ and SeaWiFs satellite chlorophyll and de- biased chlorophyll in the Gulf of St. Lawrence .....	117
Figure 4.3:	Comparison of simulated and observed temperature, density and mixed layer depths .....	119
Figure 4.4:	Climatological satellite and simulated surface chlorophyll annual cycles in the model sub-regions .....	122
Figure 4.5:	Maximum mixed layer depth and simulated date of the phytoplankton spring bloom peak date .....	125
Figure 4.6:	Average satellite and simulated surface chlorophyll during spring and fall.....	127
Figure 4.7:	Satellite-based and simulated vertically integrated primary production in the model sub-regions.....	129
Figure 4.8:	Seasonal average vertically integrated primary production for satellite-based estimates and model results.....	130
Figure 4.9:	Annual cycles of nitrate, ammonium, phytoplankton and zooplankton simulated surface concentrations .....	131

Figure 4.10: Specific phytoplankton growth, grazing, and mortality rates .....	134
Figure 4.11: Scotian Shelf vertically integrated average annual biogeochemical fluxes.....	135
Figure 4.12 Spatial distributions of average sea surface temperature and phytoplankton mortality rates .....	136
Figure 4.13: Simulated average zooplankton loss fluxes to detritus .....	138
Figure 4.14: Sensitivity experiments varying the reference maximum zooplankton grazing rate parameters .....	139
Figure 5.1: Hierarchical cluster of model approaches to marine N <sub>2</sub> fixation .....	158
Figure 5.2: Map of the Gulf of Aqaba .....	161
Figure 5.3: Observed nitrate and phosphate vertical distributions at Station A from 2004 to 2014.....	173
Figure 5.4: Observed N* values at Station A from 2007 to 2010 .....	175
Figure 5.5: Effect of physical nudging on temperature and density fields.....	177
Figure 5.6: Results from models without N <sub>2</sub> fixation.....	178
Figure 5.7: Observed and simulated nitrate and phosphate vertical distributions....	179
Figure 5.8: Observed and simulated vertically integrated nitrate and phosphate, and particulate organic nitrogen and phosphorus .....	181
Figure 5.9: Observed and simulated N* range in biogeochemical models tested ....	183
Figure 5.10: Observed and simulated chlorophyll and oxygen vertical distributions.....	184
Figure 5.11: Observed (circles) and simulated (lines) total nitrate in the surface and deep-waters during the model validation period from 2010 to 2014. ....	185
Figure 5.12: Primary production and N <sub>2</sub> fixation rates from 2007 to 2010.....	188
Figure 5.13: Simulated annual new, regenerated, and total primary production and N <sub>2</sub> fixation .....	190

## ABSTRACT

While both observational and modelling approaches can improve our understanding of ocean ecology, each type of approach has intrinsic limitations. Direct observations have limited temporal/spatial coverage and many quantities are not easily measured. Models rely on assumptions and parameters that are not always based on direct observation. My thesis research systematically combines observations and models through the use of parameter optimization, and further investigates model behavior with the help of sensitivity analyses and hypothesis-oriented experiments. I apply the optimization formalism in three case studies that revisit paradigms in biological oceanography including drivers of the phytoplankton spring bloom, the importance of trophic interactions in determining rates of primary production, and the biogeochemical role of nitrogen fixing organisms. The first case study juxtaposes bottom-up and top-down hypotheses to explain the initiation of the phytoplankton spring bloom. Realistic and idealized model simulations reveal that the conceptual bases of both hypotheses are ecological truisms. A spring bloom can develop in the absence of mixed layer fluctuations, and both its magnitude and timing are strongly dependent on nutrient and light availability. Changes in zooplankton grazing modulate phytoplankton biomass, but do not produce significant shifts to explain bloom initiation. In the second case study I compare ecosystem models of different trophic complexity. I found that models of low complexity can accurately respond to bottom-up drivers of phytoplankton phenology; however, aspects like the spring bloom termination, accurate simulation of primary production, and partitioning of nitrogen cycling pathways require a higher degree of complexity that is insufficiently constrained by presently available observations. In the third case study, I demonstrate that the inclusion of specific planktonic traits, such as heterotrophic diazotrophy, is necessary to explain biogeochemical characteristics at certain geographical locations. Despite the regional scope of these study cases, my conclusions provide insights that can be extrapolated to large-scale applications.

## LIST OF ABBREVIATIONS AND SYMBOLS USED

### Abbreviations:

1D	One-dimensional
3D	Three-dimensional
AZMP	Atlantic Zone Monitoring Program
CbPM	Carbon-based Productivity Model
CZCS	Coastal Zone Color Scanner
DIN	Dissolved Inorganic Nitrogen
DIP	Dissolved Inorganic Phosphorus
DOY	Day of Year
ECMWF	European Centre for Medium-range Weather Forecasts
FNMOC	Fleet Numerical Meteorology and Oceanography Center
GOTM	General Ocean Turbulence Model
HPLC	High Performance Liquid Chromatography
IUI	Inter-University Institute
MLD	Mixed Layer Depth
MODIS	Moderate Resolution Imaging Spectroradiometer
NEMURO	North Pacific Ecosystem Model for Understanding Regional Oceanography
NMP	National Monitoring Program
NPZD	Nutrient-Phytoplankton-Zooplankton-Detritus
PAR	Photosynthetic Active Radiation
PCA	Principal Component Analysis
PON	Particulate Organic Nitrogen
POP	Particulate Organic Phosphorus
RMSE	Root-mean-square-error
ROMS	Regional Ocean Modeling System
SeaWiFs	Sea-Viewing Wide Field-of-View Sensor

SODA	Simple Ocean Data Assimilation model
VGPM	Vertically Generalized Production Model
WOA	World Ocean Atlas

### Symbols<sup>1</sup>:

$\alpha$	Phytoplankton initial photosynthetic slope, units vary in each Chapter
$\beta$	Zooplankton assimilation coefficient, dimensionless
<i>Chl-a</i>	Chlorophyll-a, mg Chl-a m <sup>-3</sup>
$Day^{P*}$	Biomass-based phytoplankton bloom initiation metric, DOY
$Day^{r*}$	Net accumulation rate phytoplankton bloom initiation metric, DOY
$F$	Model cost in Chapters 1 and 2
$g$	Zooplankton grazing, d <sup>-1</sup>
$\gamma$	Nudging strength, d <sup>-1</sup>
$H_{MLD}$	Mixed layer depth, m
$H_{cr}$	Critical depth, m
$H_{euph}$	Euphotic zone depth, m
$J$	Model cost in Chapters 3, 4 and 5
$k_D$	Diffusivity coefficient, m <sup>2</sup> d <sup>-1</sup>
$Lim_I$	Light limitation, dimensionless
$Lim_N$	Nutrient limitation, dimensionless
M1	Base model used in Chapter 2
M2	Modified M1 with temperature-dependent biological rates
M3	Modified M2 with increased number of planktonic groups
N <sub>2</sub>	Di-nitrogen gas
NH <sub>4</sub>	Ammonium
NO <sub>3</sub>	Nitrate
$\mu_0$	Reference phytoplankton maximum growth rate at $T = 0^\circ\text{C}$ , d <sup>-1</sup>

---

<sup>1</sup> Further details provided in Chapters 2 to 5.

$\mu_{max}$	Phytoplankton maximum growth rate, $d^{-1}$
$O_2$	Oxygen
$PO_4$	Phosphate
$\vec{p}$	Model parameters vector
$\Psi$	Microphytoplankton chlorophyll fraction, dimensionless
$\sigma_\theta$	Potential density anomaly, $kg\ m^{-3}$
$\varphi$	System state in the Taylor decomposition analysis
$Q$	Model sensitivity metric
$t$	Time, d
$T$	Sea temperature, $^{\circ}C$
$\theta_{max}$	Maximum chlorophyll-to-carbon ratio, $mg\ Chl-a\ (mg\ C)^{-1}$
$z$	Water depth, z

## ACKNOWLEDGEMENTS

I would like to thank my supervisor, Katja Fennel, for her continuous trust and understanding throughout these years. I would also like to thank the members of my academic committee: Marlon Lewis, Michael Dowd and Hugh MacIntyre, for their always constructive and supportive advice. I thank the collaborators of my work, especially my colleagues and friends Paul Mattern and Laura Bianucci. My work in the Gulf of Aqaba was enriched by the collaboration of Ilana Berman-Frank, Boaz Lazar and Etai Landou, and by insightful discussions with E. Boss and S. Kienast. I gratefully acknowledge those who have provided access to the different datasets used in these studies: M. Behrenfeld, C. Johnson, J. Urrego-Blanco, and A. Genin. This work was financially supported by the Scientific Committee on Oceanic Research (SCOR; Professor F. Ronald Hayes International Scholarship), K. Fennel's National Sciences and Engineering Research Council of Canada (NSERC) grants, the Marine Environmental Observation, Prediction and Response Network (MEOPAR), the Schulich Ocean Studies Centre Initiative, and the Faculty of Graduate Studies Nova Scotia Graduate Scholarship (Dalhousie University).

I must thank Stuart Banks and Gene C. Feldman, who years ago inspired me to follow this path. I also thank my past and present lab-mates, and other friends in the Oceanography Department for sharing the rollercoaster ride with me. Special thanks also go to Lisa White.

I thank my parents for their prayers and blessings. I also thank the support of my siblings, specially my sister Ingrid, who first taught me the ABC, and despite the distance is always by my side. Thanks to the friends who became my family overseas,

especially those who were there when I needed them the most: Noelia, Iván, Anahí, Angela (a.k.a. bio-Angela), and Ana.

This list would be incomplete without thanking Jorge for loving my strengths and weaknesses, and for helping me to keep the road in perspective.

## CHAPTER 1:

### INTRODUCTION

Marine biogeochemical models are widely used numerical tools that allow us to summarize information about ecosystem functioning. Models serve as flexible frameworks to perform experiments that are unfeasible in reality; therefore helping to test, and generate hypotheses. Ecosystem models can also be used to quantify ocean biogeochemical cycles (e.g., Moore, Doney, and Lindsay 2004; Bopp et al. 2005; Le Quéré et al. 2005) and to assess the ecosystem response under changing environmental conditions (e.g., Sarmiento et al. 1998; Joos et al. 1999; Orr et al. 2005; Bopp et al. 2013). However, several uncertainties surround the process of modelling. These include the form of the governing equations, the pathways that drive the ecosystem's interactions, the level of ecosystem complexity that models need to properly represent a system's responses, and the values of many biological and chemical rates of change (Anderson 2005; Anderson, Gentleman, and Sinha 2010; Dowd, Jones, and Parslow 2014; Friedrichs et al. 2007; Ward et al. 2010). In this thesis, I explore these concepts using a numerical methodology, known as parameter optimization, to objectively inform models of the available observational data. The focus is on analyzing ecological problems while systematically taking into account the uncertainties found in the observations, the ecosystem models themselves, and the conceptual assumptions they are built upon. The approaches and methodologies I used emphasize the fundamental connection between improvements of ecosystem models and observation networks: models can help to

identify critical gaps in observations, but high-resolution observational datasets are required for the constraint of model parameters and subsequent model validation.

Biogeochemical models depend on mathematical formulations, which in general include many poorly known or unconstrained parameters (Anderson 2005; Franks 2009). For instance, more than 90% of a sample of 153 models published between 1990 and 2002 reported subjective tuning of the parameters within the literature range (Arhonditsis and Brett 2004). This approach can increase the risk of overlooking structural inadequacies in the models and can become complicated by the number of parameters in play and their co-dependencies. This limitation can be better addressed by using parameter optimization techniques (Bagniewski et al. 2011; Fennel et al. 2001; Ward et al. 2010). In general, parameter optimization refers to any quantitative method by which parameters are estimated to provide the best possible fit to a given dataset, under considerations of computational efficiency, the model implicit constraints, and the uncertainties in both the model and the observations. Parameter optimization methodologies represent a comprehensive approach to bridging the knowledge gap in marine ecosystem dynamics, with the combined use of models, and both traditional and novel observations at different scales and resolutions.

From the observational perspective, undersampling of the biogeochemical properties of the ocean is still one of the main impediments to a complete understanding and quantification of biogeochemical cycles. Technological constraints impede the direct measurement of key variables and fluxes of ecological interest. Moreover, traditional sampling methods are limited to small spatial and temporal scales and/or resolutions. Ship-based datasets are limited to a few weeks due to logistic and economic reasons, and

there exist only a few long-term monitoring stations in the world, and even fewer of these measure biogeochemical variables regularly. Starting in the late 1970's with a proof-of-concept mission of the Coastal Zone Color Scanner (CZCS), and more extensively since the 1990's, satellite measurements of ocean color represented a significant boost for biological oceanography. Using mathematical algorithms, these remotely sensed ocean color measurements are transformed into bio-optical properties and provide high frequency, quasi-synoptic estimates of the surface chlorophyll concentration. These have been widely used in conjunction with modeling studies (e.g., Fennel et al., 2006; Gregg, 2008; Previdi et al., 2009). Nevertheless, remotely sensed chlorophyll products only measure the upper limit of the euphotic zone, missing important processes in the ocean interior (Joint and Groom 2000). Furthermore, they are mathematically derived quantities, and *in situ* data are still required to validate them (Cota, Wang, and Comiso 2004; O'Reilly et al. 2001, 1998).

Throughout this thesis, I implement a parameter optimization method in a suite of models, and use different observational datasets, including both *in situ* and satellite-based measurements. I analyze open paradigms in biological oceanography, exemplified in three regional case studies. As the available observational data differs in each case, specific model and optimization designs are required. The limitations of each observational data set are addressed in the specific details of the optimization procedure, as well as in the discussion of the results of each case study.

## **1.1 OBJECTIVES**

The general objectives of this thesis are threefold: i) Implementing an assimilative model framework that can be applied to traditional and novel observational datasets; ii) Optimizing biogeochemical models within the framework with the aim of improving the models' skill and potentially its parameterizations; and iii) Analyzing the optimization and optimized models' results (i.e., resulting parameters, state variables and fluxes) to evaluate biogeochemical processes with an emphasis on improving the understanding of ecosystem functioning.

## **1.2 CASE STUDIES AND RESEARCH QUESTIONS**

### **1.2.1 SUBPOLAR NORTH ATLANTIC OPEN WATERS**

This case study is intended to evaluate the mechanistic process that annually initiates the North Atlantic phytoplankton spring bloom. The event is key to understanding and forecasting climate feedbacks and trophic interactions, as it constitutes the largest and most predictable accumulation of phytoplankton biomass during the year. The dynamics of its onset are a long-discussed question in biological oceanography. In this case study I optimize a one-dimensional (1D) ecosystem model to represent satellite-based phytoplankton biomass of the Subpolar North Atlantic Ocean. The optimized model acts as a control run to perform model experiments on the phytoplankton spring bloom initiation. The experiments' design is based on two competing hypotheses and aims to determine the processes controlling the initiation of the spring bloom on a seasonal scale, and whether these processes follow a bottom-up or top-down nature.

### 1.2.2 NORTHWEST NORTH ATLANTIC CONTINENTAL SHELF

This geographic region is dynamically complex and considered the most oceanographically variable area of both the North Atlantic and Pacific Oceans (Townsend et al., 2004). In this case study I evaluate the role of ecosystem model complexity in determining spatial and temporal patterns of chlorophyll and primary production with a three-dimensional (3D) regional model. Determining the appropriate level of ecosystem model complexity is an unresolved question in ecology, due to the number of uncertainties related to the comparison of models with varying degrees of complexity. Here, I use the optimization method to obtain standard simulations of ecosystem models with different ecological complexities. Optimizing parameters in a 3D environment is computationally expensive and inefficient in terms of time. For this reason, the optimization is performed using a mechanistic surrogate composed of 1D models for the locations where *in situ* data is available. The use of statistical emulators or – as in this case – reduced-order model surrogates is a promising method to improve computational efficiency when optimizing complex numerical models (Leeds et al. 2012; Prieß, Koziel, and Slawig 2013; Prieß et al. 2013). Optimization experiments within this reduced-order setting explore spatial patterns in optimized model parameters, as well as model geographical portability.

### 1.2.3 GULF OF AQABA, RED SEA

This case study aims to quantify the importance of nitrogen fixation in the Gulf of Aqaba, as well as to demonstrate relative importance of different autotrophic and heterotrophic nitrogen fixing organisms in determining the chemical characteristics of the

Gulf of Aqaba. The Gulf of Aqaba is an oligotrophic extension of the Red Sea, where autotrophic and heterotrophic nitrogen fixing organisms have been reported. Nitrogen fixation is a microbially mediated process that refers to the uptake of dinitrogen gas ( $N_2$ ), and its conversion into bioavailable forms of nitrogen for other marine organisms. Supply of “new” nitrogen, such as that resulting from  $N_2$  fixation, regulates the amount of “new” primary production, which is assumed to be equal to the quantity of organic matter exported to deep regions of the ocean (Eppley and Peterson 1979). Consequently, understanding  $N_2$  fixation has the potential to improve quantitative estimates of biogeochemical cycles and climate feedbacks. In particular, heterotrophic organisms may exhibit significant  $N_2$  fixation activity in aphotic environments, challenging previous assumptions about the limited distribution of  $N_2$  fixation to well-lighted surface areas of the ocean.

### **1.3 ASSIMILATIVE FRAMEWORK**

The assimilative framework used throughout this thesis is a heuristic method to determine model parameters. As mentioned before, this is referred as *parameter optimization* and consists of systematically adjusting the parameters, in order to minimize a *cost function* that measures the mismatch between observations and their model counterparts. Parameter optimization is therefore a special case of data assimilation for the iterative calibration of models, in which the goals of the model are clearly defined in the cost function, and model parameters are chosen systematically to fulfill such goals. The parameter optimization method I use is known as an *evolutionary algorithm*, as it borrows ideas from ecological evolutionary theory. The algorithm is used for the

calibration of a suite of marine biogeochemical models intended to evaluate the lower trophic level ecosystem interactions within my three case studies. The algorithm is flexible to allow the use of the diverse observational information available for each case study. The selection of which and how many parameters to optimize depends on the specific case analyzed, and is described for each of the case studies in their corresponding chapters.

In general, the cost function  $F(p)$  of the algorithm takes the generic form of a model-data difference, such as a weighted root-mean-square-error (RMSE):

$$F(\vec{p}) = \sqrt{\frac{\sum_{i=1}^n w_i (\hat{\chi}_i(\vec{p}) - \chi_i)^2}{\sum_{i=1}^n w_i}} + \sum_{j=1}^m f_j, \quad (1.1)$$

where  $\chi$  represents the  $n$  number of records for an observed variable (or set of variables), and  $\hat{\chi}(\vec{p})$  are the corresponding simulated results obtained using the a  $\vec{p}$  parameter set vector. The weight  $w$  allows the cost function to account for the uncertainties of the different observed variables, at different magnitude ranges or to give emphasis to specific subsets of the results (e.g., certain times of the year or depths in the water column). Note that if a set of variables is compared, instead of a single variable,  $\chi$ ,  $\hat{\chi}(\vec{p})$  and  $w$  are vectors. Optionally, a number ( $m$ ) of penalty functions  $f$  can be added to the right-hand-side of the equation to set additional rules that help to shape the behavior of variables unconstrained by the observational data or represent *a priori* knowledge.

In order to search for optimal values within the parametric space, the evolutionary algorithm simulates a process of natural selection by imposing a “survival of the fittest” strategy (Houck et al., 1995) on a population composed of predefined number different

vector parameter sets  $\vec{p}$ . Each vector  $\vec{p}$  represents an individual within the population and the initial parameter population can be selected from *a priori* knowledge or randomly generated within a range of minimum and maximum parameter values based on the literature. Every iteration of the algorithm represents a generation of the parameter population, where a predefined number of the top parameter sets with the smallest cost function values are allowed to survive and become parents of the next generation. Parent parameter sets reproduce and create an offspring by a crossover mechanism: each parameter in a new offspring parameter set is randomly drawn from either one of two randomly chosen parents. Offspring are produced until the population is replenished to its full size. Additionally, the offspring parameter sets are subjected to random mutations in a subset of their parameter values.

#### **1.4 THESIS OUTLINE**

This thesis is presented as a series of chapters analyzing each of the case studies. Chapter 2 is based on Kuhn et al., (2015), and describes in more detail the motivation, methodology, results and conclusions of the Subpolar North Atlantic Open Waters case study.

The Northwest North Atlantic Continental Shelf case study is divided into two chapters. Chapter 3 concerns the development of the mechanistic surrogate-based optimization method, sensitivity analyses and optimization experiments performed to systematically minimize the differences between the biogeochemical models evaluated. In Chapter 4, the optimized parameters are applied in a three-dimensional application of the Regional Ocean Modelling System (ROMS) for the northwest North Atlantic Ocean.

Model estimates are evaluated against satellite-based surface chlorophyll and primary production. The causes of differences among simple and complex models are discussed in the context of simulated standing stocks, rates and fluxes.

The Gulf of Aqaba case study is presented in Chapter 5, where I compare results from different ecosystem model versions in terms of their simulated vertical distribution of inorganic nitrogen and phosphate, as well as chlorophyll and dissolved oxygen. I present estimates of primary productivity and nitrogen fixation rates, and discuss them in the context of local, regional, and global previous estimates in the literature.

In Chapter 6, I finalize this thesis with an overarching summary of the conclusions of all study cases, and their relevance for understanding the effects of physical dimensionality, temporal scales and ecological complexity in plankton ecosystem models.

## CHAPTER 2:

# MODEL INVESTIGATIONS OF THE NORTH ATLANTIC SPRING BLOOM INITIATION<sup>1</sup>

## 2.1 INTRODUCTION

The annually occurring massive growth of phytoplankton during winter-spring in mid and high latitudes, referred to as the spring bloom, is recognized as key to better understand the uncertainties concerning the oceanic carbon cycle and its consequent climate feedbacks under global warming scenarios (Joos et al., 1999; Maier-Reimer et al., 1996; Sarmiento et al., 1998). However, the mechanisms that determine when and how the spring bloom initiates are not yet agreed upon. The traditional model for bloom initiation is based on the concept that there exists a critical depth at which vertically integrated phytoplankton production equals phytoplankton losses. According to this conceptual model, the spring bloom can occur only when the depth of the mixed layer is smaller than this critical depth, allowing phytoplankton production to exceed losses by spending enough time in the euphotic zone (Sverdrup, 1953). Under the assumptions of a constant phytoplankton photosynthetic efficiency, constant loss rates, and a thoroughly mixed layer, Sverdrup estimated that this condition is not met during periods of deep mixing in winter, before thermal stratification establishes in spring.

---

<sup>1</sup> Kuhn, A.M., Fennel, K., Mattern, J.P., 2015. Model investigations of the North Atlantic spring bloom initiation. *Prog. Oceanogr.* 176–193.

The bottom-up control of bloom dynamics implied by Sverdrup's critical depth model has been a cornerstone of marine ecology for more than half a century. Nevertheless, it has been criticized for its inability to explain observations of phytoplankton growth before the onset of stable stratification (Garside & Garside, 1993; Townsend et al., 1992; Behrenfeld 2010). Several studies diverge only nominally from the original critical depth model, suggesting that weak or temporary stratification can be sufficient to initiate blooms in winter (Colebrook, 1979; Townsend et al., 1992; Wasmund et al., 1998). Along that same line of thought, Huisman et al. (1999a, 1999b, 2002) argued that there exists a critical turbulence level, below which phytoplankton growth can occur in winter. Attention has also been called to the difference between mixed layer and the mixing or turbulent layer (Brainerd and Gregg, 1995) suggesting that after the mixed layer reaches its maximum depth, the bloom can be triggered by a shutdown of turbulent convection (Fennel, 1999; Taylor and Ferrari, 2011a) or by mixing occurring only in surface layers (Chiswell, 2011). Others have argued that strong winter convection actually enhances the chances of sinking phytoplankton to be transported back into the euphotic zone and receive light (Backhaus et al., 2003; Lande and Wood, 1987). The latter idea is consistent with theoretical and observational considerations about the annual succession of phytoplankton species, which postulate that non-motile diatoms benefit from turbulent, high-nutrient conditions while motile cells dominate during stratified, low-nutrient periods (Margalef, 1978; Ward and Waniek, 2007).

The discussion about the causes of spring bloom initiation was reinvigorated by analyses that departed from assuming a bottom-up system controlled by vertical mixing and light, as portrayed in the classical critical-depth model. Top-down control by

zooplankton (e.g., Banse, 1994) regained interest with the formulation of the dilution-recoupling hypothesis (Behrenfeld, 2010; Boss and Behrenfeld, 2010; Mariani et al., 2013), which suggests that mixed layer deepening plays a dominant role in bloom initiation by forcing the dilution of phytoplankton and zooplankton during winter. As is known from incubation experiments (e.g., Landry and Hassett, 1982), such dilution negatively affects grazing success and may reduce phytoplankton losses enough for positive net phytoplankton growth to occur in the open ocean in winter (Behrenfeld, 2010). The dilution-recoupling hypothesis has since broadened, recognizing that the decoupling of planktonic feedbacks through dilution is one of many physical and ecological disturbances that continuously act together to determine the initiation, development rate and climax of blooms (Behrenfeld et al., 2013).

The specific objective of this chapter is to assess which of the assumptions inherent to the bottom-up and top-down theoretical approaches are met inside a typical numerical ecosystem model or, in other words, whether and under what conditions the different mechanisms of spring bloom initiation occur. The model's low computational cost and flexibility allows us to perform a set of idealized experiments designed to isolate the effects of mixed layer depth fluctuations and zooplankton grazing on bloom initiation. In this chapter, I use a vertically resolved Nutrient – Phytoplankton – Zooplankton – Detritus (NPZD) model, resembling those used in early studies on model behavior (Evans and Parslow, 1985; Franks et al., 1986; Steele and Henderson, 1992). NPZD models also form the base for functional-type ecosystem models (e.g., Fasham et al., 1990; Fennel et al., 2006) now widely used in coupled physical-biological climate models (Bopp et al., 2005; Doney et al., 1996; Franks et al., 2013). Even the simplest of these models rely on a

number of parameters with values that are either poorly known or exhibit a large range in the experimental and field literature due to taxonomical differences, date and location of sampling or methodological constraints (e.g., Fahnenstiel et al., 1995; Putland, 2000; Sarthou et al., 2005). For that reason, model optimization techniques are increasingly used to define model parameters objectively (Bagniewski et al., 2011; Fennel et al., 2001; Friedrichs et al., 2007; Schartau et al., 2001; Ward et al., 2010). Here I follow this approach and apply an evolutionary algorithm for model optimization based on climatological values of observed surface chlorophyll in the Subpolar North Atlantic. I further investigate the sensitivity of the model using a second-order Taylor series decomposition to identify the variables that influence the simulated phytoplankton annual cycle most strongly.

My results are in line with the view of the spring bloom as the climax of a continuous process in which bottom-up and top-down forcings act simultaneously (Riley, 1965; Strom, 2002; Behrenfeld et al., 2013), and different processes dominate at different points in time to shape the annual cycle of phytoplankton biomass. The conceptual bases of both the critical-depth and the dilution–recoupling hypotheses are shown to be true within my modelling framework; however, neither of their bloom initiation mechanisms fully applies in the experiments.

The mechanisms through which a simple model like the one I examine here develops a spring bloom could differ from those at play in reality. Rather than providing a new explanation for the spring bloom initiation, this analysis is aimed at emphasizing the processes that require further testing in more realistic models and using observational data sets. The remainder of this chapter is organized as follows: section 2.2 describes the

methods used in the study, including the configuration of the base model; section 2.3 describes the optimized model results and their sensitivity to parameters and variables; in section 2.4 I describe the idealized experiments' configuration and results. Discussion and final conclusions are presented in sections 2.5 and 2.6.

## **2.2 METHODS**

### 2.2.1 DATA SETS

The study region in this chapter is the North Atlantic Ocean, between 40°N – 50°N and 45°W – 15°W (Figure 2.1). I analyze models for six of the twelve 5° latitude by 10° longitude bins presented in Behrenfeld (2010), using satellite-based phytoplankton biomass ( $\text{mg C m}^{-3}$ ) observations and mixed layer depth (m) climatologies from the same study. The analysis includes the lower latitude bins (NA1 to NA3) located at the transition zone from subtropical to subpolar bloom regimes (Henson et al., 2009); and the subpolar region characterized by higher chlorophyll in bins NA4 to NA6. The bins north of 50° N are not used because chlorophyll observations in winter are missing.

The satellite-based phytoplankton biomass climatology ( $P^{obs}$ ) is used to optimize the biological parameters of the base model described in section 2.2, whereas the mixed layer depth climatology ( $H_{MLD}$ ) is used as a model forcing variable to impose time- and depth-varying diffusivities. For details on these climatologies I refer the reader to Behrenfeld (2010) and <http://www.science.oregonstate.edu/ocean.productivity/>. In general, the  $P^{obs}$  climatology is based on eight-day Sea-viewing Wide Field-of-view (SeaWiFS) satellite chlorophyll values from January 1998 to December 2006, spatially averaged for each bin. From there, phytoplankton carbon concentrations were derived by

Behrenfeld (2010) using the Garver-Siegel-Maritorea algorithm for particulate backscattering coefficients (Garver and Siegel, 1997; Maritorea et al., 2002; Behrenfeld et al., 2005). I transformed the phytoplankton carbon concentrations into nitrogen units ( $\text{mmol N m}^{-3}$ ) using the Redfield ratio (106C:16N) as an average approximation, and linearly interpolated the eight-day data to daily resolution for comparison with the model output.

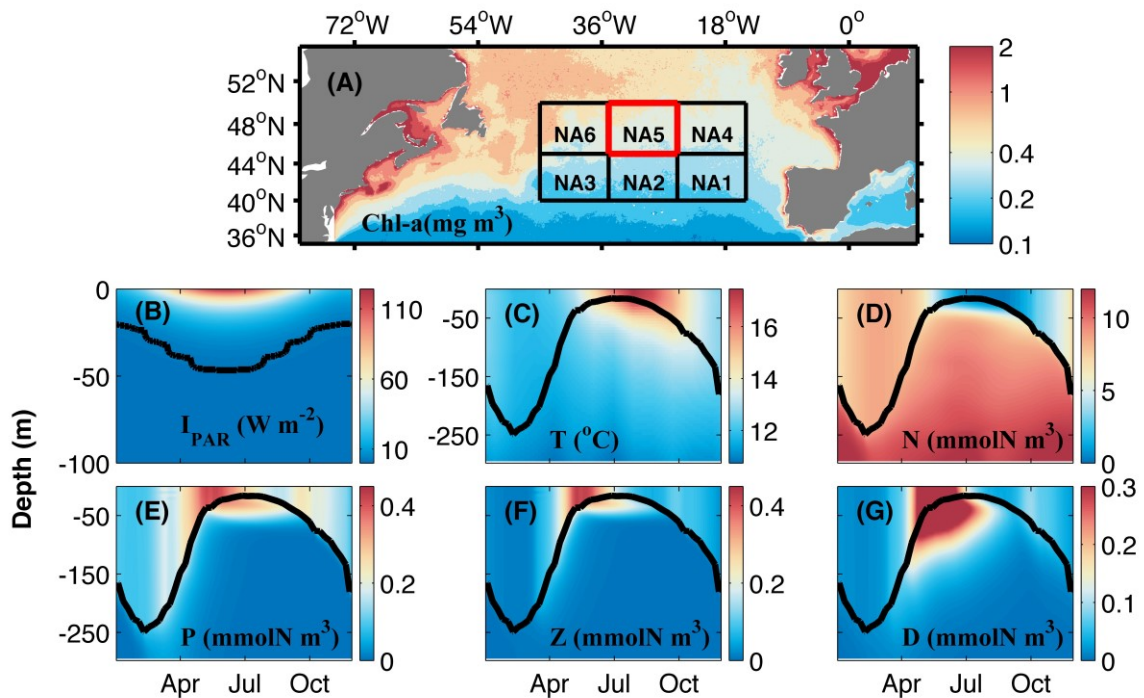


Figure 2.1: (A) Location of the study bins showing, as a reference, the mean annual surface chlorophyll concentration ( $\text{Chl-a}$ ,  $\text{mg m}^{-3}$ ) calculated from eight-day resolution SeaWiFS satellite data from January 1998 to December 2006. The northern bins exhibit higher mean annual chlorophyll than the southern bins. Subplots (B) to (G) correspond to bin NA5. (B) Simulated average daily photosynthetic active radiation ( $I_{PAR}$ ,  $\text{W m}^{-2}$ ). This subplot is restricted to the top 100 m of the water column, and shows the depth of the euphotic zone defined as the depth at which light limitation is lower than 1% ( $\text{Lim}_1 \leq 10^{-2}$ , solid line). (C) Climatological WOA temperature ( $T$ ,  $^{\circ}\text{C}$ ). Optimized NPZD model daily averaged concentrations of (D) nutrients, (E) phytoplankton, (F) zooplankton, and (G)

detritus in  $\text{mmol N m}^{-3}$ . The black solid lines in panels (C) to (G) show the climatological mixed layer depth.

Although phytoplankton carbon biomass estimates derived from scattering properties may be influenced by the particle size distribution (Dall'Olmo et al., 2009), they have been shown to represent phytoplankton biomass well (Behrenfeld and Boss, 2006, 2003; Siegel et al., 2005; Westberry et al., 2008). Comparing the model results against such estimates, instead of satellite chlorophyll, also avoids further model assumptions about the Chl:C ratio, as chlorophyll concentrations may vary independently from biomass due to physiological changes driven by light and nutrient availability (Geider, 1987; Geider et al., 1998; Wang et al., 2009).

I also use the corresponding mixed layer depth climatology for each bin, which was constructed using output from the Simple Ocean Data Assimilation (SODA) model (1998 to 2004) and the Fleet Numerical Meteorology and Oceanography Center (FNMOC) model (2005 to 2006) (see Behrenfeld, 2010 and citations therein). Both models are data-assimilative (i.e., they incorporate available observations to attain the best possible representation of the ocean state), and the resulting mixed layer depth climatology agrees well with climatological values derived from available high vertical resolution temperature and salinity profiles from 1941 to 2002 (de Boyer Montégut et al., 2004). In addition, sea temperature profiles from the World Ocean Atlas 2009 (WOA) climatology provide physical forcing to the model, and WOA nitrate profiles (Garcia et al., 2010) are used to restore nutrient concentrations at depth.

### 2.2.2 BASE MODEL DESCRIPTION

I use a vertically resolved, nitrogen-based NPZD model to replicate the climatological annual cycles of satellite-based phytoplankton biomass in my study bins. While more complex models (i.e., those that simulate more state variables and pathways) may be more realistic than this simple NPZD model, the increased complexity adds more parameterizations and more poorly known parameters (Denman, 2003; Anderson, 2005). Choosing a simple model makes it easier to constrain the model dynamics with limited observations, and allows for easier exploration and interpretation of the effects of perturbing isolated variables.

The model simulates the top 300 m of the ocean with a vertical resolution of 5 m. The vertical grid is divided into two distinct layers: a turbulent surface mixed layer (layer 1) and a quiescent layer below (layer 2). The annual cycle of mixed layer depth ( $H_{MLD}$  in m) is imposed and determines how many grid cells are in each layer at a given point in time. A high diffusivity is assigned to all grid cells above the prescribed  $H_{MLD}$  (representing the active layer 1) and ensures complete mixing within the mixed layer on a time scale of 1 day ( $k_{D1} = H_{MLD}^2$ ;  $\text{m}^2 \text{d}^{-1}$ ). A low diffusivity ( $k_{D2} = k_{D1} \times 10^{-3}$ ;  $\text{m}^2 \text{d}^{-1}$ ) is assigned to all grid cells below (representing the quiescent layer 2). All biological parameters along with their units, and other symbols used throughout the text are listed in Table 2.1.

Phytoplankton (P;  $\text{mmol N m}^{-3}$ ) and zooplankton (Z;  $\text{mmol N m}^{-3}$ ) prey-predator dynamics are represented as follows:

$$\frac{\partial P}{\partial t} = \mu_{max} Lim_N Lim_I P - gZ - l_{PN} P - l_{PD} P - w_P \frac{\partial P}{\partial z} + \frac{\partial}{\partial z} \left( k_D \frac{\partial P}{\partial z} \right) \quad (2.1)$$

$$\frac{\partial Z}{\partial t} = \beta gZ - l_{ZN} Z - l_{ZD} Z^2 + \frac{\partial}{\partial z} \left( k_D \frac{\partial Z}{\partial z} \right), \quad (2.2)$$

where the phytoplankton maximum growth rate ( $\mu_{max}$ ;  $d^{-1}$ ) is modulated by nutrient limitation ( $Lim_N$ ) and light limitation ( $Lim_I$ ) factors, both dimensionless. Nutrient limitation follows  $Lim_N = \frac{N}{k_N + N}$ , where  $k_N$  ( $mmol\ N\ m^{-3}$ ) is the half-saturation constant for nutrient uptake. Light limitation is formulated as  $Lim_I = \frac{\alpha I_{PAR}}{\sqrt{\mu_{max}^2 + \alpha^2 I_{PAR}^2}}$  (Evans and Parslow, 1985; Smith, 1936), where the photosynthetically active radiation ( $I_{PAR}$ ,  $W\ m^{-2}$ ) is a fraction equal to 43% of the total solar radiation.  $I_{PAR}$  decreases exponentially with depth ( $z$ ;  $m$ ) according to  $I_{PAR}(z) = 0.43 I_0^{-z k_I}$ , where  $k_I = 0.1\ m^{-1}$  is the light attenuation coefficient.  $I_0$  is the total incoming solar radiation below the sea surface; it is simulated using the astronomical formula (Brock, 1981), allowing for diel variations and assuming a 40% attenuation by the atmosphere and a solar constant of  $1366.1\ W\ m^{-2}$ . Temperature dependency of the maximum growth rate of phytoplankton is included by a  $Q_{10}$  formulation according to  $\mu_{max} = \mu_0 1.88^{T/10^\circ C}$  ( $d^{-1}$ ; Eppley, 1972), where  $\mu_0$  is the maximum growth rate at  $0^\circ C$ , and  $T$  is the local temperature. The parameters  $l_{PN}$ ,  $l_{PD}$  ( $d^{-1}$ ) are the metabolic loss and mortality rates of phytoplankton, and depend on temperature according to the same  $Q_{10}$  formulation as  $\mu_{max}$ . Phytoplankton metabolic losses feed into the nutrient pool, while mortality losses feed into the detritus pool. The last two terms of equation 2.1 represent phytoplankton sinking at a speed  $w_P$  and vertical mixing.

In Equation 2.2, zooplankton grazing follows a sigmoidal functional form  $g = g_{max} \frac{P^2}{k_p^2 + P^2}$ , where  $g_{max}$  ( $d^{-1}$ ) is the maximum grazing rate and  $k_p$  ( $mmol\ N\ m^{-3}$ ) is the half-saturation for phytoplankton ingestion. Zooplankton assimilates only a dimensionless fraction  $\beta$  of the total consumed phytoplankton; the rest enters the detritus pool. The parameters  $l_{ZN}$  ( $d^{-1}$ ) and  $l_{ZD}$  ( $d^{-1}$  ( $mmol\ N\ m^{-3}$ ) $^{-1}$ ) represent zooplankton excretion and mortality rates, which feed into the nutrient and detritus pools, respectively. They also depend on temperature according to the  $Q_{10}$  formulation described above. The equations for detritus and nutrients are:

$$\frac{\partial D}{\partial t} = ((1 - \beta)g + l_{ZD} Z)Z + l_{PD} P - r_{DN} D - w_D \frac{\partial D}{\partial z} + \frac{\partial}{\partial z} \left( k_D \frac{\partial D}{\partial z} \right) \quad (2.3)$$

$$\frac{\partial N}{\partial t} = -\mu_{max} Lim_N Lim_I P + l_{PN} P + l_{ZN} Z + r_{DN} D + \frac{\partial}{\partial z} \left( k_D \frac{\partial N}{\partial z} \right) + \gamma(N_{WOA} - N). \quad (2.4)$$

Sources of the detrital pool are phytoplankton mortality ( $l_{PD} P$ ), zooplankton mortality ( $l_{ZD} Z^2$ ) and the fraction of unassimilated ingestion ( $(1 - \beta) g Z$ ), which represents sloppy feeding and egested fecal pellets. Detritus is remineralized back to the nutrient pool at the rate  $r_{DN}$  and sinks at a velocity of  $w_D$  ( $m\ d^{-1}$ ; Equation 2.3). Taking into account the limitations of my one-dimensional model, simulated subsurface nutrient concentrations are weakly nudged to the WOA nitrate climatology with the term  $\gamma(N_{WOA} - N)$  in Equation 2.4, where  $\gamma$  is the nudging strength ( $d^{-1}$ ). The highest nudging strength is applied to the bottom grid cells, lower nudging strength to the mid-water grid cells and no nudging to the surface according to:

$$\gamma = \begin{cases} 0, & \text{for } z < \min(H_{MLD}) \\ \frac{1}{90d}, & \text{for } \min(H_{MLD}) \leq z < \max(H_{MLD}) \\ \frac{1}{30d}, & \text{for } z \leq \max(H_{MLD}) \end{cases}, \quad (2.5)$$

where  $\min(H_{MLD})$  and  $\max(H_{MLD})$  are the minimum and maximum depth of the mixed layer during the annual cycle.

### 2.2.3 COST FUNCTION DESIGN

The model is optimized for each of the 6 bins shown in Figure 2.1A, such that the simulated annual cycles of surface phytoplankton best reproduce the available observations. As stated in Chapter 1, parameter optimization consists of systematically adjusting the model parameters, in order to minimize a cost function that measures the mismatch between observations and their model counterparts. The model spins up for 7 years to reach dynamical steady state and, once it has reached equilibrium, an additional year of model output is used to calculate the cost function ( $F(p)$ ), which is defined as:

$$F(\vec{p}) = \sum_{i=1}^n w_i \left( P_i^{obs} - P_i^{sim}(\vec{p}) \right)^2 \quad (2.6)$$

where  $\vec{p}$  is a vector that contains the 13 unknown biological parameters described in Table 2.1;  $n = 365$  is the number of days in the annual cycle;  $P^{obs}$  is Behrenfeld (2010)'s satellite-based phytoplankton carbon biomass climatology transformed into units of nitrogen; and  $P^{sim}$  are daily averages of the surface phytoplankton concentrations simulated using each  $\vec{p}$ . To emphasize the initiation of the spring bloom, the first 150 days  $i=1, \dots, 150$  have a higher weight  $w_i = 3 \text{ (m}^3(\text{mmol N})^{-1})^2$ , while  $w_i = 1 \text{ (m}^3(\text{mmol N})^{-1})^2$ ,  $i=151, \dots, 365$  is used for the rest of the year.

The optimization is implemented using an evolutionary algorithm described in chapter 1. In this chapter, the algorithm runs with a total of 30 parameter sets ( $\vec{p}$ ). The initial parameter population is randomly generated within a range of minimum and maximum parameter values based on observational and modelling literature shown in Table 2.1. In addition to the algorithm crossover mechanism, parameter sets are subjected to random mutations in 6 of their 13 parameter values by adding normally distributed random values with zero mean and a standard deviation of 5% of the respective parameter's range.

As the model is compared only to phytoplankton surface observations, it is difficult to effectively constrain the complete set of parameters. Ward et al. (2010) concluded that there is not a perfect solution to deal with the problem of under-determination of model parameters: if only a subset of parameters is optimized and the unconstrained parameters are fixed to precise values, the model cost is strongly affected by these default values. As parameters may co-vary during their evolution (e.g., Schartau and Oschlies, 2003), fixing some parameters will also affect the optimized parameter values. For these reasons, specifying the possible range of parameter values becomes important (Fennel et al., 2001; Schartau et al., 2001; Schartau and Oschlies, 2003). Within the algorithm, the minimum and maximum range is enforced after the mutation step to avoid unrealistic parameter values; when a parameter value is outside of its range, it is replaced by the corresponding minimum or maximum limit, plus or minus a uniformly distributed random value multiplied by 1% of the parameter range. In comparison to gradient descent methods, the algorithm allows a free random exploration

of the whole parameter space defined by the possible range of parameter values, and is less prone to finding local optima (Ward et al. 2010).

I individually ran three replicate optimizations of 200 generations of the algorithm for each spatial bin (parameter sets NA1<sub>p</sub> to NA6<sub>p</sub>). An additional optimization was performed jointly for all bins ( $\Sigma$ NA), using a joint cost function that is the sum of the individual cost functions  $F(\vec{p})$  for each bin. In all cases, the algorithm rapidly minimizes differences between the observations and model output within approximately 10 generations and the variance in the cost values of the parent population decreases significantly after 20 generations. For example, in bin NA5 the variance in the cost values of the parent population decreases from  $\sigma^2 = 85.91 \text{ (mmol N m}^{-3}\text{)}^2$  to  $\sigma^2 = 0.06 \text{ (mmol N m}^{-3}\text{)}^2$  after 20 generations. At the end of the algorithm, the individual optimizations show an average cost reduction of  $87.8 \pm 10\%$ , while the joint optimization reduces the cost function by 86%.

#### 2.2.4 BASE MODEL SENSITIVITY

I estimated the sensitivity of the model results to the biological parameters qualitatively by doubling and halving each optimal parameter value and rerunning the model (section 2.3.2). I also analyzed the model sensitivity to perturbations in forcing and state variables using a second-order Taylor series expansions of the system of equations (section 2.3.3).

Taylor series expansions have been used to evaluate non-linear radiative feedbacks in atmospheric models (Colman et al., 1997) and interannual variability in air-sea CO<sub>2</sub> flux in a biogeochemical ocean model (Previdi et al., 2009). For this analysis,

the model is denoted as  $\frac{\partial \vec{x}}{\partial t} = \varphi(\vec{x})$  where  $\vec{x}$  is the vector of forcing and state variables including  $N, P, Z, D, PAR, T$  and  $H_{MLD}$ . A small perturbation of the model state,  $\delta \vec{x}$ , will produce a change  $\delta \varphi$  in the model dynamics, that can be approximated by the first two terms of the Taylor Series:

$$\delta \varphi(\vec{x}) \approx \sum_{i=1}^n \frac{\partial \varphi(\vec{x})}{\partial x_i} \delta x_i + \frac{1}{2} \sum_{i=1}^n \sum_{j=1}^n \frac{\partial^2 \varphi(\vec{x})}{\partial x_i \partial x_j} \delta x_i \delta x_j \quad (2.7)$$

The first-order partial derivatives provide estimates of the model's sensitivity to a change in each individual variable; the second-order derivatives provide an indication of how the model's sensitivity to changes in  $x_i$  depends on  $x_j$  and vice versa. I perturb each variable individually by +10% of its annual range (for  $H_{MLD}$ ) or its range at the surface (for the vertically resolved variables). The perturbations are imposed over the optimized steady cycle solution throughout the whole year and at all depths (for the vertically resolved variables).

## 2.2.5 SPRING BLOOM INITIATION METRICS

In my analysis of spring bloom initiation I use two timing metrics, which have been previously used in the literature: 1) the day when a surface phytoplankton concentration threshold is exceeded ( $Day^{P*}$ ) and 2) the day when the net phytoplankton accumulation rate becomes positive ( $Day^{r*}$ ). Defining when the spring bloom effectively starts or which of these two metrics should be used to define it is not an objective of this study and left to other investigators (e.g., Brody et al., 2013). The metrics are intended to evaluate the effects of different processes on spring bloom initiation.

The concentration threshold is a commonly used metric defining bloom initiation as the first day that concentrations rise more than 5% above the median of the annual cycle (Henson et al., 2009, 2006; Platt et al., 2009; Siegel et al., 2002). A drawback of this method is that the amplitude and duration of the bloom affect the threshold value and thus can compromise the ability of this method to identify timing dissimilarities between individual annual cycles, as illustrated by Brody et al. (2013). While this is not a problem when comparing observations and optimized model results, which have similar threshold values, the experimental simulations discussed in section 2.4 exhibit a large range of annual amplitudes and bloom characteristics. In order to use the same threshold metric for both optimized and experimental simulations, I define the bloom onset,  $Day^{P*}$ , after normalizing the simulated surface phytoplankton annual cycles according to:

$$normalized\ P = \frac{P - \min(P)}{\max(P) - \min(P)} \quad (2.8)$$

The threshold for bloom onset is then defined as 5% above the median of the normalized annual cycle.

The second metric of bloom timing,  $Day^{r*}$ , identifies the date when the transition from a decreasing to an increasing phytoplankton inventory occurs. It is based on the phytoplankton inventory accumulation rate ( $r^*$ ), which is defined as the rate of change of vertically integrated phytoplankton. While this inventory value can be calculated from model output, satellite observations do not provide information of the phytoplankton vertical structure. Thus I approximate  $r^*$  as in Behrenfeld (2010) and Behrenfeld et al. (2013). The time-varying depth of the euphotic zone required for this calculation is

defined as the depth at which  $Lim_I \leq 10^{-2}$  (Figure 2.1B). High frequency variability in  $r^*$  is smoothed by applying a 90-day boxcar averaging, and  $Day^{r^*}$  is then defined as the first day (in between one spring bloom and the next) when  $r^*$  becomes positive (Figure 2.3).

Table 2.1: Ecosystem model parameters and symbols used throughout the text. For parameters that were optimized the allowed range during the optimization is shown. Sources: <sup>a</sup>Fennel et al. (2006); <sup>b</sup>Schartau and Oschlies (2003); <sup>c</sup>Sarthou et al. (2005); <sup>d</sup>Fahnenstiel et al. (1995); <sup>e</sup>Veldhuis et al. (2005); <sup>f</sup>Bagniewski et al. (2011), <sup>g</sup>Smayda (1974); <sup>h</sup>Bienfang (1981); <sup>i</sup>Smayda and Bienfang (1983); <sup>j</sup>Walsby and Holland (2006); <sup>k</sup>Gifford et al. (1995); <sup>l</sup>Netjstgaard et al. (2001, 1997); <sup>m</sup>Landry et al. (1984); <sup>n</sup>Tande and Slagstad (1985); <sup>o</sup>Evans and Parslow (1985); <sup>p</sup>Behrenfeld (2010)

Parameter	Description	Range or value	Units
<i>Phytoplankton (P) parameters</i>			
$\alpha$	Initial photosynthetic slope	0.02 – 0.25 <sup>a, b</sup>	(Wm <sup>-2</sup> ) <sup>-1</sup> d <sup>-1</sup>
$\mu_0$	Maximum growth rate at T = 0°C	0.02 – 2.0 <sup>c, d, e</sup>	d <sup>-1</sup>
$k_N$	Half-saturation coefficient of nutrient uptake	0.05 – 3.5 <sup>c</sup>	mmol N m <sup>-3</sup>
$l_{PN}$	Phytoplankton respiration rate at T = 0°C	0.005 – 0.25 <sup>c</sup>	d <sup>-1</sup>
$l_{PD}$	Phytoplankton mortality rate at T = 0°C	0.01 – 0.25	d <sup>-1</sup>
$w_P$	Sinking rate of phytoplankton	0.025 – 2.5 <sup>c, g, h, i, j</sup>	m d <sup>-1</sup>
<i>Zooplankton (Z) parameters</i>			
$g_{max}$	Maximum grazing rate	0.2 – 3.0 <sup>c, d, k, l</sup>	d <sup>-1</sup>
$k_P$	Half-saturation coefficient of grazing	0.5 – 5.0 <sup>a</sup>	mmol N m <sup>-3</sup>
$\beta$	Zooplankton assimilation efficiency	0.25 – 0.95 <sup>m, n</sup>	non-dimensional
$l_{ZN}$	Zooplankton excretion rate at T = 0°C	0.01 – 0.25 <sup>a</sup>	d <sup>-1</sup>
$l_{ZD}$	Zooplankton mortality rate at T = 0°C	0.02 – 0.35 <sup>a, b</sup>	d <sup>-1</sup>
<i>Detritus (D) parameters</i>			
$r_{DN}$	Remineralization rate	0.015 – 0.15 <sup>b</sup>	d <sup>-1</sup>
$w_D$	Sinking rate of detritus	0.05 – 25 <sup>a</sup>	m d <sup>-1</sup>
<i>Additional symbols and non-optimized parameters</i>			
$p^{obs}$	Phytoplankton biomass climatology from satellite	-	mmol N m <sup>-3</sup>
$T$	WOA Temperature climatology	-	°C
$N_{WOA}$	WOA NO3 climatology	-	mmol N m <sup>-3</sup>
$H_{MLD}$	SODA & FNMOC mixed layer depth climatology	-	m
$I_0$	Total incoming solar radiation at the ocean's surface	-	W m <sup>-2</sup>
$I_{PAR}$	Photosynthetic active radiation	-	W m <sup>-2</sup>
$Lim_I$	Light limitation factor for phytoplankton growth	-	non-dimensional

Parameter	Description	Range or value	Units
$Lim_N$	Nutrient limitation factor for phytoplankton growth	-	non-dimensional
$k_{D1}$	Diffusivity coefficient above the mixed layer depth	-	$m^2 d^{-1}$
$k_{D2}$	Diffusivity coefficient below the mixed layer depth	-	$m^2 d^{-1}$
$k_I$	Light attenuation coefficient	$0.1^\circ$	$m^{-1}$
$\gamma$	Nudging strength	Eq. 2.5	$d^{-1}$
$R$	Vertically integrated phytoplankton growth minus vertically integrated phytoplankton losses	Eq. 2.9	$mmol N m^{-2}$
$H_{cr}$	Critical-depth, defined as where $R = 0$	-	m
$H_{euph}$	Depth of the euphotic zone, defined as the depth at which $Lim_1 < 1\%$	-	m
<i>Optimization</i>			
$\vec{p}$	Parameter set (P, Z, and D parameters in this table)	-	-
$F(\vec{p})$	Cost value of parameter set $p$	Eq. 2.6	-
$p^{sim}$	Simulated surface phytoplankton in the cost function	-	$mmol N m^{-3}$
$w$	Weight in the cost function	-	$(m^3 (mmol N)^{-1})^2$
$NA\#_p$	Individually optimized parameter set	-	-
$\sum NA_p$	Jointly optimized parameter set	-	-
<i>Sensitivity analyses</i>			
$\Delta max(P)$	Change in maximum annual surface phytoplankton concentrations	-	$mmol N m^{-3}$
$\Delta max(r^*)$	Change in maximum annual phytoplankton inventory accumulation rates	-	$d^{-1}$
$\Delta Day^{P^*}$	Change in the date of bloom initiation according to $Day^{P^*}$	-	d
$\Delta Day^{r^*}$	Change in the date of bloom initiation according to $Day^{r^*}$	-	d
$\varphi$	System state in the Taylor decomposition analysis	-	-
$\vec{x}$	Vector of the model's variables in the Taylor decomposition analysis	-	-
<i>Bloom timing metrics</i>			
normalized P	Normalized annual cycle of surface phytoplankton biomass used to define $Day^{P^*}$	Eq. 2.7	non-dimensional
$r^*$	Phytoplankton inventory accumulation rate <sup>p</sup> , shortly referred as accumulation rate, used to define $Day^{r^*}$	-	$d^{-1}$
$Day^{P^*}$	Date of bloom initiation, biomass-based metric	-	Day of Year
$Day^{r^*}$	Date of bloom initiation, phytoplankton inventory accumulation rate metric	-	Day of Year
<i>Experimental simulations</i>			

Parameter	Description	Range or value	Units
$\xi$	Zooplankton accumulation term or entrainment	Exp. I	$\text{mmol N m}^{-3}\text{d}^{-1}$
$\frac{\xi}{Z \beta g}$	Zooplankton entrainment over grazing	Exp. I	non-dimensional
$Z_{total}$	Total zooplankton biomass in the mixed layer	Exp. III	$\text{mmol N m}^{-2}$
$H_{MLD}^*$	Idealized mixed layer depth	Exp. III	m

## 2.2.6 EXPERIMENTAL SIMULATIONS

Using the optimized models as a base, I proceed to perform three experiments aimed to examine whether and under what conditions the bloom initiation mechanisms portrayed in the critical-depth and dilution-recoupling hypotheses occur in the system. The experiments are summarized in Table 2.4, and changes made to the model configurations in order to run each experiment are explained along the experiments' results in section 2.4. Experiment I tests the addition of a mechanism that concentrates zooplankton in response to a shoaling mixed layer. Experiment II evaluates the system's response in the absence of mixed layer fluctuations. The final Experiment III further focuses on the effects of direct and physically driven changes in zooplankton biomass, forcing them to be completely decoupled from changes in food availability. Results of the experiments are here exemplified using bin NA5 and are consistent over all bins (Appendix A).

## 2.3 OPTIMIZED SIMULATION RESULTS

### 2.3.1 PLANKTON ANNUAL CYCLES

In general, the optimized simulations represent the observed surface phytoplankton well (Figure 2.2), especially during the spring bloom initiation. The

solutions also show low bias and root-mean-square errors, and are highly correlated with the observations (Table 2.2), accomplishing the purpose of the optimization algorithm. The model tends to underestimate phytoplankton during the bloom peak, and produces a delayed fall bloom in the northern bins. A fall bloom, which is not present in the observations, is also simulated in the southern bins. Aside from differences in the fall concentrations, the development of the spring bloom and the annual cycle of phytoplankton are captured remarkably well in the individually and jointly optimized models, especially when considering the model's simplicity. The model also captures other aspects of real plankton communities such as a subsurface phytoplankton biomass maximum during summer (Figure 2.1E) and the spatial increase in average phytoplankton concentrations from southern to northern bins (Figure 2.2, Appendix A).

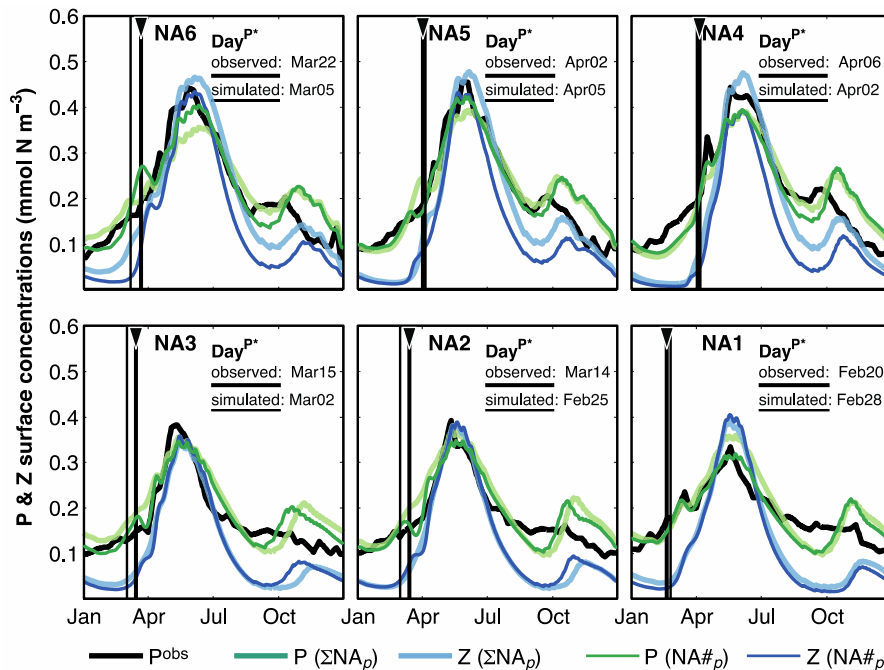


Figure 2.2: Comparison between satellite-based phytoplankton biomass ( $P^{\text{obs}}$ ) and daily averaged simulated phytoplankton using jointly ( $\Sigma NA_p$ ) and individually ( $NA\#_p$ ) optimized parameters. The solid vertical lines mark the day of bloom initiation

according to the biomass based metric  $Day^{P*}$  in the observations (thick line with inverted triangle on top) and individually optimized simulations (thin line).

Simulated zooplankton concentrations are very low in winter, start increasing rapidly in April and peak about the same time as phytoplankton, matching or exceeding phytoplankton concentrations. Zooplankton then decrease in parallel with phytoplankton from June to October and remain low throughout winter. Unfortunately no observations specific to the area can be directly used to validate or constrain parameters of the zooplankton functional group in my model (i.e., a combination of micro- and mesozooplankton). Because they are limited to larger species, zooplankton estimates from Continuous Plankton Recorder observations are better used to qualitatively validate models with a separate mesozooplankton group (e.g., Lewis et al., 2006). Nonetheless, the simulated zooplankton cycles agree qualitatively with the annual cycle of copepod abundances in the area (Colebrook, 1979).

The individually optimized models replicate the observed  $Day^{P*}$  accurately with an average bias of 7.8 days (Table 2.3, Figure 2.2); that is, according to the biomass threshold method, the simulated bloom initiation precedes the observed by about a week. The second metric  $Day^{r*}$  is also accurate, exhibiting an average bias of 4.3 days. In my simulations, positive accumulation rates occur during winter as in the observations (Figure 2.3, 2. 3), which is a key criticism of the critical depth hypothesis. In comparison to the individually optimized results, slightly larger misfits are observed using the jointly optimized parameters, especially with respect to  $Day^{P*}$  and  $Day^{r*}$  (Table 2.3). For that

reason I choose to use the individually optimized parameters throughout the remainder of the manuscript.

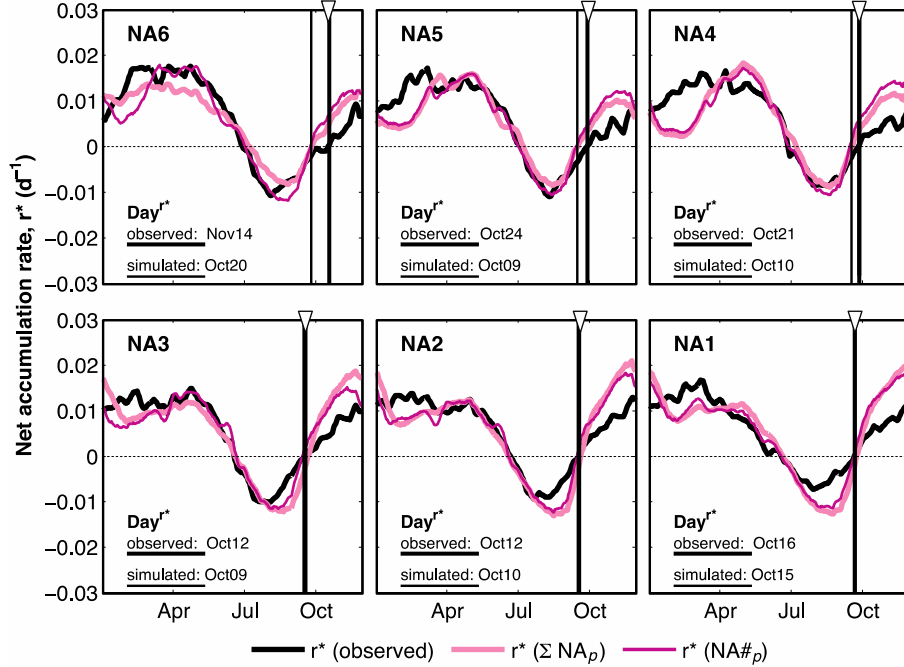


Figure 2.3: Phytoplankton inventory net accumulation rates,  $r^*$ , estimated from the phytoplankton biomass observations (black line) and from the simulations using jointly ( $\Sigma NA_p$ , thick pink line) and individually ( $NA\#_p$ , thin purple line) optimized parameters. The solid vertical lines mark the day of bloom initiation according to the accumulation rate metric ( $Day^{r^*}$ ) in the observations (thick line with inverted triangle on top) and individually optimized simulations (thin line). In the bottom panels the thick and thin vertical lines coincide.

### 2.3.2 OPTIMAL PARAMETER VALUES

The individually optimized parameters show spatial differentiation between northern and southern bins (Figure 2.4), mainly driven by the parameter values of detrital sinking ( $w_D$ ), grazing rate ( $\mu_{max}$ ), the nutrient uptake half-saturation ( $k_N$ ), and the phytoplankton growth parameter ( $\mu_0$ ). The first and second principal components (PC1

and PC2) explain 87% and 6.4% of the variance among parameter sets. The parameter  $w_D$  explains 98% of PC1 and 15% of PC2 (85% of total variance);  $\mu_{max}$   $g_{max}$  explains 11% of PC1 and 75% of PC2 (7% of total variance);  $k_N$  explains 9% of PC1 and 62% of PC2 (6.8% of total variance); and  $\mu_0$  explains 6% of PC1 and 15% of PC2 (0.6% of total variance). The parameter  $w_D$  is higher in the southern bins, whereas  $g_{max}$  and  $w_P$   $\mu_0$  are higher in the northern bins.  $k_N$  does not vary consistently with latitude. As northern and southern bins are different in terms of light, mixed layer depth, nutrient and chlorophyll regimes (Henson et al., 2009), the differences in parameter values reflect these features (Appendix B.). It is important to reiterate that despite the small spatial differences in these parameters, model solutions using the jointly optimized parameter set  $\sum NA_p$  are very similar to the individually optimized ones (Table 2.2, 2.3; Figure 2.2, 2.3).

Table 2.2: Optimal parameters resulting from individual and jointly optimizations. The variance ( $\sigma^2$ ) of optimal parameters with respect to all bins and the joint optimization is shown as a reference of spatial differences in parameter values. The cost value (F), root mean square error (RMSE) and goodness of fit ( $r^2$ ) are shown as metrics comparing the performance of simulated surface phytoplankton with respect to satellite-based phytoplankton biomass.

	NA1	NA2	NA3	NA4	NA5	NA6	$\sum NA$	$\sigma^2$
$\alpha$	0.1149	0.1472	0.1115	0.1835	0.2099	0.1249	0.1953	0.0017
$\mu_0$	0.9174	0.9280	0.9918	0.5976	0.7894	0.6548	0.6989	0.0232
$k_N$	2.4856	2.0795	1.7406	2.1135	3.4151	2.3549	2.3868	0.2754
$g_{max}$	3.4191	2.6684	2.4796	2.1533	2.0811	1.8010	2.1522	0.2832
$k_P^2$	0.8048	0.5208	0.5012	0.5109	0.5373	0.5470	0.5573	0.0113
$\beta$	0.9108	0.9178	0.9169	0.8038	0.8781	0.9463	0.9116	0.0021
$l_{PN}$	0.0065	0.0061	0.0094	0.0052	0.0062	0.0088	0.0066	0.0000
$l_{PD}$	0.0116	0.0124	0.0124	0.0102	0.0109	0.0109	0.0101	0.0000
$l_{ZN}$	0.0191	0.0109	0.0102	0.0193	0.0133	0.0102	0.0102	0.0000
$l_{ZD}$	0.2757	0.3948	0.3984	0.3693	0.3998	0.3954	0.3395	0.0021
$r_{DN}$	0.1217	0.1490	0.1218	0.1402	0.1401	0.1455	0.1213	0.0001

	NA1	NA2	NA3	NA4	NA5	NA6	$\sum$ NA	$\sigma^2$
$w_D$	4.3870	2.7667	2.2903	6.9805	5.0400	6.3737	2.7489	3.4671
$w_P$	0.1260	0.1279	0.1115	0.1330	0.1117	0.1118	0.2551	0.0027
$F$	0.4095	0.3800	0.5840	0.8760	0.5475	0.8395	5.3290	-
RMSE (NA# $_p$ )	0.0313	0.0308	0.0334	0.0446	0.0354	0.0405	-	-
RMSE ( $\sum$ NA $_p$ )	0.0409	0.0406	0.0429	0.0406	0.0383	0.0455	-	-
$r^2$ (NA# $_p$ )	0.75	0.84	0.84	0.83	0.90	0.85	-	-
$r^2$ ( $\sum$ NA $_p$ )	0.75	0.80	0.78	0.85	0.88	0.89	-	-

Overall, the algorithm favored optimal values of  $\mu_0$  between 0.6 d<sup>-1</sup> and 1 d<sup>-1</sup>. Accounting for the effect of temperature dependency on phytoplankton growth, realized maximum growth rates ( $\mu_{max}$ ), are within the range of observed values (Fahnenstiel et al., 1995b; Sarthou et al., 2005). For example, in bin N5  $\mu_{max}$  ranges between 1.48 d<sup>-1</sup> and 2.46 d<sup>-1</sup> given temperatures between 10°C and 18°C. The phytoplankton metabolic loss and mortality rates consistently show a tendency toward the lower limit imposed in the optimization. The excretion rate of zooplankton also tends toward low values, whereas the zooplankton mortality rates and assimilation efficiency tend toward values at the upper limit (Table 2.2). Although these estimates are close to those applied in other ecosystem models, the algorithm's behaviour may be influenced by the limited availability of observations (Schartau and Oschlies, 2003). A detailed discussion of these tendencies is outside the scope of this manuscript and may distract from the objectives of this analysis. Nevertheless, as experimental results may be influenced by the choice of parameter values, it is important to estimate how they affect the model response.

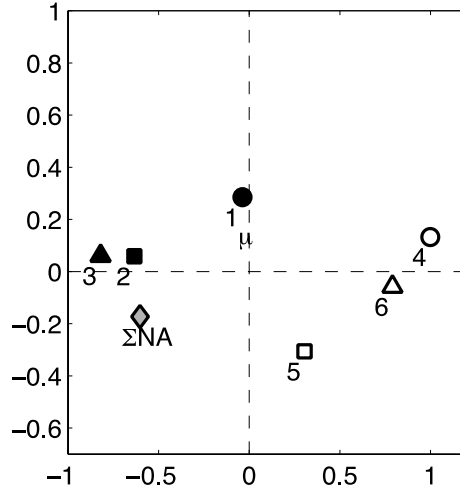


Figure 2.4: Results of the principal component analysis of optimized parameters, showing the scaled arrangement of optimized parameter sets projected onto the first and second principal component (PC1, PC2). Solid black symbols represent parameter sets for the southern bins ( $\Sigma NA_p$  NA1<sub>p</sub> to NA3<sub>p</sub>), empty symbols are for the northern bins (NA4<sub>p</sub> to NA6<sub>p</sub>), and the gray diamond corresponds to the jointly optimized parameter set ( $\Sigma NA$ ). The distance between their symbols is representative of how different the parameter sets are. The location of the symbols  $w_D$ ,  $g_{max}$ ,  $k_N$ ,  $\mu_0$  represents the scaled contribution of these parameters to the variance explained by PC1 and PC2.

By analyzing the model sensitivity to doubling and halving each optimized parameter value (Figure 2.5), I observe that  $w_D$  has a negligible impact on the phytoplankton annual cycle, which explains why  $\Sigma NA_p$  parameters are able to fit all observed cycles despite differences in this parameter (Figure 2.4). Most interestingly, I find that parameters that primarily affect the phytoplankton formulation ( $\alpha$ ,  $\mu_0$ ,  $k_N$ ,  $w_P$ ,  $l_{PN}$ ,  $l_{PD}$ ) modify the shape of the climatological annual cycle, and affect the slope of bloom development and thus timing of the bloom. In particular, the model is highly sensitive to changes in  $\mu_0$ ; doubling its value produces an earlier increase in phytoplankton, while halving it produces a delayed and more abrupt bloom.

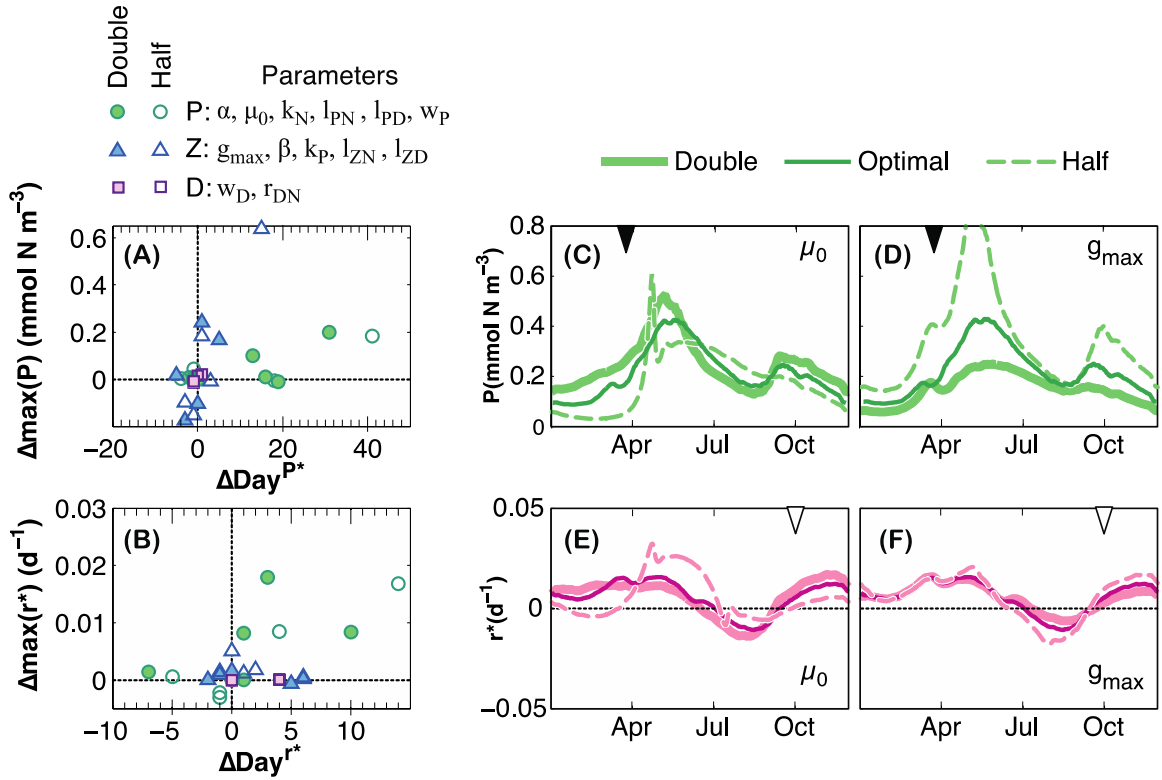


Figure 2.5: Sensitivity of the simulated surface phytoplankton biomass ( $P$ ) and inventory accumulation rate ( $r^*$ ) to halving (empty symbols) and doubling (filled symbols) optimal parameter values, exemplified by results in bin NA5. (A) and (B) show the change in the date of bloom initiation according to the biomass-based metric ( $\Delta\text{Day}^{P^*}$ ) and the accumulation rate metric ( $\Delta\text{Day}^{r^*}$ ), as well as the change in maximum phytoplankton biomass and accumulation rates ( $\Delta\max(P)$  and  $\Delta\max(r^*)$ , respectively). Different symbols are used to represent the biological variable each parameter primarily modifies (i.e., phytoplankton ( $P$ , green circles), zooplankton ( $Z$ , blue triangles) or detritus ( $D$ , purple squares)). These values were obtained by comparing the optimized results against the sensitivity tests (i.e., test minus optimized simulation). Subplots (C) to (F) show how the temporal evolution of phytoplankton biomass and net phytoplankton accumulation rate responds to variations in parameters  $\mu_0$  and  $g_{max}$ . As a reference, the inverted triangles on top of the x-axes show the date of bloom initiation in the observations according to the biomass-based metric (black, (C) and (D)) and the metric based on the accumulation rate (white, (E) and (F)).

The opposite effect is observed when modifying the loss rates  $l_{PN}$  and  $l_{PD}$ . Parameters that directly affect grazing ( $g_{max}, k_P, \beta, l_{ZN}, l_{ZD}$ ) modify the average

phytoplankton concentrations throughout the year, but mostly preserve the shape of the phytoplankton annual cycle. Phytoplankton is not sensitive to changes in zooplankton excretion ( $l_{ZN}$ ), and only sensitive to zooplankton mortality ( $l_{ZD}$ ) during summer.

Table 2.3: Spring bloom initiation metrics estimated using the satellite-based phytoplankton biomass ( $P^{obs}$ ), and simulated surface phytoplankton using individually optimized parameters ( $NA\#_p$ ) for each bin, and jointly optimized parameters ( $\sum NA_p$ ) for all bins.  $Day^{P^*}$  is the biomass-based metric and  $Day^{r^*}$  is the metric based on the phytoplankton inventory accumulation rate.

	$Day^{P^*}$			$Day^{r^*}$		
	$P^{obs}$	$NA\#_p$	$\sum NA_p$	$P^{obs}$	$NA\#_p$	$\sum NA_p$
NA1	52	57	51	290	289	293
NA2	74	60	57	286	284	290
NA3	75	62	52	286	283	292
NA4	97	95	93	294	284	286
NA5	93	96	75	298	283	286
NA6	82	68	61	319	294	296

### 2.3.3 MODEL SENSITIVITY TO VARIABLES

Results of the analysis of model sensitivity to perturbations in physical and biological variables (Figure 2.6) show that independent perturbations (i.e., 1<sup>st</sup> derivative) of light, zooplankton and temperature result in the strongest effects on phytoplankton surface concentrations in spring, when increases in light and temperature lead to increases in phytoplankton, while increases in zooplankton lead to a decrease. Perturbations in light and temperature affect predominantly the surface, while zooplankton perturbations affect the entire water column. As nutrients are abundant during winter and spring, perturbing N only affects phytoplankton in summer and fall. Locally, changes produced by perturbing  $H_{MLD}$  can be up to two orders of magnitude greater than those that result from perturbing

the other variables, but they only act to redistribute concentrations within the water column. The vertically integrated change in phytoplankton produced by perturbing the mixed layer is negligible ( $<10^{-10}$  mmol N  $m^{-2}$ ) when compared against vertically integrated changes produced by perturbations in all other variables (Figure 2.6F).

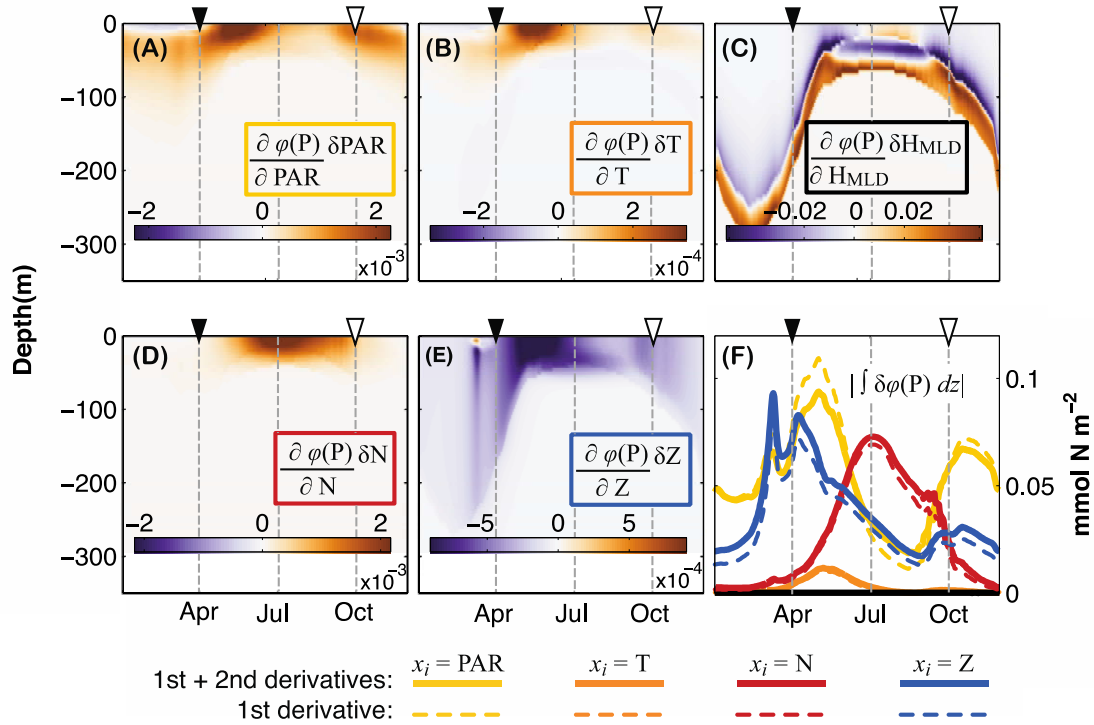


Figure 2.6: Phytoplankton sensitivity to small perturbations in physical and biological variables, using a 2<sup>nd</sup> order Taylor approximation. The surface subplots show the first order phytoplankton response to perturbations in (A) photosynthetic active radiation; (B) temperature; (C) mixed layer depth; (D) nutrient; and (E) zooplankton. Subplot (F) shows the absolute vertically integrated 1<sup>st</sup> (dashed) and 1<sup>st</sup> + 2<sup>nd</sup> (solid) order terms of the Taylor approximations. The vertically integrated effect of perturbations to the mixed layer is negligible, as changes above and below the mixed layer offset each other. As a reference, the inverted triangles on top of the x-axes show the date of bloom initiation in the observations according to the biomass-based metric (black) and the metric based on the accumulation rate (white).

When comparing the absolute vertically integrated values, I notice that for the given set of optimized parameters the model is most sensitive to light and zooplankton, where the model's sensitivity to light is the larger of the two terms for most of the year. When the second derivative terms are added (solid lines in Figure 2.6F), the overall effect of light is slightly decreased, but is still significantly higher than the effect of zooplankton during winter. The effect of perturbing zooplankton is equivalent in magnitude to the effect of perturbing light during April, at the time when the shoaling of the  $H_{MLD}$  and the highest phytoplankton accumulation rates occur.

Table 2.4: Brief description of the idealized experiment configurations and main conclusions.

Experiment	Treatment	Conclusions
Exp. I. Zooplankton accumulation mechanism (i.e., entrainment): - Modified Eq. 4 - Section 4.1 - Figure 7	Accumulation mechanism term added to Equation 4.	Effects of zooplankton entrainment over phytoplankton are small. Zooplankton response is dominated by food availability.
Exp. II. Constant mixed layer depth: - No seasonal fluctuations of mixed layer - 10 years experimental conditions - Section 4.2 - Figure 8	a. Constant $H_{MLD} = \max(H_{MLD})$ b. Constant $H_{MLD} > \max$ (Euphotic depth) c. Constant $H_{MLD} > \min$ (Euphotic depth) d. Constant $H_{MLD} = \min(H_{MLD})$	Shoaling of the mixed layer enhances phytoplankton growth by improving light conditions; as long as the shoaling does not compromise nutrient availability or phytoplankton residence time within the mixed layer. Zooplankton response is dominated by food availability.
Exp. III. Part I: Constant zooplankton biomass, varying total zooplankton concentrations: - Disrupted P to Z feedback - Climatological $H_{MLD}$ - 10 years experimental conditions - Section 4.3 - Figure 9A-E	a. Low zooplankton biomass ( $Z_{total} = 5 \text{ mmol N m}^{-2}$ ) b. High zooplankton biomass ( $Z_{total} = 10 \text{ mmol N m}^{-2}$ )	Lower zooplankton biomass produces higher phytoplankton biomass overall. Changes in bloom initiation are small because the same nutrient level is available.

Experiment	Treatment	Conclusions
Exp III. Part 2: Constant zooplankton biomass, varying winter zooplankton dilution levels by changing winter mixed layer depth: <ul style="list-style-type: none"> <li>- Disrupted P to Z feedback</li> <li>- Idealized <math>H_{MLD}^*</math> with varying maximum winter depths</li> <li>- 10 years experimental conditions</li> <li>- Section 4.3</li> <li>- Figure 9F-J</li> </ul>	a. Low zooplankton biomass ( $\max(H_{MLD}^*) = \max(H_{MLD})$ ) b. High zooplankton biomass ( $\max(H_{MLD}^*) = 25$ m)	Shallow winter mixed layers produce increased winter phytoplankton biomass and accumulation rates despite high grazing rate and decreased nutrient availability. Shallow winter mixed layers enhance phytoplankton growth by improving light conditions.

## 2.4 EXPERIMENTAL SIMULATIONS

### 2.4.1 EXPERIMENT I: ZOOPLANKTON RESPONSE TO A SHOALING MIXED LAYER

Early experiments with an idealized 0D model by Evans and Parslow (1985) examined how simulated phytoplankton annual cycles were influenced by seasonal fluctuations of the mixed layer. When conceptualizing their model, they postulated that phytoplankton and zooplankton respond asymmetrically to the shoaling of the mixed layer assuming that a deepening mixed layer equally dilutes both types of organisms, but that a shoaling of the mixed layer would affect motile zooplankton by concentrating them in the mixed layer while a fraction of the relatively motionless phytoplankton would remain below the mixed layer. This asymmetric response to a shoaling mixed layer is in line with the dilution-recoupling hypothesis, in the sense that the physically driven accumulation of zooplankton contributes to the recoupling of the planktonic prey-predator relationship (Behrenfeld, 2010). However, Evans and Parslow also showed that spring blooms can occur in the absence of mixed layer fluctuations (see section 2.4.2), which argues against the shoaling of the mixed layer as a mechanism for spring bloom initiation,

and indirectly dismisses the asymmetric response as a process involved in seasonal bloom dynamics. Furthermore, motile zooplankton may stay below the mixed layer to follow their prey, instead of tracking the mixed layer shoaling, because non-motile phytoplankton are not concentrated during the shoaling.

In order to verify whether the hypothetical accumulation of zooplankton in response to a shoaling mixed layer has any effect on phytoplankton annual cycles in my model, I followed Evans and Parslow's formulation of the mechanism by introducing the zooplankton accumulation term  $\xi = -\frac{1}{H_{MLD}} \frac{dH_{MLD}}{dt} Z$  on the right hand side of Equation 2.2, and allowing it to take effect only when the mixed layer shoals, i.e.,  $\frac{dH_{MLD}}{dt} < 0$ . I expect a noticeable direct effect on zooplankton concentrations in the surface mixed layer and an indirect one on phytoplankton only if the term  $\xi$  is significant in comparison to the zooplankton growth rate (i.e., the first term in Equation 2.2). The ratio of these two terms, the non-dimensional number  $\frac{\xi}{Z \beta g}$ , is plotted in Figure 2.7A for a preliminary inspection of the potential effects of the zooplankton concentrating mechanism. High values of this number would indicate that the accumulation of zooplankton driven by the mixed layer shoaling contributes significantly to total biomass changes in the mixed layer, a condition that can only occur at low  $\beta g$  (i.e., low phytoplankton concentrations) and high  $\frac{\xi}{Z}$  (i.e., small  $H_{MLD}$  and a rapidly shoaling mixed layer). The black dots in Figure 2.7A show that high values of  $\frac{\xi}{Z \beta g}$  do not occur at any time throughout year ( $\frac{\xi}{Z \beta g}$  is always smaller than 0.3).

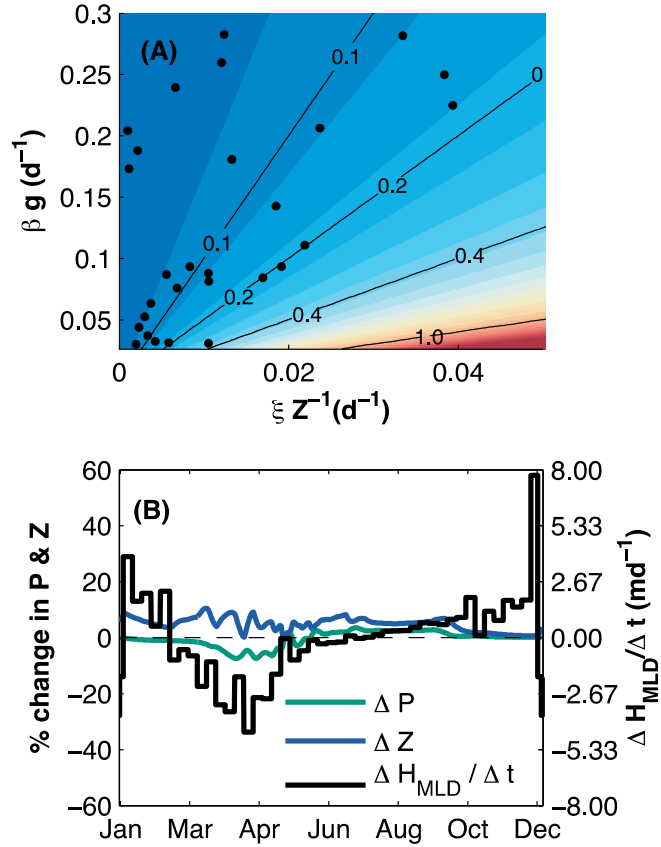


Figure 2.7: (A) Relative contribution of the accumulation of zooplankton biomass due to a shoaling mixed layer ( $\xi Z^{-1}$ ) over changes in zooplankton biomass due to assimilated grazing ( $\beta g$ ) in bin NA5. Black dots show actual values of the non-dimensional number  $\frac{\xi}{Z \beta g}$  from the optimized annual cycles, subsampled every 4 days. (B) Annual cycle of changes in the mixed layer ( $\frac{\Delta H_{\text{MLD}}}{\Delta t}$ , black line) and percent change in simulated surface phytoplankton (green line) and zooplankton (blue line) concentrations caused by the application of an explicit zooplankton response to the mixed layer shoaling.

When the zooplankton accumulation mechanism is added to the model, only small differences in phytoplankton and zooplankton concentrations are observed. For instance, the metrics of bloom initiation change only by up to 2 days. Percentage changes in phytoplankton and zooplankton (Figure 2.7B) were evaluated by comparing model results

with and without the additional term in the zooplankton equation  $\left(\frac{\text{Experiment}-\text{Optimized}}{\text{Optimized}} \times 100\right)$ . The mechanism produces a 10% increase in zooplankton concentrations between March and April; however, as zooplankton concentrations are very low during these months, the change in zooplankton concentration translates into a ~7% decrease in surface phytoplankton during the peak of the spring bloom and a 3% increase of fall concentrations. This suggests that although the active zooplankton response to a shoaling mixed layer is plausible and does affect phytoplankton biomass and accumulation rates, it is not a major contributor to changes in the community phenology of the Subpolar North Atlantic as portrayed in my model.

#### 2.4.2 EXPERIMENT II: SYSTEM RESPONSE IN THE ABSENCE OF MIXED LAYER FLUCTUATIONS

I address another of Evans and Parslow's considerations, which had implications for the critical-depth paradigm: the development of blooms in the absence of mixed layer fluctuations. Specifically, I present results obtained by setting the mixed layer depth as constant year-round at its minimum and maximum climatological values (e.g., 16 m and 249 m for NA5). I also use two intermediate constant mixed layers (50 and 25 m), which are shallower than the annual maximum but deeper than the maximum and minimum euphotic zone depth, respectively. The euphotic zone depth is defined as the depth at which light limitation for phytoplankton growth is lower than 1% ( $\text{Lim}_I < 1\%$ ). For the experiments, the model is initialized with the distribution of state variables resulting from the optimized simulations and forced with a constant  $H_{MLD}$  for 10 years. Nutrient nudging ( $\gamma = 1/30$ ) is limited to the bottom 15 m, as it would otherwise introduce dynamics similar to a time varying mixed layer.

When analyzing the resulting spring bloom initiation according to both metrics (Figure 2.8A-B), the constant mixed layers which were shallower than the minimum euphotic zone (25 and 16 m) produced delayed blooms in comparison with the one obtained with a very deep mixed layer. In contrast, the treatment with a mixed layer of 100 m produced the earliest of the blooms (Figure 2.8A-B). These patterns can be better understood when observing the conditions during the initial years of the experimental runs (Figure 2.8C-E). When experimental conditions are first enforced, all simulations have non-limiting nutrient conditions. All experimental mixed layers shallower than the maximum produce an immediate abrupt increase in phytoplankton concentrations followed by an increase in zooplankton. This abrupt increase in biomass can be explained by improved light conditions. Over time, the shallower mixed layer depths (i.e. 100, 25 and 16 m) inhibit an effective injection of nutrients to the surface, resulting in year-round low-nutrient concentrations within the mixed layer (Figure 2.8E). Phytoplankton growth can still occur below these shallow mixed layers, where nutrients and light are available, but the stagnant bottom layer allows phytoplankton to sink rapidly (Lande and Wood, 1987). The combined effect of surface nutrient depletion and aggravated sinking losses diminishes phytoplankton surface concentrations and delays the bloom initiation according to both  $Day^{P^*}$  and  $Day^{Z^*}$  metrics in the 25 m and 16 m mixed layer cases. Nonetheless, the constant 100 m mixed layer is able to improve phytoplankton exposure to light, without significantly increasing its sinking losses and thus, over time, it maintains higher biomass than the deepest mixed layer case.

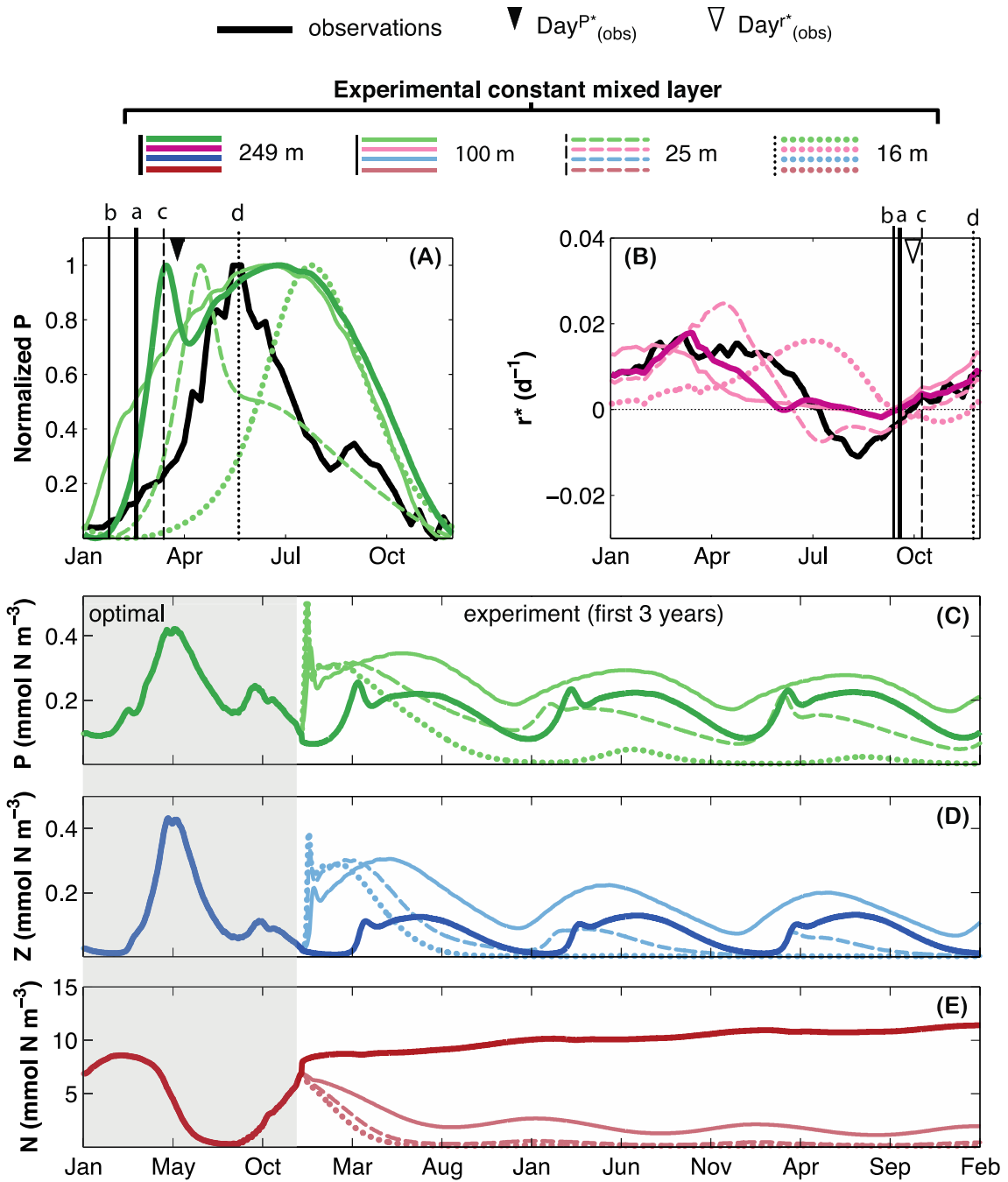


Figure 2.8: Results of Experiment II in bin NA5: model runs during 10 years using constant mixed layer depths equal to a.249m (maximum time varying  $H_{MLD}$ ), b.50m (below maximum euphotic depth), c.25m (below minimum euphotic depth), and d.16m (minimum time varying  $H_{MLD}$ ). (A) Normalized satellite-based phytoplankton biomass (“observations”) and simulated surface phytoplankton of the last experimental cycle, used to determine the date of bloom initiation according to the biomass based metric ( $\text{Day}^{P^*}$ ). (B) Net phytoplankton accumulation rate estimated from “observations” and experimental simulations of the last experimental cycle, used to determine the date of bloom initiation according to the rate metric ( $\text{Day}^{r^*}$ ). Vertical lines in (A) and (B) respectively mark

Day<sup>P\*</sup> and Day<sup>r\*</sup> in each experiment, while the inverted triangles at the top x-axes mark Day<sup>P\*</sup> and Day<sup>r\*</sup> in the observations as a reference. (C), (D) and (E), show the corresponding surface phytoplankton, zooplankton and nutrient optimal cycles and the first 3 annual cycles of experimental conditions.

I can therefore generalize that a shoaling of the mixed layer enhances phytoplankton growth by improving light conditions; this may result in an increase in phytoplankton biomass and accumulation rates, as long as the shoaling does not compromise nutrient availability or phytoplankton residence time within the mixed layer.

#### 2.4.3 EXPERIMENT III: EFFECTS OF ZOOPLANKTON DILUTION AND CONCENTRATION

Results of experiments I and II demonstrate that food availability dominates the zooplankton response in the model (Figure 2.6, 2.7D). To avoid that dominant response, in this experiment I intentionally disrupted the bottom-up feedback from phytoplankton to zooplankton by directly prescribing different zooplankton biomasses in the mixed layer. Therefore, this experiment goes a step further than the zooplankton concentrating experiment (experiment I) in terms of testing the dilution-recoupling mechanism. It is possible that in experiment I winter zooplankton concentration is lower than in reality and thus the effect of dilution/recoupling is not as strong as it should be. By artificially imposing zooplankton, here we circumvent this issue and directly test whether a deepening/shoaling of the mixed layer creates large enough changes in grazing pressure to significantly affect phytoplankton concentrations. By prescribing a constant, vertically integrated zooplankton biomass ( $Z_{total}$  in  $\text{mmol N m}^{-2}$ ) in the mixed layer,  $H_{MLD}$  effectively dilutes and concentrates zooplankton ( $Z$  in  $\text{mmol N m}^{-3}$ ) in these simulations (see schematic of the experiment in Figure 2.10A). I aim to answer whether and how these

physically driven changes in zooplankton concentrations affect the timing of the phytoplankton spring bloom according to my two timing metrics. Again all experiments were run for 10 years.

The resulting cycles illustrate that the amount of zooplankton diluted in the mixed layer influences phytoplankton concentrations (Figure 2.9A,C) and accumulation rates (Figure 2.9B) in a similar fashion as modifying zooplankton parameters did (Figure 2.5): the main change is in the magnitude of the bloom, with small shifts in timing. When low  $Z_{total}$  is present in the mixed layer, the phytoplankton bloom peak is larger than in the case with high  $Z_{total}$ . In both cases, the peak is significantly larger than in the observations, and a  $Z_{total}$  as large as 20 mmol N m<sup>-2</sup> would be needed to produce a bloom peak of similar magnitude as the observations. In the scenario with high  $Z_{total}$ , zooplankton concentrations effectively keep the growth of phytoplankton in check, resulting in lower winter phytoplankton, a smaller bloom peak, and a shorter bloom.

The bloom initiation metrics have opposite patterns in this experiment. Low  $Z_{total}$  produces an earlier  $Day^{P*}$  than high  $Z_{total}$ , but a delayed  $Day^{r*}$ . That is, the biomass-based bloom initiation metric pattern agrees with the dilution-recoupling hypothesis (i.e., lower zooplankton = earlier bloom); but the metric based on the accumulation rate, which was used to develop the hypothesis, does not. Somewhat counter-intuitively, high zooplankton biomass during summer not only decreases phytoplankton biomass through heavy grazing, but also increases phytoplankton growth rates by providing recycled nutrients through excretion. The change in  $Day^{P*}$  by doubling  $Z_{total}$  from 5 to 10 mmol N m<sup>-2</sup> is only 8 days in bin NA5 (6.3 days on average for all bins). There are larger differences in the bloom initiation date according to  $Day^{r*}$  (16 days in bin NA5, and 13.6 days on

average for all bins), but given that it behaves opposite to what was envisioned by the dilution-recoupling hypothesis, I consider that neither of the bloom timing metrics supports the idea that an increase in winter zooplankton biomass, decoupled from ecosystem feedbacks, can significantly delay the spring bloom; i.e., more zooplankton does not necessarily produce a delayed bloom, but a smaller one. As seen in Figure 2.5D, F, phytoplankton biomass in the model appears to be more sensitive to changes in zooplankton parameters than the accumulation rates.

As the dilution-recoupling hypothesis discusses variations in grazing forced by the mixed layer deepening, in a new set of experiments I use equal values of constant zooplankton biomass to evaluate the effect of different winter dilution levels independently (Figure 2.9F-J). In these experiments, I configure  $Z_{total} = 10 \text{ mmol N m}^{-2}$  as constant within the mixed layer and vary the maximum depth of the mixed layer annual cycle (249m and 25m, in Figure 2.9). For this purpose, I define an idealized climatological evolution of the mixed layer depth,  $H_{MLD}^*$ , that allows us to control maximum depth values while preserving the minimum summer values in all cases, such that zooplankton concentrations are equal during summer, but diluted to different concentrations as the mixed layer deepens.  $H_{MLD}^*$  is similar to that of Evans and Parslow (1985) and replicates the timing of deepening and shoaling of the climatological mixed layer depth used in the optimized simulations (Figure 2.9A).

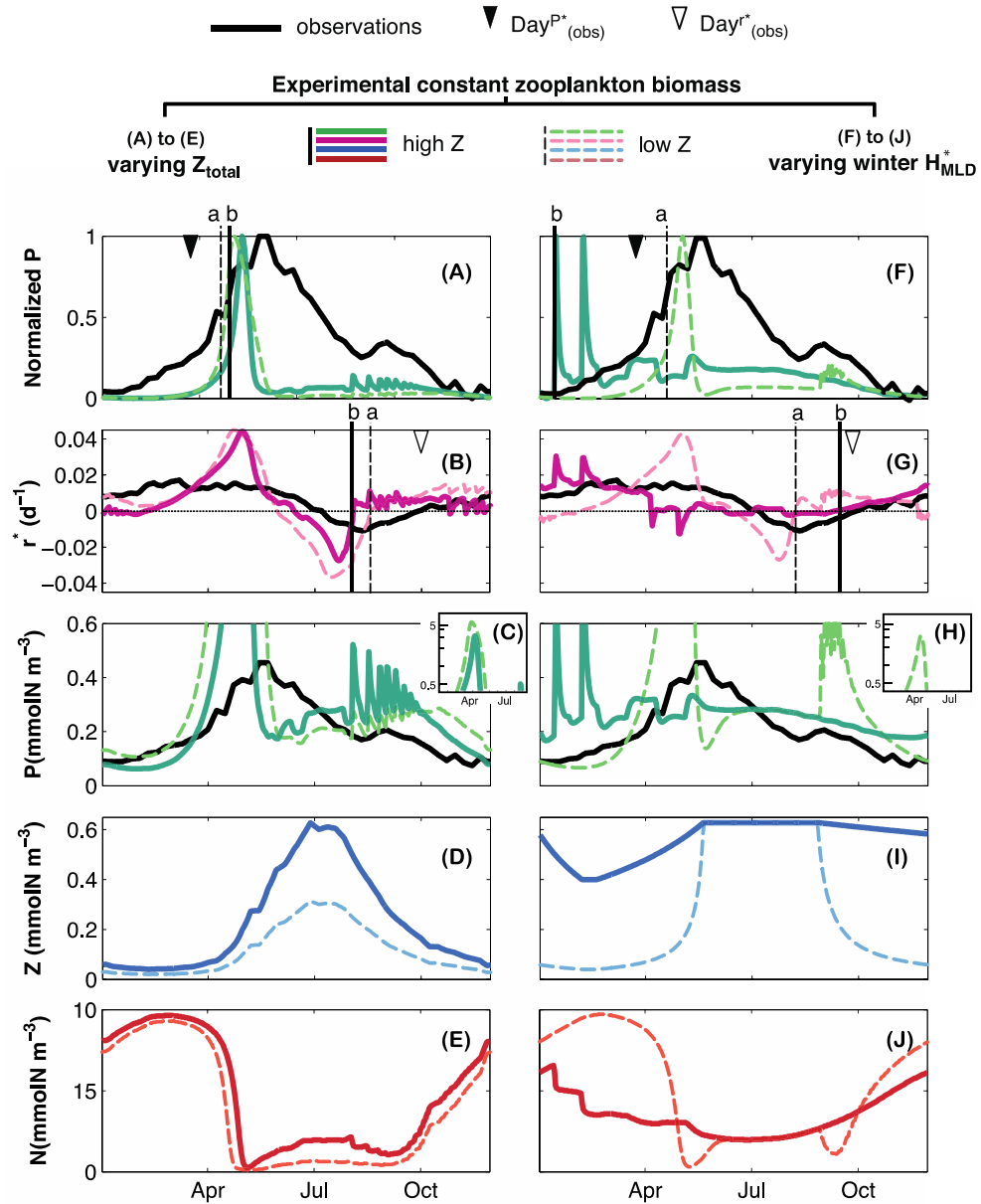


Figure 2.9: Results of Experiment III in bin NA5: constant zooplankton biomass experiments in bin NA5 after 10 years of experimental conditions. Subplots (A) to (E) use the prescribed mixed layer annual cycle in  $H_{MLD}$ , but prescribe the total amount of zooplankton in the mixed layer such that: a. “low Z” refers to  $Z_{total} = 5$  mmol N  $m^{-2}$  and b. “high Z” to  $Z_{total} = 10$  mmol N  $m^{-2}$ . Subplots (F) to (J) use  $Z_{total} = 10$  mmol N  $m^{-2}$  and the idealized mixed layer annual cycle  $H_{MLD}^*$  to compare results with different winter mixed layer depths, as a proxy to impose different winter dilution levels to zooplankton: a. “low Z” is achieved with  $\max(H_{MLD}^*) = 249$  m and b. “high Z” uses  $\max(H_{MLD}^*) = 25$  m. (A) and (F) Normalized phytoplankton satellite-based biomass (“observations”) and simulated surface phytoplankton of the last experimental cycle, used to determine the date of bloom initiation according to the biomass based metric ( $DayP^*$ ). (B) and (G) Net

phytoplankton accumulation rate estimated from “observations” and experimental simulations of the last experimental cycle, used to determine the date of bloom initiation according to the rate metric ( $Day^{r^*}$ ). Vertical lines in the normalized P and  $r^*$  subplots mark the date of bloom initiation according to the biomass and rate based metrics ( $Day^{P^*}$  and  $Day^{r^*}$ , respectively) in the experiments. The inverted triangles at the top x-axes mark  $Day^{P^*}$  and  $Day^{r^*}$  in the observations, as a reference. (C) and (H) show the corresponding phytoplankton satellite-based biomass (“observations”) and simulated surface phytoplankton of the last experimental cycle. (D), (I) and (E), (J) show the corresponding surface zooplankton and nutrient annual cycles, respectively.

Based on the dilution-recoupling hypothesis, deeper winter mixing would be expected to produce early positive accumulation rates that translate into an early spring bloom. The bloom initiation metric based on accumulation rate,  $Day^{r^*}$ , supports this theoretical behavior. The first positive accumulation rates for shallow winter mixing occur later than for deep winter mixing ( $Day^{r^*} = 358$  and  $278$ , respectively); but rates in the shallow winter mixing case are consistently increasing from October onward and exceed those obtained in winter for the case with deep winter mixing (Figure 2.9G). In terms of phytoplankton biomass (Figure 2.9F, H), the bloom appears to initiate earlier when the winter mixed layer is shallow ( $Day^{P^*} = 15$  for a winter mixed layer of 25 m, compared to  $Day^{P^*} = 120$  when using 249 m). This occurs as the intermediate mixed layer depth of 25 m maintains phytoplankton in the upper ocean layers and exposes them to better light conditions during winter, allowing high positive growth rates despite low incoming light and high grazing. In coherence with the results of the constant mixed layer experiment, here the shallow winter mixed layer hinders annual nutrient replenishment (Figure 2.9J) and determines the upper limit of phytoplankton concentrations.

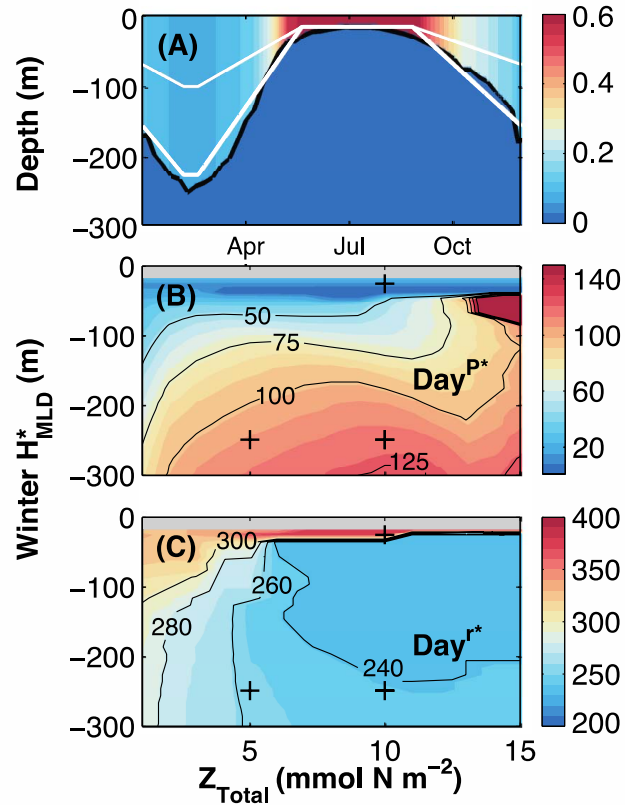


Figure 2.10: (A) Scheme of Experiment III: shows a constant zooplankton biomass  $Z_{\text{total}} = 10 \text{ mmol N m}^{-2}$  prescribed in the mixed layer, being diluted and concentrated by the climatological mixed layer depth  $H_{\text{MLD}}$  (black). Zooplankton concentrations below the mixed layer are  $0 \text{ mmol m}^{-3}$ . White lines show examples of the idealized mixed layer,  $H_{\text{MLD}}^*$ , with two different winter values: 100 m and 225 m. (B) Date of bloom initiation according to the biomass-based metric  $\text{Day}^{\text{P}^*}$ , in Julian days. (C) Date of bloom initiation according to the accumulation rate-based metric  $\text{Day}^{\text{r}^*}$ , in Julian days. The symbol “+” in (B) and (C) marks  $Z_{\text{total}}$  versus the  $\max(H_{\text{MLD}}^*)$  conditions used in Figure 2.9. Winter mixed layers shallower than the climatological minimum were not tested (gray background).

I tested 450 combinations of winter  $H_{\text{MLD}}^*$  and  $Z_{\text{total}}$  and compare the results in terms of  $\text{Day}^{\text{P}^*}$  and  $\text{Day}^{\text{r}^*}$  (Figure 2.10B, C). The response is non-linear; however, it reproduces the same conclusions derived from Figure 2.9: when the bloom initiation is estimated using the biomass-based metric ( $\text{Day}^{\text{P}^*}$ ), deep winter dilution produces a late

bloom initiation, shallow dilution an early one (Figure 2.9B). This is opposite to what one would expect if physical decoupling of phytoplankton growth and grazing had a major effect on the spring bloom onset. When the phytoplankton inventory accumulation rates are considered ( $Day^{r*}$ ), the changes in bloom initiation due to changes in winter mixed layer depth are coherent with the dilution–recoupling mechanism; however, shifts in timing are only significant when the winter mixed layer is shallow (winter  $H_{MLD}^* < 100$  m) and when zooplankton biomass is very low ( $Z_{total} = 5 \text{ mmol N m}^{-2}$ ).

This agrees with the results of experiment I (section 2.4.1) and suggests that a different regime exists where physical dilution of zooplankton is a significant factor determining the bloom initiation. This different regime may be exemplified by subtropical areas and High-Nutrient-Low-Chlorophyll areas with little deep mixing. These areas are characterized by small phytoplankton sizes, and low and rather constant biomass, where grazing is recognized as an important control (Fasham et al., 1990; Miller et al., 1991; Steele and Henderson, 1992).

## **2.5 DISCUSSION**

### **2.5.1 IS THE OPTIMIZED MODEL CONSISTENT WITH THE CRITICAL-DEPTH HYPOTHESIS?**

My optimized model results replicate observations with positive phytoplankton inventory accumulation rates starting in late autumn and throughout winter (Table 2.3, Figure 2.3); the inability of the critical-depth hypothesis to explain positive net accumulation is one of its most frequently reiterated criticisms. In discussing my results, I distinguish two key aspects of the critical-depth hypothesis: 1. the bloom initiation criterion, and 2. the critical-depth model.

The bloom initiation criterion simply states that “bloom can occur only if the depth of the mixed layer is less than the critical value” (Sverdrup, 1953). This critical depth value has been calculated with the help of analytical models (e.g., Siegel et al., 2002; Sverdrup, 1953; Platt et al., 1991) as the depth where the vertically integrated phytoplankton production is matched by the vertically integrated phytoplankton “destruction” by respiration. If the term “destruction”, used by Sverdrup (1953), is assumed to include all community losses, mixing and sinking, rather than only phytoplankton metabolism (Smetacek and Passow, 1990), the critical depth ( $H_{cr}$ ) at any point in time can be found directly from the vertically resolved model output as the depth at which depth-integrated growth equals depth-integrated losses, or:

$$R(z, t) = \left[ \int_{-z}^0 (\mu_{max} Lim_N Lim_I P) dz \right] \quad (2.9)$$

$$- \left[ \int_{-z}^0 \left( gZ + l_{PN}P + l_{PD}P + \frac{\partial}{\partial z} \left( k_D \frac{\partial P}{\partial z} \right) \right) dz + w_P \frac{\partial P}{\partial z} \Big|_{-z} \right] = 0$$

That is,  $H_{cr} = z$ , when  $R(z, t) = 0$ . The values of  $R(z, t)$  are plotted in Figure 2.11 and show that my estimates of  $H_{cr}$  differ significantly from previous analytical calculations:  $H_{cr}$  is very deep during the phytoplankton accumulation phase (positive  $r^*$ ), hence the critical depth criterion ( $H_{cr} > H_{MLD}$ ) holds for all simulations. In my model, the critical depth dramatically deepens in winter (Figure 2.11) as a combined result of sufficient nutrient supply, low winter grazing rates and small increases in light. This occurs because my model breaks an initial assumption of the critical depth model: the relationship between phytoplankton growth and loss rates is not constant in time as Sverdrup had assumed (see Sverdrup (1953) assumption 7 and equation 6).

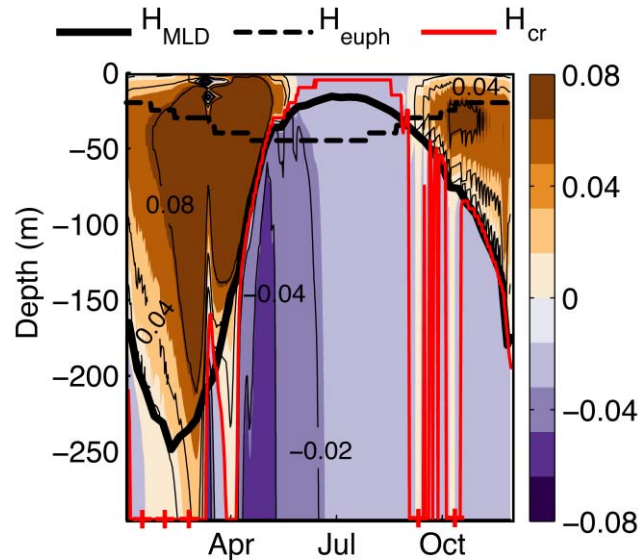


Figure 2.11: Vertically integrated phytoplankton growth minus vertically integrated phytoplankton losses as function of integration depth calculated downward from the surface (i.e.,  $R(z,t)$  in equation 2.9), for bin NA5. The critical depth ( $H_{cr}$ ) is found where  $R(z,t) = 0$ , which lies deeper than the mixed layer depth ( $H_{MLD}$ ) prior to the spring and fall blooms. The critical-depth criterion for bloom initiation ( $H_{cr} > H_{MLD}$ ) is therefore satisfied. Red + symbols denote periods when the critical depth is deeper than the model domain.  $H_{euph}$  marks the depth of the euphotic zone as a reference.

This inadequate assumption affected Sverdrup's critical-depth values and led him to assume the mixed layer shoaling as being key to bloom initiation. My experimental results about the role of the mixed layer are consistent with considerations in Evans and Parslow (1985): spring blooms develop in the absence of mixed layer fluctuations, and large early blooms are produced when the mixed layer is constantly deep while small delayed ones occur when it is constantly shallow. Nonetheless, the small and delayed blooms simulated with shallow constant mixed layers do not contradict Sverdrup's view of an enhanced phytoplankton growth due to the mixed layer shoaling. In both, Evans and

Parslow's and my experiments, experimental conditions were maintained for several years producing low surface nutrient concentrations and small phytoplankton winter seed populations; hence, they violate Sverdrup's assumptions and are not testing the effects of shoaling *per se*. The immediate effect of imposing shallow mixed layers under non-limiting nutrient conditions is indeed an abrupt increase in phytoplankton biomass (see experiment II).

The main effects of the mixed layer fluctuations in my experimental results are the modification of nutrient availability in the euphotic zone, and the control of phytoplankton losses below the mixed layer, which is thought to act as a driver for phytoplankton species succession (Margalef, 1978). Deep mixed layers not only supply the amount of nutrients that determines bloom magnitude, but may also allow fast-sinking species, such as diatoms, to return to the euphotic zone (Lande and Wood, 1987) and become part of the seed population that dominates early stages of the spring bloom. On the other hand, the shallowing of the mixed layer plays an important role in nutrient depletion and selection of slow-sinking species, which are characteristic of the fall and winter phytoplankton composition.

An enhancement of phytoplankton growth due to improved light exposure is also observed in the zooplankton dilution experiment (experiment III) where, despite high grazing and low winter nutrient availability, a shallow winter mixed layer produces higher winter phytoplankton biomass and inventory accumulation rates than those obtained using a deep winter mixed layer. Therefore, my results show that the critical-depth criterion is always satisfied when the system achieves positive net phytoplankton accumulation rates and that improvement in light availability due to mixed layer

shallowing as envisioned by Sverdrup occurs in my model, however it is not a strictly required process for the spring bloom initiation.

#### 2.5.2 IS THE OPTIMIZED MODEL CONSISTENT WITH THE DILUTION-RECOUPLING HYPOTHESIS?

The simulated zooplankton annual cycles (Figure 2.1F; Figure 2.2) are consistent with top-down control, as proposed by Behrenfeld (2010), in that the deepening of the mixed layer, which in the forcing data begins in August, may contribute to phytoplankton survival during winter by relieving grazing pressure. Moreover, the results of my experiments with zooplankton dilution agree with incubation experiments (e.g., Landry, 1993; Putland, 2000) in the sense that high maximum accumulation rates are achieved when zooplankton biomass is low (Figure 2.9B), and when winter dilution is increased (Figure 2.9G). Similar to my discussion about the critical-depth hypothesis, in discussing the dilution-recoupling hypothesis I distinguish its two main statements: 1. The spring bloom starts as the consequence of a decoupling between total phytoplankton growth and losses; 2. The main reason for this decoupling is a decrease in zooplankton grazing caused by dilution when the mixed layer deepens.

In Figure 2.12, I show that the optimized model meets the first statement. Phytoplankton losses (i.e., grazing + mortality + respiration) vertically integrated over the entire model domain closely match phytoplankton growth throughout the year. Slight imbalances (i.e., a “decoupling”) between total growth and losses occur prior to both the spring and fall blooms, the spring bloom being the larger and roughly starting in January. Following Behrenfeld (2010)’s methodology (i.e.,  $r^*$  and  $Day^{r^*}$ ), the imbalances can occur as early as October of the year preceding the spring bloom. Regardless of whether I integrate the entire vertical water column or use Behrenfeld (2010)’s methodology, the

imbalance leading to spring bloom development occurs prior to the shoaling of the mixed layer.

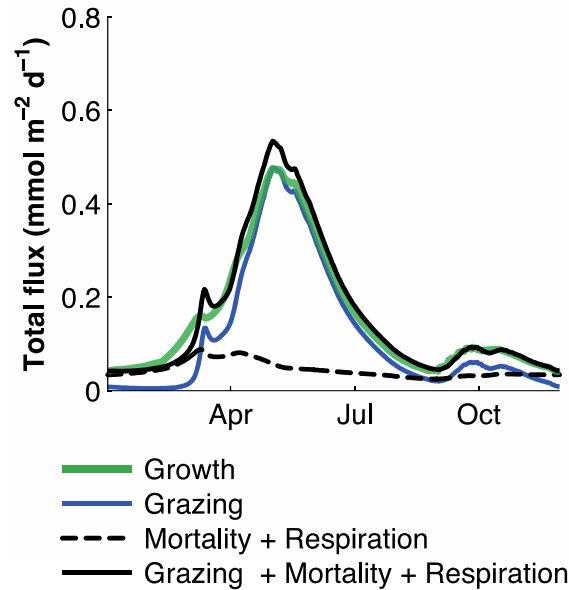


Figure 2.12: Phytoplankton growth and loss (grazing, mortality, respiration) rates, vertically integrated over the model domain (total flux in  $\text{mmol m}^{-2} \text{d}^{-1}$ ). Small imbalances of “decoupling” between total growth and losses determine the bloom initiation and termination.

My results do not support the second statement. Under a realistic model configuration, represented by the optimized model, the effects of changes in grazing parameters on initiation of positive accumulation rates ( $Day^{*}$ ) are negligible ( $< 6$  days); however the grazing parameters affect maximum phytoplankton concentrations. Even when the shoaling of the mixed layer is assumed to actively stimulate zooplankton accumulation (experiment I), the overall effect on phytoplankton is small (the dominant effects are feedbacks via the zooplankton response); such that the depth to which zooplankton are diluted is not as important as whether there are sufficient food resources

(e.g., experiment II). Behrenfeld et al., (2013) also already acknowledged the dominance of food availability over the zooplankton response, leading them to restate the dilution-recoupling hypothesis as disturbance-recovery hypothesis. Under this broader concept, the decoupling between phytoplankton growth and losses can be caused by any disturbance of ecological or physical nature. For instance, when experimentally imposing changes in zooplankton concentrations that are independent of changes in food availability, significant shifts in bloom initiation can occur (Figure 2.10).

In summary, simulated zooplankton populations do strongly modulate phytoplankton biomass throughout the year, and thus an appropriate low grazing (i.e., “decoupling” of growth and grazing rates) is a required condition for phytoplankton to achieve positive growth during winter. As discussed by Strom (2002), systems where growth and grazing are more tightly coupled throughout the entire year will be more stable and less reactive to perturbations (Pimm, 1984), such as events that change the light or nutrient availability.

### 2.5.3 LIMITATIONS

As in all modelling studies, the results of my experiments are tied to the model’s assumptions and limitations, which I discuss here in order to highlight processes that require further investigation to discern between competing hypotheses for the bloom initiation.

My model represents a system that is highly sensitive to light, zooplankton and nutrients; where parameters involved in phytoplankton growth have the ability of modifying both the shape and maximum magnitude of the phytoplankton biomass annual

cycle. Parameters involved in zooplankton grazing mainly determine the average annual phytoplankton biomass, by modifying phytoplankton concentrations throughout the year without changing the temporal pattern of the annual cycle. My model also replicates a decoupling between phytoplankton growth and grazing prior to the bloom initiation. This model behavior is probably caused by the inherent lag between phytoplankton and zooplankton that results from the grazing functional form. The sigmoidal grazing function used here produces a slower slope of increase in grazing when phytoplankton concentrations are low, implying a type of threshold feeding behavior. Threshold feeding is originally based on empirical evidence of mesozooplankton feeding (e.g., Frost, 1975; Gismervik and Andersen, 1997; Wickham, 1995) and has been also shown to apply to microherbivory (Lessard and Murrell, 1998). Such thresholds may correspond to nutritional inadequacy of phytoplankton, zooplankton physiology or changes in feeding strategies. Representing grazing in this form for a natural community may also account for phytoplankton evolutionary strategies to prevent grazing, such as morphological and chemical defenses (Strom, 2002). Different grazing functional forms, as well as higher predation functional forms (i.e., zooplankton mortality) can significantly affect the behavior of simple and more complex ecosystem models (Anderson et al., 2010; Edwards and Yool, 2000; Steele and Henderson, 1992). For instance, Mariani et al. (2013) concluded that an increase in biomass, observed on idealized 0D simulations with adaptive grazing, was driven by changes in predation rather than increases in nutrients or light. Furthermore, other processes not resolved by simple models may also affect the zooplankton phenology independently from phytoplankton biomass, such as horizontal advection, changes in zooplankton composition and zooplankton migration patterns (Aita et al., 2003; Ji et al., 2010). Grazing rates at low prey concentrations and on natural

plankton assemblages remain a key uncertainty in the understanding of phytoplankton net growth during winter (Strom et al., 2000); in this sense, models depend on field and laboratory observations to properly define their assumptions about prey-predator relationships.

Another limitation of my approach is the analysis of spatially averaged climatologies. The approach is used to gain understanding about the cyclical conditions that lead to an annually recurring bloom development (Evans and Parslow, 1985). Nonetheless, understanding spatial and intraseasonal variations is necessary to better predict regional interannual variability of phytoplankton biomass. Franks (2014) warns about the possibility of representing misleading plankton dynamics with the analysis of spatially averaged climatological properties, because of the highly non-linear behavior of quantities such as phytoplankton growth and turbulence. The seasonal deepening of the mixed layer plays a key role in my simulations to replenish nutrients in the euphotic zone; but the model environment used in this chapter cannot test the role of other factors that can determine bloom initiation by affecting nutrient availability, such as ocean fronts and eddies (Taylor and Ferrari, 2011b; Mahadevan et al., 2012). Moreover, imposed diffusivities effectively redistribute planktonic organisms in the climatological mixed layer in the model, such that more intense high-frequency mixing events may produce different phytoplankton and zooplankton dynamics.

Also concerning my use of the mixed layer depth forcing, large uncertainty exists on the differentiation between the actively mixed layer (i.e., turbulent layer) and mixed layer diagnosed from density profiles (Brainerd and Gregg, 1995; Franks, 2014). For instance, the appearance of spring blooms in unstratified water columns has been

explained by weak turbulence (Colebrook, 1979; Townsend et al., 1992; Wasmund et al., 1998; Chiswell, 2011; Huisman et al., 1999a, 1999b) or by the cessation of convective mixing (Fennel, 1999; Taylor and Ferrari, 2011a). In order to fulfill the critical-depth model assumption of a thoroughly mixed top layer, I assumed that the mixing and mixed layer depths are identical in the model. The imposed mixed/mixing depth thus defines a simplified vertical structure for turbulence, which is in reality a highly variable property (Franks, 2014). The vertical structure of turbulence may play a key role in determining the residence time of phytoplankton cells within the euphotic zone (Backhaus et al., 2003; Huisman et al., 2002; Lande and Wood, 1987; Ward and Waniek, 2007). I can argue that the optimized parameters in my model represent a type of phytoplankton community that benefits from intermediate to deep mixing, such that sinking cells are able to recirculate within the euphotic zone. When the constant  $H_{MLD}$  is shallow, a large amount of sinking phytoplankton is lost below the mixed layer, resulting in a delayed bloom of lower magnitude. In a more realistic scenario, species succession may determine the dominance of small, slow-sinking cells during summer months (Margalef, 1978). Further investigation, combining observations and models, is required to discern whether simplified climatological forcing is indeed representative of the processes leading to the spring bloom development in nature. In particular, it is important to define how the planktonic community as a whole, as well as individual functional groups, react to high-frequency fluctuations in turbulence and the turbulence vertical structure.

Given these limitations, my results support the general idea that under sufficient nutrient supply, improved light conditions in combination with low zooplankton populations allow “turbulence-adapted” cells to initiate the spring bloom.

## 2.6 CONCLUSION

My optimized and experimental results suggest that the spring bloom initiation cannot be seen as a purely bottom-up or top-down process. The conceptual bases of both, the critical-depth and the dilution-recoupling hypotheses, are shown to be true within my modelling framework and cannot be considered in absolute isolation under realistic simulations. It has to be pointed out that the fundamental ideas of both hypotheses are ecological truisms: a) positive net growth of phytoplankton occurs when the critical depth is greater than the mixed layer depth (Sverdrup, 1953), and b) low zooplankton concentrations during winter allow phytoplankton growth to exceed its losses (Behrenfeld, 2010). Under realistic and idealized configurations, both conditions occur in my model prior to a bloom development; however, neither the critical-depth nor the dilution-recoupling hypothesis fully applies during bloom initiation in my experiments.

The bottom-up and top-down approaches mainly diverge on their view of the role that the mixed layer plays in regulating plankton populations. The critical depth model postulates that the shoaling of the mixed layer at the beginning of spring triggers the bloom by enhancing available light for phytoplankton. More specifically, the model predicts that the bloom starts when the mixed layer depth becomes shallower than the critical depth. This implies that the critical depth is shallower than the mixed layer depth in winter – a condition that is not met in my model simulations and also likely not met in reality. Sverdrup's conclusions about the critical depth and the role of stratification onset were probably affected by his assumption of a constant ratio between phytoplankton growth and losses. As noted already by Smetacek and Passow (1990) and Behrenfeld (2010), this assumption is incorrect and also is not met in my model, where a profound

critical depth is present during winter when positive phytoplankton accumulation rates occur. However, maximum phytoplankton accumulation rates and bloom onset do indeed coincide with the time when the mixed layer becomes shallower than the critical depth.

An imbalance or “decoupling” of growth and grazing rates occurs prior to bloom development, but it occurs as result of ecological feedbacks rather than physical forcings as had been postulated in the dilution-recoupling hypothesis. Nonetheless, appropriate low grazing should be seen as a required condition for bloom development to the same extent that phytoplankton light and nutrient requirements have to be satisfied. In this sense, there might not exist a unique “trigger” for the spring bloom initiation but it will depend on the system’s base line conditions at the end of the preceding year, and the bloom development may closely track the last of these “bloom-forming conditions” that remains unsatisfied. Overall, caution should be used when extrapolating experimental conclusions to reality.

## **CHAPTER 3:**

### **EVALUATING ECOSYSTEM MODEL COMPLEXITY IN THE NORTHWEST NORTH ATLANTIC, PART I: SURROGATE-BASED OPTIMIZATION**

#### **3.1 INTRODUCTION**

Since the emergence of numerical marine ecology, models have diversified from describing simple prey predator relationships (e.g., Riley, 1965) to representing multiple plankton functional groups and chemical variables, with dependencies on the characteristics of the physical environment (e.g., Kishi et al., 2007; Follows and Dutkiewicz, 2011). To date there is no consensus on the most appropriate level of ecosystem complexity, model structure, and parameterizations of functional relationships. Both simple and complex models have advantages and disadvantages. As demonstrated in Chapter 2, the use of simple marine ecosystem models under idealized conditions has proven to be valuable in identifying and understanding underlying mechanisms (e.g., Evans and Parslow, 1985; Fasham et al., 1990; Kuhn et al., 2015). However, it has been argued that more realistic representations of the plankton community composition and the interrelationships of marine food webs are required to improve forecasting capabilities in regional and global models (Le Quéré, 2006).

Regardless of its complexity, any model depends on many parameters that describe biological and chemical rates of change such as growth, mortality, and degradation rates, including maximum rates and half-saturation concentrations in nutrient uptake and predation formulations. As models are developed for specific regions or

periods, their parameters are typically calibrated to fit observations for those specific regions or time periods. This may lead to overfitting, a loss of model forecasting skill and of portability to different geographic locations. In general, the number of parameters increases with the number of state variables in a model (Denman, 2003); thus, complex models are at a higher risk of overfitting. Moreover, most of these parameters are poorly known with wide ranges reported in the literature. Studies using systematic calibration methods, known as parameter optimization, have shown that typically available observational sets are often not sufficient to determine more than a few of these parameters (Fennel et al. 2001, Friedrichs et al., 2007; Ward et al., 2010). Parameter values may also change depending on the plankton community composition, and thus it is possible that models need to consider parameter variations with geography (Losa et al., 2004) or time (Mattern et al., 2012).

Following the principle of parsimony, the simplest model able to fit the observations should be favoured over more complex ones. Failure of a model to replicate observations suggests that the model structure may be missing key components of the system's behaviour. Conversely, the ability of a model to replicate a given set of observations does not unequivocally mean that all processes are properly represented. When models differ not only in their level of ecological complexity, but also in the degree to which they were calibrated and in the model pathways that were affected during calibration, it is tenuous to argue that differences in model performance are due to structural complexity (Friedrichs et al., 2007; Kriest et al., 2010). To better discern the effects of increased ecosystem complexity from differences in a model's response due to

its parameter values, it is necessary to calibrate the model versions to comparable levels of performance and through comparable pathways.

During the 90's, the calibration of marine ecosystem models to a specific study region was predominantly subjective (Arhonditsis and Brett, 2004). As previously mentioned, this approach is inefficient, increases the risk of overlooking structural inadequacies in the models, and is complicated by the number of parameters in play and their co-dependencies. Parameter optimization provides a more objective framework for comparing models with different degrees of trophic complexity, but optimization experiments require a large number of model runs and thus, their direct application to computationally expensive 3D models is difficult.

An alternative, which I choose here, is to perform the optimization using a simplified faster model that replicates the results of the computationally more expensive 3D model. The computationally efficient model is referred to as a model surrogate or emulator. The surrogate can be a statistical model, a coarser resolution model, or a reduced order model that allows one to perform a large number of simulations required for parameter sensitivity analyses and model calibration. Different techniques for the construction of statistical emulators of 3D biogeochemical models have been tested in recent years (Hooten et al., 2011; Leeds et al., 2012; Mattern et al., 2012). Other tested approaches include reduced temporal resolution (Prieß et al., 2013a, 2013b), and reduced physical dimensionality (Hemmings and Challenor 2012, Hemmings et al. 2015). My methodology resembles the latter reduced dimensionality studies in that my model surrogate is a mechanistic emulator constructed with an ensemble of 1D models, located at points where in situ chlorophyll-a and nitrate profiles are available. The surrogate (1D

models) and the target model (3D model) share the same ecosystem model. Therefore, in comparison with statistical and reduced process-resolution surrogates, the reduced dimensionality approach provides insight into the ecosystem responses most affected by the physical dynamics. Features that are well replicated in 1D are likely controlled by the ecosystem model itself (structure, equations and parameter values), whereas biases between 1D and 3D are likely a consequence of the simplified physical framework.

In this case study, the application of the surrogate-based parameter optimization aims to compare three different ecosystem models in a 3D ocean model of the northwest North Atlantic continental shelf. The overarching goal is to better understand the variability of phytoplankton and primary production in the region, while addressing the unresolved question of how much ecological complexity is needed. In this chapter, I focus on the methodology used to bring models with different ecological structures to a comparable level of calibration by analyzing model results from several optimization experiments. I specifically aim to answer three questions: 1. Does the ecosystem model structure affect the surrogate-based optimization performance? 2. Is the optimization affected by the number of observed variables compared, or by the number of parameters optimized? 3. Which of the optimized models is geographically most portable? I demonstrate that, despite its simplicity, the surrogate approach is effective as a calibration tool. An in-depth comparison of chlorophyll and primary production patterns is presented in Chapter 4, as Part II of this case study.

## **3.2 STUDY AREA: THE NORTHWEST NORTH ATLANTIC**

My model domain covers the continental shelf and adjacent open ocean waters of the northwest North Atlantic Ocean, including the Newfoundland Shelf, the Grand Banks, the Gulf of St. Lawrence, the Scotian Shelf, and the Gulf of Maine (Figure 3.1). The region is at the confluence of the two major North Atlantic current systems, the equatorward flowing Labrador Current and the northeast flowing Gulf Stream, and is influenced by their adjoining Shelf and Slope Water currents (Loder et al., 1998). This leads to complicated dynamics, including both cold and warm sub-regions originating from the North Atlantic subpolar and subtropical gyres (Townsend et al., 2004).

## **3.3 MODEL DESCRIPTIONS**

### **3.3.1 PHYSICAL CONFIGURATION**

The 3D physical framework uses the Regional Ocean Modeling System (ROMS, version 3.5, <http://myroms.org>, Haidvogel et al. (2008)). The model is nested within the regional ocean-ice model of the northwest North Atlantic of Urrego-Blanco and Sheng (2012). Brennan et al. (2016) describe the physical model implementation, and detailed sensitivity analyses and validation of the simulated physical variables of this model application. Similar to the biogeochemical application by Bianucci et al. (2015), ocean temperature and salinity are weakly nudged (time scale of 140 days) to climatological fields from Geshelin et al. (1999).

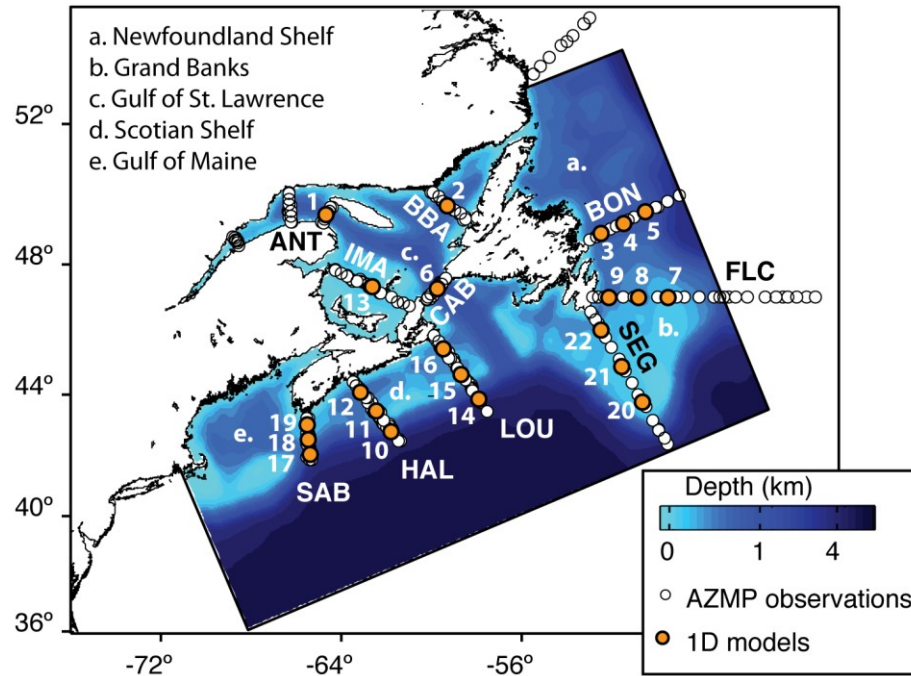


Figure 3.1: Map of the study area showing the domain of the 3D ocean model, sampling locations along transects of the Atlantic Zone Monitoring Program (AZMP) as white circles with transect acronyms are given in capital letters, and locations of the surrogate 1D models as orange circles. The background color scale depicts the bathymetry of the area.

### 3.3.2 ECOSYSTEM MODELS

I compare three nitrogen-based ecosystem model versions, which are shown schematically in Figure 3.2 and referred to as M1, M2 and M3 in increasing order of complexity. M1 has previously been used in the Mid-Atlantic Bight, a region south of my model domain (Fennel et al., 2006). M3 is based on the North Pacific Ecosystem Model for Understanding Regional Oceanography (NEMURO) structure (Kishi et al., 2007). An optimized version of NEMURO has been shown to outperform simple models in the California Current area (Mattern et al., 2016). M2 represents an intermediate step between M1 and M3.

M1 and M2 have 7 compartments tracking nitrate, ammonium, phytoplankton, chlorophyll, zooplankton, and two detritus size classes. In M1, only phytoplankton growth depends on temperature (Eppley, 1972). In M2, I introduce temperature dependency in other biological rates (i.e., phytoplankton mortality, zooplankton grazing, excretion and mortality). In M3, I further increase ecological complexity by adding plankton functional groups. M3 has 11 compartments that include 2 nutrient and 2 detritus pools similar to M1 and M2, 2 phytoplankton groups (representing small and large phytoplankton), and 3 zooplankton groups (small, large, and predatory zooplankton). While the trophic structure of M3 (i.e., the interactions among planktonic groups) is based on NEMURO, it utilizes the same functional forms as my M1 and M2 model versions (e.g., Holling III grazing, as in Fennel et al. (2006), instead of the Ivlev equation used in NEMURO) for sake of better comparability.

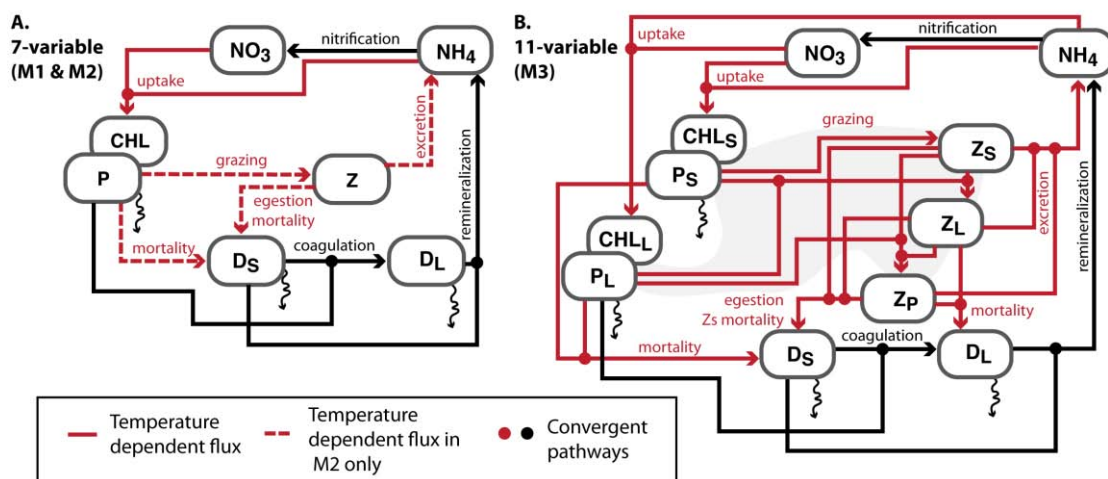


Figure 3.2: Schematic depictions of the ecosystem models used in the study. A.) M1 and M2 both have the same 7 state variables, but in M2 more parameterizations are temperature-dependent. B.) M3 has 11 state variables. The gray shading indicates fluxes related to grazing.

In summary, the three model versions I compare introduce additional ecological complexity in a step-wise fashion. In this way, I aim to tease apart the effects of increasing the dependency of the system on environmental factors, such as temperature, and increasing the trophic complexity itself. The equations for the three model versions are included in Appendix C.

Boundary and initial conditions for  $\text{NO}_3$  are based on a monthly climatology constructed using in situ observations (see section 3.4.1) and World Ocean Atlas monthly averages (Garcia et al., 2010). Initial and boundary conditions for all other biological variables are set to  $0.1 \text{ mmol N m}^{-3}$  as in Fennel et al. (2006, 2008). These variables adjust on short time scales (days); hence, the system has no memory of the initial values after a short spin-up phase. A phytoplankton-to-chlorophyll ratio of  $0.76 \text{ mmol N (mg Chl)}^{-1}$  is assumed for the chlorophyll initial and boundary conditions (Bianucci et al., 2015).

### 3.3.3 SURROGATE MODEL

I apply the simple 1D framework, described in Chapter 2, to 22 locations on the continental shelf (Figure 3.1), which are referred to as the “1D models” from now on. In general, the 1D models solve a vertical diffusion term  $k_D \frac{\partial^2 C}{\partial z^2}$  using the Crank-Nicholson scheme, where  $k_D$  is the diffusivity,  $z$  is depth, and  $C$  refers to the biological state variables. The vertical resolution is 5 m, and the vertical grid is divided into two distinct layers with respect to mixing: a turbulent surface mixed layer (layer 1) and a quiescent layer below (layer 2). The interface between both layers is determined by the time-varying mixed layer depth, which is estimated using a criterion for the maximum density

gradient. For this purpose, the density field is obtained from a base run of the 3D model. In 1D, a high diffusivity is assigned to all grid cells above the prescribed mixed layer depth ensuring complete mixing within the mixed layer ( $H_{MLD}$ ) on a time scale of 1 day with a minimum diffusivity of  $100 \text{ m}^2 \text{ d}^{-1}$  imposed ( $k_{D1} = \max[H_{MLD}^2 \text{d}^{-1}, 100]$ ). A lower diffusivity ( $k_{D2} = k_{D1} \times 10^{-2}$ ) is assigned to all grid cells below the mixed layer depth. This 1D framework has been previously used (Lagman et al., 2014; Kuhn et al., 2015).

The 1D models also require shortwave radiation and temperature as inputs. The shortwave radiation is the same as in the 3D model and comes from the European Centre for Medium-range Weather Forecasts (ECMWF) global atmospheric reanalysis (ERA-Interim) (Dee et al., 2011). Temperature is taken from the 3D model base simulation. As 1D models do not include horizontal advection,  $\text{NO}_3$  below the mixed layer depth is nudged to the 3D results from the 3D base simulation with a nudging time scale of 60 days. It is assumed that biological activity has the strongest effect on nitrate in the photic surface layers; therefore, there is no conflict between the nudging treatment and the optimization (i.e., deep nitrate does not change with changes in the parameter values on the timescales considered here). Total depth in the 1D models is equal to the depth in the 3D model or truncated at 50 m below their maximum mixed layer depth, whichever is shallower. This treatment further reduces the surrogate computational time, without affecting its performance. Acronyms, geographical coordinates, depths, mean temperature, chlorophyll-a, and nitrate values for each location are presented in Table 3.2.

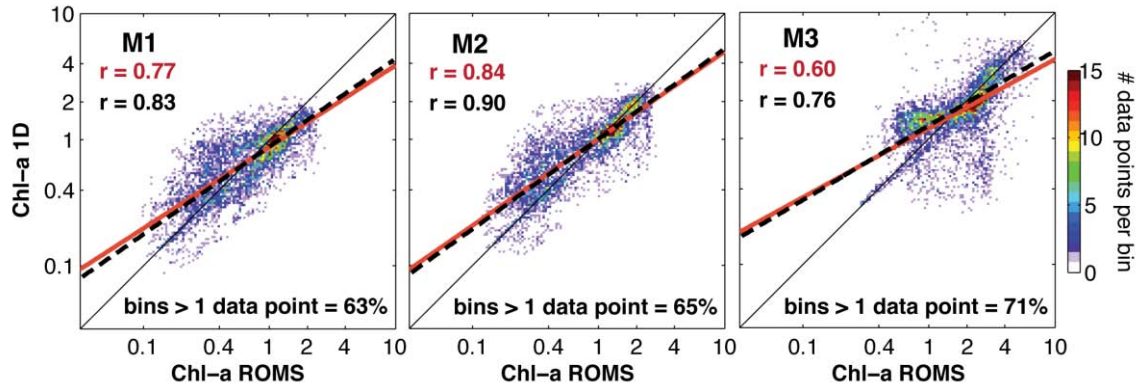


Figure 3.3: Two-dimensional histograms showing the performance of the model surrogates with respect to surface chlorophyll for the three ecosystem model versions. The color indicates the number of data points per bin.

Despite its simplicity, the mechanistic emulator replicates the results of the full 3D model well for all three biogeochemical models. Figure 3.3 shows 2D histograms comparing 5-day averages of surface chlorophyll simulated by the 3D (ROMS) and the 1D models for the initial parameter guess and the optimized parameters. The target model (ROMS) and surrogate surface chlorophyll results are significantly correlated ( $p < 0.01$ ), with correlation coefficients of 0.77, 0.84 and 0.60, for M1, M2, and M3, respectively. If bins with only 1 data point in the 2D histograms are excluded from the calculations, the correlation coefficients increase to 0.83, 0.90 and 0.76. This reduced regression involves 63% to 71% of the data-points. Nevertheless, the surrogate of M3 is challenged to replicate low chlorophyll values and tends to overestimate them. Differences in chlorophyll (1D minus 3D) before the optimization are shown for two locations, BON (49.21° N 51.48° W, location 4) and HAL (43.46° N 62.43° W, location 11) in Figure 3.4. All model versions exhibit discrepancies at the beginning and end of the mixed layer-shoaling period. Biases in the position of the deep-chlorophyll maximum occur during

summer stratification, with the 1D models predicting a shallower position than the 3D model.

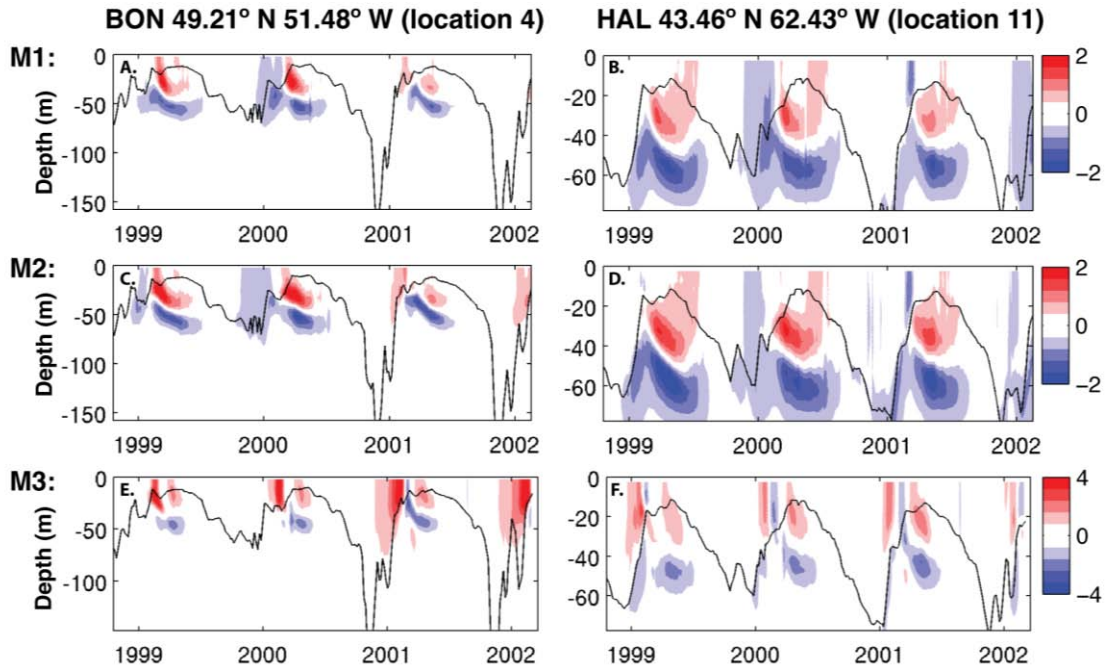


Figure 3.4 Surrogate-target chlorophyll biases (1D minus 3D results) at two locations, using the three model versions. Note that the color scales changes in the subplots. The black line shows an estimate of mixed layer depth using a fixed threshold criterion.

### 3.4 OPTIMIZATION PROCEDURE AND SENSITIVITY ANALYSIS

The optimization is implemented using an evolutionary algorithm and applied for 3 years (January 1999 - December 2001). Details of the evolutionary algorithm used here are described in Chapter 2. I optimized subsets of the complete parameter sets required by each model version (Table 3.4), which were selected based on the sensitivity analysis described in section 3.4.2.

Table 3.1 Correlation between satellite chlorophyll and surface in situ chlorophyll (1-m and 3-m depth averages). Acronyms refer to the Atlantic Zone Monitoring Program (AZMP) transect lines depicted in Figure 3.1. \* denotes statistically significant relationships ( $p < 0.01$ ).

<b>1m</b>	<b>N</b>	<b>RMSE</b>	<b>BIAS</b>	<b>Slope</b>	<b>Intercept</b>	<b>R</b>
SeaWiFs vs. in situ (1 m averages)						
ANT*	32	5.347	2.590	1.719	1.282	0.471
BBA*	34	0.659	0.457	0.895	0.513	0.535
IMA*	45	0.798	0.466	0.784	0.660	0.445
MLO	36	4.918	2.455	0.500	3.026	0.232
STL	31	12.56	5.695	-0.170	13.069	-0.103
Gulf of St. Lawrence*	178	6.144	2.159	0.727	2.701	0.386
BON	0	-	-	-	-	-
CAB*	50	2.879	-1.083	0.152	0.933	0.687
FLC	0	-	-	-	-	-
HAL	31	1.257	0.001	0.349	0.615	0.274
LOU*	69	4.183	-2.228	0.232	0.754	0.791
SAB*	24	0.897	-0.545	0.328	0.529	0.703
SEG	0	-	-	-	-	-
SIL	0	-	-	-	-	-
outside the Gulf*	174	3.117	-1.269	0.218	0.773	0.708
SeaWiFs vs. in situ (3 m averages)						
ANT*	50	4.429	1.871	0.948	1.978	0.396
BBA*	58	0.800	0.511	0.662	0.677	0.316
IMA*	91	0.836	0.422	0.761	0.655	0.466
MLO	83	6.053	2.314	0.312	3.383	0.129
STL	49	13.070	6.597	0.170	10.334	0.083
Gulf of St. Lawrence*	331	6.144	2.045	0.783	2.418	0.344
BON	0	-	-	-	-	-
CAB*	94	3.006	-0.947	0.106	0.925	0.519
FLC	0	-	-	-	-	-
HAL*	51	1.509	-0.264	0.199	0.633	0.308
LOU*	76	4.571	-2.620	0.198	0.791	0.707
SAB*	30	1.317	-0.692	0.200	0.702	0.624
SEG	0	-	-	-	-	-
SIL	0	-	-	-	-	-
outside the Gulf*	251	3.222	-1.284	0.175	0.785	0.628

Table 3.2 List of 1D model locations used in the optimization experiments. Surface *in situ* NO<sub>3</sub>, *in situ* Chl-a and satellite Chl-a are observed mean surface concentrations between 1999 and 2001. The 3D model depth differs from the 1D model depth when the bottom is deeper than the maximum mixed layer depth plus 50 m. Station numbers and transect acronyms are as in Figure 3.1.

Station number and transect acronym	Lat.	Lon.	3D model depth	1D model depth	Max MLD	Min MLD	<i>in situ</i> NO <sub>3</sub> (surface)	<i>in situ</i> Chl-a (surface)	satellite Chl-a	
1	ANT	49.44	-64.61	315	92	42.4	2.5	5.59±3.14	0.98±1.57	1.02±0.8
2	BBA	49.69	-59.25	214	117	68.0	9.5	5.27±4.41	0.66±1.17	0.38±0.29
3	BON	48.89	-52.47	276	276	247.9	9.1	6.76±6.45	1.49±2.84	0.87±1.00
4	BON	49.21	-51.48	295	171	121.8	10.0	5.45±4.38	1.25±2.34	0.78±1.03
5	BON	49.52	-50.50	308	172	122.3	2.1	5.50±4.43	1.17±2.14	0.78±0.81
6	CAB	47.27	-59.77	421	128	79.0	4.5	4.89±3.88	1.36±2.46	1.24±2.24
7	FLC	47.00	-49.50	77	77	68.5	13.0	3.93±3.49	1.75±3.07	1.26±2.93
8	FLC	47.00	-50.83	127	127	89.0	10.0	4.79±3.68	1.52±2.83	0.63±0.76
9	FLC	47.00	-52.17	128	128	85.0	9.0	4.78±4.13	1.47±2.72	0.57±0.32
10	HAL	42.83	-61.74	1180	116	66.9	9.0	4.79±4.11	1.39±2.64	0.67±0.67
11	HAL	43.46	-62.43	83	83	71.0	10.0	4.05±3.70	1.49±2.68	0.72±0.50
12	HAL	44.09	-63.13	162	103	53.5	9.0	4.48±3.94	1.33±2.51	0.92±0.61
13	IMA	47.31	-62.63	63	63	61.0	8.5	3.26±3.21	1.59±2.73	0.68±0.89
14	LOU	43.86	-57.89	2443	125	75.9	5.1	4.71±4.10	1.29±2.47	0.67±0.49
15	LOU	44.65	-58.69	81	81	56.0	2.1	3.93±3.59	1.50±2.71	0.87±0.63
16	LOU	45.44	-59.48	107	107	62.5	7.6	4.59±3.96	1.42±2.74	1.24±1.00
17	SAB	42.09	-65.35	1110	118	69.0	3.0	4.62±3.94	1.39±2.69	0.71±0.42
18	SAB	42.56	-65.41	105	105	82.9	2.0	4.62±3.93	1.36±2.63	0.84±0.65
19	SAB	43.02	-65.47	104	104	64.0	3.0	4.65±3.91	1.34±2.58	0.97±0.75
20	SEG	43.76	-50.63	62	62	59.5	5.2	3.04±3.03	1.69±2.84	0.65±0.57
21	SEG	44.89	-51.55	62	62	61.5	2.0	2.94±3.00	1.71±2.83	1.09±2.19
22	SEG	46.02	-52.47	83	83	82.0	9.5	3.63±3.46	1.54±2.69	0.79±1.03

### 3.4.1 OBSERVATIONAL DATASETS FOR CALIBRATION

In situ and satellite observations were used to calibrate the models. Surface chlorophyll satellite observations come from the Sea-viewing Wide Field-of-view Sensor (SeaWiFs) 8-day averages with 9-km resolution. In situ observations were obtained from the Atlantic Zone Monitoring Program (AZMP, <http://www.meds-sdmm.dfo-mpo.gc.ca/isdm-gdsi/azmp-pmza/index-eng.html>), which performs biannual monitoring along the 13 transect lines shown in Figure 3.1. The AZMP dataset includes quality controlled CTD measurements of temperature and salinity (Mitchell et al., 2002) from which density was calculated using the Gibbs SeaWater TEOS-10 oceanographic toolbox. Bottle measurements used in this study include in situ chlorophyll-a and nitrate, as these are variables with direct counterparts in the model. The standardized chlorophyll-a analysis method is Turner fluorometry and the nitrate analysis is colorimetric on a Technicon AutoAnalyzer II (AA II) segmented flow analyzer (Mitchell et al., 2002).

Satellite observations were validated against the in situ chlorophyll-a observations from the top 3 m after identifying all matching records between 1997 and 2010 (i.e., the duration of the SeaWiFs record). Using vertical averages over the top 3 meters increased the number of match-ups and did not significantly affect the regression, compared to using only the top 1 meter (Table 3.1). Matching satellite records were searched within a 0.1-degree radius of each corresponding in situ measurement and averaged. Additionally, the same cross-validation matchup analysis was performed using GlobColour (<http://hermes.acri.fr/>; a combined MODIS and SeaWiFS product), and non-standard AZMP measurements of HPLC (High Performance Liquid Chromatography) chlorophyll-a in situ; the results of these analyses (Appendix D) reveal the same patterns of satellite

performance as the SeaWiFs vs. standard measurements in Table 3.1 and Figure 3.5A. The comparison shows systematic biases at certain locations. To correct the most pronounced bias, satellite time series inside the Gulf of St. Lawrence were debiased by subtracting  $e_{GoSL} = 0.01 + 0.19 x^{1.42}$  from the observations, where  $x$  is the log-transform SeaWiFs satellite observation and  $e_{GoSL}$  is the bias (Figure 3.5A).

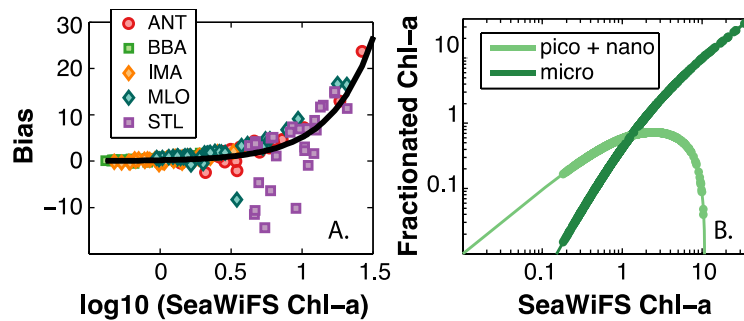


Figure 3.5 Information used in the design of the cost function: A. De-biasing function for satellite chlorophyll, used for locations inside the Gulf of St. Lawrence. The function is based on systematic biases between in situ and satellite surface chlorophyll. B. Fractions of chlorophyll corresponding to small (pico- and nano-) and large (micro-) phytoplankton from satellite chlorophyll, following Hirata et al. (2011). Dots plotted on top of the lines correspond to calculation of fractionated chlorophyll using SeaWiFS observations in the study area.

In order to provide observed counterparts to both small and large phytoplankton groups in M3, I estimated the chlorophyll-a fractions from small and large phytoplankton in the satellite observations using the empirical relationships of Hirata et al. (2011). This study provides a set of equations and coefficients to estimate the chlorophyll concentration of various phytoplankton size classes and functional groups based on a global classification of HPLC pigment data into phytoplankton size classes. Here, I

specifically used their equation to estimate the fraction  $\Psi$  of chlorophyll corresponding to microphytoplankton:

$$\Psi = [\psi_0 + \exp(\psi_1 x + \psi_2)]^{-1}, \quad (3.1)$$

where  $x$  is the log-transform SeaWiFs satellite observation, and the coefficient values are  $\psi_0 = 0.9117$ ,  $\psi_1 = -0.27330$ , and  $\psi_2 = 0.4003$ . I regard this fraction of chlorophyll as an observational counterpart of the large phytoplankton chlorophyll component in M3; the remaining fraction (nano- and picophytoplankton) is considered the counterpart of small phytoplankton chlorophyll (Figure 3.5B). Since Hirata et al.'s (2011) relationship was designed with SeaWiFs observations, I cannot apply the same formula to in-situ measurements with any confidence.

### 3.4.2 SENSITIVITY ANALYSIS

In order to identify the most sensitive parameters and reduce the parameter space to be searched during optimization, the 1D models were rerun after perturbing each parameter one at a time. A reduced parameter space is desirable because parameters that are insensitive to the observations used in the optimization cannot be estimated. The sensitivity of the models to each of their parameter values is estimated as:

$$Q(Y, p) = \sum_{i=1}^m \sum_{j=1}^n \frac{|Y_{test} - Y_{base}|}{Y_{base}}, \quad (3.2)$$

which is the sum of the normalized absolute differences in the model state variables ( $Y$ ), between the results of a base simulation ( $Y_{base}$ ) and a test simulation ( $Y_{test}$ ), where  $n$  is the total number of values compared.  $Q$  is calculated by varying each parameter  $p$  in  $m = 5$

different tests. The tests change each of the base simulation parameter values to the minimum, 25%, 50%, 75% and maximum values of their corresponding ranges shown in Table 3.3. These minimum and maximum parameter values are based on the literature and also imposed in the optimization algorithm as bounds to avoid unrealistic values (Kuhn et al., 2015; Ward et al., 2010). The base simulations using the initial guess parameter values are also shown in Table 3.3.

Table 3.3 A priori model parameter estimates and ranges. For M1, a priori parameter values are from Fennel et al. (2008). For M2, I assume that the fixed biological rates are reference values at the average surface temperature in the domain (approximately  $T = 10$  °C), and back-calculated the corresponding reference value at  $T = 0$  °C. M3 uses the M2 parameters, except for zooplankton grazing rates. Zooplankton grazing rates for different preys were scaled following Kishi et al. (2007). Parameters in bold font were optimized in at least one of the optimization exercises.

<b>Parameters</b>		<b>M1</b>	<b>M2</b>	<b>M3</b>	<b>Range</b>	<b>Units</b>
Reference phytoplankton maximum growth rate at $T = 0^\circ\text{C}$ (generic, small and large, respectively)	$\mu_0$	0.69	0.69	-	0.1 – 3.5	$\text{d}^{-1}$
	$\mu_{0PS}$	-	-	0.69	0.1 – 3.5	$\text{d}^{-1}$
	$\mu_{0PL}$	-	-	0.69	0.1 – 3.5	$\text{d}^{-1}$
Phytoplankton $\text{NO}_3$ uptake half-saturation (generic, small and large, respectively)	$k_{\text{NO}_3}$	0.5	0.5	-	0.2 - 2	$\text{mmol m}^{-3}$
	$k_{\text{NO}_3PS}$	-	-	0.5	0.2 - 2	$\text{mmol m}^{-3}$
	$k_{\text{NO}_3PL}$	-	-	0.5	0.2 - 2	$\text{mmol m}^{-3}$
Phytoplankton $\text{NH}_4$ uptake half-saturation (generic, small and large, respectively)	$k_{\text{NH}_4}$	0.5	0.5	-	0.2 - 2	$\text{mmol m}^{-3}$
	$k_{\text{NH}_4PS}$	-	-	0.5	0.2 - 2	$\text{mmol m}^{-3}$
	$k_{\text{NH}_4PL}$	-	-	0.5	0.2 - 2	$\text{mmol m}^{-3}$
Phytoplankton, initial slope of photosynthetic response	$\alpha$	0.125	0.125	-	0.007 – 0.13	$\text{mg C (mg Chl Watts m}^{-2} \text{ day)}$
	$\alpha_{PS}$	-	-	0.125	0.007 – 0.13	$\text{mg C (mg Chl Watts m}^{-2} \text{ day)}$
	$\alpha_{PL}$	-	-	0.125	0.007 – 0.13	$\text{mg C (mg Chl Watts m}^{-2} \text{ day)}$
Phytoplankton mortality rate	$m_P$	0.15	-	-	0.01 – 0.25	$\text{d}^{-1}$

Parameters		M1	M2	M3	Range	Units
Reference phytoplankton mortality rate at T = 0 °C	$m_{P0}$	-	0.13	-	0.01 – 0.25	d <sup>-1</sup>
(generic, small and large, respectively)	$m_{PS0}$	-	-	0.13	0.01 – 0.25	d <sup>-1</sup>
	$m_{PL0}$	-	-	0.13	0.01 – 0.25	d <sup>-1</sup>
Zooplankton maximum grazing rate	$g_{max}$	0.6	-	-	0.2 - 4	d <sup>-1</sup>
Reference zooplankton maximum grazing rate at T = 0 °C (generic, small, large, and predatory on each of their preys)	$g_0$	-	0.54	-	0.2 - 4	d <sup>-1</sup>
	$g_{0Z_S P_S}$	-	-	0.54	0.2 - 4	d <sup>-1</sup>
	$g_{0Z_L P_S}$	-	-	0.13	0.05 - 4	d <sup>-1</sup>
	$g_{0Z_L P_L}$	-	-	0.54	0.2 - 4	d <sup>-1</sup>
	$g_{0Z_L Z_S}$	-	-	0.54	0.2 - 4	d <sup>-1</sup>
	$g_{0Z_P P_L}$	-	-	0.27	0.1 - 4	d <sup>-1</sup>
	$g_{0Z_P Z_S}$	-	-	0.27	0.1 - 4	d <sup>-1</sup>
	$g_{0Z_P Z_L}$	-	-	0.27	0.1 - 4	d <sup>-1</sup>
Square zooplankton grazing half-saturation (generic, small, large, and predatory on each of their preys)	$k_P$	2	2	-	0.5 - 5	(mmol m <sup>-3</sup> ) <sup>2</sup>
	$k_{Z_S P_S}$	-	-	2	0.5 - 5	(mmol m <sup>-3</sup> ) <sup>2</sup>
	$k_{Z_L P_S}$	-	-	2	0.5 - 5	(mmol m <sup>-3</sup> ) <sup>2</sup>
	$k_{Z_L P_L}$	-	-	2	0.5 - 5	(mmol m <sup>-3</sup> ) <sup>2</sup>
	$k_{Z_L Z_S}$	-	-	2	0.5 - 5	(mmol m <sup>-3</sup> ) <sup>2</sup>
	$k_{Z_P P_L}$	-	-	2	0.5 - 5	(mmol m <sup>-3</sup> ) <sup>2</sup>
	$k_{Z_P Z_S}$	-	-	2	0.5 - 5	(mmol m <sup>-3</sup> ) <sup>2</sup>
	$k_{Z_P Z_L}$	-	-	2	0.5 - 5	(mmol m <sup>-3</sup> ) <sup>2</sup>
Zooplankton base metabolic rate	$l_{BM}$	0.1	-	-	0.01 – 0.35	d <sup>-1</sup>
Reference zooplankton base metabolic rate at T = 0 °C (generic, small, large, and predatory)	$l_{BM0}$	-	0.09	-	0.01 – 0.35	d <sup>-1</sup>
	$l_{BM0Z_S}$	-	-	0.09	0.01 – 0.35	d <sup>-1</sup>
	$l_{BM0Z_L}$	-	-	0.09	0.01 – 0.35	d <sup>-1</sup>
	$l_{BM0Z_P}$	-	-	0.09	0.01 – 0.35	d <sup>-1</sup>
Zooplankton excretion rate	$l_E$	0.1	-	-	0.02 – 0.35	d <sup>-1</sup>
Reference zooplankton excretion rate at T = 0 °C (generic, small, large, and predatory)	$l_{E0}$	-	0.09	-	0.02 – 0.35	d <sup>-1</sup>
	$l_{EZ_S}$	-	-	0.09	0.02 – 0.35	d <sup>-1</sup>
	$l_{EZ_L}$	-	-	0.09	0.02 – 0.35	d <sup>-1</sup>
	$l_{EZ_P}$	-	-	0.09	0.02 – 0.35	d <sup>-1</sup>
Zooplankton mortality rate	$m_Z$	0.025	-	-	0.02 - 0.35	d <sup>-1</sup>
Reference zooplankton mortality rate at T = 0 °C (generic, small, large, and predatory)	$m_{Z0}$	-	0.022	-	0.02 - 0.35	d <sup>-1</sup>
	$m_{0Z_S}$	-	-	0.022	0.02 - 0.35	d <sup>-1</sup>
	$m_{0Z_L}$	-	-	0.022	0.02 - 0.35	d <sup>-1</sup>
	$m_{0Z_P}$	-	-	0.022	0.02 - 0.35	d <sup>-1</sup>
Phytoplankton and small detritus aggregation rate	$\tau$	0.01	0.01	-	0.001 - 1	d <sup>-1</sup>
Large phytoplankton and	$\tau_{P_L}$	-	-	0.01	0.001 - 1	d <sup>-1</sup>

Parameters		M1	M2	M3	Range	Units
small detritus aggregation rate						
Maximum chlorophyll to carbon ratio (generic, small and large)	$\theta_{max}$	0.053	0.053	-	0.005 – 0.15	mg Chl (mg C) <sup>-1</sup>
	$\theta_{maxP_S}$	-	-	0.053	0.005 – 0.15	mg Chl (mg C) <sup>-1</sup>
	$\theta_{maxP_L}$	-	-	0.053	0.005 – 0.15	mg Chl (mg C) <sup>-1</sup>
Zooplankton assimilation efficiency (generic, small, large, and predatory)	$\beta$	0.75	0.75	-	0.25 – 0.95	non-dim.
	$\beta_{Z_S}$	-	-	0.75	0.25 – 0.95	non-dim.
	$\beta_{Z_L}$	-	-	0.75	0.25 – 0.95	non-dim.
	$\beta_{Z_P}$	-	-	0.75	0.25 – 0.95	non-dim.
Small detritus remineralization rate	$r_{SD}$	0.4	0.4	0.4	0.005 – 0.6	d <sup>-1</sup>
Large detritus remineralization rate	$r_{LD}$	0.1	0.1	0.1	0.005 – 0.1	d <sup>-1</sup>
Nitrification rate	$n_{max}$	0.2	0.2	0.2	0.01 – 0.5	d <sup>-1</sup>
Half-saturation radiation for nitrification inhibition	$k_I$	0.1	0.1	0.1	0.05 – 0.15	Wm <sup>2</sup>
Radiation threshold for nitrification inhibition	$I_0$	0.0095	0.0095	0.0095	0.008 - 0.015	Wm <sup>2</sup>
Vertical sinking velocity for phytoplankton (generic, small, and large)	$w_P$	0.1	0.1	-	0.05 – 1.5	md <sup>-1</sup>
	$w_{P_S}$	-	-	0.1	0.05 – 1.5	md <sup>-1</sup>
	$w_{P_L}$	-	-	0.1	0.05 – 1	md <sup>-1</sup>
Vertical sinking velocity for small detritus	$w_{SD}$	0.1	0.1	0.1	0.05 – 1.5	[m/day]
Vertical sinking velocity for large detritus	$w_{LD}$	5	5	5	0.5 - 10	[m/day],
Eppley temperature coefficient	$\phi$	1.066	1.066	1.066	1.05 – 1.08	non-dim.

Results of this sensitivity analysis are shown in Figure 3.6. Each stacked bar shows the contribution of all model variables to the total sensitivity. In order to select the parameters most sensitive to the available observations, the parameters were ranked with respect to the chlorophyll and nitrate contributions to  $Q$ . In models M1 and M2 equivalent parameters have similar rankings: the 3 most sensitive parameters are the maximum phytoplankton growth ( $\mu_0$ ), the mortality ( $m_P$ ,  $m_{P0}$ ), and the coagulation rate ( $\tau$ ). The initial photosynthetic slope ( $\alpha$ ) and grazing rate ( $g_{max}$ ,  $g_0$ ) have different ranks in M1 and

M2, but are among the six most sensitive parameters. In addition to being important for the estimation of chlorophyll, this subset of parameters also has a significant effect on zooplankton and detritus. M1 and M2 are also sensitive to the zooplankton base metabolic rate ( $l_{BM}$ ,  $l_{BM0}$ ) and the remineralization of small detritus ( $r_{SD}$ ); however, these parameters dominantly affect zooplankton and detritus, which are not part of the observation data used in the optimization.

In M3, parameters related to small phytoplankton are more sensitive than those related to large phytoplankton, e.g., the most sensitive parameter is the reference maximum growth rate of small phytoplankton ( $\mu_{0PS}$ ). There are some similarities in parameter ranking with the rankings of M1 and M2, e.g., the small phytoplankton mortality rate ( $\mu_{0PS}$ ), the grazing rate of small zooplankton on small phytoplankton ( $g_{maxZsPs}$ ), and the coagulation rate ( $\tau$ ) are among the most sensitive. The most sensitive parameters of M3 are similar to those reported for NEMURO (Yoshie et al., 2007).

The parameter rankings in Figure 3.6 guided the selection of parameters to be optimized, as detailed in the next section and in Table 3.4.

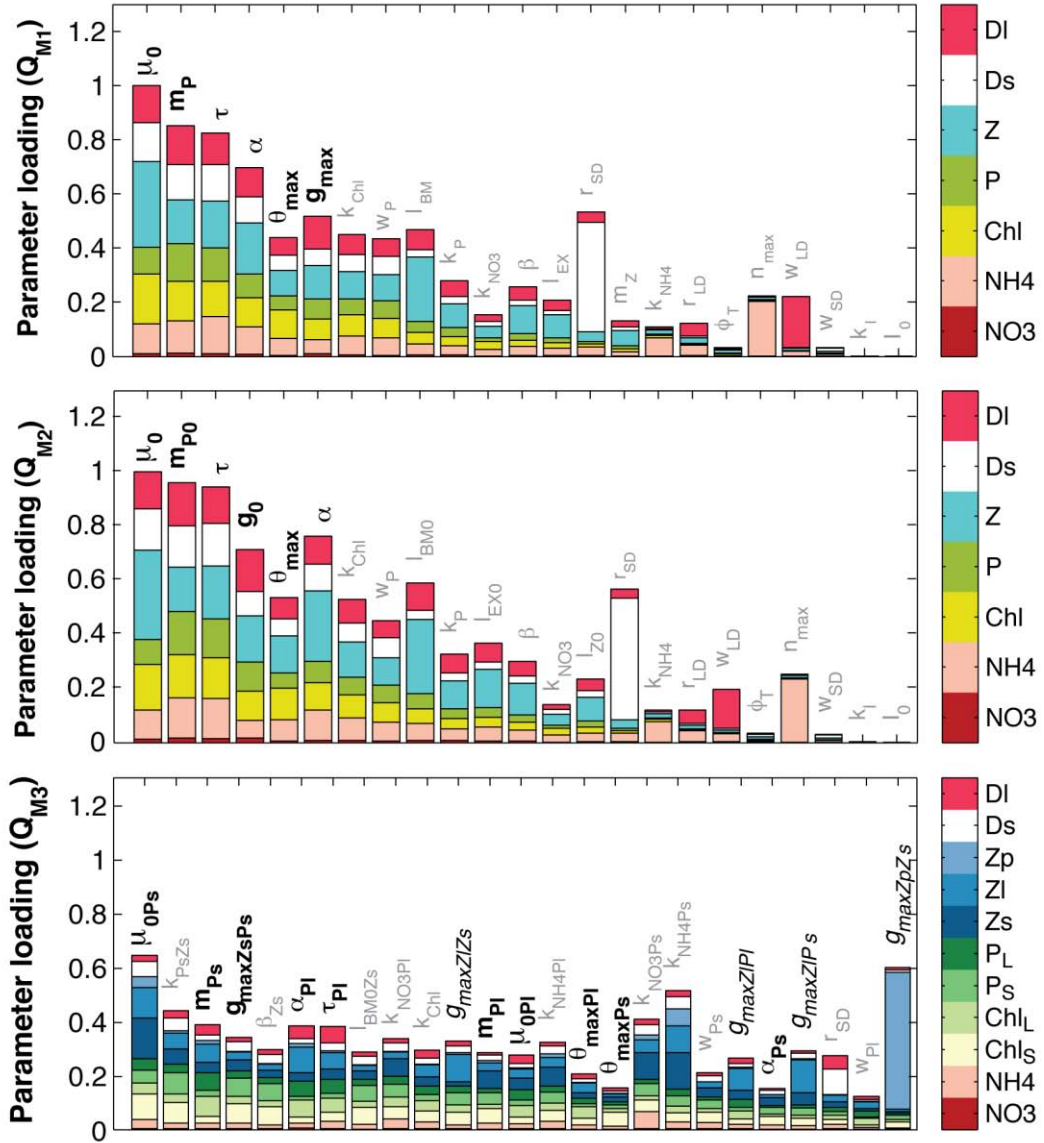


Figure 3.6 Parameter sensitivities for M1, M2 and M3. Each stacked bar represents the total sensitivity of the model to a specific parameter, and is composed of the contribution of each model variable to the total. Parameters in bold black font are included in the main optimization exercise. In M3, parameters in italics are grazing rates that were indirectly optimized (i.e., the ratio between all grazing rates was maintained constant).

### 3.4.3 OPTIMIZATION EXPERIMENTS

I performed five common optimization experiments for each model (E1 to E5) and two additional experiments for M3 (E4b and E5b). Each optimization experiment ( $E$ ) utilizes a different cost function  $J_E$ , depending on its objective. Table 3.4 summarizes the optimization experiments, describing the number of parameters, locations, and observed variables used in each. Due to the different cost functions of the experiments, the function  $F$  is used as a unifying metric to evaluate differences between optimized models:

$$F(\vec{p}) = \frac{1}{L} \sum_{l=1}^L \frac{1}{\omega_l} (R_{chl1} + R_{chl2} + R_{NO3}), \quad (3.3)$$

where  $\vec{p}$  refers to parameter vector, and  $L = 22$  is the total number of 1D model locations ( $l$ ). The location weighting factor  $\omega_l = \frac{1}{L} \sum_{v=1}^V \frac{\bar{y}_v^2}{\sigma_v^2}$  uses the mean ( $\bar{y}$ ) and standard deviation ( $\sigma$ ) of the observed variables ( $v$ ) to avoid biasing the cost towards locations with lower variability.  $R_v$  is the weighted root mean square difference between the simulated ( $\hat{y}$ ) and observed ( $y$ ) values of satellite chlorophyll ( $R_{chl1}$ ), in situ chlorophyll ( $R_{chl2}$ ) and in situ nitrate ( $R_{NO3}$ ), according to:

$$R_v = \frac{w_v^2}{N} \sum_{n=1}^N (\hat{y}_{l,n} - y_{l,n})^2 \quad (3.4)$$

where  $N$  is the number of observed values, and the weight  $w_v = \phi_v/\sigma_v$  of each variable at each location is inversely proportional to the standard deviation of its observations. Based on preliminary tests and due to the large variability in its values, higher weight was assigned to satellite chlorophyll by setting the weight coefficients  $\phi_v = 3$  for satellite

chlorophyll and  $\phi_v = 1$  for the other two data types. In the case of M3,  $R_{chl}$  was modified to compare both the small and large phytoplankton chlorophyll fractions against corresponding satellite-derived fractions estimated using the Hirata et al. (2011) algorithm (see section 3.4.1).

Experiments E1 and E2 (using cost functions  $J_1$  and  $J_2$ , respectively) optimize a reduced number of observed variables in the cost function:

$$J_1(\vec{p}) = \frac{1}{L} \sum_{l=1}^L \frac{1}{\omega_l} R_{chl1} \quad (3.5)$$

$$J_2(\vec{p}) = \frac{1}{L} \sum_{l=1}^L \frac{1}{\omega_l} (R_{chl1} + R_{chl2}) \quad (3.6)$$

All other experiments compare the three available observed variables. The cost functions in experiments E4, E5, E4b and E5b are equal to  $F$  ( $J_4 = J_5 = J_{4b} = J_{5b} = F$ ), thus they evaluate optimizations for all compared variables, at all compared locations. Comparing results of E1, E2 and E4 aims to evaluate differences between “single-objective” and “multiple-objective” optimizations.

The experiments described above are performed as “joint” optimizations where all 22 locations are included. In contrast, experiment E3 (Eq. 3.7) corresponds to “single-site” optimizations (i.e., the optimization algorithm runs independently for each 1D model location). Note that the location-specific weight is not needed in this cost function:

$$J_3(\vec{p}, l) = (R_{chl1} + R_{chl2} + R_{NO3}) \quad (3.7)$$

Comparison between the results of E3 and E4 evaluates the compromise required when fitting all observed variables at all locations using one common set of parameters (section 3.5.2). The results of E3 were used to assess spatial patterns in the optimized parameters in a principal component analysis. I also compared the portability of my three model versions by running the 1D models of each location with parameters optimized for the rest of them.

As described in Table 3.4, the cost function of experiment E5 includes all observed variables at all locations, but differs from E4 in the number of parameters optimized. Results from the sensitivity analysis (section 3.4.2) show that the 6 most sensitive parameters in M1 and M2 are either the same or equivalent (Figure 3.6). Experiments E1 to E4 aimed to optimize these top 6 most sensitive parameters in M1 and M2, or their equivalents in M3. For example, the M3 equivalents of the phytoplankton reference growth rate  $\mu_0$ , used in the single phytoplankton models (M1 and M2), are both the small and large phytoplankton reference growth rates  $\mu_{0Ps}$  and  $\mu_{0Pl}$ . Due to lack of observational constraints for zooplankton, only one of the grazing rates is optimized ( $g_{maxZsPs}$ ), keeping the ratio to other grazing rates constant. In Experiment E5, I optimized only the top 3 most sensitive parameters of M1 and M2, or their equivalents in M3. Thus, the comparison between E4 and E5 evaluates how the number of optimized parameters affects the results (section 3.5.3). In preliminary tests, optimizing more than 6 parameters in M1 or M2 did not result in significant improvements.

Table 3.4 Summary of optimization experiments, detailing observed variables included in the cost function, and the number of parameters optimized.

Exp.	Stations included	M1 & M2		M3	
		Observations in cost function	Optimized parameters	Observations in cost function	Optimized parameters
E1	All	Satellite chl-a	$\mu_0$ , $m_P$ (or $m_{P0}$ ), $\tau$ , $\alpha$ , $\theta_{max}$ , $g_{max}$ (or $g_0$ )	Size fractionated satellite chl-a	$\mu_{0PS}$ , $\mu_{0PL}$ , $m_{PS0}$ , $m_{PL0}$ , $\tau_{PL}$ , $\alpha_{PS}$ , $\alpha_{PL}$ , $\theta_{maxPS}$ , $\theta_{maxPL}$ , $g_{maxZsPs}$
E2	All	Satellite + in situ chl-a	Like E1	Size fractionated satellite chl-a + in situ chl-a	Like E1
E3	Single	Satellite + in situ chl-a + in situ NO3	Like E1	Size fractionated satellite chl-a + in situ chl-a + in situ NO3	Like E1
E4	All	Satellite + in situ chl-a + in situ NO3	Like E1	Size fractionated satellite chl-a + in situ chl-a + in situ NO3	Like E1
E4b	All	(Performed for M3 only)		Like E4	$\mu_{0PS}$ , $k_{PsZs}$ , $m_{PS0}$ , $g_{maxZsPs}$ , $\beta_{Zs}$ , $\alpha_{PL}$
E5	All	Satellite + in situ chl-a + in situ NO3	$\mu_0$ , $m_P$ (or $m_{P0}$ ), $\tau$	Size fractionated satellite chl-a + in situ chl-a + in situ NO3	$\mu_{0PS}$ , $\mu_{0PL}$ , $m_{PS0}$ , $m_{PL0}$ , $\tau_{PL}$
E5b	All	(Performed for M3 only)		Like E5	$\mu_{0PS}$ , $k_{PsZs}$ , $m_{PS0}$

By optimizing equivalent parameters I aim to ensure an objective comparison. For instance, it has been theorized and shown that different models can produce similar fits to observations despite portraying different dynamics (Friedrichs et al., 2007; Quine, 1975). However, due to this parameter selection procedure, the number of optimized parameters in experiments E1 to E5 is higher for M3 than for M1 and M2. It could be argued that a

better performance of M3 may be a consequence of more degrees of freedom. In order to address this issue, the additional experiments E4b and E5b, which were performed only for M3, replicate experiments E4 and E5, but using the same number of optimized parameters as for M1 and M2 (i.e. the 6 and 3 most sensitive parameters, respectively). In all cases, parameters not included in the optimization subsets are kept fixed at their initial guess value (Table 3.3).

### **3.5 RESULTS**

Figure 3.7 summarizes the results of the optimization experiments (Table 3.4) in terms of the cost metric  $F$  (Eq. 3.3) of each model version in 1D. 3D simulations were performed only with parameters obtained in experiment E4 and their corresponding costs are also shown. Overall, model M3 presents lower costs than M1 and M2 in experiments E1 to E4, as well as in experiment E5b. However, in experiments E5 and E4b model M3 presents large model-data differences with respect to satellite chlorophyll. I describe and discuss these results in more detail in the following sections.

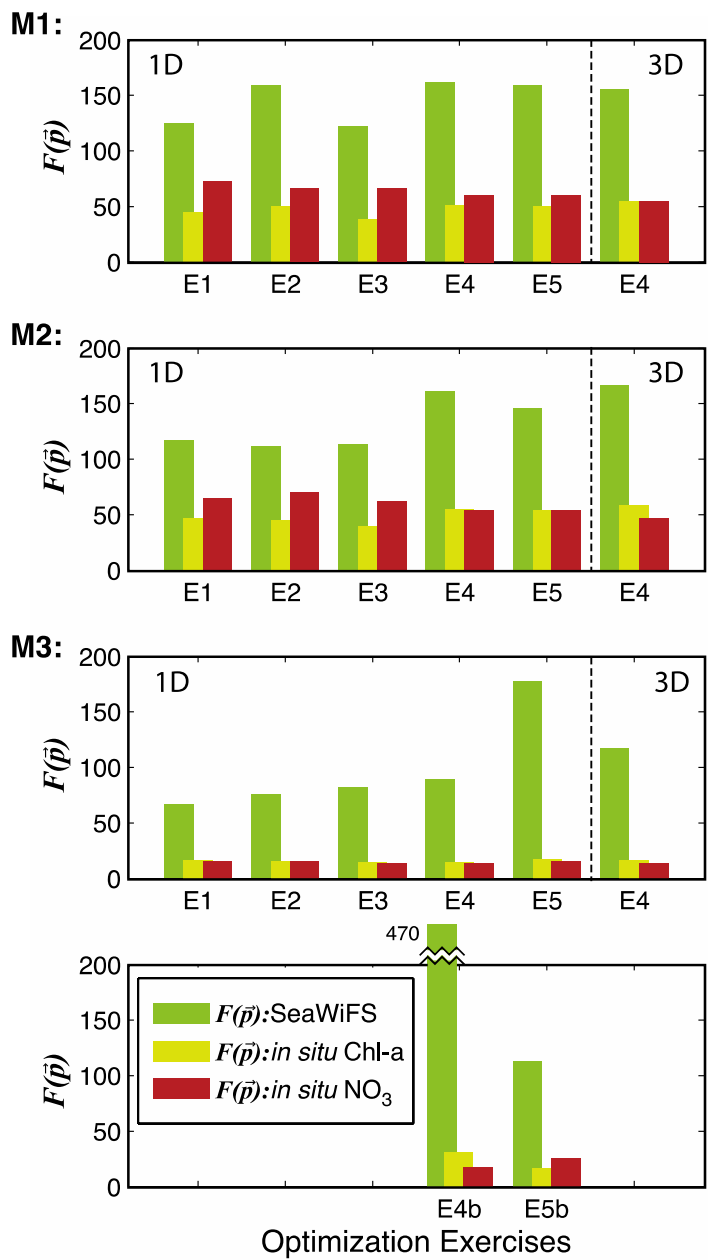


Figure 3.7 Final cost metrics of the optimization experiments (see Table 3.4). Optimized three-dimensional models were only run for the parameters obtained in E4.

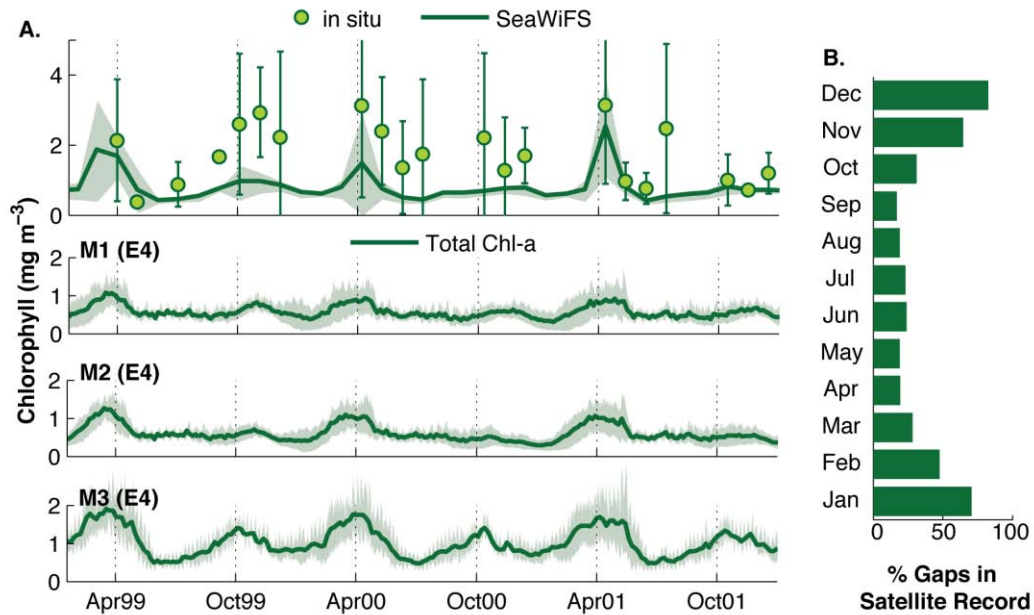


Figure 3.8 A. Mean surface SeaWiFS satellite and in situ chlorophyll (top), compared to surface chlorophyll simulated by the three model versions (M1, M2, M3) with optimal parameters from experiment E4. Shading and errorbars represent the standard deviation between locations. B. Percentage of gaps in the satellite record per month.

### 3.5.1 SINGLE VS. MULTIPLE OBSERVED VARIABLES

Comparison of experiments E1, E2 and E4 illustrates the effects of optimizing the models against satellite chlorophyll alone, i.e., using the most commonly available biological observation, versus including information about the vertical structure of chlorophyll and nitrate. The inclusion of chlorophyll profiles in the optimization (E2, Eq. 3.6) degrades the performance of M1 with respect to satellite chlorophyll, but has no significant effect on the performance of M2 and M3. The inclusion of both chlorophyll and nitrate profiles (E4) results in lower model costs with respect to nitrate, but higher costs with respect to both satellite and in situ chlorophyll. Figure 3.8A shows the

optimized results of E4 in comparison to surface chlorophyll; large discrepancies between satellite and in situ surface chlorophyll are observed between October and January. These months have the largest gaps in the satellite records (Figure 3.8B).

### 3.5.2 SINGLE VS. MULTIPLE LOCATIONS

In experiment E3, optimized parameters were found for each location individually using Eq. 3.7, but the  $F$  in Figure 3.7 was calculated using all individually optimized results as in Eq. 3.3. Allowing different optimal parameters for the different locations makes it easier to fit the individual patterns of variability, and thus a lower total cost is achieved. The results of experiment E3 are used to analyze whether spatial patterns in the biological parameters emerge (section 3.5.2.1) and to evaluate model portability from one location to another (section 3.5.2.2).

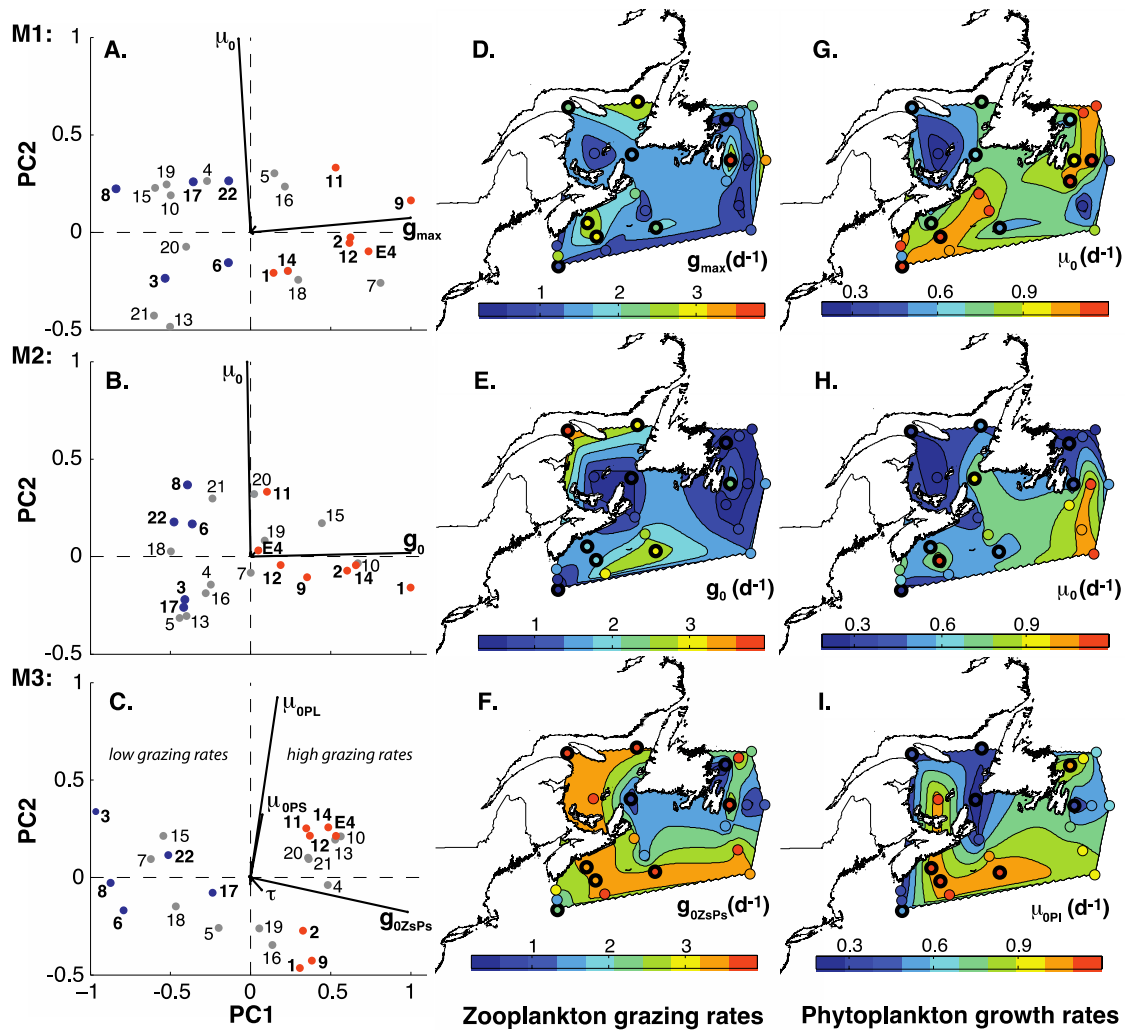


Figure 3.9 Analysis of spatial patterns in optimal parameters for individual locations: Subplots A. to C. show the principal components analysis for the three model versions in the study. Numbers refer to the locations as depicted in Figure 3.1. Some locations tended to consistently arrange themselves along PC1. Locations in blue are in the negative side for all three model versions, whereas locations in orange are always on the positive side. All other locations are shown in grey. Subplots D. to I. show the spatial distribution of the optimized parameters that dominated the variability on PC1 (reference zooplankton grazing rates), and PC2 (reference phytoplankton maximum growth rates). Circles of the locations with consistent behavior on the PC analysis have thick edges.

### 3.5.2.1 Spatial Patterns in Parameters

The analysis of the individually optimized parameters may reveal spatial patterns with dominance of specific plankton groups in different areas. A principal component analysis was performed on the optimal parameter sets obtained for each model version (Figure 3.9). In all model versions, the variability among locations is dominated by differences in the zooplankton grazing rates (PC1) and phytoplankton growth rates (PC2). Clearly defined clusters of locations are not identified by the analysis; however, some locations consistently arrange themselves along PC2 in all model versions. That is, some locations are consistently characterized by either high or low grazing rates. Spatial patterns in the grazing rates are, however, difficult to discern.

### 3.5.2.2 Model Portability

Model portability experiments were performed in the 1D environment, by iteratively applying the optimized parameters from one location (“optimized model”) to the rest of them (“test models”). Results are summarized in Figure 3.10, where the cost of the test models is normalized by the corresponding optimized model cost. M2 has the largest percentage of test models with cost equal to or lower than the optimized model (M1: 23.3%, M2: 32.9%, M3: 17.4%). The highest percentage of tests with cost larger than the optimized run occur in M3 (M1: 76.7%, M2: 67.1%, M3: 82.6%); however, M1 presented the highest percentage of tests with cost larger than twice the optimized run (M1: 32.3%, M2: 25.5%, M3: 26.7%). According to these results, M2 is the most portable of the three model versions, whereas M3 appears as the least portable.

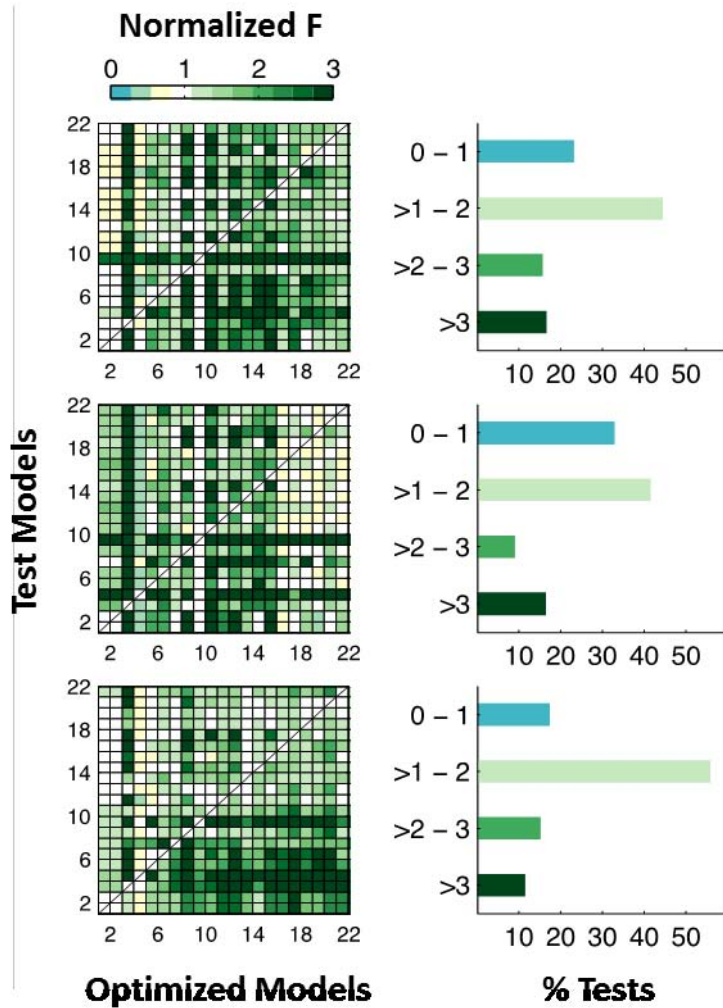


Figure 3.10 Results of the portability experiments. On the left panels, the color scale represents the cost of running the 1D model at locations on the y-axis (test models), using parameters optimized for locations on the x-axis (optimized models). Cost (F) values have been normalized to the corresponding optimal cost, such that all optimized models have a cost equal to one (bins along the diagonal). On the right panels, bars summarize the results in four cost categories.

Figure 3.11 shows an example of the portability experiments for two locations: location 4 (BON 49.21° N – 51.48° W) and location 11 (HAL 43.46° N – 62.43° W). The satellite observations at the BON location have a distinct spring bloom peak, which is well replicated by M2 using either parameters optimized for this location (Figure 3.11A)

or for the HAL location (Figure 3.11C). However, M3 can only replicate the annual peak when using the locally optimized set of parameters. The magnitude of the spring bloom at the HAL location is lower than at BON, the peak occurs earlier in the year, and other peaks of equal magnitude can occur at different times of the year. Due to this more irregular variability, both models are challenged to replicate the HAL location even when using locally optimized parameters. When locally optimized, both models appear calibrated to appropriately capturing the timing of maximum surface chlorophyll concentrations, such that large discrepancies with observations occur when the fall bloom is larger than the spring bloom, as in 1999. Locally optimized M2 favors maximum concentrations, and produces lower-than-observed summer to fall concentrations. In contrast, M3 favors average concentrations, better capturing summer to fall concentrations but underestimating the spring bloom maxima. The HAL test run of M2 maintains the spring bloom peak timing, but overall increases concentrations with emphasis on the fall. M3 generates a well-defined spring bloom of shorter duration.

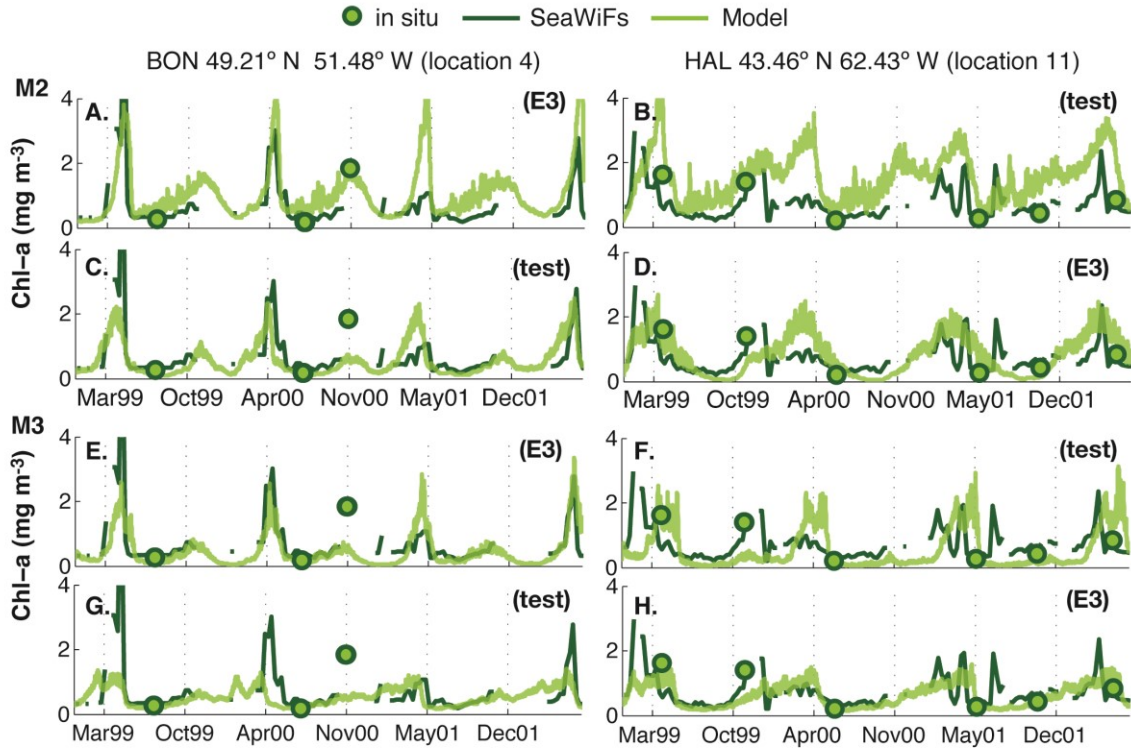


Figure 3.11 Example of the portability experiments, showing satellite, in situ, and simulated surface chlorophyll at locations BON and HAL. Subplots A. to D. correspond to results of M2, whereas subplots E. to H. correspond to results of M3. Subplots A., D., E., and H. show results of models optimized for their corresponding location. Subplots B., C., F., and G. are model results using parameters optimized for a different location.

### 3.5.3 NUMBER OF OPTIMIZED PARAMETERS

Experiments E4, E5, E4b and E5b aim to evaluate the effect of increasing or decreasing the number of optimized parameters on the optimization success. The cost metric results (Figure 3.7) show that the number of optimized parameters does not significantly affect the costs of M1 and M2. This is consistent with the results from the parameter sensitivity analysis, where the top 3 most sensitive parameters in M1 and M2 present a dominant effect on the model results in comparison with the rest of parameters

(Figure 3.6 A, B). In contrast, M3 was more evenly sensitive to all parameters (Figure 3.6C), and thus the number and choice of parameters to include in the optimization significantly affects the model results. For example, in experiment E4 a total of 16 parameters were optimized for M3. Those included sensitive parameters for all of the phytoplankton and zooplankton groups, while the subset of 6 parameters optimized in E4b only included one of the large phytoplankton parameters ( $\alpha_{p1}$ ). The optimization results of E4b successfully replicate the average small phytoplankton background concentrations, but fail to replicate the blooming of the large phytoplankton group (Figure 3.12). In other words, calibrating the initial photosynthetic slope of large phytoplankton was insufficient to obtain an adequately large phytoplankton response.

The cost of M3 in experiments E5 (5 optimized parameters) and E5b (3 optimized parameters) is within the range of those for M1 and M2, but the parameters obtained by these experiments generate unintended trophic dynamics where some functional groups become extinct in the model. The diagrams in Figure 3.12B summarize these emergent structures. In E4b, predatory zooplankton ( $Z_p$ ) disappear due to a combination of low prey biomass and low grazing rates. As large phytoplankton were not properly replicated, large zooplankton growth became inhibited by low prey densities, and both low large phytoplankton and low large zooplankton biomass affected predatory zooplankton. In E5, grazing rates were not part of the optimized parameters and did not scale with increasing phytoplankton growth rates. This resulted in the functional extinction of small zooplankton, while the model attempted to match zooplankton losses by increasing mortalities and coagulation rates. The negligible biomass of small zooplankton cascaded to the total extinction of large and predatory zooplankton. In experiment E5b, M3

essentially becomes a P-Z model similar to M1 and M2, due to the extinction of large and predatory zooplankton and the low concentrations of large phytoplankton.

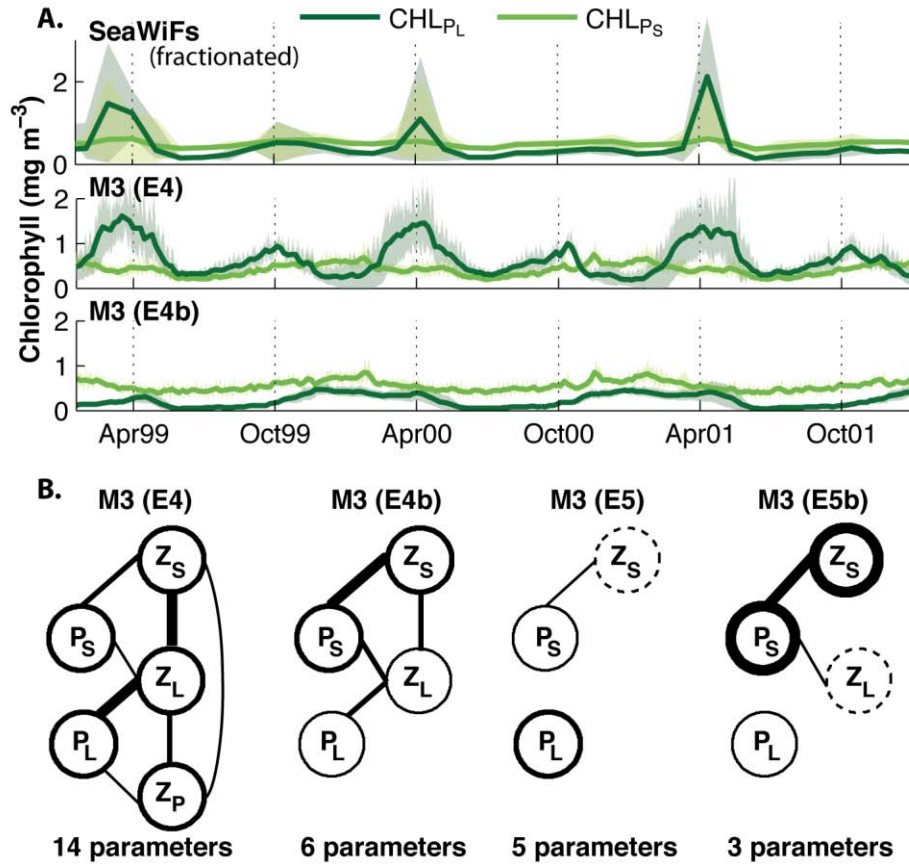


Figure 3.12 A. Comparison of satellite-derived size-fractionated mean surface chlorophyll, and their model counterparts in M3 from optimization exercises E4 and E4b. B. Diagrams depicting the trophic model structures of M3 resulting from different optimization exercises. The line thickness of the circles' edges is proportional to the plankton group mean biomass, whereas the thickness of connecting lines is proportional to the fluxes between them. Dashed lines depict groups that have negligible biomass, but that are still part of the model dynamics by receiving a small but not negligible flux of nitrogen (i.e., functionally extinct plankton groups). Groups with negligible biomass and fluxes are removed from the diagram.

#### 3.5.4 FLUXES

The choice of parameters of M3 in experiments E1 to E5 was intended to optimize comparable fluxes among all model versions. Nonetheless, differences in the resulting gross fluxes between variables are present between the 7-variable models and the 11-variable model. Figure 3.13 shows vertically integrated zooplankton grazing, phytoplankton growth (new and regenerated production), mortality and coagulation fluxes obtained for the models using parameters from E4. Differences in the new production fluxes are negligible between M1 and M2, but M1 presents a slightly higher annual peak in the regenerated production and grazing. The effect of temperature dependency on the phytoplankton mortality rates is noticeable during fall and winter, where M2 has lower rates than M1. In contrast to M1 and M2, M3 has more defined peaks in new production and more extended periods with high regenerated production. Grazing by small zooplankton is lowest in M3. Peaks in grazing by large and predatory zooplankton exceed the grazing rates in M1 and M2 by approximately  $2 \text{ mmol m}^{-2} \text{ d}^{-1}$  on average. Mortality of large phytoplankton during spring and summer is twice as high as the small phytoplankton mortality, but has approximately the same magnitude during winter. Mortality of large phytoplankton is twice the phytoplankton mortality flux in M1 and M2 during spring and summer, but the same as M2 during winter. The coagulation flux of large phytoplankton is negligible.

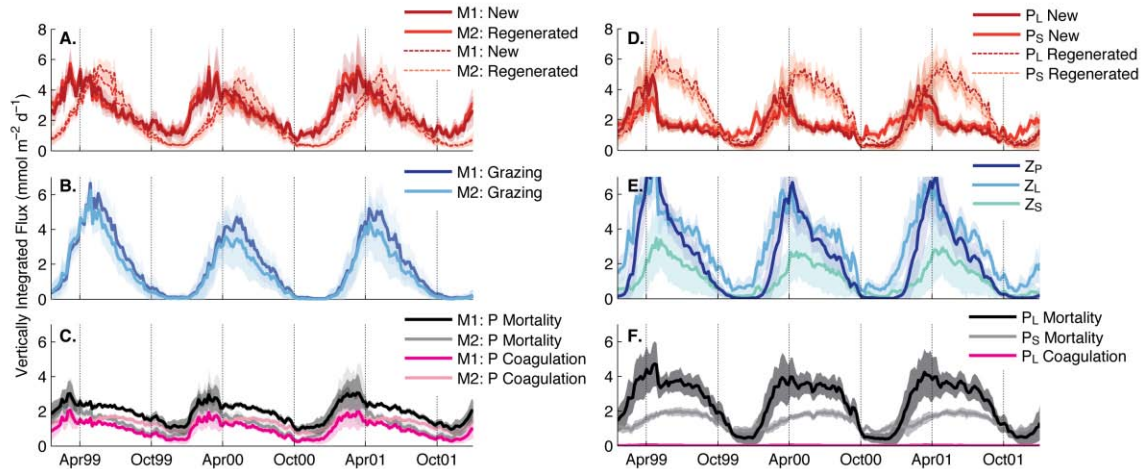


Figure 3.13 Vertically integrated phytoplankton new and regenerated growth, zooplankton grazing, and other phytoplankton sinks (mortality and coagulation). Subplots A. to C. show the fluxes in the 7-compartment models (M1 and M2). Subplots D. to F. show the fluxes in M3 for all plankton groups.

## 3.6 DISCUSSION

### 3.6.1 SURROGATES AND SURROGATE-BASED OPTIMIZATION

Simplified models allow us to avoid the computational expense of 3D models when performing sensitivity tests and calibrations. Here, a simplified 1D physical framework was shown to replicate the results of a 3D regional application at selected locations, using three different ecosystem model versions (Figure 3.3, 3.4). After optimization, the model-data misfit was reduced in both 1D and 3D applications for each of the three model versions (Figure 3.7, Appendix E). Similar types of site-based or test-bed calibrations of marine ecosystem models using 1D models have previously been shown to improve the predictive skill of 3D models (Oschlies and Schartau, 2005; Kane et al., 2011; McDonald et al., 2012). In most cases, the 1D models are built to represent averaged conditions at a climatological scale or over a relatively large spatial area (Dadou et al., 2004; Losa et al., 2004; Matear, 1995; Schartau and Oschlies,

2003a). This is intended to reduce the effect of phase biases that result from noise in both the observations and models, and the inability of models to replicate as much variability as is displayed in the observations (Hemmings et al., 2015; Leeds et al., 2012; Schartau and Oschlies, 2003a). I did not use climatological or spatial averaging; that is, surrogate-target and model-data comparisons were done on a site-by-site and date-by-date basis. Although this can be considered more challenging, the surrogates were able to capture between 36% and 70% of the variance in surface chlorophyll estimates of the 3D model sample (Figure 3.3).

The surrogate-based optimization was successful in improving the performance of the three ecosystem model versions. However, there are some systematic differences between 1D and 3D models in terms of the position of the deep chlorophyll maxima in summer. Overall, the deep chlorophyll maxima are shallower in the 1D models than in the 3D model (Figure 3.4), probably a consequence of the simplified two-layer vertical structure of turbulence in 1D. Similar discrepancies in the position and extend of the deep chlorophyll maximum have been previously noted in 1D models (Doney et al., 1996; Fasham et al., 1993), including 1D calibration studies (Schartau and Oschlies, 2003b). In the latter, the vertical diffusivities in the 1D model were directly taken from the target model. This suggests that biases in the deep chlorophyll maxima may be inherent to 1D models, and are not entirely due to the oversimplification of the diffusive component. Using diffusivities from the 3D output for site-base calibration (Hemmings et al., 2015; Schartau and Oschlies, 2003a) can increase the risk of introducing model-data misfits due to misplaced eddies or systematic mesoscale errors.

The mechanistic surrogate approach allowed us to identify features in the variables of interest that are likely dominated by the biological module from those controlled by the physics. In my case, the timing of the peak of the spring bloom was overall well captured by the 1D models (Figure 3.8, 3.11). This indicates that this phytoplankton phenological characteristic is well constrained by the observations used during the optimization, and sensitive to the choice of

parameters optimized. In Chapter 2 I established that the estimate of the winter mixed layer was key to determining an appropriate level of annual nutrient replenishment in my 1D framework (Kuhn et al., 2015). However, this may be insufficient for locations where other processes, such as advective fluxes or high frequency changes in stratification, contribute to changes in nitrate concentrations.

### 3.6.2 DECIDING ON A COMPLEXITY LEVEL

In my results, the more complex (11-compartment) model M3 was able to generate the lowest model-data misfits in all optimization experiments where the intended model structure was preserved. In particular, M3 exhibits reduced differences against the observed chlorophyll and nitrate vertical distributions. The simpler (7-compartment) model structures have a higher cost, but are also able to capture the averaged seasonal variations in surface chlorophyll. Therefore, if the objective of a modeling study is to characterize the overall seasonality in surface chlorophyll, a simple model may suffice. Complex models have obvious utility in the study of trophic interactions and may also be better able to capture vertical distributions.

Some of the earliest attempts to assess the most appropriate level of ecosystem complexity in models were inconclusive (e.g., Dadou et al., 2004; Matear, 1995); while others recognized that the differences found were likely related to the parameter selection and functional equations, rather than the model structure itself (e.g., Sailley et al., 2013). In fact, the optimization experiments of Kriest et al. (2010) demonstrated that increasing complexity of unoptimized models does not necessarily improve model performance. Among the studies unable to identify the best level of complexity, Matear (1995) investigated three different optimized ecosystem configurations and concluded that the

data from the study site were insufficient to justify the use of more complex models over the commonly used nutrient-phytoplankton-zooplankton-detritus (NPZD) model. Similarly, Dadou et al. (2004) compared three alternative optimized model configurations with similar complexity at an oligotrophic study site in the Eastern North Atlantic, and were not able to objectively discriminate between the designs. The comparison of Bagniewski et al. (2011) concluded none of the model variants could be rejected based on their misfit against constraining observations; however, they generated significantly different estimates of export carbon fluxes.

Based on poor model-data fits obtained after applying parameter optimization, Rückelt et al. (2010) argued that the structure of NPZD models is too simple and not suitable to reproduce observations from the Bermuda Atlantic Time Series station. However, other optimization studies using NPZD models and observational climatologies from the North Atlantic have been able to significantly reduce model-data differences (Kuhn et al., 2015; Schartau and Oschlies, 2003a). Moreover, it has also been shown that systematically removing some of the unconstrained aspects of an ecosystem model does not significantly increase the value of the cost metric (Ward et al., 2013). One of the most comprehensive comparisons of optimized marine ecosystem models is found in Friedrichs et al. (2007). They compared 12 individually optimized ecosystem models and showed that, when optimized for an individual location, models with only one phytoplankton and one limiting nutrient could reproduce observations as well as the more complex models. However, models with multiple phytoplankton groups outperformed the single phytoplankton group models in geographical portability experiments. My results agree with this study in the first aspect, but differ in the conclusions from portability

experiments. When applied to a different location than the one it was calibrated for, my model with multiple phytoplankton groups tended to maintain chlorophyll magnitude characteristics from its original location.

When optimizing models with multiple phytoplankton groups the value of a cost function based on total chlorophyll could be misleading. Hence, I decided to use an estimate of size-fractionated surface chlorophyll. The independent constraining of small and large phytoplankton makes the more complex model less portable when calibrated for individual locations (Figure 3.10, 3.11), as it tends to benefit one phytoplankton group over the other depending on the chlorophyll abundance of specific locations. Lower predictive ability in complex models has been posited to occur when the model becomes over-fitted to noise in the data (e.g. Friedrichs et al., 2006). If community composition information were available to compare against all simulated plankton groups, a model with more groups could become too specific to its training data set.

The most portable model in my experiments was M2, which had 7 compartments and temperature-dependent biological rates. This suggests that improving mechanistic interactions, rather than introducing unconstrained diversity, has the potential to increase the global applicability of an ecosystem model. Temperature dependent grazing and mortality rates have been previously noted to improve the performance of global models (Behrenfeld et al. 2013), and this clearly also applies to dynamically complicated regions like the northwest North Atlantic. Therefore, to benefit from the higher performance of a site-based calibrated complex model, such calibration requires including samples from all biogeographical provinces to be simulated.

I also showed that the performance of M3 could significantly degrade depending on the choice of parameters to be optimized, as biological parameter values have the ability to effectively modify the intended trophic interactions in a model (Cropp and Norbury, 2009; Sailley et al., 2013). In my optimization experiments, these unintended behaviors included the functional and/or total extinction of plankton groups. Similar extinctions occur when no scaling weights are assigned to different locations in the cost function, as the optimization becomes biased towards locations with higher biomass, and generates extinct functional groups at the locations with lower biomass (e.g., Schartau and Oschlies, 2003a). Due to the non-linear nature of ecosystem models, the extinction of one component can have unforeseen, however logical, consequences. For example, Cropp and Norbury (2009) showed that removing the predator of a given prey does not only allow such prey population to increase, but can also lead to the extinction of competing prey and their predators, and ultimately generate the system's collapse. In a subsequent study, they concluded that it is rare to find parameters that maintain the intended structure of plankton functional type models, and that delicately balanced parameter sets are required in models with multiple preys and predators (Cropp and Norbury, 2010).

### 3.6.3 UNCERTAINTIES

The main uncertainty in the use of mechanistic surrogate-based calibrations with 1D models is in neglecting horizontal advection fluxes. In addition, there are two main issues with the use of optimized simulations for analyzing the effects of ecosystem model complexity: 1) the cost function is not an entirely objective measure, thus its design can

affect the outcome of the optimization, and 2) the selection of parameters to optimize is subjective as well, and can have a dramatic effect as I have shown.

I neglected horizontal advection, as is typically done in 1D models, assuming that horizontal divergence terms are small relative to vertical mixing and to the biological sources and sinks. This treatment allowed us to have an estimate of how much a 3D application of an oceanographically complex region, the northwest North Atlantic, can be improved with the use of reduced-order models. Nonetheless, this assumption may impact the surrogate performance. Hemmings and Challenor (2015) explicitly examined the effect of introducing horizontal advective flux in a mechanistic emulator composed of 1D models representing the ocean conditions of twelve 5-degree latitudinal bands at 20° W in the North Atlantic. Their results showed that the addition of horizontal fluxes improved the correlation coefficient between 1D and 3D surface chlorophyll. The addition of horizontal advective fluxes in the surrogates is only recommended if the velocities of the target 3D model are accurate; otherwise, the biological parameters may tend to compensate biases introduced by an erroneous physical forcing. Advective fluxes can be of particular importance in certain locations. Friedrichs et al. (2007) neglected horizontal advection in the Arabian Sea, but included the horizontal advective divergence of nitrate in the Equatorial Pacific. The decision was based on a scaling study that showed that the horizontal advection of nitrate has first order effects on the biogeochemistry of that region (Friedrichs and Hofmann, 2001). In my study, some effects of neglecting advective fluxes are compensated by nudging deep nitrate in the surrogates.

The design of the cost function can partly compensate the absence of horizontal transport, as in the weak constraint approach of Losa et al. (2004), as can the use of

relaxation (like the nudging term applied here to nitrate) and correction terms to all biological variables (Hemmings and Challenor, 2012; Prieß et al., 2013a). Correction terms can also account for other systematic or random errors in the surrogate; however, as suggested in section 3.4.1, the more the 1D model is forced to behave like the 3D model, the less useful it becomes in identifying the sources of deficiencies in either the physical or the biological components of the model. A consideration in the use of correction terms is that the distribution of errors in the 1D and 3D models is not necessarily the same during the optimization. Hemmings and Challenor (2015) discussed this aspect in detail, and found that a statistical error term appeared more robust than a parameter-dependent error term.

Another issue of importance in the design of the optimization cost function is the selection of weights to balance the contributions of different variables and/or locations. In multi-objective optimizations, optimal parameters become a compromise between different biogeochemical conditions and sources of data. Hence, the optimization results are quite sensitive to the scaling approach. The lack of any explicit treatment of biases, and the weighing scheme used in the cost function are consistent with previous studies (e.g., Friedrichs et al., 2007; Ward et al., 2010). However, I emphasize the importance of correcting biases between observational data sets of the same simulated variable, as I did in the case of surface chlorophyll.

A novel inclusion in the design of the cost function was the use of fractionated chlorophyll to compare against the small and large phytoplankton groups, which influenced the results of my portability experiments. It can be expected that advancements in our understanding of how complex ecosystem models behave can be

made with the use of other empirical sources of information for the optimization of unconstrained variables. For example, zooplankton abundances from Continuous Plankton Recorder measurements cannot be directly compared to model results, but could provide estimates of seasonal variability (Lewis et al. 2009) that can be scaled to the corresponding zooplankton functional groups in optimization experiments. This might be particularly useful, since phytoplankton losses are among the least constrained parameters, even for simple NPZD models (e.g., Bagniewski et al., 2011, Fennel et al. 2001).

Poorly constrained parameters can be set to arbitrary values during the optimization without significantly affecting the model cost (Ward et al., 2010) or otherwise tend to hit their a priori distribution limits (e.g. Schartau and Oschlies, 2003). When unconstrained parameters are fixed to their a priori best estimates, the level of previous tuning to the original model domain can skew the results of geographical portability experiments (Ward et al. 2010). Previous portability experiments (Friedrichs et al. 2006, 2007) had shown that an increasing number of optimized parameters reduced the ability of complex models to simulate unassimilated observations. Nevertheless, my results comparing the effects of the number of optimized parameters showed the opposite tendency (Figure 3.12). I presume this occurred due to two aspects of my experimental design. First, the use of fractionated chlorophyll in the cost function limited the ability of the parameters of one phytoplankton group to compensate for uncalibrated parameters in the other group. Second, my most complex model had not been previously calibrated. Under this scenario, increasing the number of parameters included in the optimization

turned out to be beneficial. This confirms that the selection of parameters to be optimized should be done with consideration of the level of previous model tuning.

### **3.7 CONCLUSION**

Parameter optimization methods offer a systematic approach to reduce subjective model tuning and quantitatively compare ecosystem models with different complexities; however, optimization is not an entirely objective methodology with a unique solution. I have illustrated that, in addition to the uncertainties of the physical environment, conclusions about the accuracy and portability of a model can differ depending on decisions about the design of the cost function, the selection of parameters to be optimized, and the level of preliminary calibration of each model. Due to the limitations of applying parameter optimization in 3D coupled physical-biogeochemical models, 1D surrogates represent an efficient alternative for the exploration of the parameter space and for geographical portability experiments. In an extensive application of this concept, I used ensembles of 1D models that behave as their regional 3D model application counterparts, and used them to compare the performance of three ecosystem model versions. Processes unresolved by the 1D physical models and the level of ecosystem model complexity did affect the accuracy of the surrogates; however, successful surrogate-based model calibrations were possible and generated similar model-data misfits when applied in the 1D and 3D environments.

When an appropriate set of parameters was optimized, the model with multiple phytoplankton and zooplankton groups was better able to replicate assimilated observations than the single phytoplankton and zooplankton models. Nonetheless, the

simpler models were also able to replicate the observed averaged seasonal variations in surface chlorophyll well. These results are consistent with previous studies and suggest that more complex trophic structures in models can better capture the observed temporal variability and spatial distribution of biogeochemical variables at multiple locations. In an additional analysis, geographical portability experiments provided an indication of how each model structure behaves with respect to unassimilated information. In this case, the most complex model was found to be the least portable, as the parameters optimized at some locations tended to favor either small or large phytoplankton. I used satellite-derived estimates of fractionated surface chlorophyll as observational counterparts to compare against the simulated chlorophyll concentrations of small and large phytoplankton groups. This was likely to reduce model portability when calibrated for specific locations, as the model became overspecialized. While this result is opposed to portability experiments previously performed in other ocean regions, it is consistent with early theoretical notions about the expected behavior of complex models. Moreover, when I varied the selection of optimization parameters in the complex model, it was prone to unsatisfactory results and unintended model behaviors. Attempting to optimize an improper selection of parameters resulted in the extinction of certain plankton groups, thus modifying the intended structure of trophic relationships in the model. Hence, my results highlight that a guided selection of the parameters to be optimized is necessary, especially when – as in this case – little or no prior model tuning has been performed.

My results also highlight that in order to benefit from the improved ecosystem representation that a complex model provides, such model needs to be trained with observations from diverse geographical locations. Research is required on efficient

sampling methodologies to calibrate global surrogates, allowing us to determine the number of locations that would be sufficient, and ensuring that the most representative locations are being selected.

Finally, I also observed an improvement in my simplest model version when all biological fluxes were configured to depend on temperature. Therefore, I can conclude that improving the mechanistic relationships, rather than adding unconstrained diversity, can lead to more robust globally applicable models. Here I base this statement on the results of the model including temperature dependency in all biological rates, but the same argument may apply to the use of allometric or otherwise scaled models. In the next chapter, I analyze how these optimized model versions perform when applied to the 3D environment: Does complexity affect conclusions about the drivers underlying phenology? How does complexity affect estimates of primary production? The answers to these questions are key when making decisions about which level of complexity should be used for the northwestern North Atlantic.

## **CHAPTER 4:**

# **EVALUATING ECOSYSTEM COMPLEXITY IN THE NORTHWEST NORTH ATLANTIC, PART II: SURFACE CHLOROPHYLL VARIABILITY, PRIMARY PRODUCTION AND ECOSYSTEM DYNAMICS**

## **4.1 INTRODUCTION**

The northwest North Atlantic continental shelf is a dynamically complex area that lies at the confluence of two large-scale western boundary current systems: the Labrador Current and the Gulf Stream (Loder et al., 1998). The region has long been recognized for its high biological productivity from a fisheries perspective (Mills and Fournier, 1979), but primary production estimates are relatively scarce (Townsend et al., 2004). Previous studies have focused on specific locations within this region, with the Gulf of Maine and the Scotian Shelf being among the best documented (Fournier et al., 1977; Fournier et al., 1979; Song et al., 2001; Zhai et al. 2001). The region is confronted with several contemporary and future challenges due to natural climate variability and anthropogenic pressures, which led to a dramatic decline of commercial fisheries landings on the Scotian Shelf since the 70's (Zwanenburg et al., 2002).

In order to better manage fish stocks, for example using integrated bio-economic models (Carozza et al., 2017), an accurate view of the magnitude and patterns of primary production in the region is necessary. Different phytoplankton functional groups with their specific physiological traits have varying potential to transfer energy from primary producers to higher trophic levels (Litchman et al., 2007; Litchman and Klausmeier,

2008; Strom, 2008) . This is due to their different responses and adaptations to environmental processes (Boyd et al., 2010), as well as their different nutritional values and strategies to escape predation (Strom, 2002). On the Scotian Shelf, it has been suggested that different trophic pathways, including small and large plankton size fractions, sustain the year-round production of fish-larvae in the region (Mosseau et al., 1998).

Nevertheless, the effects of increased trophic complexity in regional ecosystem models have not yet been fully determined (Denman, 2003; Anderson, 2005; Van Nes and Scheffer, 2005; Le Quéré, 2006; Friedrichs et al., 2007). Models with few state variables, pathways, and parameters (i.e., “simple models”) are powerful tools for hypothesis testing because they are easy to interpret (e.g., Evans and Parslow, 1985; Fasham et al., 1990; Kuhn et al., 2015). These models can be limited in their generality, which may hamper their use at a global scale or in oceanographically complex regions like the northwest North Atlantic. In contrast, the “complex models” attempt to represent a more realistic ecological structure, by adding more state variables for planktonic functional groups or size classes, nutrient and organic matter pools, etc. Determining how these differences in structure affect model behavior quickly becomes complicated by the proportional increase of model parameters and pathways (Denman, 2003). Accurate simulation of multiple plankton groups would improve our understanding of species succession, the microbial loop, secondary and export production; however, observational evidence of predation rates and predator-prey interactions is scarce, limiting the ability to constrain and evaluate complex models. One recent analysis of prey-predator interactions

in global models has shown that the actual food webs represented in these complex models are different to those intended or expected (Sailley et al., 2013).

In Chapter 3, I applied an evolutionary algorithm to optimize three biological models of increasing complexity that served as surrogates for three-dimensional models of the northwest North Atlantic. In these optimization experiments, the complex model achieved lower model-data misfits than the simpler models, as expected. This result is consistent with previous studies suggesting that more complex trophic structures in models can better capture the observed temporal variability and spatial distribution of biogeochemical variables at multiple locations (Friedrichs et al., 2007). However, the complex model was prone to generating unintended trophic relations depending on the selection of optimization parameters, and exhibited reduced portability when optimized for specific locations. These results highlight the trade-off between the pursuit of ecological realism, and the danger of overfitting as the number of parameters that cannot be effectively constrained by the available observational data grows (Flynn, 2005; Ward et al., 2013, 2010).

Here I apply the optimal parameters obtained from the one-dimensional surrogates in a three-dimensional Regional Ocean Modelling System (ROMS) application for the northwest North Atlantic, in order to provide an overarching view of whether and how trophic structure could affect key ecosystem variables and primary production estimates. I aim to tease apart the effects of temperature dependence of metabolic rates from those of increased trophic complexity. Model estimates are evaluated against satellite-derived surface chlorophyll and vertically integrated primary production. The ROMS model domain includes areas that were not represented by the one-dimensional model surrogates

in the parameter optimization, therefore providing additional insights into the performance of models with respect to unassimilated data. The goal of this study is to determine the most appropriate level of complexity for the northwest North Atlantic 3D application, while aiming to answer i) how complexity affects our understanding of bottom-up and top-down drivers underlying phenology, and ii) how complexity affects estimates of primary production.

## **4.2 OCEANOGRAPHIC CHARACTERISTICS AND SUB-REGIONS IN THE NORTHWEST NORTH ATLANTIC**

The study area is the same briefly described in Chapter 3 (see Figure 4.1), and comprises coastal, slope and open waters of the northwest North Atlantic Ocean, including the Gulf of Maine and the eastern Canadian coast. The bathymetry of the region is characterized by broad continental shelves that are widest off Newfoundland and Nova Scotia. Two major current systems converge in the area: the equator-ward flowing Labrador Current, and the northeast flowing Gulf Stream, with their adjoining Shelf and Slope Water currents (Townsend et al., 2004). The Labrador Current is a cold, relatively fresh, buoyancy driven coastal current (Csanady and Hamilton, 1988; Chapman and Beardsley, 1989) that extends across isobaths and transports Labrador Slope Water (LSW). LSW is characterized by temperatures of 4 - 8 °C and salinities of 34.3 – 35 (Gatien 1976). In contrast, Warm Slope Waters adjacent to the Scotian Shelf are a mixture of Gulf Stream water and Labrador Current water, and have temperatures of 8 – 12 °C and salinity of 34.7 – 35.5 (Gatien, 1976). Lateral density fronts are present throughout the region (Loder and Greenberg, 1986; Townsend et al., 2004). In particular, the shelf-break front separates the relatively cool and fresh shelf waters from warmer

more saline slope waters. The shelf break front is present throughout the year but its structure varies seasonally (Frantantoni et al., 2000; Lozier and Gawarkiewicz, 2001).

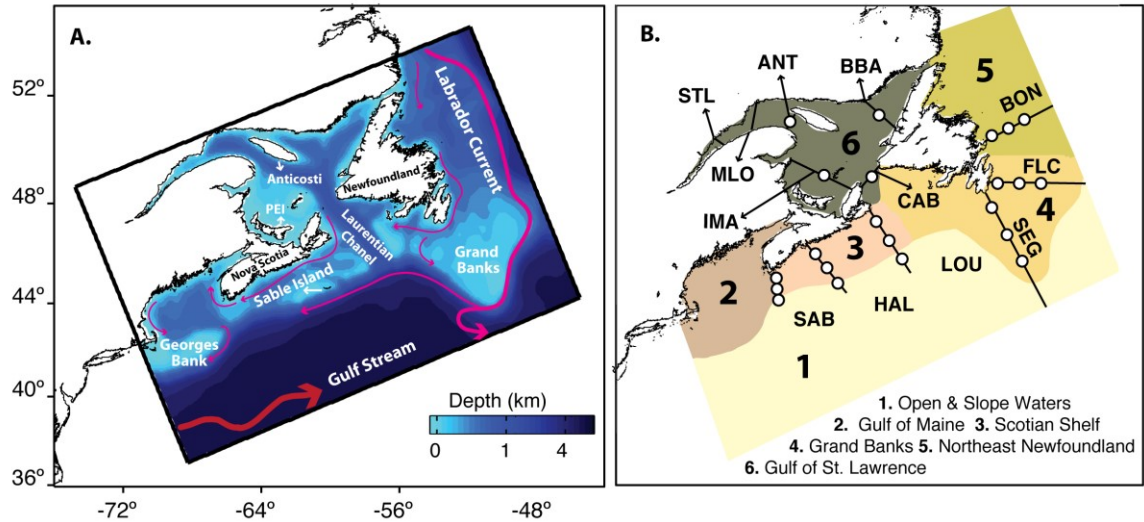


Figure 4.1: A. Model domain bathymetry, major ocean circulation characteristics based on Townsend et al., (2004), and geographical locations mentioned in the text. B. Study area sub-regions, location of the Atlantic Zone Monitoring Program (AZMP) transects (black lines), and location of the one-dimensional models used for the surrogate-based optimization (white circles).

For the evaluation of model results I divided the domain into 6 sub-regions (Figure 4.1B). The one-dimensional models used in Chapter 3 are predominantly located on the Scotian Shelf, in Gulf of St. Lawrence and on the Grand Banks, with few locations on the Newfoundland Shelf. No observations were assimilated in the sub-regions containing Open and Slope Waters (sub-region 1), and the Gulf of Maine (sub-region 2), hence observations for these regions can serve as independent validation of model performance.

### 4.3 OBSERVATIONAL DATASETS

Satellite-based chlorophyll estimates come from the Sea-viewing Wide Field-of-view Sensor (SeaWiFs) 8-day averages with a 9-km resolution (<https://oceandata.sci.gsfc.nasa.gov/SeaWiFS/>). I performed a regression analysis between satellite chlorophyll estimates and matching available records of in situ chlorophyll from 1997 (beginning of SeaWiFs record) to 2010 (end of SeaWiFs record). In situ chlorophyll comes from the Atlantic Zone Monitoring Program (AZMP, <http://www.meds-sdmm.dfo-mpo.gc.ca/isdm-gdsi/azmp-pmza/index-eng.html>) measurements. The comparison between satellite-derived and in situ surface chlorophyll (Figure 4.2) shows that SeaWiFs systematically overestimates chlorophyll inside the Gulf of St. Lawrence. The largest biases are observed at the mouth of the estuary (STL) where the satellite estimates exhibit a narrower range than the observed values. Satellite and in situ observations in the Gulf coincide in the maximum values observed at each of the monitoring lines, showing a decrease in maximum values from the innermost locations (STL, MLO, ANT) toward locations farther from the estuary mouth (IMA, BBA). At locations outside the Gulf of St. Lawrence, SeaWiFs tends to overestimate low chlorophyll values and underestimate high chlorophyll values. The overall bias is much smaller than in the Gulf. The bias in the Gulf was removed to correct satellite chlorophyll values prior to the parameter optimization (Chapter 3). De-biasing satellite chlorophyll concentrations in the Gulf of St. Lawrence results in concentrations between 1.5 and 3 mg Chl-a m<sup>-3</sup> along the estuary (STL) and Iles de la Madeleine (IMA) transects, and lower than 0.5 mg Chl-a m<sup>-3</sup> near Bonne Bay (BBA).

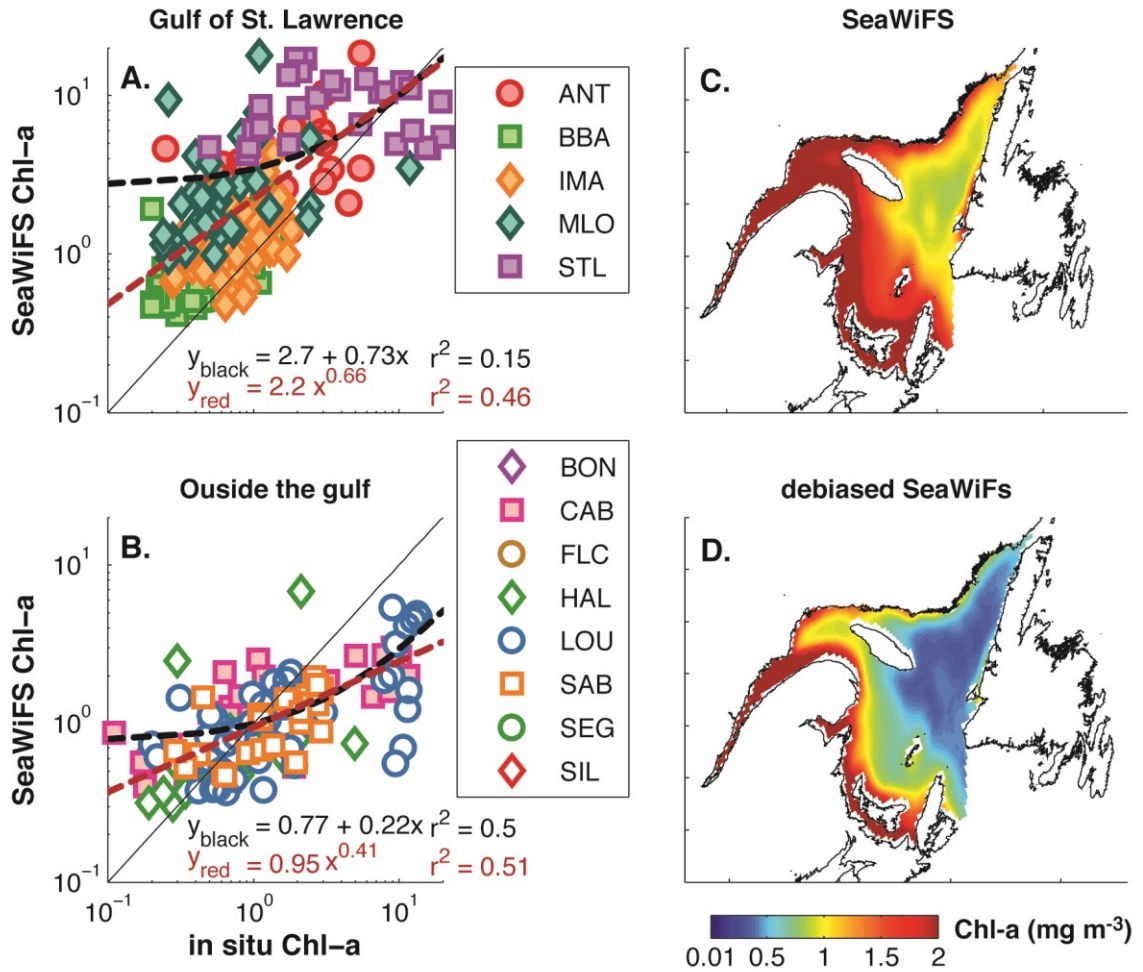


Figure 4.2: Regressions of in situ and SeaWiFS satellite chl-a inside (A) and outside (B) the Gulf of St. Lawrence. The black and red dashed lines are regressions lines between chlorophyll values ( $y_{black}$ ), and log-transformed chlorophyll values ( $y_{red}$ ), respectively. C. and D. show satellite chl-a in the Gulf before and after removing the bias estimated from A.

Satellite-derived monthly estimates of primary production come from two different algorithms: the Vertically Generalized Production Model (VGPM), and the Carbon-based Productivity Model (CbPM), both available at <http://www.science.oregonstate.edu/oceanproductivity/index.php>. The VGPM is a chlorophyll-based, light-dependent, depth-resolved algorithm (Behrenfeld and Falkowski,

1997), commonly used to estimate regional and global primary production. For consistency with the satellite chlorophyll used here, I use the VGPM results based on SeaWiFs chlorophyll and photosynthetically active radiation products. The CbPM estimates (Westberry et al., 2008) are based on the photosynthetically active radiation SeaWiFs product, and the particulate backscatter and phytoplankton absorption coefficients estimated with the GSM spectral matching algorithm (Garver and Siegel, 1997; Maritorena et al., 2002; Siegel et al., 2002b).

#### **4.4 MODEL DESCRIPTION**

##### **4.4.1 PHYSICAL MODEL**

I use a three-dimensional physical circulation model based on the Regional Ocean Modelling System (ROMS, version 3.5), a terrain-following, free-surface, primitive equation ocean model (Haidvogel et al., 2008). The model has a 240-by-120 horizontal grid cells (~10 km horizontal resolution) and 30 vertical levels, with a minimum water depth of 10 m. The model is nested within the regional ocean-ice model of the northwest North Atlantic from Urrego-Blanco and Sheng (2012) and is forced with atmospheric fields (winds, specific humidity, air temperature, precipitation, and short and long-wave radiation) from the European Centre for Medium-range Weather Forecasts (ECMWF) global reanalysis (ERA-Interim) (Dee et al., 2011). Simulated temperature, density and mixed layer depths are in good agreement with their observational counterparts obtained from the AZMP measurements (Figure 4.3). A detailed model validation and sensitivity analyses of different physical forcing configurations can be found in Brennan et al. (2015).

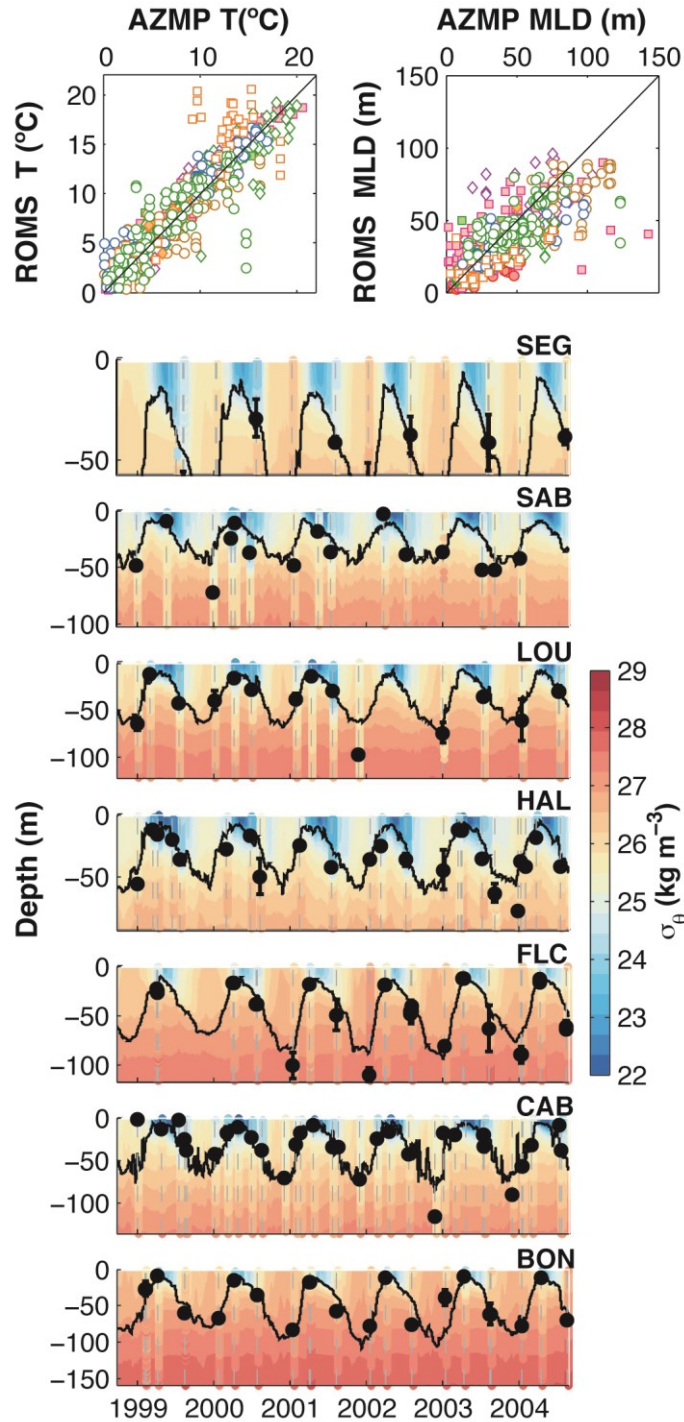


Figure 4.3: Comparison of simulated (ROMS) and observed (AZMP) temperature and mixed layer depths (A and B). Symbols for each transect line follow the same legend as Figure 4.2. The mixed layer depth is estimated with a density threshold criterion of  $\Delta\sigma_\theta = 0.025 \text{ kg m}^{-3}$  from the surface density reference. C. Simulated and observed density ( $\sigma_\theta$ ). Observed density profiles are overlaid on

top of model results using the same color scale, dates of each profile are marked by a gray dashed vertical line. The solid black line represents the depth of the mixed layer (m) estimated from model output, and the black circles represent the same estimate using observed profiles.

#### 4.4.2 BIOGEOCHEMICAL MODELS

My three ecosystem models, referred to as M1, M2 and M3, were implemented and optimized using an evolutionary algorithm implemented with a surrogate-based method (see Chapter 3). M1 is the simplest model. It has 7 model compartments and only the phytoplankton maximum growth rate depends on temperature. Model version M2 has the same number of variables and the same structure as M1, but all the biological rates depend on temperature. M3 uses the same functional forms as M2, but has a total of 11 model state variables following the structure of the North Pacific Ecosystem Model for Understanding Regional Oceanography (NEMURO; Kishi et al., 2007). M3 includes two phytoplankton and chlorophyll size classes (small and large), and three zooplankton groups (small, large and predatory). The biological model parameters used here are those obtained in optimization experiment E4 in Chapter 3. In E4, I optimized the 6 most sensitive model parameters of M1 and their equivalents for M2 and M3. The rest of the parameters are from the previous configuration in Fennel et al. (2006, 2009). The optimized parameters are a compromise between satellite chlorophyll, in situ chlorophyll, and in situ nitrate, in all 1D surrogate locations shown in Figure 4.1. According to the cost metric in Chapter 3, optimized M3 presented the best model skill when calibrated for all locations; however, geographical portability experiments suggested that M2 could replicate unassimilated data the best when calibrated only for specific locations.

## 4.5 RESULTS

### 4.5.1 SURFACE CHLOROPHYLL SEASONAL VARIABILITY

Simulated and satellite surface chlorophyll annual cycles for all six sub-regions are presented in Figure 4.4. The annual cycles of surface chlorophyll obtained by the three models are similar to each other in terms of the development of a well-defined phytoplankton spring bloom from March to May in all model domain sub-regions. The largest divergence between model responses, except for the Gulf of Maine, is from May to September, i.e., the spring bloom termination and the summer surface chlorophyll minima. In sub-regions 1, 3, 4 and 6, M3 produces the lowest chlorophyll values in summer, and the best agreement with the satellite estimates. During winter, all models underestimate the observations, except in Sub-region 1.

The Open and Slope Waters (Sub-region 1), have the lowest observed chlorophyll concentrations of all sub-regions, with maximum values around  $1.2 \text{ mg Chl-a m}^{-3}$  and low interannual standard deviations. Compared to other sub-regions, sub-region 1 has an extended period of low chlorophyll conditions in summer, and only a small fall bloom similar in magnitude to winter chlorophyll concentrations. Summer chlorophyll minima are the lowest of all sub-regions, with concentrations below  $0.4 \text{ mg Chl-a m}^{-3}$ . The three models overestimate chlorophyll concentrations during the bloom development phase, but agree in the timing of its peak. M1 diverges the most from satellite estimates. It overestimates the spring bloom magnitude and develops a pronounced fall bloom similar in magnitude to the spring bloom. M2 and M3 agree with the satellite estimates in terms of the spring bloom peak and late fall chlorophyll concentrations. M3 simulates the

lowest summer chlorophyll concentrations and thus agrees the best with the observed annual cycle.

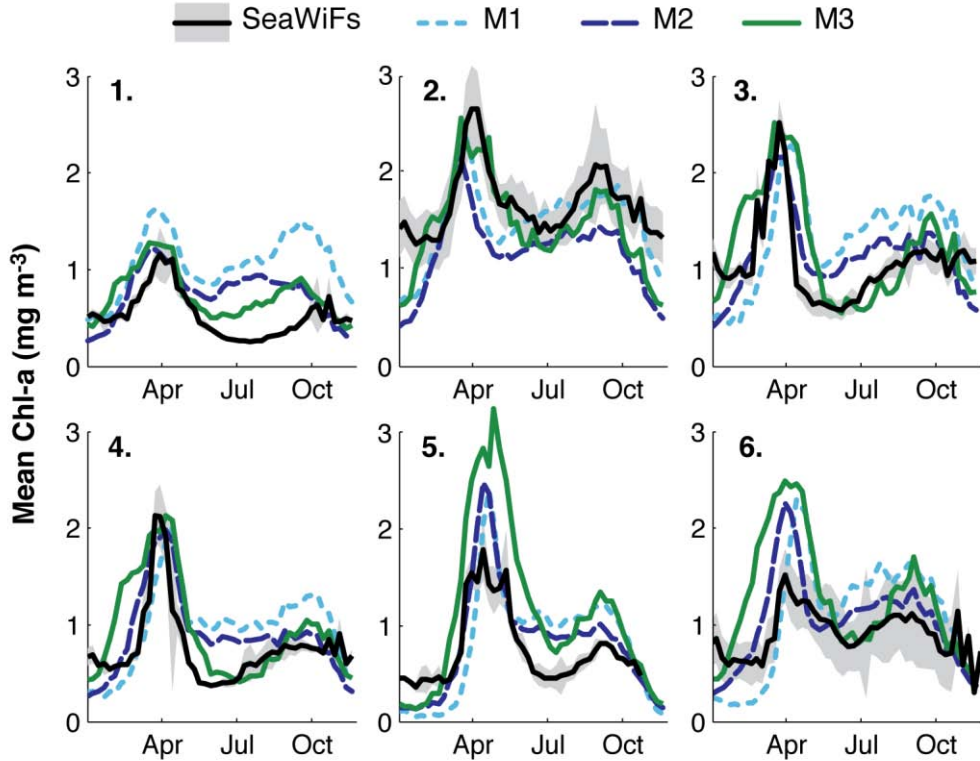


Figure 4.4: Climatological satellite and simulated surface chlorophyll annual cycles in the 6 sub-regions of our model domain.

In the Gulf of Maine (Sub-region 2) observed chlorophyll concentrations are higher than 1 mg Chl-a m<sup>-3</sup> year-round. Maximum observed concentrations exceed the 2.5 mg Chl-a m<sup>-3</sup>, and interannual standard deviations are second largest of the six sub-regions. The models underestimate chlorophyll most markedly during winter. Chlorophyll underestimation persists in M1 throughout the spring and throughout spring and fall in M2. M3 best captures the spring bloom maximum and its termination, as well as the development of a fall bloom.

Observed chlorophyll on the Scotian Shelf (Sub-region 3) has an abrupt spring bloom initiation and termination followed by low summer chlorophyll. The summer minimum is ~36% lower than winter chlorophyll concentrations – the largest difference between the two low chlorophyll seasons in all sub-regions. Chlorophyll concentrations are underestimated from November to April in M1, from November to February in M2, and from November to January in M3. In M1, chlorophyll underestimation during spring bloom initiation leads to a temporal phase difference and a delayed bloom peak compared to M2, M3 and the observations. M2 agrees best with the spring bloom development and early stages of termination, but underestimates the spring bloom peak and overestimates summer concentrations. In contrast, M3 overestimates chlorophyll during spring bloom development and termination, but agrees best with the spring maxima and summer minima.

The Grand Banks region (Sub-region 4) has similar characteristics as the Scotian Shelf. However, chlorophyll concentrations are lower than in the Scotian Shelf during most of the year. The three models also exhibit similar behaviors as in Sub-region 3. However, in this sub-region M1 agrees best with the slope of the spring bloom development, while M2 and M3 overestimate chlorophyll concentrations during this period. The three models agree on the chlorophyll magnitudes during bloom termination until May, when M1 and M2 reach concentrations close to their summer minima and flatten out. As in other sub-regions, M3 continues to decrease until reaching values similar to the observed summer minima, and develops a fall bloom afterwards.

In the northeast of Newfoundland (Sub-region 5), observed concentrations from November to March are the lowest among all sub-regions. Average observed chlorophyll

reaches a maximum of  $\sim 2 \text{ mg Chl-a m}^{-3}$ , and this concentration stays nearly constant between April and June. All models underestimate the winter minimum values and significantly overestimate the spring bloom maximum. As on the Scotian Shelf, M1 underestimates concentrations during the spring bloom development, M2 captures this period the best, and M3 slightly overestimates it. M3 produces the largest overall deviations from the satellite values, overestimating chlorophyll during spring bloom onset, maximum and termination, as well as in summer and fall; however, its seasonal cycle is similar to that from the satellite.

Finally, the de-biased satellite chlorophyll estimates in the Gulf of St. Lawrence (Sub-region 6) are characterized by large interannual standard deviations, the largest of all sub-regions. All models exceed the satellite-based spring bloom and fall maxima. M1 underestimates winter concentrations the most. M3 presents the largest deviations with respect to observed values during most of the year, but agrees best with the summer minima.

Differences between the observed and simulated chlorophyll annual cycles are summarized in Table 4.1. Despite the differences described here, the simulated chlorophyll annual cycles are overall statistically similar to each other and to the satellite observations (see analysis of variance in Appendix F). In general, M2 has the lowest root-mean-square-deviations in most regions, but M3 outperforms M2 in regions without information assimilated during the optimization (i.e., Sub-regions 1 and 2). Nevertheless, M3 has the highest correlation ( $r^2$ ) with the observations in all sub-regions, except the Gulf of St. Lawrence. The timing of the summer minima is best replicated by M3, but all three models estimate the timing of the spring bloom peak well, with an average

difference of  $1.5 \pm 12$  days against the satellite estimate. Considering that satellite observations for the comparison come from 8-day averages, these are minor deviations.

Figure 4.5 shows the spatial distribution of the spring bloom peak timing. In early March, the spring bloom peaks simultaneously on the Gulf of Maine, the southwest of the Scotian Shelf, and the slope water along the shelf-break (Figure 4.5B). This is followed by the mid-March spring bloom peaks of the northeastern Scotian Shelf, the Gulf of St. Lawrence (except near-shore STL and IMA), the Grand Banks, and waters adjacent to the slope waters. Around April, the spring bloom peaks on the Newfoundland Shelf, and the latest spring bloom peak corresponds to the off-shelf open waters. Spring bloom peak timing has a moderate but significant correlation with the maximum mixed layer depth during winter ( $r_{M1} = 0.49$ ;  $r_{M2} = 0.61$ ;  $r_{M3} = 0.50$ ;  $p < 0.01$ ; Figure 4.5A) Areas with shallow maximum mixed layers depths during winter coincide with the earliest spring bloom peaks, whereas late spring bloom peaks correspond to areas of deep maximum mixed layer depths.

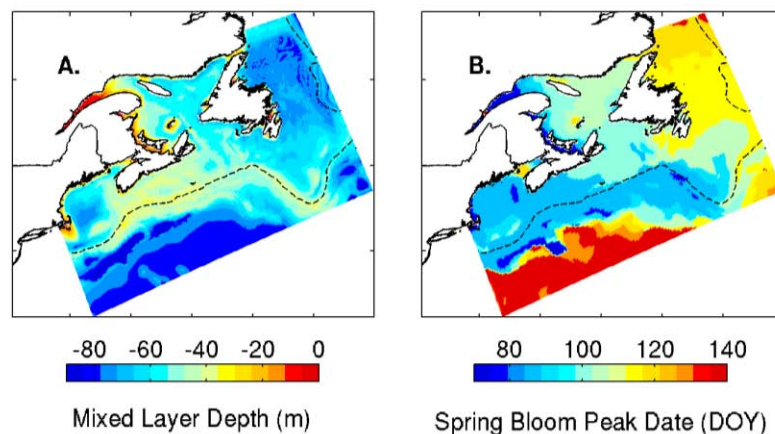


Figure 4.5: A. Maximum mixed layer depth, and B. Simulated spring bloom peak date (M2) in Days-of-Year (DOY). The dashed line is the 1000 m isobath.

Table 4.1: Metrics comparing satellite-based and simulated surface chlorophyll annual cycles. Duration of the spring bloom is defined as the time between the winter and the summer minima. The best model estimate compared to SeaWiFs is marked in bold.

Metric	Satellite/Model	Sub-regions					
		1	2	3	4	5	6
RMSE	SeaWiFs	0	0	0	0	0	0
	M1	0.61	<b>0.36</b>	0.58	0.43	0.43	0.5
	M2	0.36	0.58	<b>0.34</b>	<b>0.32</b>	<b>0.32</b>	<b>0.36</b>
	M3	<b>0.27</b>	<b>0.36</b>	0.43	0.38	0.67	0.63
$r^2$	SeaWiFs	1	1	1	1	1	1
	M1	0.18	0.46	0.09	0.29	0.41	0.53
	M2	0.13	0.4	0.47	0.57	0.72	<b>0.56</b>
	M3	<b>0.56</b>	<b>0.6</b>	<b>0.49</b>	<b>0.58</b>	<b>0.85</b>	0.36
Spring max Chl-a (mg m <sup>-3</sup> )	SeaWiFs	1.15	2.62	2.52	2.13	1.77	1.49
	M1	1.62	2.33	2.28	2	<b>2.38</b>	2.29
	M2	<b>1.21</b>	2.11	2.16	1.98	2.45	<b>2.26</b>
	M3	1.28	<b>2.52</b>	<b>2.51</b>	<b>2.13</b>	3.71	2.49
Summer min Chl-a (mg m <sup>-3</sup> )	SeaWiFs	0.3	1.49	0.58	0.37	0.43	0.55
	M1	0.84	<b>1.26</b>	1.02	0.74	0.13	<b>0.31</b>
	M2	0.69	1.09	0.93	0.8	<b>0.41</b>	0.95
	M3	<b>0.5</b>	1.22	<b>0.55</b>	<b>0.49</b>	0.84	0.83
Winter min Chl-a (mg m <sup>-3</sup> )	SeaWiFs	0.46	1.23	0.91	0.54	0.35	0.28
	M1	<b>0.48</b>	<b>0.64</b>	0.44	0.25	0.05	0.18
	M2	0.27	0.4	0.41	0.27	0.12	<b>0.29</b>
	M3	0.39	0.61	<b>0.67</b>	<b>0.43</b>	<b>0.13</b>	0.44
Date of spring bloom peak (day-of-year)	SeaWiFs	98	98	91	91	114	98
	M1	<b>91</b>	<b>91</b>	106	114	121	114
	M2	84	84	<b>91</b>	<b>106</b>	<b>114</b>	<b>98</b>
	M3	84	84	84	<b>106</b>	128	<b>98</b>
Date of winter Chl-a minimum (day-of-year)	SeaWiFs	338	24	24	31	24	346
	M1	1	<b>1</b>	<b>24</b>	<b>24</b>	<b>24</b>	24
	M2	1	<b>1</b>	1	1	<b>24</b>	<b>1</b>
	M3	<b>346</b>	<b>1</b>	1	1	<b>24</b>	8
Date of summer Chl-a minimum (day-of-year)	SeaWiFs	181	174	174	166	181	181
	M1	166	136	144	<b>166</b>	166	166
	M2	166	151	151	<b>166</b>	174	144
	M3	<b>174</b>	<b>174</b>	<b>174</b>	<b>166</b>	<b>181</b>	<b>174</b>
Spring bloom duration (day-of-year)	SeaWiFs	203	150	150	135	157	195
	M1	165	135	120	<b>142</b>	142	142
	M2	165	<b>150</b>	<b>150</b>	165	150	143
	M3	<b>188</b>	173	173	165	<b>157</b>	<b>166</b>

#### 4.5.2 SURFACE CHLOROPHYLL SPATIAL PATTERNS

The satellite-derived chlorophyll climatology in the northwest North Atlantic region has distinct spatial patterns that all three models are challenged to reproduce (Figure 4.6). Satellite chlorophyll is persistently high on Georges Bank, in the Gulf of Maine, and around Sable Island on the Scotian Shelf. During spring, chlorophyll concentrations above  $1 \text{ mg Chl-a m}^{-3}$  occur on the shallow areas of the Scotian Shelf and extend up to the shelf break and to areas of the Grand Banks. During fall, high chlorophyll concentrations are restricted to coastal areas and shallow banks.

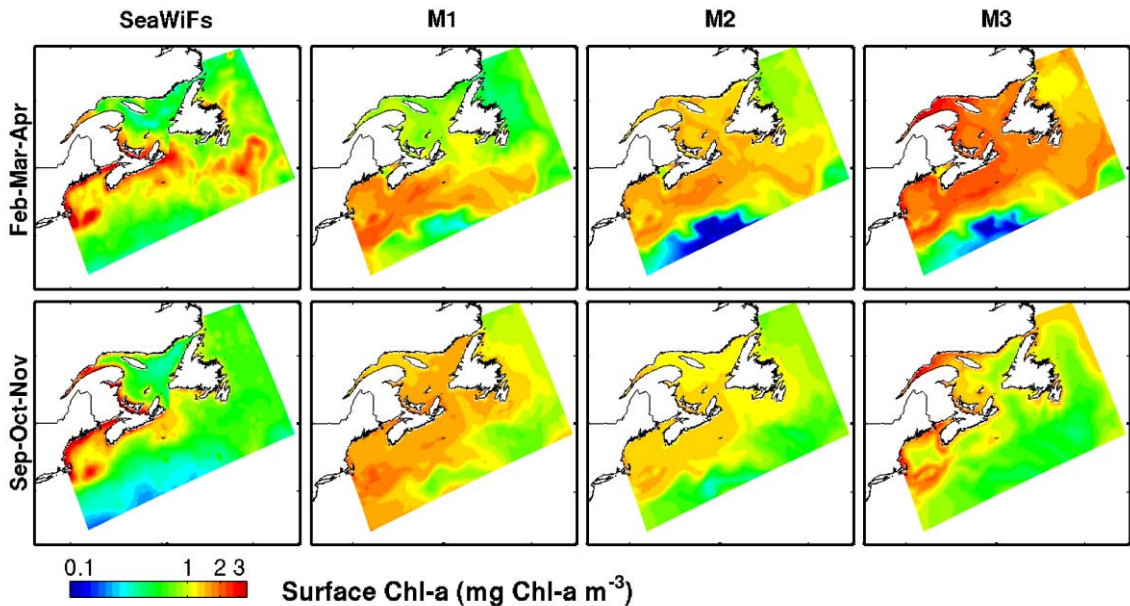


Figure 4.6: Average satellite (SeaWiFS) and simulated surface chlorophyll during spring (Feb-Mar-Apr) and fall (Aug-Sep-Oct) from 1999 to 2003.

M1 simulates the contrast between high chlorophyll on the Scotian Shelf and Grand Banks areas, and low chlorophyll on the northeast Newfoundland shelf. M3 agrees

with maximum satellite chlorophyll concentrations on the Scotian Shelf; however, as seen in Figure 4.4, it overestimates chlorophyll in the northeast Newfoundland shelf and the Gulf of St. Lawrence. During fall, M1 simulates higher-than-observed chlorophyll concentrations, and overestimates chlorophyll in the Open and Slope Waters region. Model M2 better captures fall chlorophyll concentrations; however, near-shore concentrations are lower than the satellite estimate. Detailed patterns of high chlorophyll associated with near-shore and shallow areas during fall are best simulated with M3.

#### 4.5.3 PRIMARY PRODUCTION

Estimates of primary production from satellite are different depending on the underlying algorithm (Figure 4.7). According to the VGPM, total annual primary production in the sub-regions ranges between  $\sim 170 \text{ g C yr}^{-1}$  in the northeast Newfoundland Shelf (region 5) to higher than  $400 \text{ g C yr}^{-1}$  in the Gulf of Maine and Gulf of St. Lawrence (regions 2 and 6). The CbPM algorithm agrees with the VGPM estimates in the northeast Newfoundland Shelf, but estimates lower primary productivity than VGPM everywhere else (and the lowest values of  $\sim 160 \text{ g C yr}^{-1}$  in the Open and Slope Waters region). According to CbPM, the highest primary productivity between  $250 - 300 \text{ g C yr}^{-1}$  occurs in the Gulf of Maine and Gulf of St. Lawrence, but is much lower than the VGPM estimates.

Model M3 produces estimates similar to those of the CbPM algorithm, while M1 and M2 present magnitudes of about half of the same algorithm estimates in all regions. Based on its agreement with the satellite-based estimates, M3 represents regional primary production the best. According to M3, the open waters have the lowest total primary

production of all regions ( $\sim 158.4 \text{ g C m}^{-2} \text{ yr}^{-1}$ ). Total production of the Gulf of St. Lawrence ( $175.7 \text{ g C m}^{-2} \text{ yr}^{-1}$ ), the Scotian Shelf ( $196 \text{ g C m}^{-2} \text{ yr}^{-1}$ ), and the Grand Banks ( $167.2 \text{ g C m}^{-2} \text{ yr}^{-1}$ ) are closely similar. The Gulf of Maine and the Labrador Sea are the most productive regions according to M3 ( $275.7$  and  $209 \text{ g C m}^{-2} \text{ yr}^{-1}$ , respectively).

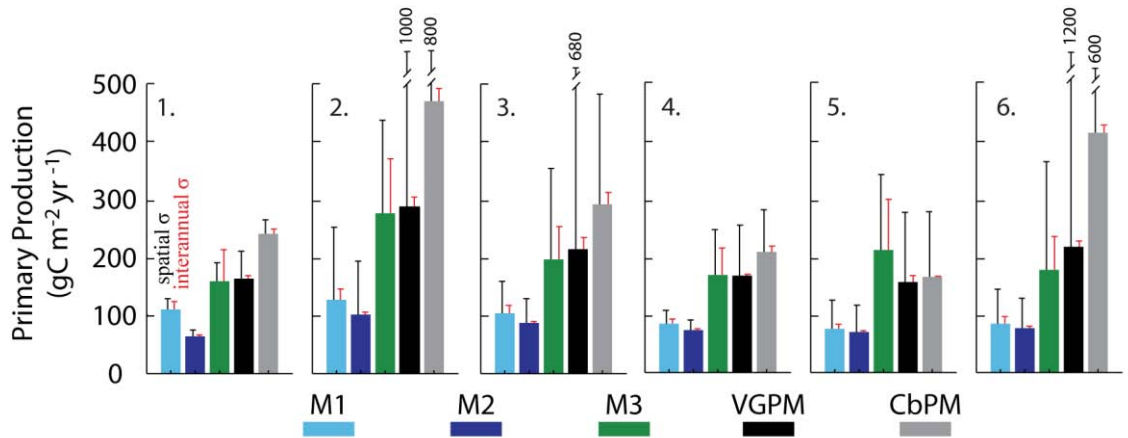


Figure 4.7: Satellite-based (CbPM and VGPM) and simulated vertically integrated primary production in the six sub-regions (indicated by number in each panel; see Figure 1). Black error bars are the spatial standard deviation within the region, and red error bars are the interannual standard deviation.

In Figure 4.8, I include seasonal average spatial distributions of primary production estimated from the satellite-based algorithms and the models. Despite the differences in magnitudes, described here, all estimates have similar spatial and seasonal patterns.

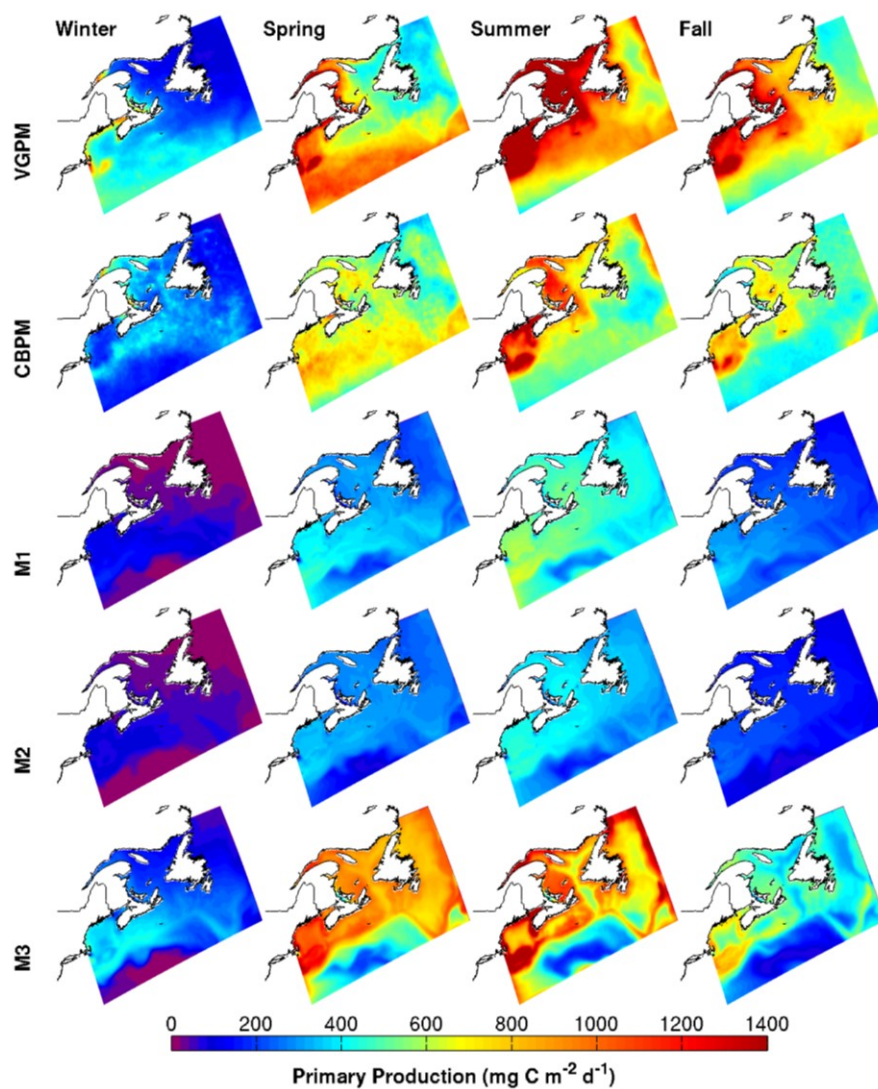


Figure 4.8: Seasonal average vertically integrated primary production for satellite-based estimates (CbPM and VGPM) and M1, M2, and M3 models in the northwest North Atlantic.

#### 4.5.4 STANDING STOCKS

In Figure 4.9 I show nitrate, ammonium, phytoplankton and zooplankton annual cycles simulated by the three models. Annual cycles obtained with M1 and M2 are very similar, but differ from those simulated with M3. The  $\text{NO}_3$  annual cycles have similar

seasonal amplitude in all models, but M3 has a more severe drawdown of  $\text{NO}_3$  than M1 and M2 in summer. A large difference between minimum surface  $\text{NO}_3$  in M1, M2 and M3 is evident on the Scotian Shelf. Maximum  $\text{NO}_3$  concentrations are below  $5 \text{ mmol m}^{-3}$  in the Open and Slope waters, but higher than that in all other regions.

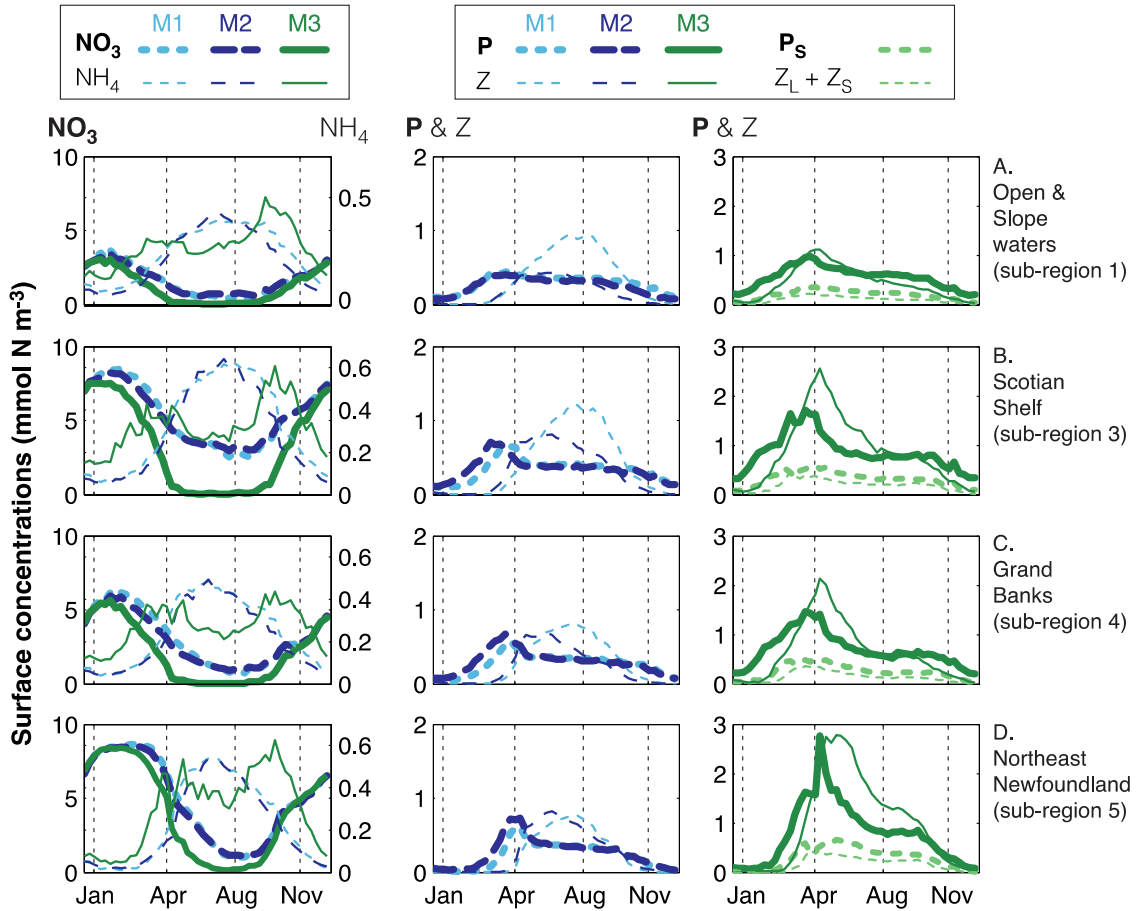


Figure 4.9: Annual cycles of nitrate, ammonium, phytoplankton and zooplankton surface concentrations simulated by M1, M2 and M3. P and Z refer to total phytoplankton and zooplankton biomass, respectively. For M3, P is the sum of small phytoplankton ( $P_S$ ) and large phytoplankton ( $P_L$ ). Z is the sum of small, large and predatory zooplankton ( $Z_S$ ,  $Z_L$ , and  $Z_P$ ).

In addition to differences in magnitude, surface  $\text{NH}_4$  cycles obtained with M1, M2

and M3 also exhibit phase differences in seasonal variability. In M1 and M2,  $\text{NH}_4$  reaches a maximum of  $0.55 \pm 0.09 \text{ mmol N m}^{-3}$  during summer. In contrast,  $\text{NH}_4$  concentrations in M3 have two maxima, one during spring and one during fall, and the fall peak tends to be higher than the spring one in all regions. During summer, M1 and M2 simulate high  $\text{NH}_4$ , but M3 exhibits a valley in the  $\text{NH}_4$  concentrations.

Despite simulating similar chlorophyll annual cycles, M3 total phytoplankton biomass is higher than that of M1 and M2, due to differences in the optimized maximum chlorophyll-to-carbon ratio parameter (M1:  $\theta_{\text{max}} = 0.081 \text{ mg Chl (mg C)}^{-1}$ ; M2:  $\theta_{\text{max}} = 0.066 \text{ mg Chl (mg C)}^{-1}$ ; M3:  $\theta_{\text{maxPs}} = 0.033 \text{ mg Chl (mg C)}^{-1}$ ,  $\theta_{\text{maxPl}} = 0.035 \text{ mg Chl (mg C)}^{-1}$ ). M3 zooplankton biomass is dominated by predatory zooplankton, with approximately equal contributions of small and large zooplankton at ratios of  $1 Z_S : 1.14 Z_L : 7.14 Z_P$ . In general, the zooplankton annual cycle in M3 tracks changes in phytoplankton biomass more closely than M1 and M2, exhibiting maximum zooplankton biomass only a month after the phytoplankton peak. M1 and M2 also exhibit a phase difference in the delay between maximum phytoplankton biomass and maximum zooplankton biomass. M1 zooplankton peaks between July and August, approximately three months after the phytoplankton biomass peak. Zooplankton in M2 peaks in July, a month before M1's.

#### 4.5.5 PHYTOPLANKTON SPECIFIC GROWTH AND LOSS RATES

Figure 4.10 shows the realized specific phytoplankton growth and mortality rates and grazing rates. Phytoplankton growth rates in M1 and M2 are approximately equal, and are highest during summer, due to increased temperatures. As phytoplankton

maximum growth rates are temperature dependent in both models, this is an expected behavior. In M3, the magnitudes of small and large phytoplankton growth rates are similar to each other, and similar to the phytoplankton growth rates of M1 and M2. The similarity in growth rates of M3's small and large phytoplankton is due to similar parameter values for both groups found in the optimization. Nevertheless, seasonal patterns in M3's phytoplankton growth are different than in M1 and M2. For instance, the difference between phytoplankton growth and nitrate-limited phytoplankton growth shows that  $\text{NH}_4$  has a higher contribution to the growth rates during summer, in all models. In M1 and M2, it is the result of increased ammonium concentrations, while in M3 it is a consequence of the severe depletion of  $\text{NO}_3$ .

The three model versions differ significantly in their realized loss rates. M1 and M2 have a peak in grazing rates between March and April, driven by prey density. In M1 grazing rates decline abruptly afterwards and remain low for the rest of the year. In M2, the temperature dependence of both the phytoplankton mortality rate and the grazing rate produces a secondary increase from summer to fall in these rates. In M3, small phytoplankton grazing and mortality rates are higher than those of M1 and M2. Although all biological rates are temperature dependent, the effect of temperature is only noticeable on the small phytoplankton mortality rates, as grazing rates are strongly influenced by prey density effects. Large phytoplankton mortality and grazing rates are lower than those of small phytoplankton, and both reflect a temperature increase in summer.

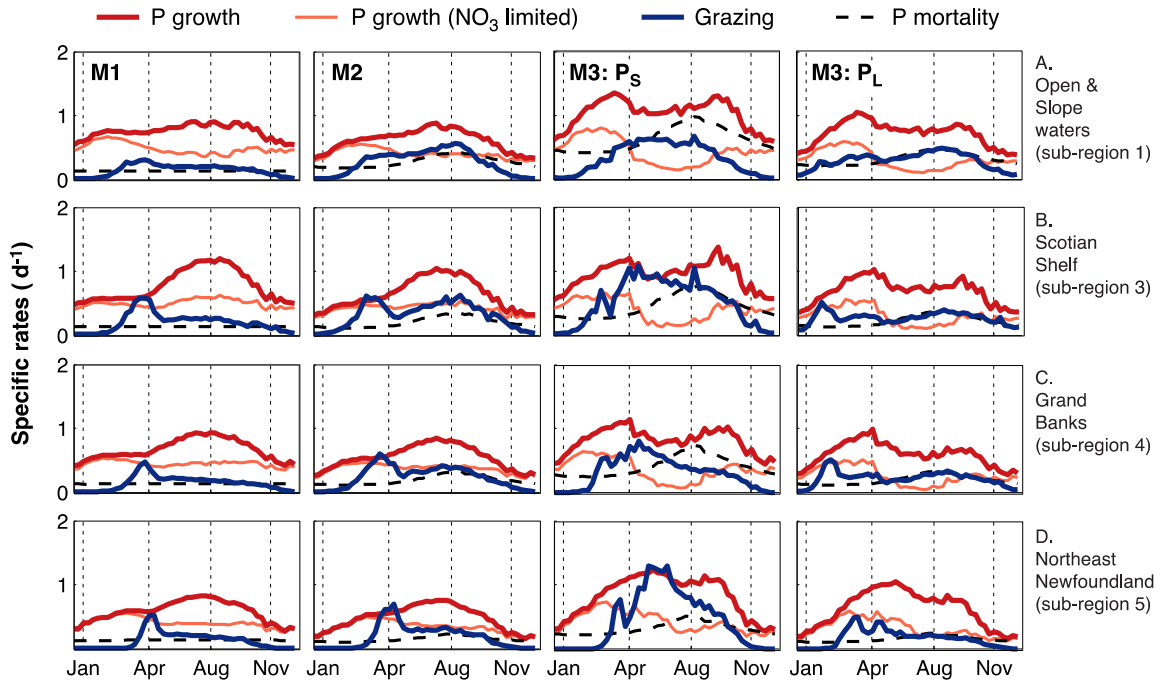


Figure 4.10: Specific phytoplankton growth, grazing, and mortality rates in models M1, M2 and M3 for sub-regions 1, 3, 4 and 5. Note that the mortality rate in M1 is constant, but varies in time in the other models due to its temperature dependence. The phytoplankton growth rate varies in time because of its dependence on nutrient and light supply. The grazing rate varies because of its dependence on phytoplankton availability (M1, M2 and M3) and temperature (M2 and M3).

#### 4.5.6 ECOSYSTEM FLUXES

Vertically integrated ecosystem fluxes (i.e., top layer realized rates multiplied by the corresponding standing stock) are presented for the Scotian Shelf in Figure 4.11. In general, M3's fluxes are larger than in the other two models, while differences between M1 and M2 are insignificant. In terms of average annual fluxes (Figure 4.11), M2's phytoplankton growth is only slightly lower than in M1, and M2's phytoplankton mortality ( $P \rightarrow D$  flux) and grazing losses ( $P \rightarrow Z$  flux) are larger. Also, M2's temperature dependency of the zooplankton excretion and metabolic rates also results in a somewhat

higher contribution of zooplankton to the dissolved inorganic pool (DIN;  $Z \rightarrow N$  flux). In the case of M3, the phytoplankton growth flux is four times as high as those of M1/M2, and phytoplankton mortality and grazing are approximately doubled. M3's zooplankton flux to detritus and DIN, as well as the detritus flux to DIN are also increased.

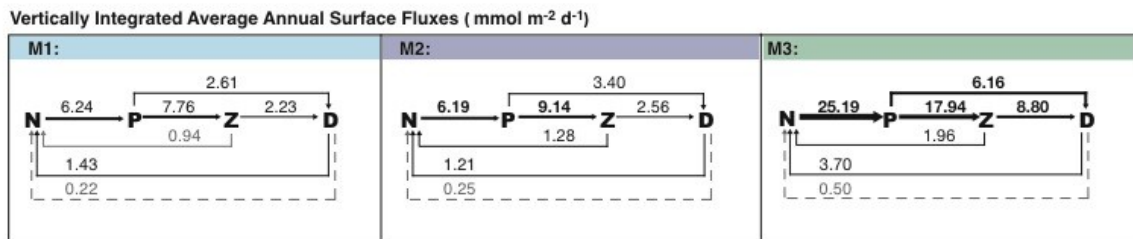


Figure 4.11: Scotian Shelf vertically integrated average annual fluxes in nitrogen units simulated by M1, M2, and M3. The ecosystem structure is simplified to nutrients, phytoplankton, zooplankton and detritus (NPZD) components for sake of simplicity. The solid line flux from detritus to nutrients represents the fast-remineralizing small detritus flux, and the dashed line is for the slow-remineralizing large detritus flux. The thickness of the arrows is related to the magnitude of the fluxes.

To gain more insight into the role that temperature-dependent phytoplankton loss rates play in increasing mortality fluxes, Figure 4.12 shows the spatial distribution of phytoplankton average surface mortality fluxes in M1 and M2 during winter and summer. The effects of temperature on phytoplankton mortalities are relatively easy to interpret because they directly depend only on phytoplankton biomass and the mortality rates. In M1 the mortality rate is constant, so fluxes are controlled by spatial and seasonal differences in phytoplankton biomass. In M2, fluxes represent the interplay between changes in biomass and the effect of temperature on the realized mortality rates.

During winter and summer, M1 and M2 phytoplankton surface concentrations are nearly equal throughout the entire domain (Figure 4.9, Appendix F). However, in winter M2's mortality fluxes are lower than M1's because at temperatures below 10°C its mortality rates are lower than the constant rate in M1 (Figure 4.12B-C). In the region influenced by the Gulf Stream (Sub-region 1), winter temperatures above 10°C do not have a significant positive effect on M2's mortality fluxes because winter phytoplankton biomass in this sub-region is very low compared to the rest of the domain (Figure 4.12A-C). M2's low phytoplankton mortality leads to a higher phytoplankton standing stock than in M1 at the end of winter and into spring (Figure 4.9). This is also reflected in M2's high chlorophyll concentrations during the latter season, noticeable inside the Gulf of St. Lawrence and in the northeast of Newfoundland (Figure 4.6).

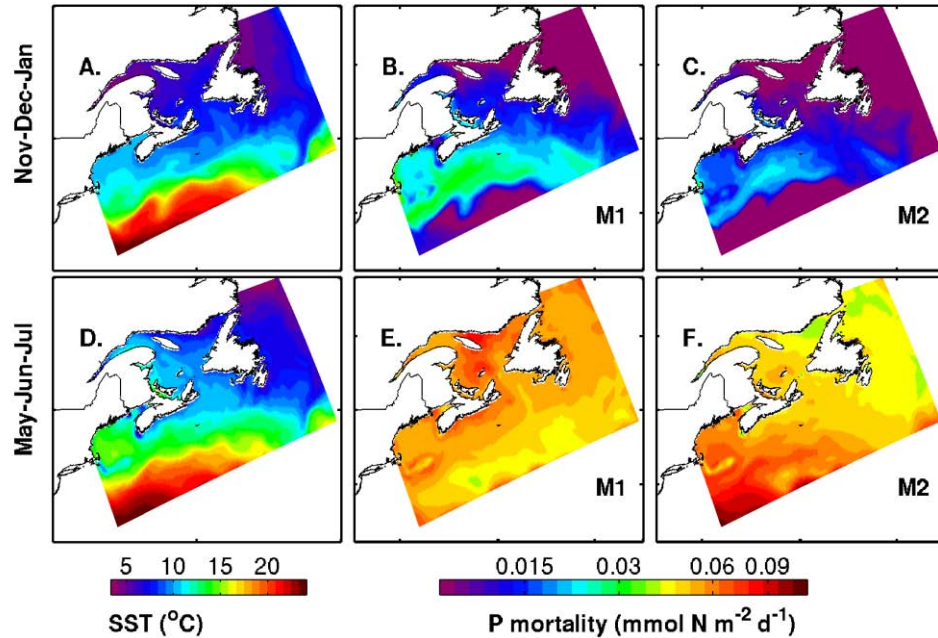


Figure 4.12: Spatial distributions of average sea surface temperature (A. and D.) and phytoplankton mortality fluxes during Feb-Mar-Apr and May-Jun-Jul for models M1 (constant mortality rate; B. and E.) and M2 (temperature dependent rate; C. and F.).

Spatial differences in temperature affect M2's phytoplankton mortalities more clearly during summer (Figure 4.12D-F). As previously mentioned, spring phytoplankton biomass in M2 is slightly higher than in M1, except in Sub-region 1 (Figure 4.6, Figure 4.9, Appendix F). In summer, the coldest temperatures in the domain are in Gulf of St. Lawrence and in the northeast of Newfoundland (Figure 4.12D-F). M2's temperature dependent spring-to-summer mortality fluxes for these regions become lower than in M1 due to low temperatures, and despite M2's high phytoplankton biomass in these regions. In Sub-region 1, phytoplankton biomass at the end of spring is low in comparison with the rest of the domain, but higher than during winter (Figure 4.6, Figure 4.9 and Appendix F). Due to this seasonally increased biomass, the effect of the Gulf Stream's warm temperatures over mortality fluxes is more noticeable during summer (Figure 4.12F). M2's increased mortalities in the open waters lead to reduced phytoplankton biomass and chlorophyll in this area in the fall, when compared to M1's results (Figure 4.6). Overall, temperature effects on mortality rates during summer result in summer phytoplankton biomass becoming very similar among models and homogeneous among regions.

#### 4.5.7 EFFECT OF MULTIPLE GRAZERS ON NUTRIENTS

Return fluxes from zooplankton to the dissolved inorganic nitrogen pool (in the form of  $\text{NH}_4$ ) and small detritus exhibit different temporal behaviors in M1/M2 and M3 (Figure 4.13). In M1/M2, these fluxes peak during August, when grazing fluxes and zooplankton biomass are high. In M3, they peaking during March and flatten out for the

rest of the year. Also in M3, the flux from large and predatory zooplankton to large detritus, exclusive of this model version, accounts for a larger fraction of zooplankton losses than the excretion to dissolved inorganic nitrogen.

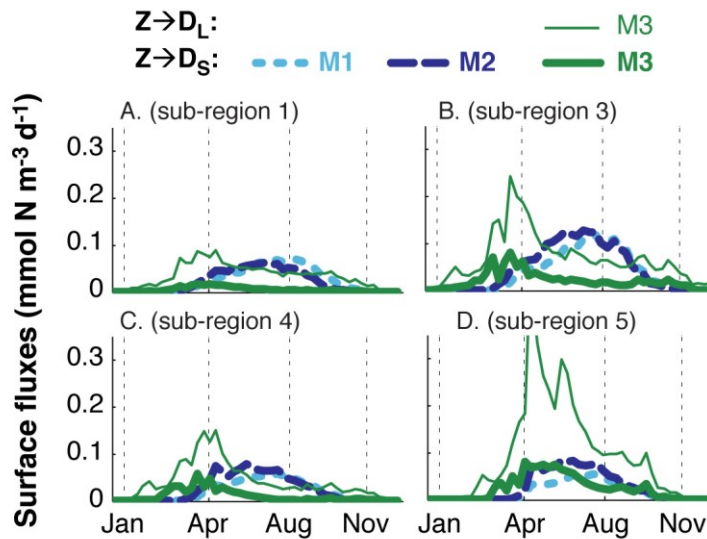


Figure 4.13: Simulated average zooplankton loss fluxes to detritus in model domain sub-regions 1, 3, 4 and 5. Note that fluxes to large detritus are only present in model M3.

To better understand how the dynamics of multiple predators affect the dissolved inorganic nitrogen (DIN) seasonal cycle, I performed a series of sensitivity experiments varying the values of the reference maximum grazing rate of each zooplankton group. For computational efficiency, these experiments were performed in the one-dimensional model used for model optimization. Figure 4.14A shows a summary of these experiments in terms of the percentage change in surface DIN and phytoplankton concentrations. Independently increasing or decreasing the reference grazing rates generates significant changes in DIN concentrations only between April and November. Effects on large phytoplankton are also limited to the summer and fall period. Modifying grazing rates

only affects the magnitude of phytoplankton biomass, but has negligible effects on the timing of the spring and fall blooms. A delay in bloom timing would be characterized by negative changes in phytoplankton biomass followed by positive changes, whereas an earlier bloom would produce positive changes followed by negative changes. Neither of these behaviors occurs.

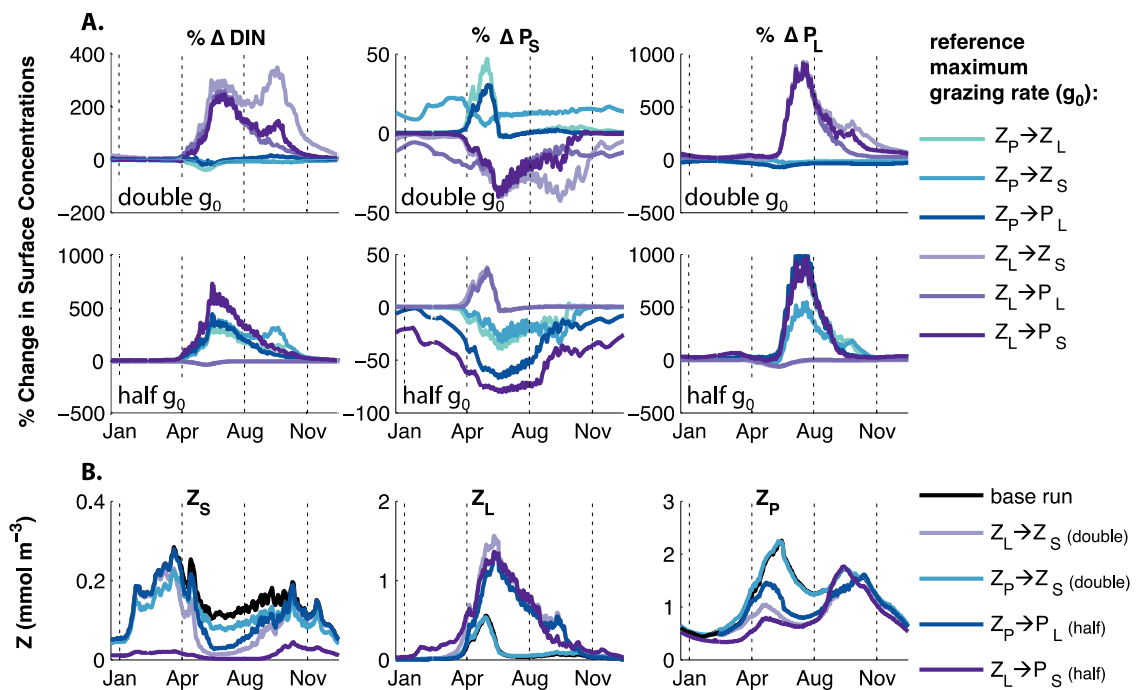


Figure 4.14: Sensitivity experiments varying the reference maximum zooplankton grazing rate parameters ( $g_0$ ) one-at-a-time. A. Percentage change in surface dissolved inorganic nitrogen (DIN =  $\text{NO}_3 + \text{NH}_4$ ), small phytoplankton, and large phytoplankton annual cycles. B. Small, large, and predatory annual cycles obtained by a sub-set of the experiments in A. In the legend, grazing parameters are denoted with the predator symbol followed by its prey (predator  $\rightarrow$  prey).  $Z_P$ : predatory zooplankton,  $Z_L$ : large zooplankton,  $Z_S$ : small zooplankton,  $P_L$ : large phytoplankton, and  $P_S$ : small phytoplankton.

In general, modifying the grazing rates of one predator may have unexpected responses in the biomass of other predators (Figure 4.14B). For example, increasing the large zooplankton grazing rate on small zooplankton produces lower small zooplankton

concentrations from March to October, accompanied by higher large zooplankton concentrations. Interestingly, this produces an indirect effect of decreasing predatory zooplankton concentrations. The same zooplankton behavior occurs for all other cases at varying levels.

#### **4.6 DISCUSSION**

In terms of chlorophyll magnitudes and seasonality, the three model versions simulate seasonal cycles that capture some aspects of satellite chlorophyll, but fail to capture others. The three models are also similar in terms of primary production spatial and seasonal patterns. Nevertheless, the three model versions differ on their ability to reproduce details of chlorophyll seasonality in specific sub-regions, and obtain significantly different primary production magnitudes.

Models agree with observed values of chlorophyll during specific seasons (Figure 4.4, 4.6), as well as with *in situ* measurements of temperature, density, and estimates of mixed layer depth (Figure 4.3). For instance, in each sub-region models exhibit the expected spring bloom maxima followed by a summer decline in chlorophyll. Models also agree in simulating high chlorophyll concentrations extending from the coast to the shelf break during spring. The development of enhanced chlorophyll concentrations on the shelf has been previously discussed in observational and model studies with focus on the Scotian Shelf and the Gulf of Maine (Fournier, 1978; Ryan et al., 1999; Zhai et al., 2011).

Among the aspects where the models differ, M1 and M2 tend to simulate higher summer chlorophyll than M3 in several sub-regions; and M1 shows significant overestimation of fall chlorophyll in the Gulf Stream, slope and open waters. Differences among models

can be explained by three main aspects of the regional ecosystem dynamics controlling chlorophyll seasonal variability: i) the sequential nature of bottom-up and top-down drivers during the annual cycle; ii) regional primary production; and iii) the role of temperature-dependent phytoplankton loss rates.

#### 4.6.1 SPRING BLOOM BOTTOM-UP DRIVERS

Chlorophyll time series of the three model versions broadly agree during the spring bloom period, but disagree during summer and fall. This seasonal difference between models suggests that the processes controlling ecosystem dynamics during different periods of the annual cycle have a distinct nature. Model similarities during the spring bloom peak and initial stages of bloom decline, suggest that their drivers are not affected by the ecosystem complexity of the models, and that observational data used in the optimization was sufficient to calibrate the parameters involved in determining these features. Model versions also agree in the characterization of a pattern of early spring bloom initiation in areas with shallow winter mixed layer depths (Figure 4.5). This spatial pattern of spring bloom timing agrees with spatial differences in timing found on the Scotian Shelf by Zhai et al. (2011). They fitted a Gaussian model to satellite chlorophyll from the Scotian Shelf (40°N – 46 °N; -66°E – -58°E), and showed an early spring bloom initiation on the shallow banks of Sable Island and along the shelf break, in comparison to off-shelf waters.

Areas with shallow maximum mixed layer depths during winter are geographically related to the shelfbreak front. The association of the shelfbreak front with elevated phytoplankton biomass has long been recognized (Fournier, 1978). In the Mid-

Atlantic and New York Bights, observational evidence suggests that increased vertical stability due to sloping isopycnals at the shelf break frontal zone generates a region of high light availability (Malone et al., 1983; Marra et al., 1990; Linder and Gawarkiewicz, 1998). Here, I show that during winter a region of strong stratification is present along the shelf break of the northwest North Atlantic, demonstrated by shallow winter mixed layer depths (Figure 4.5A). The mixed-layer depth affects the nutrient and light availability in opposite directions: shallow mixed layers inhibit vertical nutrient replenishment, but improve the light conditions that phytoplankton experience by concentrating cells in the photic zone. Surface nutrient conditions prior to the spring bloom are favourable in all regions of the domain (Figure 4.9), but low winter irradiance in February limits phytoplankton growth at high latitudes of the northern hemisphere (Siegel et al., 2002a). Therefore, it is expected that the initialization of the phytoplankton bloom in this region would be particularly sensitive to the winter mixing effects on the light field. My results support the idea that regions of shallow mixed layer depths contribute to an earlier spring bloom initiation and peak timing in certain locations. These regions modify the expected latitudinal progression of the bloom caused by seasonal changes in irradiance. For instance, areas of the Gulf of St. Lawrence and the northeast Newfoundland Shelf are at the same latitude, but the spring bloom peaks first in the Gulf of St. Lawrence, and later in the Newfoundland Shelf (Figure 4.5). In the less stratified waters of the northern Newfoundland Shelf, deep winter mixed layers impose unfavorable light conditions and favorable surface nutrient replenishment causing nitrate to remain unconsumed until late spring, resulting in a late spring bloom peak. In very shallow areas, bloom timing may be directly linked to seasonal light intensity, rather than stratification, as suggested by results of a two-dimensional model of Georges Bank (Ji et al., 2006). In summary, my three

models support a canonical bottom-up perspective to explain the spring bloom process. In the absence of nutrient limitation, shallow mixed layers favour earlier spring blooms due to an enhanced light field (Sverdrup, 1953), while the magnitude and duration of the event may be modified by the winter nutrient carrying capacity (Ji et al., 2006; Kuhn et al., 2015). A similar mechanism may also explain interannual variability in spring bloom timing (Schartau and Oschlies, 2003a).

In any numerical model, the response of phytoplankton to variations in temperature, light and nutrient regimes is largely determined by model parameters. Proper emergent patterns of behaviour are a consequence of the calibration of phytoplankton parameters to the predefined environmental conditions, under the implicit assumption that the physics of the model are correct (Hemmings and Challenor 2012), which is supported for my model (Figure 4.3; Brennan et al. 2016). In preliminary simulations I noticed that phytoplankton parameters, in particular the reference maximum growth rate and the initial photosynthetic slope, affect the timing of the spring bloom peak in the three models. The offset in timing between model results and satellite chlorophyll was one of the main corrections achieved during the optimization in Chapter 3. The effect of phytoplankton growth parameters on the spring bloom timing has been previously discussed in other 1D model studies for the North Atlantic Ocean (Schartau and Oschlies, 2003b; Kuhn et al., 2015) and a 3D model study for the Baltic Sea (Neumann, 2000). Therefore, this model behaviour appears to be independent of model complexity and physical dimensionality, at least in northern mid-latitude regions.

#### 4.6.2 SUMMER MINIMA TOP-DOWN DRIVERS

There are noticeable differences between the models' chlorophyll and other state variables during summer and the fall. After the spring bloom peak, chlorophyll concentrations start declining in all models and in the satellite observations, but minimum magnitudes in summer differ. Models M1 and M2 reach their summer minima before the observed minimum occurs, and overestimate its magnitude. M3 best simulates the observed patterns in summer. The termination of the spring bloom is canonically attributed to multiple factors including nutrient depletion (Waite et al., 1992), as well as increased predation (Banse, 1994) and viral lysis (Bratbak et al., 1993). The differences between the models at the end of the spring bloom and in summer suggest that trophic complexity may play an important role in simulating the minimum chlorophyll concentrations in summer.

Comparison of the three optimized models and the sensitivity experiments related to grazing rates in M3 show that differences in the treatment of predators can modify summer/fall phytoplankton concentrations. This model effectively modifies the nitrogen return fluxes from phytoplankton, zooplankton and dead organic matter (small and large detritus) to the inorganic nitrogen pools. The first type of return fluxes include metabolism and excretion fluxes, which can be interpreted as an effect of modifying the representation of the microbial loop by introducing trophic complexity. Previous modelling studies have posited that the microbial loop has an important role in controlling the rate of organic nutrient return to the inorganic pool (Fasham et al., 1993; Doney et al., 1996; Schartau et al., 2001; Schartau and Oschlies, 2003a). The model structure of M3

also modifies the pathways that organic matter follows after being ingested by zooplankton. In M3 the pathways from large and predatory zooplankton to large detritus increases the fraction of organic matter that becomes part of large detritus (Figure 4.10). Large detritus sinks more rapidly than small detritus and has a slower remineralization rate. Therefore, zooplankton excretion and mortality pathways in M3 modify the composition of dead organic matter, which affects the depth and velocity at which it decomposes. (Lampitt et al., 1990; Lenz et al., 1993; Armstrong et al., 2001; Klaas and Archer, 2002; Christina and Passow, 2007). In other words, this model comparison demonstrates that different assumptions about the fate of dead phytoplankton are important to determining export estimates and nitrogen cycling.

Zooplankton metabolism and mortality, as well as remineralization fluxes are largely unconstrained by the datasets available for validation. The significant impact of predator interactions on trophic dynamics during the summer/fall period (Figure 4.14) is also in agreement with zero-dimensional idealized model results that suggest that adaptive zooplankton grazing behaviour (i.e., switching preys) drives the seasonal succession of phytoplankton species (Mariani et al., 2013). There is a significant gap in knowledge of rates of plankton predator-prey interactions, and several model studies acknowledge that it is difficult to estimate zooplankton parameters with reliability (Fennel et al., 2001; Schartau and Oschlies, 2003b; Bagniewski et al., 2011). Many of the grazing and mortality parameters are difficult to elucidate from in situ observations. Targeted laboratory and mesocosm experiments together with analogous model representations of these controlled systems may be used to bring our understanding of

predator-prey feedbacks and zooplankton export mediation to a similar level to that of the bottom-up drivers.

#### 4.6.3 MAGNITUDE DIFFERENCES IN PRIMARY PRODUCTION

I obtained significant differences between models in the simulated primary production rates. M3, the model with increased complexity, provides the best estimates of primary production with respect to satellite-based estimates from the VGPM and CbPM algorithms. The latter range between 160 and 480 g C m<sup>-2</sup> yr<sup>-1</sup> and are similar to 1979's estimates of 154 and 431 g C m<sup>-2</sup> yr<sup>-1</sup> derived from the Coastal Zone Color Scanner (CZCS) ocean color imagery for the whole northwest North Atlantic region (Sathyendranath et al., 1995). On the Grand Banks, Coastal Zone Color Scanner estimates are specifically in the order of 200 g C m<sup>-2</sup> yr<sup>-1</sup> (Prasad and Haedrich, 1993). Later SeaWiFs satellite-based estimates in the Gulf of Maine region by O'Reilly et al. (1998) report primary production between 260 and 455 g C m<sup>-2</sup> yr<sup>-1</sup>. Satellite and M3's estimate grossly agree with C<sup>14</sup> measurements on the Scotian Shelf between 1991 and 1992 reporting an annual primary production average of about 179.4 g C m<sup>-2</sup> yr<sup>-1</sup> (Mosseau et al., 1998).

Model versions M1 and M2 estimate annual rates about half the VGPM and CbPM satellite estimates compared here. However, M1 and M2 estimates are close to the in situ estimates reported by Fournier et al. (1977) on the Scotian Shelf. They estimated an annually averaged primary production of 96 g C m<sup>2</sup> yr<sup>-1</sup> measured using C<sup>14</sup> incubations; but their measurements missed the spring bloom period, resulting in a probable underestimation of primary production. These low estimates also agree with

model results from Song et al., (2001). They analyzed interannual variability using 1D models of a location at the Gulf of Maine and one in the Scotian Shelf, finding averages of total primary production in the euphotic zone of  $138 \pm 6.5 \text{ g C m}^2 \text{ yr}^{-1}$  and  $123 \pm 6.5 \text{ g C m}^{-2} \text{ yr}^{-1}$ , respectively.

#### 4.6.4 ROLE OF TEMPERATURE

Temperature dependence of loss rates appears to play only a minor role in determining the seasonal variability of chlorophyll and phytoplankton stocks; more important is its modulation of summer and fall rates. Similarly, observations of phytoplankton biomass and carbon fixation rates in polar, temperate and tropical regions have demonstrated that resource supply plays a stronger role in the variability of phytoplankton growth (Marañón et al., 2014).

However, noticeable improvements occur in the ability of the simple ecosystem model structure to replicate chlorophyll in the open waters, a region where no observations were assimilated during the parameter optimization process. This shows that increased complexity in the form of mechanistic relationships with environmental variables can be effective in improving model generality and geographical portability. The positive effect of temperature-dependent grazing and mortality rates has also been reported to improve other North Atlantic model applications, such as the Biogeochemical Element Cycling-Community Climate System Model (BEC-CCSM) (Doney et al., 2009; Behrenfeld et al., 2013). Given the scarcity of observational information, this dependency is commonly characterized with a single temperature relationship and the same Q10 value for all processes. However, neither individual processes, nor plankton groups necessarily

follow the same temperature relationships (Eppley, 1972; Rhee and Gotham, 1981). Also, it has been shown that the temperature optima of different phytoplankton groups contribute to seasonal succession (Litchman and Klausmeier, 2008) and that there exist large-scale patterns in thermal traits (Thomas et al., 2012).

Spatial differences achieved with temperature dependence in both the phytoplankton growth and loss rates may also be important to understanding interannual variations in the planktonic community. For example, lower abundances of the copepod *Calanus finmarchicus* were found in Continuous Plankton Recorder data from the Gulf of Maine during the cold years of the 1960s, when the North Atlantic Oscillation index was low. This phenomenon has been interpreted both from trophic and physical advection perspectives (Jossie and Goulet, 1993; Conversi et al., 2001; Greene and Pershing, 2003). Understanding biological and chemical processes mediated by temperature will be increasingly important under a changing climate with sustained increasing trends in temperatures.

#### 4.6.5 SUCCESSION OF SMALL AND LARGE PHYTOPLANKTON IN M3

The optimization of M3 assigned similar growth parameter values to both phytoplankton groups (Figure 4.9), such that differences among them are actually enforced by natural mortality and the predefined trophic relations of their predators. However, laboratory experiments show that different phytoplankton taxa have specific maximum growth rates (Miller and Wheeler, 2012), as well as initial photosynthetic slope parameters and Chl:C ratios (MacIntyre et al., 2002). Moreover, cytometric measurements within my study area have revealed that different phytoplankton size

classes relate to total chlorophyll concentrations with a defined pattern (Li, 2002). At low chlorophyll concentrations, picoplankton ( $<2 \mu\text{m}$ ) dominates, but its fraction decreases as chlorophyll and large nanoplankton ( $10\text{-}20 \mu\text{m}$ ) concentrations increase (Li, 2002). M3 simulates larger biomass of large phytoplankton relative to small phytoplankton during the spring bloom, but summer biomass is composed by approximately equal concentrations of both groups. Both groups also follow similar temporal variability.

My optimization design allowed small and large phytoplankton parameters to vary without predetermined constraints on each based only on satellite-derived size-fractionated chlorophyll estimates (Chapter 3). This approach, therefore, is not sufficient to constrain differences in growth rates of individual functional groups to environmental conditions.

It is not uncommon that models with multiple plankton groups are limited in their ability to replicate the succession of functional groups (e.g., Lewis et al., 2006; Ciavatta et al., 2016). For instance, NEMURO exhibits similar decadal variability and amplitude in both phytoplankton groups when used in a basin-wide three-dimensional application for the sub-polar North Pacific (Aita et al., 2007). In order to better simulate the seasonal succession of different functional groups, models may require *a priori* theoretical constraints during the optimization. NEMURO applications have achieved geographical differences in seasonal phytoplankton community composition by modifying the reference growth rates of phytoplankton, to which the model nutrient, phytoplankton, and zooplankton variables are highly sensitive (Yoshie et al., 2007). At a Station in the western sub-polar North Pacific, the growth rate of large phytoplankton was configured as larger than that of small phytoplankton, but a larger rate for small than for large

phytoplankton was needed at Station P in eastern sub-polar North Pacific (Fujii et al., 2007). It is also possible that the addition of silicate, a variable included in NEMURO, would further constrain the annual cycle of large phytoplankton, if considering the group as composed of diatoms. It has been demonstrated that depletion of silicate is highly correlated with the change in composition of the phytoplankton community (Conley and Malone, 1992).

#### 4.6.6 SIMPLE VS. COMPLEX MODELS

The largest difference between the models considered in this study was that, despite achieving similar chlorophyll magnitudes and variability, M3, the most complex model, simulated larger phytoplankton and zooplankton standing stocks, as well as larger primary production values. This reflects early theoretical understanding of model construction, which posits that many different and conflicting models could be constructed to fit a set of observations equally well (Quine 1975), despite portraying quite different dynamics. M3's primary production agreed the best with unassimilated satellite-based estimates. M3 also outperforms the simple models in terms of chlorophyll in sub-regions that were not considered during the optimizations, especially, the slope and open waters region. These results agree with previous studies that show high variability in model skill and primary production estimates from different models (Friedrichs et al., 2007; Friedrichs et al., 2009; Bagniewski et al., 2011). On the one hand, this study reiterates that, in terms of surface chlorophyll, models with very simplified trophic dynamics have limitations to fit the characteristics of unassimilated geographical locations. On the other hand, the high primary production estimates obtained with a

model with multiple preys and predators is likely to be due to model structural differences. For instance, in the model comparison of Friedrichs et al. (2007), models with single phytoplankton groups also exhibited larger misfits against observed primary production, even though primary production was assimilated during the optimization of all models.

As discussed in Chapter 3, the model with fewer state variables and no temperature dependence (M1) is also limited in its ability to simultaneously fit the observations at multiple locations. This is a consequence of the compromise required to fit all variables and locations, which leads the optimization algorithm to select a different parameters than the ones that would be fitted for individual locations (Schartau and Oschlies 2003; Friedrichs et al 2007). In that sense, M3 allows more flexibility when calibrated with sufficient information about different regimes in the area. These results support the idea that processes unresolved within simple models may reduce their generality and applicability to different conditions than the ones they were calibrated for (Doney et al 2002; Riley et al. 1949), including global applications, and predicting the responses to environmental change. In Part I of this study (Chapter 3), I demonstrated this is also true for complex models when these become overfitted to a single location.

The environmental heterogeneity of the northwest North Atlantic may require at least a moderate level of model ecosystem complexity to better capture spatial and temporal phytoplankton variability. The effect of introducing temperature dependence in all biological rates was small, but it improved model performance at thermal extremes in the domain. That is, improvement were obtained in cold conditions during winter in the Gulf of St. Lawrence and warm conditions in the area of influence of the Gulf Stream

(Figure 4.12). During portability experiments performed in a one-dimensional environment, this model (M2) was also best suitable when applied to a different location than the one it was calibrated for (Chapter 3). Previous model comparisons have also demonstrated that the relevance of certain processes is likely to vary between the different environments, and the addition of specific processes to models of certain sites may be required to simultaneously fit observations at different locations. This was the case in the optimization experiments of Hurtt and Armstrong (1999) and Friedrichs et al. (2007). In the first study, an iron parameterization was required at the Bermuda site, but not at the northern North Atlantic OWS-INDIA station. In the second one, iron was needed to simulate conditions in the North Pacific, but not in the Arabian Sea. Previous conclusions about the most appropriate level of model complexity in other geographical regions are conflicting. In their analysis of non-optimized results from global models, Kriest et al. 2010 concluded that increasing the model complexity beyond the simplest formulations did not demonstrably improve model performance; however, they acknowledged that optimization may have allowed better model performance among the more complex models. Both Hurtt and Armstrong (1996) and McDonald and Urban (2010) concluded that the most appropriate ecosystem models were simpler than expected *a priori* for the Bermuda area, and a freshwater ecosystem, respectively. As a last example, Ward et al. (2013) used an optimization method to remove unconstrained parameters from a model, thus systematically reducing model complexity. These parameter reductions demonstrated that a large number of model parameters could be removed to fit specific geographical locations without significantly affecting model's performance. However, not even the original un-reduced model was able to fully reproduce the observed behavior simultaneously at the two locations tested.

All models here analyzed may maintain a certain dependence on the parameters that were not optimized, but fixed to their *a priori* guesses (Chapter 3). In other words, it is possible that some of the deficiencies in the simpler models (M1 and M2) can be attributed to these un-calibrated parameters, which are unconstrained by the available observations.

## **4.7 CONCLUSIONS**

Understanding the drivers behind differences in the system dynamics simulated by models of different complexities is challenging due to their dependencies on many adjustable parameters. I tried to overcome this limitation by controlling the number of calibrated parameters and standardizing the pathways to be optimized. These efforts were intended to elucidate the effects of additional complexity, rather than evaluating the success of the optimizations.

My results show that patterns of spring bloom development and peak can be simulated equally well by the simple and complex models. Thus, complexity may not be necessary to address questions related to the bottom-up drivers of these periods. For instance, even the simplest models can be successfully fitted to replicate the spring bloom onset, serving as efficient tools to study it (e.g., Chapter 2). However, trophic complexity appears to play a role during the last stages of bloom termination, to set the summer chlorophyll minima, and to replicate levels of primary production close to the satellite estimates. Assumptions followed by complex models modify the pathways of nitrogen return from the organic to the inorganic pools. Complexity might be, therefore, required to fully understand the spring bloom termination and the transfer of energy to higher

trophic levels in the northwest North Atlantic. Overall, my results illustrate that the selection of an appropriate level of ecosystem model complexity is tied to the research questions to be addressed.

I also notice that bottom-up processes leading to the initiation of the spring bloom and controlling its peak appear better constrained by the available observations. This suggests that aspects of the system's dynamics that are well constrained by the observations can be similarly replicated by different models, independent of model complexity. On the contrary, no information about predators was included in my optimization experiments. The comparison of optimized models, and sensitivity experiments on the model with multiple predators, demonstrate that model trophic complexity affects biogeochemical annual cycles most strongly during summer and fall. Trophic complexity introduces changes in the pathways of plankton mortality and predation, which affect the velocity and phase of nitrogen return from the organic pool to inorganic forms. Also during the summer and fall period, the effect of temperature dependence on phytoplankton losses is evident, being important to define chlorophyll spatial patterns, but having little effect on plankton standing stocks and primary production estimates.

I highlight that the scarce availability of observations places significant limitations on the ability to mechanistically comprehend the effects of ecological feedbacks. Data limitations also affect the ability to conclusively compare model complexity. For this reason, decisions about an appropriate level of model complexity for a specific geographical area may also vary depending on the observational datasets available for model calibration, validation and the metrics used to evaluate model skill (Chapter 3).

Under current data limitations, unguided parameter optimization is an imperfect method for identifying optimal parameters, especially in the high-dimensional parameter space of complex models. For example, the model with two phytoplankton groups (M3) does not follow the expected ecological spring-to-summer succession from large to small phytoplankton. Moreover, computational power still sets some limitations for the use of complex biological models in basin-wide, global, and/or long-term simulations of coupled ocean circulation models. Considering this, and following parsimony principles, models with simple trophic dynamics can be as suitable as more complex models for diagnosing biogeochemical cycles at single locations or areas with homogenous environmental conditions.

A focus shift towards better understanding pathways of plankton metabolism and mortality is necessary to address model construction uncertainties with respect to trophic structure. Potential future modelling research directions may include the use of optimization experiments to replicate controlled laboratory and mesocosm experiments, and twin experiments assimilating all state variables using synthetic model data. These types of optimization experiments can help identify patterns of common behavior among models, and the development of improved dynamical parameterizations of trophic complexity in simple models without increasing the number of unconstrained variables to be solved. Nevertheless, real progress in both modelling and ecological research can only be achieved to the extent that we obtain more comprehensive observational datasets.

## CHAPTER 5:

# HETEROTROPHIC AND AUTOTROPHIC N<sub>2</sub> FIXATION IN A BIOGEOCHEMICAL MODEL OF THE GULF OF AQABA (ISRAEL), RED SEA

## 5.1 INTRODUCTION

Nitrogen fixation refers to the conversion of dinitrogen gas (N<sub>2</sub>) into bioavailable forms of nitrogen by diazotrophs, a specialized group of microbial organisms, via reduction to ammonium (NH<sub>4</sub>). On geological timescales, the size of the oceanic reservoir of bioavailable nitrogen, and thus the ocean's capacity for exporting carbon, is controlled by the balance between removal of fixed nitrogen by denitrification and input by N<sub>2</sub> fixation (Falkowski, 1997; Haug et al., 1998; Deutsch et al., 2007; Gruber and Galloway, 2008; Fennel et al., 2009). The amount of organic matter exported from the surface to the deep ocean (i.e., export production) depends on allochthonous inputs of nitrogen (i.e., "new nitrogen") into the euphotic zone (Eppley and Peterson, 1979). These new nitrogen inputs determine the amount of "new production", which is directly related to the exported fraction. Locally the supply of new nitrogen can occur through several mechanisms, including microbially mediated N<sub>2</sub> fixation, upwelling, diapycnal mixing injecting deep nitrate (NO<sub>3</sub>) into the surface, lateral transport and riverine input. While the injection of deep NO<sub>3</sub> is often regarded as the dominant source of new nitrogen for the ocean and controlling the seasonal cycle of marine primary production, there is significant interest in better understanding the importance and quantifying the

contribution of N<sub>2</sub> fixation to primary production, particularly in oligotrophic areas (Capone et al., 2005; Karl, 2002; Zehr and Ward, 2002).

Diazotrophs are able to produce nitrogenase enzymes, the catalyst for N<sub>2</sub> reduction, which are encoded by *nif* genes. *Trichodesmium spp.*, a group of non-heterocystous cyanobacteria that forms large colonies, was long considered the most ubiquitous marine N<sub>2</sub> fixing organism, and the main contributor to N<sub>2</sub> fixation in the ocean (Carpenter and McCarthy, 1975; Capone et al., 2005). Increased sampling efforts and methodological improvements subsequently led to the discovery of a variety of other diazotroph groups including heterocystous endosymbiotic cyanobacteria (Carpenter et al., 1999; Zehr et al., 1998) and free-living unicellular cyanobacteria (Moisander et al., 2010; Montoya, 2004; Zehr et al., 2001), and a number of cyanobacterial symbiotic relationships (Zehr et al., 2000). Most recently, genetic techniques have allowed the detection of *nif* genes in a number of anaerobic and heterotrophic phylotypes (Zehr et al., 2008; Zehr, 2011; Rahav et al., 2013, 2015). The abundance of *nif* genes does not necessarily imply that these organisms are actively fixing N<sub>2</sub> (Zehr et al., 2000); however, the correlation between bacterial productivity and N<sub>2</sub> fixation rates suggests that significant aphotic N<sub>2</sub> fixation may occur in the Red Sea (Rahav et al., 2013, 2015). The differences in size and physiology of these diverse diazotrophic organisms suggest that they occupy distinct niches, and thus may affect primary productivity and export production differently (Moisander et al., 2010).

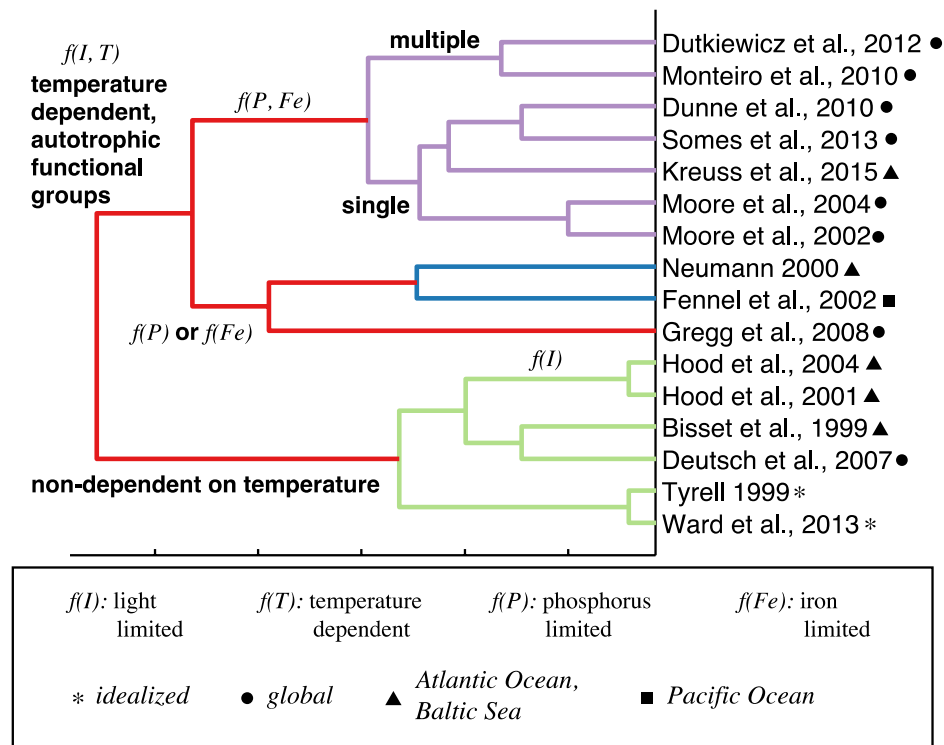


Figure 5.1: Hierarchical cluster tree depicting differences and similarities of published biogeochemical models including  $N_2$  fixation. The cluster analysis was performed by assigning numerical values to 23 characteristics identified for these models, focusing on assumptions about diazotrophy. Limiting growth factors refer only to the diazotrophic functional groups. “Single” and “Multiple” refer to the number of diazotrophic functional groups. The method to compute distance between models was an unweighted average distance.

Most biogeochemical models treat  $N_2$  fixation as a purely light-dependent, autotrophic process (see Figure 5.1). These models either use mechanistic formulations of light limitation for the diazotrophic groups (e.g., Fennel et al., 2002; Moore, et al., 2004; Gregg, 2008; Dutkiewicz et al., 2012), or include theoretical considerations to introduce an empirical  $N_2$  fixation flux in the model (e.g., Bisset et al., 1999). Some approaches neglect light limitation on diazotrophy and instead infer global  $N_2$  fixation patterns from

the distribution of dissolved inorganic nitrogen and phosphorus, and estimates of ocean circulation (e.g., Deutsch et al., 2007). In mechanistic models, diazotrophs are usually accounted for by a single functional group, with biological parameters intended to represent either *Trichodesmium spp.* or unicellular cyanobacteria, or a generic autotrophic diazotroph. Only a few modelling studies have evaluated multiple autotrophic diazotrophs groups simultaneously, by considering separate groups for *Trichodesmium spp.*, unicellular cyanobacteria and diatom-cyanobacterial associations (e.g., Monteiro et al., 2010; Duckiewicz et al., 2012). To my knowledge, heterotrophic N<sub>2</sub> fixation has not been yet explicitly considered in biogeochemical models.

Understanding the ecological dynamics of different types of diazotrophs should significantly improve predictive capabilities in biogeochemical models, and lead to more accurate estimates of global N<sub>2</sub> fixation rates. It has been suggested that N<sub>2</sub> fixation rates are underestimated globally due to limited knowledge about the distribution and characteristics of N<sub>2</sub> fixing organisms (Montoya, 2004; Zehr, 2011). It is also assumed that marine N<sub>2</sub> fixation may increase globally, as a result of ocean warming and higher concentrations of dissolved CO<sub>2</sub> in sea water (Hutchins et al., 2007; Levitan et al., 2007).

In this chapter, I explore the biogeochemical signatures that result from different assumptions about the ecological niches occupied by diazotrophs. I aim to answer the following two questions: i) How important is N<sub>2</sub> fixation as a source of new nitrogen in the Gulf of Aqaba, part of the Red Sea? ii) How important is heterotrophic, light-independent N<sub>2</sub> fixation? To address these questions, I implemented a one-dimensional model at a monitoring station for which monthly measurements of physical and biogeochemical variables are available from 2004 to the present. I then systematically

tested different model assumptions about diazotrophy and calibrated selected model parameters to facilitate an objective comparison between different biogeochemical model versions. The different assumptions about diazotrophy consider the characteristics of organisms identified in the Gulf of Aqaba, including heterotrophic N-fixing bacteria  $\alpha$  and  $\gamma$  (Rahav et al., 2013), unicellular cyanobacteria and *Trichodesmium spp.* (Foster et al., 2009; Post et al., 2002). My most important conclusion is that aphotic N<sub>2</sub> fixation is necessary to reproduce the observed excess nitrogen in deep waters of the Gulf, while maintaining surface N<sub>2</sub> fixation rates similar to those locally observed. Estimates of annual N<sub>2</sub> fixation rates from my best performing model are in overall agreement with local and large-scale estimates, and concur with some of the highest observational estimates in the literature.

## **5.2 STUDY AREA: THE GULF OF AQABA**

The Gulf of Aqaba is a quasi-rectangular, 200-km long, 20-km wide, semi-enclosed basin in the northeast region of the Red Sea (Figure 5.2). The Gulf's average depth is 800 m, its deepest point approximately 1800 m, and it is surrounded by arid mountains that steer the dominantly northerly winds (Berman et al., 2003). Two shallow sills, the Bab el Mandeb (~140 m) and the Strait of Tiran (~240 m), inhibit the entrance of cold and dense deep waters from Indian Ocean waters in the deeper layers of the Red Sea. Since inflow is restricted to warm surface waters, the Gulf does not have permanent vertical stratification. Another important consequence of the restricted deep-water exchange is that the Gulf's deep water masses (>300 m) are locally formed (Wolf-Vecht

et al., 1992; Biton et al., 2008) and have negligible horizontal velocities towards the exterior (Klinker et al., 1976; Manasrah et al., 2006).

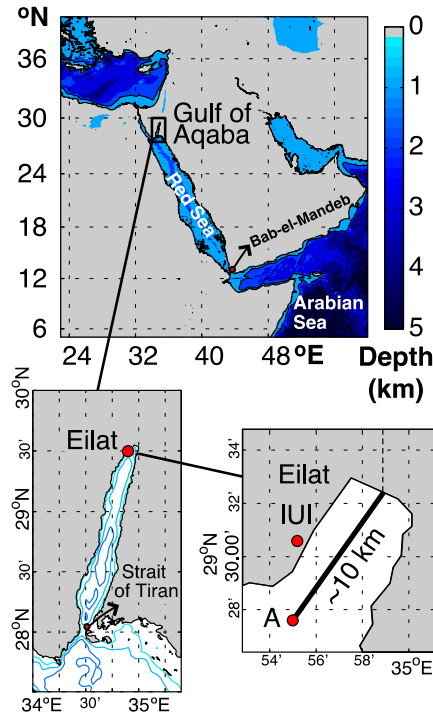


Figure 5.2: Map of study area showing the location of monitoring stations and geographical references.

The annual hydrographical cycle exhibits a well-defined seasonality where vertical temperature and salinity distributions are dominantly affected by surface heat fluxes and modified by surface advective fluxes (Carlson et al., 2014). During winter (September to March), convective vertical mixing usually extends to depths  $>300$  m (Labiosa et al. 2003), and even reaches the bottom in some extreme years (Figure 5.3 and 5.4). From April to September the water column is thermally stratified, and inflowing warm surface waters from outside the Gulf occupy the layer above the thermocline (Genin and Paldor, 1998; Berman et al., 2000; Biton and Gildor 2011). At the end of

September, surface cooling and high evaporation rates erode the seasonal stratification and re-establish a well-mixed water column (Berman et al., 2003; Monismith and Genin, 2004). The Gulf experiences a net evaporation of approximately  $1.6 \text{ m yr}^{-1}$  (Ben-Sasson et al., 2009) due to negligible precipitation and run-off (Wolf-Vecht et al., 1992).

The Gulf is oligotrophic, with surface  $\text{NO}_3$  and phosphate ( $\text{PO}_4$ ) concentrations usually close to their detection limits during summer stratification (Fuller et al. 2005; Mackey et al. 2009; Meeder et al. 2012). Deep winter mixing supplies inorganic nutrients to the surface, and  $\text{NO}_3$  and  $\text{PO}_4$  reach  $\sim 0.1 \text{ }\mu\text{M}$  and  $\sim 2 \text{ }\mu\text{M}$ , respectively (Figure 5.3; Lindell and Post 1995; Lazar et al. 2008). Dust from the desert provides a sufficient atmospheric source of soluble iron (Fe), so that dissolved Fe exceeds the requirements for microbial growth in the Gulf (Chase et al., 2006; Chen et al., 2007). Interannual variability in the depth of winter convective mixing results in periods of accumulation of nutrients in the deep-waters (Figure 5.3 and 5.4; Wolf-Vecht et al., 2002; Lazar et al., 2008; Carlson et al., 2012) followed by a re-set during extreme winter mixing events approximately every four years (Silverman and Gildor, 2007). The periodicity of these extreme mixing events has been associated with regional weather patterns that modify the Red Sea temperatures (Silverman and Gildor, 2007).

### **5.3 METHODS**

I analyze the role of autotrophic and heterotrophic  $\text{N}_2$ -fixing organisms in determining biogeochemical patterns at Station A by testing four alternative ecosystem model versions. The ecosystem models are evaluated in terms of their ability to replicate observations of oxygen ( $\text{O}_2$ ),  $\text{NO}_3$ , phosphate ( $\text{PO}_4$ ), and chlorophyll. In this section I first

describe the available observations, then the models, and finally the systematic model calibration method.

### 5.3.1 OBSERVATIONS

Meteorological and oceanographic observations come from the database of the Inter-University Institute (IUI) for Marine Sciences in Eilat, Israel (<http://www.iui-eilat.ac.il/Research/NMPMeteoData.aspx>). Meteorological observations are used to calculate surface heat and momentum fluxes for the physical model and incoming light for the biological models. Observed meteorological variables include wind speed, air temperature, air humidity, air pressure, irradiance and cloud cover. This data is collected continuously and automatically at 10 min intervals by the meteorological instrumental array at the end of the IUI pier since 2006.

Monthly CTD and bio-chemical profiles at Station A (29.5° N, 34.9° E) were collected during monthly surveys of the National Monitoring Program (NMP) from 2004 to 2014. CTD profiles are used to nudge temperature and salinity in the physical model (see section 5.4.2.1). Bio-chemical profiles, including nitrate (NO<sub>3</sub>), nitrite (NO<sub>2</sub>), ammonium (NH<sub>4</sub>), phosphate (PO<sub>4</sub>), dissolved oxygen (O<sub>2</sub>) and chlorophyll-a (Chl-a), are used for biogeochemical model calibration, and in the assessment of model performance against assimilated data. Nutrients are measured using spectrophotometry (QuickChem 8000 flow injection), O<sub>2</sub> was determined by Winkler titrations, and Chl-a concentrations are estimated using fluorometry (Turner Designs 10-AU).

### 5.3.2 MODEL DESCRIPTIONS

The ecosystem models are implemented within the General Ocean Turbulence Model (GOTM), a one-dimensional physical model that computes solutions to differential equations for the vertical transport of momentum, salt and heat using state-of-the-art numerical schemes (Burchard et al., 1999). GOTM is implemented for the 700-m deep Station A with a vertical resolution of 3 m, and forced with hourly-averaged meteorological observations from the IUI pier. Temperature and salinity are nudged to observed CTD profiles from Station A with a nudging time scale of 30 days. This is done to account for the influence of horizontal advection of heat and salt in the one-dimensional model, and ensures a realistic representation of density stratification. The effect of temperature and salinity nudging on the results is analyzed (section 5.4.2.1). As model calibration is computationally expensive, model simulations run only from January 2005 to September 2010. The first year of each simulation is considered model spin-up and excluded from further analysis (climatologically meteorological forcing is used for the first year, as this database starts in 2006).

Four main ecosystem model versions of increasing complexity (referred to as H0, H1, H2 and H3) are treated as alternative hypotheses of how biological processes, especially diazotrophy, control the vertical distribution and temporal variability of dissolved inorganic nutrients and oxygen. H0 is the base model without explicit N<sub>2</sub> fixation (i.e., no diazotrophic plankton groups are included) and follows the model equations described in Fennel et al., (2006, 2013). I test this model with and without explicit inclusion of a sediment denitrification flux, denoted as H0 and H0', respectively.

Thus, H0 fully neglects N<sub>2</sub> fixation, while H0' implicitly assumes that inputs from N<sub>2</sub> fixation and losses of fixed nitrogen due to denitrification are balanced.

H1, H2 and H3 are modified versions of H0, in which different groups of diazotrophic organisms are added sequentially. H1 introduces a generic autotrophic diazotroph; H2 replaces H1's generic diazotroph with two autotrophic diazotrophs representing unicellular and colonial (e.g., *Trichodesmium spp.*) cyanobacteria. A minimum temperature limit for the growth of *Trichodesmium spp.* is implemented in the model by setting the maximum growth rate to 0 when temperature drops below 20°C, based on the inability to culture this type of organism below this temperature (Breitbarth et al., 2007). However, temperatures below 20.5°C have not been recorded in Gulf of Aqaba. The unicellular diazotroph group overall follows the same formulation as the generic diazotroph, except that no coagulation term is included in this equation as they represent free-living picoplanktonic cells that do not form large colonies. Instead, this group is grazed by zooplankton similar to grazing on non-fixing phytoplankton. This difference between colonial and unicellular groups is consistent with studies suggesting that colonies represent an evolutionary adaptation to decrease grazing pressure (Nielsen 2006). Aside from their size, *Trichodesmium spp.* colonies may be less palatable and harder to digest due to toxins; grazing is not a major fate of this group (O'Neil and Roman, 1994).

The last model version, H3, adds a heterotrophic diazotroph group to the model structure of H2. This group of organisms is not limited by light availability, and grows by consuming both dissolved inorganic and organic phosphorus from detritus. In a subsequent set of four experiments (H3a, H3b, H3c, and H3d), I remove complexity from

H3. The heterotrophic group remains, but I sequentially test the autotrophic diazotrophs groups one-at-a-time: first the colonial cyanobacteria (H3a), then the unicellular cyanobacteria (H3b), then the generic autotrophic diazotroph (H3c), and finally I remove all autotrophic diazotrophs (H3d). A summary of all model versions is included in Table 5.1, and a description of state variables and full model equations are given in Appendix I.

Table 5.1: Summary of model versions characteristics and different assumptions about each diazotrophs group. N = no diazotrophs; A = autotrophic diazotrophs; H = heterotrophic diazotrophs. Checkmarks (✓) represent presence of a model characteristic / functional diazotrophic group in the model; dashes represent their absence.

Model Version	Characteristics / Diazotrophs Groups	Denitrification	Generic (A)	Unicellular (A)	Colonial (A)	Heterotrophic (H)
H0	N	✓	-	-	-	-
H0'	N	-	-	-	-	-
H1	A	✓	✓	-	-	-
H2	A	✓	-	✓	✓	-
H3	A H	✓	-	✓	✓	✓
H3a	A H	✓	-	-	✓	✓
H3b	A H	✓	-	✓	-	✓
H3c	A H	✓	✓	-	-	✓
H3d	H	✓	-	-	-	✓
<b>Diazotrophs characteristics:</b>						
	Inorganic phosphorus uptake		✓	✓	✓	✓
	Organic phosphorus uptake		-	-	-	✓
	Light growth limitation		✓	✓	✓	-
	Temperature dependent maximum growth rate		✓	✓	✓	✓
	Minimum temperature limit for growth (20°C)		-	-	✓	-
	Predation		-	✓	-	-

### 5.3.3 MODEL PARAMETERS

#### 5.3.3.1 Cost Function Design

For this study case, the optimization algorithm starts with a randomly generated population of 30 parameter sets  $\{\vec{p}\}$ . During each generation of the population, the cost  $F(\vec{p})$  of the model running with a set of parameters  $\vec{p}$  is calculated as:

$$F(\vec{p}) = \frac{1}{V} \sum_{v=1}^V \frac{w_v}{N} \sum_{i=1}^N (\hat{y}_{v,i} - y_{v,i})^2,$$

where  $\hat{y}$  represents a model estimate and  $y$  the corresponding observation.  $N$  is the number of observations included for each variable  $v$ . Here the number of variables  $V$  is 5 and includes nitrate + nitrite, ammonium, phosphate, chlorophyll-a, and oxygen measured as profiles at Station A between 2006 and 2010. Model-data misfits are weighted by a factor  $w_v = 1/\sigma_v$ , i.e, the inverse standard deviation of each variable. Half of the parameter sets with the lowest  $F$  values “survive” to the next generation. The other half of the population is generated from new parameter sets obtained by recombination of two random “parent” sets the better performing half. Parameters also randomly “mutate”, i.e. random noise is added, for additional variability in the parameter space. An allowable range of values is set for each parameter based on the literature (Table 5.2).

Table 5.2: Parameters used in the base biogeochemical model (H0), including minimum and maximum parameters ranges based on the literature. Parameters values followed by \* were obtained by the optimization.

Parameters	Value	Range	Description	Units	References
$\mu_{Phy}^0$	0.76*	0.1 – 3	Reference phytoplankton maximum growth rate at $T = 0^\circ\text{C}$	$\text{d}^{-1}$	a, b, c
$k_{Phy}^{NO_3}$	0.05	0.01 – 0.5	Phytoplankton $\text{NO}_3$ uptake half-saturation	$\text{mmol m}^{-3}$	d, e
$k_{Phy}^{NH_4}$	0.1*	0.01 – 0.5	Phytoplankton $\text{NH}_4$ uptake half-saturation	$\text{mmol m}^{-3}$	d, e
$k_{Phy}^{DIP}$	0.004*	0.001 – 0.5	Phytoplankton DIP uptake half-saturation	$\text{mmol m}^{-3}$	a, f, g
$\alpha_{Phy}$	0.1*	0.01 – 0.125	Phytoplankton, initial slope of photosynthetic response	$\text{molC gChl}^{-1} (\text{W m}^{-2})^{-1} \text{d}^{-1}$	d, h
$m_{Phy}$	0.1	0.01 – 0.2	Phytoplankton mortality rate	$\text{d}^{-1}$	d
$g_{Phy}^{max}$	1.16*	0.1 - 4	Zooplankton maximum grazing rate	$\text{d}^{-1}$	b, i
$k_{Zoo}^{Phy}$	0.5*	0.01 – 0.5	Square zooplankton grazing half-saturation	$(\text{mmol m}^{-3})^2$	d, e
$l_{BM}$	0.011*	0.01 – 0.15	Zooplankton base metabolic rate	$\text{d}^{-1}$	d
$l_E$	0.1	0.05 – 0.35	Zooplankton excretion rate	$\text{d}^{-1}$	d
$m_Z$	0.35*	0.02 - 0.35	Zooplankton mortality rate	$\text{d}^{-1}$	d
$\tau$	0.1	0.01 - 25	Small detritus aggregation rate	$\text{d}^{-1}$	d, e
$\theta_{Phy}^{max}$	0.142*	0.015 – 0.15	Maximum chlorophyll to carbon ratio	$\text{mg Chl (mg C)}^{-1}$	h
$\beta$	0.74*	0.25 – 0.75	Zooplankton assimilation efficiency	non-dim.	j, k
$r_{DOM}$	0.2	0.05 – 0.5	DOM remineralization rate	$\text{d}^{-1}$	l
$r_D$	0.01	0.005 – 0.15	Detritus remineralization rate	$\text{d}^{-1}$	l, m
$n_{max}$	0.3*	0.01 – 0.35	Nitrification rate	$\text{d}^{-1}$	d, e
$k_I$	0.1	0.01 – 0.5	Half-saturation radiation for nitrification inhibition	$\text{Wm}^{-2}$	d
$I_{th}$	0.0095	0.005 – 0.01	Radiation threshold for nitrification inhibition	$\text{Wm}^{-2}$	d
$w_{Phy}$	0.1	0.01 – 1	Vertical sinking velocity for non-fixing phytoplankton	$\text{md}^{-1}$	n
$w_{DL}$	-4.44*	0.01 – 25	Vertical sinking velocity for large detritus	$\text{md}^{-1}$	d

a. Fennel et al. (2002) b. Fahnenstiel et al. (1995) c. Veldhuis et al. (2005) d. Fennel et al. (2006) e. (Lima and Doney (2004) f. Ward et al. (2013) g. Moore, et al.(2002) h. Geider et al. (1997) i. Gifford et al. (1995) j. Landry et al. (1984) k. Tande and Slagstad (1985) l. Amon and Benner (1996) m. Enríquez et al. (1993) n. Smayda and Bienfang (1983)

### 5.3.3.2 Optimized Parameters

There are certain limitations for the use of parameter optimization. In general, the optimization cannot estimate with confidence parameters that are unconstrained by the observations (Schartau and Oeschies, 2003; Ward et al., 2010). In order to avoid attempting to optimize parameters that cannot be constrained by the observations, a subset of H0's most sensitive parameters was selected for optimization through a preliminary sensitivity analysis (Appendix I). Optimized and fixed parameters for H0 are identified in Table 5.1 along with the obtained optimized values. This subset of parameters was optimized by running 10 optimization replicates over 100 generations using the algorithm described in section 5.3.3.1. Thus, I tested an approximate total of 15000 different parameter sets. Non-optimized parameters are fixed to a priori estimates based on Fennel et al. (2006; 2013).

For each model version with diazotrophs (H1, H2 and H3), some of the previously optimized parameters required re-calibration to properly accommodate the changes in system dynamics. Re-calibrated parameters for each model version are presented in Table 5.3. No re-calibration was performed for model sub-versions (H0' and H3a-d), as they are aimed to test the relative importance of individual components on their corresponding model version results.

Table 5.3: Diazotrophs parameters and re-calibrated non-fixing phytoplankton parameters for each model version. H0 = no N<sub>2</sub> fixers; H1 = generic autotrophic diazotrophs; H2 = unicellular and colonial cyanobacteria; H3 = heterotrophs, unicellular and colonial cyanobacteria.

Model version:	H0	H1	H2	H3	Units	Description
$\mu_{Phy}^0$	0.76	2.20	1.5	1.5	d <sup>-1</sup>	Reference phytoplankton maximum growth rate at T = 0°C
$\theta_{Phy}^{max}$	0.022	0.076	0.076	0.05	mg Chl (mg C) <sup>-1</sup>	Maximum chlorophyll to carbon ratio – non fixing phytoplankton
$k_{Phy}^{NH_4}$	0.076	0.076	0.076	0.076	mmol m <sup>-3</sup>	Phytoplankton NH <sub>4</sub> uptake half-saturation
$k_{Phy}^{DIP}$	0.001	0.015	0.015	0.015	mmol m <sup>-3</sup>	Phytoplankton DIP uptake half-saturation
$m_{Phy}$	0.1	0.06	0.06	0.06	d <sup>-1</sup>	Phytoplankton mortality rate
$g_{Phy}^{max}$	1.16	4.0	1.95	1.95	d <sup>-1</sup>	Zooplankton maximum grazing rate
$\beta$	0.36	0.7	0.7	0.7	non-dim.	Zooplankton assimilation efficiency
$\mu_{GF}^0$	-	0.25	-	-	d <sup>-1</sup>	Reference generic diazotrophs maximum growth rate at T = 0°C
$k_{GF}^{DIP}$	-	0.001	-	-	mmol m <sup>-3</sup>	Generic diazotrophs DIP uptake half-saturation
$\theta_F^{max}$	-	0.053	-	-	mg Chl (mg C) <sup>-1</sup>	Maximum chlorophyll to carbon ratio – generic diazotrophs
$\alpha_{GF}$	-	0.01	-	-	molC gChl <sup>-1</sup> (W m <sup>-2</sup> ) <sup>-1</sup> d <sup>-1</sup>	Generic diazotrophs, initial slope of photosynthetic response
$m_{GF}$	-	0.18	-	-	d <sup>-1</sup>	Generic diazotrophs mortality rate
$l_{GF}$	-	0.05	-	-	d <sup>-1</sup>	Generic diazotrophs respiration rate
$\mu_{UF}^0$	-	-	0.25	0.25	d <sup>-1</sup>	Reference unicellular cyanobacteria maximum growth rate at T = 0°C
$k_{UF}^{DIP}$	-	-	0.004	0.004	mmol m <sup>-3</sup>	Unicellular cyanobacteria DIP uptake half-saturation
$\theta_{UF}^{max}$	-	-	0.053	0.053	mg Chl (mg C) <sup>-1</sup>	Maximum chlorophyll to carbon ratio – unicellular cyanobacteria
$\alpha_{UF}$	-	-	0.05	0.05	molC gChl <sup>-1</sup> (W m <sup>-2</sup> ) <sup>-1</sup> d <sup>-1</sup>	Unicellular cyanobacteria, initial slope of photosynthetic response
$m_{UF}$	-	-	0.20	0.2	d <sup>-1</sup>	Unicellular cyanobacteria mortality rate
$l_{UF}$	-	-	0.05	0.05	d <sup>-1</sup>	Unicellular cyanobacteria respiration rate

Model version:	H0	H1	H2	H3	Units	Description
$g_{UF}^{max}$	-	-	0.2	0.2	$d^{-1}$	Zooplankton maximum grazing rate on unicellular cyanobacteria
$k_{ZOO}^{UF}$	-	-	0.001	0.001	$(mmol\ m^{-3})^2$	Square zooplankton grazing half-saturation on unicellular cyanobacteria
$\mu_{CF}^0$	-	-	0.25	0.25	$d^{-1}$	Reference colonial cyanobacteria maximum growth rate at $T = 0^{\circ}C$
$k_{CF}^{DIP}$	-	-	0.004	0.004	$mmol\ m^{-3}$	Colonial cyanobacteria DIP uptake half-saturation
$\theta_{CF}^{max}$	-	-	0.053	0.053	$mg\ Chl\ (mg\ C)^{-1}$	Maximum chlorophyll to carbon ratio – colonial cyanobacteria
$\alpha_{CF}$	-	-	0.05	0.05	$molC\ gChl^{-1}\ (W\ m^{-2})^{-1}\ d^{-1}$	Colonial cyanobacteria, initial slope of photosynthetic response
$m_{CF}$	-	-	0.18	0.05	$d^{-1}$	Colonial cyanobacteria mortality rate
$l_{CF}$	-	-	0.05	0.18	$d^{-1}$	Colonial cyanobacteria respiration rate
$\mu_{HF}^0$	-	-	-	0.2	$d^{-1}$	Reference heterotrophs maximum growth rate at $T = 0^{\circ}C$
$k_{HF}^{DIP}$	-	-	-	0.001	$mmol\ m^{-3}$	Heterotrophs DIP uptake half-saturation
$k_{HF}^{DS}$	-	-	-	0.001	$mmol\ m^{-3}$	Heterotrophs organic phosphorus uptake half-saturation
$m_{HF}$	-	-	-	0.2	$d^{-1}$	Heterotrophs mortality rate
$l_{HF}$	-	-	-	0.05	$d^{-1}$	Heterotrophs respiration rate

### 5.3.3.3 Diazotrophs Parameters

None of the parameters directly related to the diazotroph groups are constrained by the available observations. That is, there is no measure of the amount of chlorophyll corresponding to cyanobacteria only, or of the amount of  $PO_4$  consumed by these organisms. Moreover, to date there are only few reported  $N_2$  fixation measurements in the

Gulf of Aqaba, which are reserved for model validation. Therefore, I predefined the parameters of the diazotrophic groups introduced in H1, H2 and H3, based on values found in the observational and modelling literature (Table 5.3).

For example, previous modelling studies have used maximum generic  $N_2$  fixers growth rates ranging from  $0.4 \text{ d}^{-1}$  (Moore, et al., 2004) to  $1.25 \text{ d}^{-1}$  (Ward et al., 2013); whereas when the diazotrophs are assumed to represent *Trichodesmium spp.* values range between  $0.17 \text{ d}^{-1}$  (Hood et al., 2001) to  $0.3 \text{ d}^{-1}$  (Fennel et al., 2002). From the observational literature, *Cyanothece* (unicellular cyanobacteria) and *Trichodesmium spp.* cultured under various combinations of Fe and light availability exhibit maximum rates around  $0.3 \pm 0.05 \text{ d}^{-1}$  (Berman-Frank et al., 2001; Capone et al., 1997; Hutchins et al., 2007). For all photosynthetic diazotrophs, I chose a standard maximum growth rate value of  $0.25 \text{ d}^{-1}$ , such that differences between the model versions are largely dependent on the different assumptions about the losses of each organism (e.g., predation of unicellular cyanobacteria vs. sinking of large aggregates). Based on growth rates measured for cultured heterotrophic bacteria, I chose a value of  $0.2 \text{ d}^{-1}$  for the heterotrophic diazotrophs (Pomeroy and Wiebe, 2001). Observational and modelling studies were also considered to set the photosynthetic initial slope of photosynthetic diazotrophs (Geider et al., 1997; Hutchins et al., 2007; Moore, et al., 2004). Other parameters are based on Fennel et al. (2002).

## 5.4 RESULTS

### 5.4.1 OBSERVED $\text{NO}_3$ AND $\text{PO}_4$ PATTERNS

In order to provide context for the evaluation of my model simulations, I first describe observed  $\text{NO}_3$  and  $\text{PO}_4$  interannual and seasonal variability for the complete time series (i.e. 2004 to 2014) at Station A (Figure 5.3).

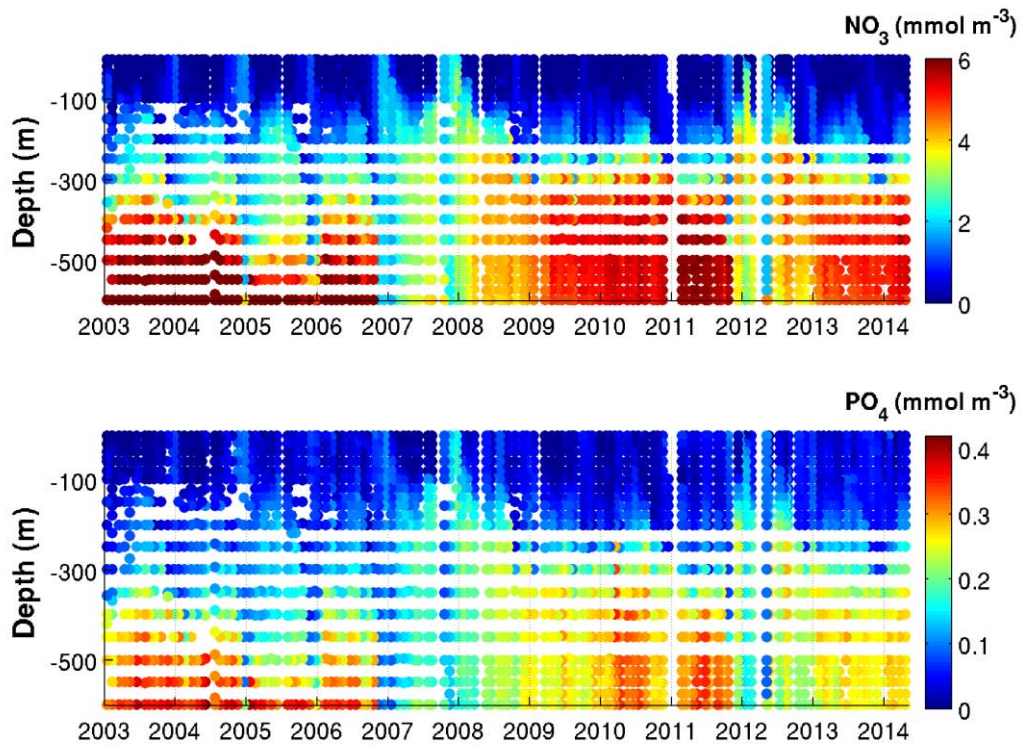


Figure 5.3: Nitrate and phosphate vertical distributions at Station A from 2004 to 2014, showing seasonal and interannual variability. Ticks are placed on April 1<sup>st</sup> of every year.

Seasonally, from May to January vertical distributions of  $\text{NO}_3$  and  $\text{PO}_4$  are depleted in the euphotic zone and characterized by a nutricline between 100 and 200 m.

Between February and April, nutrient concentrations decrease in the deep waters (>200 m) and increase in the surface as result of vertical mixing. Multi-year periods of accumulation of nutrients in the deep-waters are observed from: i) the beginning of the series to the end of 2006, ii) after the winter of 2008 until February 2012, and iii) after the winter of 2013 until the end of the series. These periods are bookended by winters with extremely deep mixing events in 2007, 2008, 2012 and 2013 that nearly homogenize nutrient concentrations in the entire water column. Two prolonged periods of these vertically homogenous conditions were observed in 2007 and 2008, lasting two to three months.

My model simulations are from 2006 to 2010, allowing us to analyze two years with deep winter mixing (2007 and 2008) and two years with moderate winter mixing (2009 and 2010). Figure 5.4 shows the linear metric  $N^*$  ( $N^* = \text{DIN} - 16\text{DIP}$ ) for my simulation period which allows us to quantify excess and deficit of observed nitrogen relative to phosphorus with respect to the canonical Redfield ratio (N:P=16:1). This metric allows diagnosing patterns of net nitrogen addition, i.e. the balance of  $N_2$  fixation and denitrification, on global and local scales (e.g., Gruber and Sarmiento, 1997; Fennel et al., 2009). Using the Redfield ratio as a reference,  $N^*$  is insensitive to changes in the nutrient concentrations that result from nutrient uptake by non-fixing phytoplankton and remineralization organic matter, assuming these processes occur in Redfield stoichiometry. Negative  $N^*$  values reflect an excess of phosphate (DIP) and can be interpreted as a signature of denitrification. Positive  $N^*$  reflects an excess of nitrogen (DIN) and can be interpreted as a signature of  $N_2$  fixation.

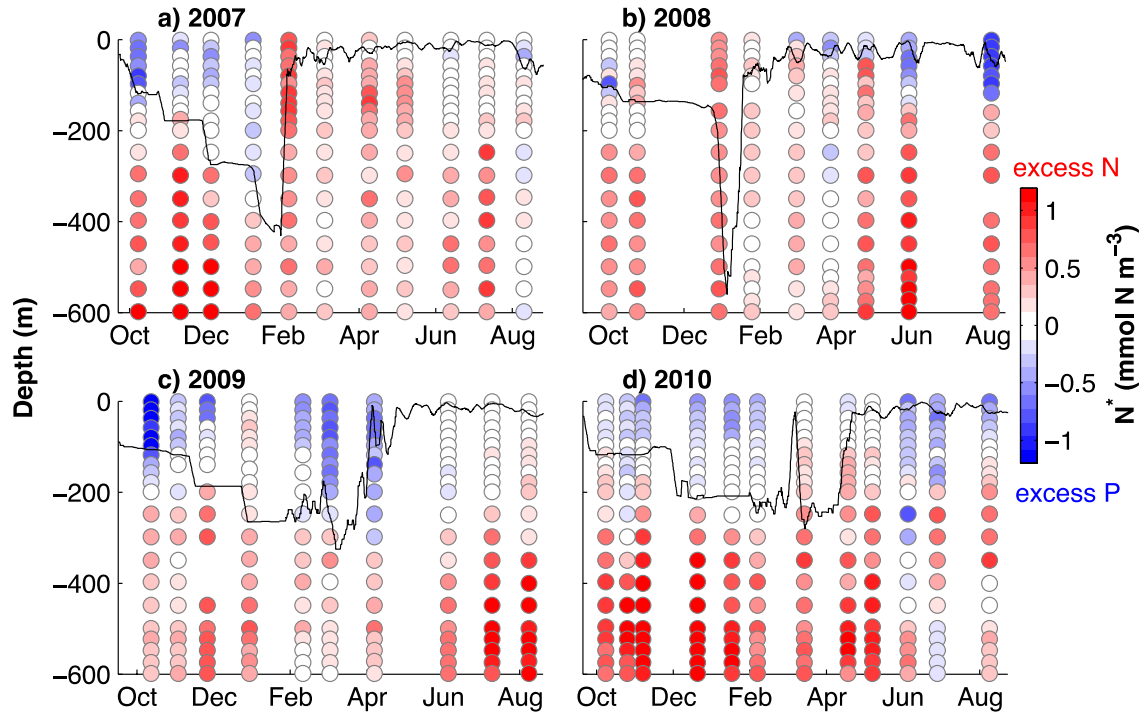


Figure 5.4:  $N^*$  calculated from  $\text{NO}_3$  and  $\text{PO}_4$  profiles at Station A from 2007 to 2010. The black line shows estimated mixed layer depth using a maximum density gradient criterion.

$N^*$  values presented in Figure 5.4 are calculated using the observations in Figure 5.3.  $N^*$  values shows that excess nitrogen (between  $+0.20$  and  $+1.06 \text{ mmol N m}^{-3}$ ) dominates throughout most of the water column, except at the surface during stratified summer conditions, when nutrients are depleted and surface waters exhibit an excess of phosphate ( $-0.35 \pm 0.25 \text{ mmol N m}^{-3}$ ). Waters with excess nitrate are brought to the surface during winter; however,  $N^*$  values rapidly return to negative at the surface. The magnitude and duration of occurrence of positive surface  $N^*$  values appear to be related to the depth of winter mixing. As previously mentioned, winter mixing in 2007 and 2008 was stronger than in 2009 and 2010. In the surface, maximum positive  $N^*$  values reach

0.95 mmol N m<sup>-3</sup> during the first two years, but only reach 0.59 mmol N m<sup>-3</sup> in the latter two years. Below the mixed layer depth, N\* positive deviations on the order of 0.69 ± 0.37 mmol N m<sup>-3</sup> occur between 2009 and 2010 due to accumulation of NO<sub>3</sub> in deep waters during years with moderate winter mixing.

## 5.4.2 MODEL RESULTS

### 5.4.2.1 Sensitivity to Physical Nudging

Figure 5.5 shows the temperature and density differences between model runs with and without temperature and salinity nudging towards observations. Temperature and salinity nudging has a negligible effect below 200 m, indicating that horizontal advection does not modify the lower part of the water column in a significant way. Above 200 m, differences in temperature and density are observed during summer, when the water column is stratified. Here nudging is correcting model errors in representing vertical mixing and errors in surface forcing. The average magnitude of the differences due to nudging in the top 200 m is 0.20±0.45 °C and 0.5±0.16 kg m<sup>-3</sup>. Overall, since its effects are small and limited to the surface, I conclude that neither the nudging nor the neglect of horizontal advection affects my conclusions about the importance of heterotrophic N<sub>2</sub> fixation.

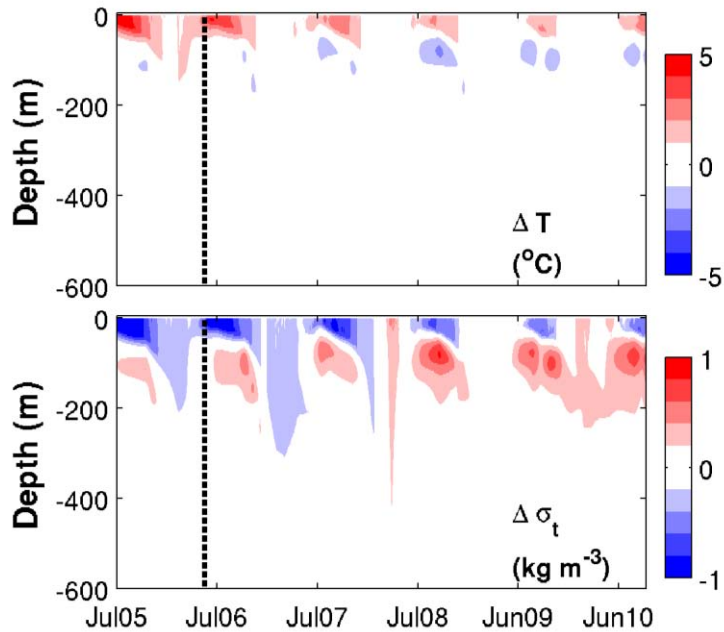


Figure 5.5: Effect of physical nudging on temperature and density fields estimated from a model run with nudging minus a model run without nudging. The dashed vertical line marks the simulation period used as a model spin-up.

#### 5.4.2.2 Optimized Model Without N<sub>2</sub> Fixation

Panels a) – c) in Figure 5.6 show the mean and standard deviation of simulated surface chlorophyll, NO<sub>3</sub> and PO<sub>4</sub> obtained by H0 and H0' when using the best fitting parameters obtained in the 10 replicate optimizations. From visual inspection, simulated surface chlorophyll fits the observations well, with root-mean-square errors between 0.0132 and 0.0217 mg Chl-a m<sup>-3</sup>, and a small spread among the individual optimizations. Model results have larger deviations in NO<sub>3</sub> and PO<sub>4</sub> surface values. H0' better represents maximum surface nutrient concentrations in winter than H0. Both models are challenged to replicate surface PO<sub>4</sub> observations between May and July, with simulated PO<sub>4</sub> being too low in all optimized results except for 2007.

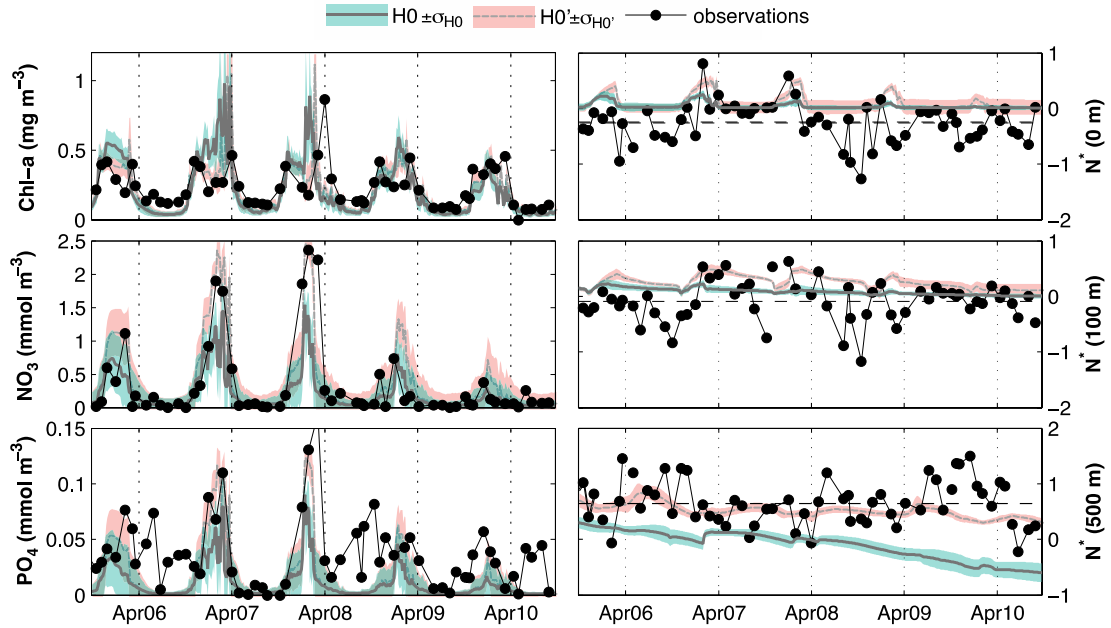


Figure 5.6: Results from model version H0 and sub-version H0' neglecting  $N_2$  fixation. Left panels show observed and simulated surface Chl-a,  $NO_3$  and  $PO_4$ . The mean and standard deviation refer to the model results using the best parameters obtained in 15 optimization exercises. Right panels show  $N^*$  at three depth levels. Horizontal axes start after spin-up period.

Panels d) – f) show simulated  $N^*$  values at three depth levels (0, 100 and 500 m). Both models reproduce average observed surface and mid-water  $N^*$  values, but do not capture the negative deviations at 0 and 100 m during summer. Simulated surface  $N^*$  values remain close to zero with positive deviations in winter. H0 exhibits the largest model-data deviations in deep waters, where simulated  $N^*$  values decline steadily towards negative values during the study period, while observed values are positive. In the absence of sediment denitrification, H0' produces higher deep-water  $N^*$  values; however it does not reproduce the observed positive anomalies.

### 5.4.2.3 Effects of N<sub>2</sub> Fixation on NO<sub>3</sub> and PO<sub>4</sub>

Figure 5.7 shows simulated NO<sub>3</sub> and PO<sub>4</sub> concentrations from models H0, H1, H2 and H3, along with the corresponding measurements at Station A. Observed NO<sub>3</sub> and PO<sub>4</sub> concentrations exhibit a defined increase in deep-water after the strong winter of 2008. Weaker winter mixing after 2008 produces deep-nutrient accumulation. This accumulation is stronger in the NO<sub>3</sub> profiles than in PO<sub>4</sub>.

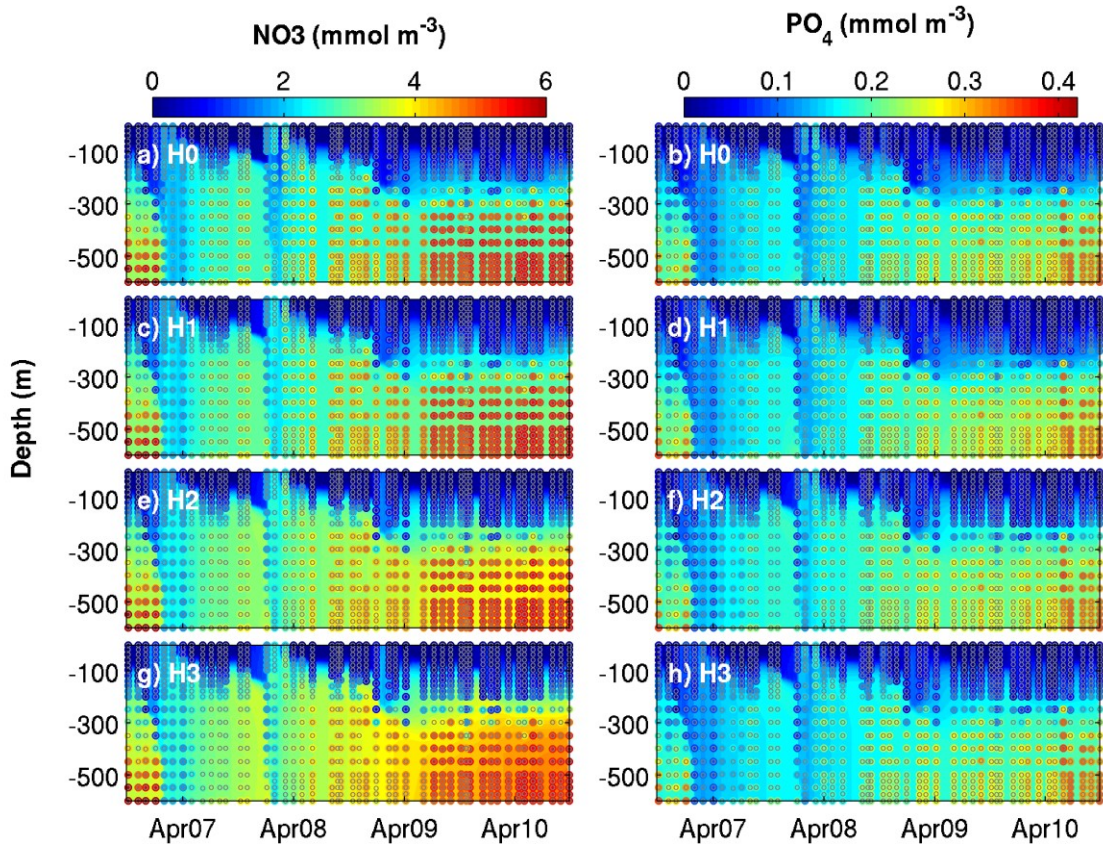


Figure 5.7: Observed (coloured circles) and simulated (background) NO<sub>3</sub> and PO<sub>4</sub> using model versions H0 (no nitrogen fixers), H1 (generic autotrophic fixer), H2 (unicellular and colonial autotrophic fixers), H3 (heterotrophic, and unicellular and colonial autotrophic fixers). Horizontal axes start after spin-up period.

Model H0 underestimates inorganic nutrients by up to 3 mmol N m<sup>-3</sup> and 0.1 mmol P m<sup>-3</sup>. Model H1, where N<sub>2</sub> fixation was introduced via a generic autotrophic, generates only small changes in the vertical distribution of nutrients. In model H2 the representation of NO<sub>3</sub> below the nutricline is slightly improved; however, underestimation of mid-water NO<sub>3</sub> and PO<sub>4</sub> is still noticeable. Model H3 further improves the pattern of deep NO<sub>3</sub> accumulation.

These model differences are more clearly summarized in Figure 5.8a, which shows the total (i.e., vertically integrated) simulated and observed NO<sub>3</sub> and PO<sub>4</sub> in surface and deep waters. From the observations I estimate that deep NO<sub>3</sub> accumulation between 2007 and 2010 occurs at a rate of  $0.59 \pm 0.08$  mmol m<sup>-2</sup> d<sup>-1</sup>, whereas deep PO<sub>4</sub> accumulates at  $0.015 \pm 0.009$  mmol m<sup>-2</sup> d<sup>-1</sup>. That is, during this accumulating period approximately 36 mmol NO<sub>3</sub> per mmol PO<sub>4</sub> are returned to the deep waters. All five model versions compared simulate similar temporal variability of PO<sub>4</sub> and resemblance of the observations. However, NO<sub>3</sub>, in particular total NO<sub>3</sub> below 100 m, diverges over time. H0 has the largest deviations with approximately constant deep NO<sub>3</sub> after 2007. H0', the version without denitrification, produces a rate of increase in deep NO<sub>3</sub> similar to that of model version H2. Nonetheless, H3 has the highest accumulation rate of deep NO<sub>3</sub>, matching the observed slope the best. In Figure 5.8b, I show total particulate organic nitrogen and phosphorus (PON and POP), defined as the sum of plankton and detritus groups. During the summer, models with N<sub>2</sub> fixation have higher PON than H0.

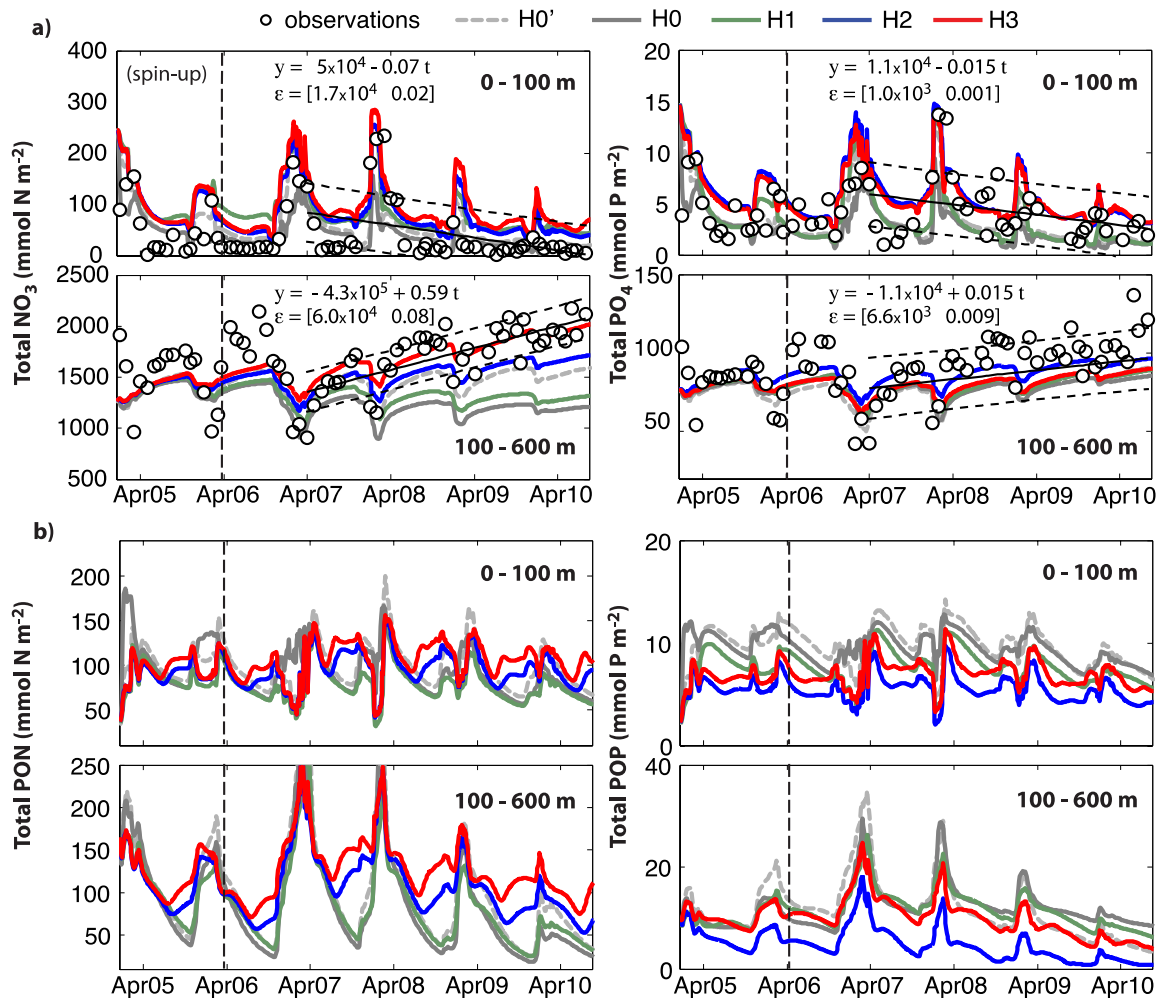


Figure 5.8: a) Observed and simulated vertically integrated NO<sub>3</sub> and PO<sub>4</sub> between 0 – 100 m and between 100 – 600 m using model versions H0 (no nitrogen fixers), H0' (no sediment denitrification – no fixers), H1 (generic autotrophic fixer), H2 (unicellular and colonial autotrophic fixers), H3 (heterotrophic, and unicellular and colonial autotrophic fixers). b) Contributions of different processes to changes in the simulated dissolved inorganic nitrogen (NO<sub>3</sub> + NH<sub>4</sub>): uptake by autotrophic non-fixing phytoplankton, vertical mixing, zooplankton base metabolism and excretion, small and large detritus remineralization, and excretion by diazotrophs.

The PO<sub>4</sub> versus NO<sub>3</sub> plots of Figure 5.9 visualize these results in terms of N\* values. For reference, observed N\* values above 200 m depth tend to remain close to zero, with positive deviations at intermediate NO<sub>3</sub> and PO<sub>4</sub> concentrations, and negative

deviations at low concentrations (Figure 5.9a). In waters below 200 m depth, maximum  $\text{PO}_4$  and  $\text{NO}_3$  concentrations reach 0.45 and 7  $\text{mmol m}^{-3}$ , respectively. Observed  $\text{N}^*$  values in deep waters are overall positive. This observed pattern in the distribution of nutrients and  $\text{N}^*$  values is not replicated by models H0 to H2, where maximum DIP and DIN concentrations only reach to 0.25 and 3.87  $\text{mmol m}^{-3}$ , respectively. In model H0, simulated  $\text{N}^*$  values are skewed towards negative deviations from zero. In model H1, negative  $\text{N}^*$  deviations are found at the surface, and both positive and negative  $\text{N}^*$  deviations occur in waters below 200 m.  $\text{N}^*$  results from model H2 are mostly centered at zero, with few deviations towards negative values. Model H3, where heterotrophic diazotrophs co-exist with colonial and unicellular autotrophic diazotrophs, is the model version best able to replicate the range of  $\text{NO}_3$  and  $\text{PO}_4$  concentrations. Simulated  $\text{N}^*$  in this model presents excess nitrogen in waters below 200 m, as in the observations; however, deviations are lower than observed at high nutrient concentrations.

Figure 5.9f-h shows results from the three of the four additional model versions based on H3 (H3a, H3c and H3d), in which autotrophic diazotrophs were sequentially removed from the model. In addition to heterotrophic diazotrophs, model H3a includes only the colonial autotrophic diazotrophs group and its results are closest to model H3, but show lower maximum nutrient concentrations. Inorganic nutrient results from the model with heterotrophic and generic autotrophic diazotrophs (H3c) are remarkably similar to those of model H2, while results in total absence of autotrophic diazotrophs (H3d) exhibit the narrowest nutrient concentrations range and become skewed towards positive  $\text{N}^*$  deviations. Results from H3b are similar to H3d due to low total nitrogen fixation rates, and are not shown in the plot.

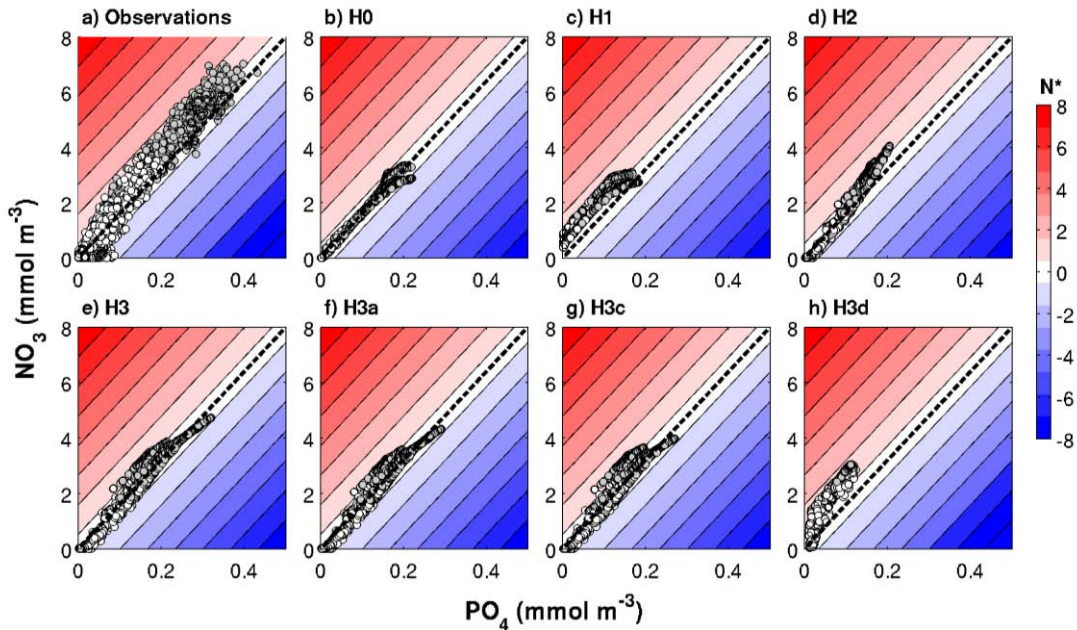


Figure 5.9: Observed and simulated  $N^*$  range in biogeochemical model versions tested. H3b (unicellular autotrophic and heterotrophic) behaves similarly to H3d, and is excluded from the figure for visual purposes. The dashed black diagonal line marks the  $N^* = 0$ , or  $N:P = 16$  line.

#### 5.4.2.4 Effects of $N_2$ Fixation on Chlorophyll and $O_2$

Figure 5.10 shows simulated and observed chlorophyll and dissolved oxygen values in the Gulf of Aqaba. The seasonal variability of total chlorophyll concentrations is reproduced well by all model variations, with increased chlorophyll values occurring between November and April. During these months, simulated chlorophyll concentrations are homogeneous up to 200 m. In 2007 and 2008, chlorophyll concentrations of  $\sim 0.13 \text{ mg m}^{-3}$  are observed in the measurements reaching as deep as 500 m. This feature is also captured well by my models, as is the location of the deep chlorophyll maximum (DCM) at  $\sim 80$  m between March and October. However, some discrepancies between model results and observations can be highlighted. The models overestimate spring bloom peak

concentrations in 2007 and peak timing is offset by two months in 2008. Model H0 tends to underestimate chlorophyll concentrations from the surface to the DCM during summer months. As chlorophyll concentrations are extremely low during this time of the year, these model-data differences are on the order of 0.05 to 0.1  $\text{mg m}^{-3}$ . Nonetheless, the discrepancies during summer months are corrected in the models with  $\text{N}_2$  fixation.

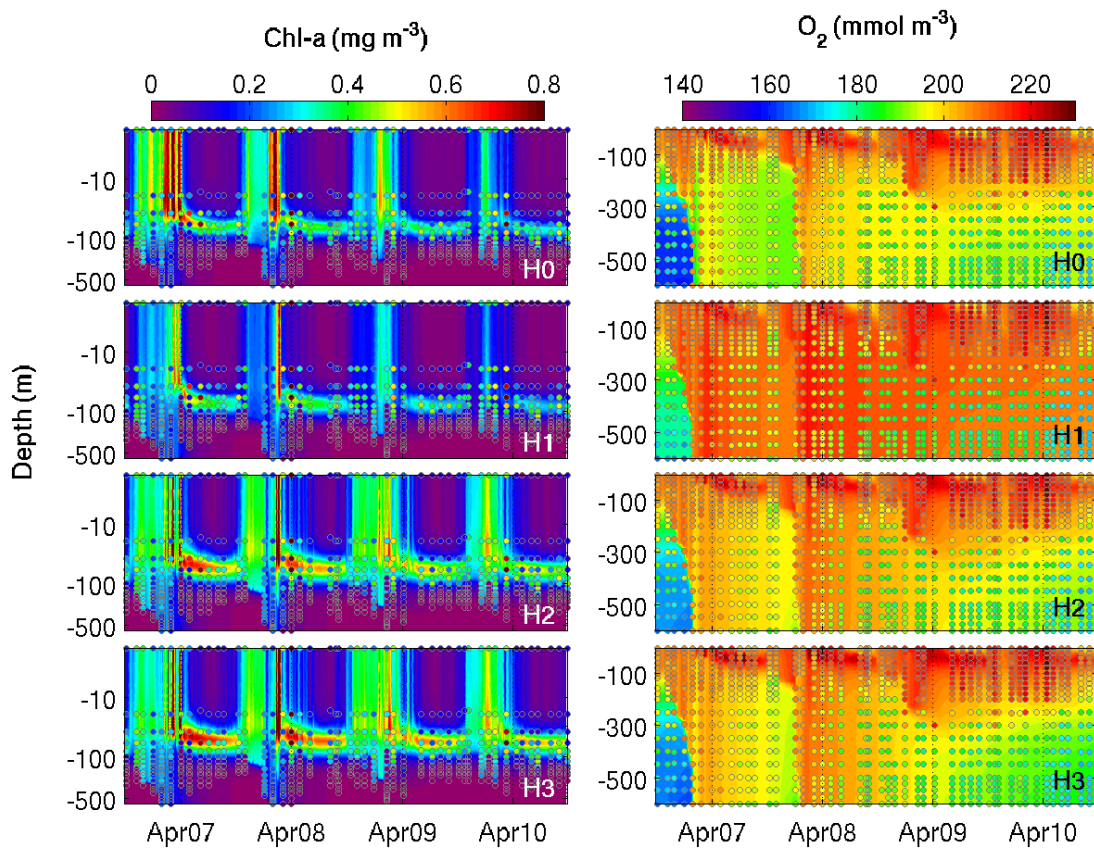


Figure 5.10: Observed (coloured circles) and simulated (background) Chl-a and  $\text{O}_2$  using model versions H0 (no nitrogen fixers), H1 (generic autotrophic fixer), H2 (unicellular and colonial autotrophic fixers), H3 (heterotrophic, and unicellular and colonial autotrophic fixers). Vertical scale in the Chl-a subplots is logarithmic to exaggerate the surface. Horizontal axes start after spin-up period.

Simulated oxygen concentrations exhibit larger differences between models and observations, in particular at mid- and deep waters, where air-sea fluxes do not directly affect oxygen concentrations.

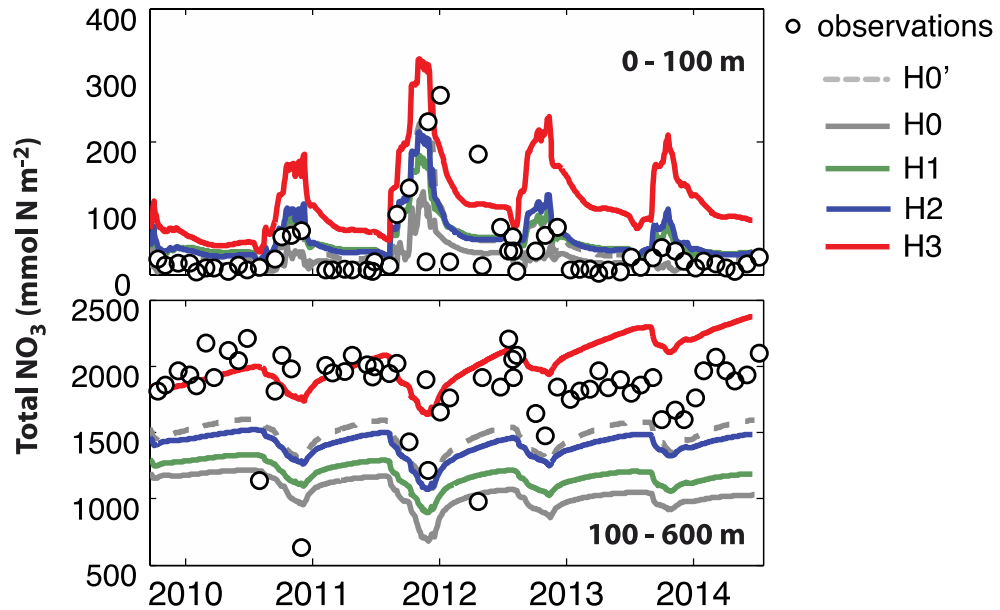


Figure 5.11: Observed (circles) and simulated (lines) total nitrate in the surface and deep-waters during the model validation period from 2010 to 2014.

#### 5.4.2.5 Long-term validation

Observational data from 2010 to 2014 was used to validate the models independently from the information assimilated during the optimization. Table 5.4 shows that, in terms of chlorophyll,  $PO_4$  and surface  $O_2$ , all model versions behave similarly and achieve similar RMSE values against both assimilated and independent observations. As demonstrated in the previous sections, the model versions mainly diverge in their behaviour with respect to  $NO_3$ . Between 0 and 200 m, model version H3 has the largest

RMSE values against NO<sub>3</sub> observations. Nevertheless, below 200 m, model version H3 has the lowest RMSE values, particularly against unassimilated NO<sub>3</sub>. This model behaviour is exemplified in Figure 5.10, which shows observed and simulated total NO<sub>3</sub> at 0 – 200 m and below 200 m for the unassimilated data period. Figure 5.11 shows that, in comparison with the rest of model versions, model version H3 increasingly overestimates surface NO<sub>3</sub> over time. High deep total NO<sub>3</sub> is represented the best by H3, but the minimum annual winter values are not well captured. By the end of the observational series, between 2013 and 2014, H3 starts to also overestimate deep NO<sub>3</sub>.

Table 5.4: Root-mean-square-errors between observations and corresponding simulated variables. Observations between 2005 and 2010 were used during model calibrations (i.e., assimilated). Observations between 2011 and 2014 are used for independent model validations (non-assimilated)

<i>Surface</i>								
	<b>2005 – 2010 (assimilated)</b>				<b>2011 – 2014 (non-assimilated)</b>			
	<b>NO<sub>3</sub></b>	<b>PO<sub>4</sub></b>	<b>CHL</b>	<b>O<sub>2</sub></b>	<b>NO<sub>3</sub></b>	<b>PO<sub>4</sub></b>	<b>CHL</b>	<b>O<sub>2</sub></b>
H0	0.71	0.04	0.15	7.57	0.60	0.04	0.16	6.39
H1	0.77	0.04	0.14	6.99	0.66	0.04	0.15	7.08
H2	<b>0.78</b>	0.04	0.14	6.96	0.75	0.04	0.14	6.66
H3	1.04	0.05	0.14	7.35	1.50	0.05	0.13	6.22
H3a	1.04	0.06	0.12	7.10	1.41	0.09	0.14	6.47
H3b	1.91	0.05	0.14	7.94	2.15	0.05	0.16	8.13
H3c	1.01	0.06	0.12	7.05	1.06	0.08	0.14	6.55
H3d	1.60	0.05	0.19	7.91	1.78	0.05	0.19	8.21
<i>Deep</i>								
	<b>NO<sub>3</sub></b>	<b>PO<sub>4</sub></b>	<b>CHL</b>	<b>O<sub>2</sub></b>	<b>NO<sub>3</sub></b>	<b>PO<sub>4</sub></b>	<b>CHL</b>	<b>O<sub>2</sub></b>
H0	1.53	0.05	0.08	15.54	2.26	0.06	0.06	17.34
H1	1.43	0.05	0.07	15.09	2.02	0.05	0.06	21.70
H2	1.29	0.05	0.07	14.17	1.56	0.04	0.06	17.57
H3	<b>1.05</b>	0.05	0.07	13.28	0.89	0.05	0.06	10.03
H3a	1.12	0.05	0.07	13.42	0.93	0.07	0.06	11.98
H3b	1.26	0.10	0.07	18.29	1.51	0.14	0.06	29.99
H3c	1.14	0.05	0.07	14.37	1.18	0.05	0.06	16.16
H3d	1.41	0.11	0.14	18.39	1.85	0.14	0.13	30.38

#### 5.4.2.6 Primary Production and N<sub>2</sub> Fixation Rates

In order to compare my estimates of primary production with those reported for the Gulf of Aqaba by Rahav et al. (2015), Figure 5.11 shows the average simulated primary production at the same three depth levels used in that study: the DCM, and averages above and below DCM. The depth-resolved discrete in situ primary production rates reported by Iluz et al. (2009) were also averaged at these three levels for comparison.

Simulated primary production above the DCM ranges from 0.02 to 0.85 mmol N m<sup>-3</sup> d<sup>-1</sup>, and exhibits an annual cycle with peaks of productivity in October and April. A prolonged period of low primary production extends from April to September. Model versions H3 and H3a produce higher primary production rates than other versions, while maintaining the same temporal variability. The exceptions to this model behaviour are model versions H3b and H3d, which maintain rates twice as large as the rest of the models during the summer/fall period.

At the DCM and below, simulated primary production rates range from 0 to 0.5 mmol N m<sup>-3</sup> d<sup>-1</sup>. The lowest simulated primary production rates are the ones obtained by version H2, while the base model H0 presents the highest rates during certain periods. Differences between all other models are negligible, and my model rates agree with those measured by Iluz et al. (2009) and Rahav et al. (2015).

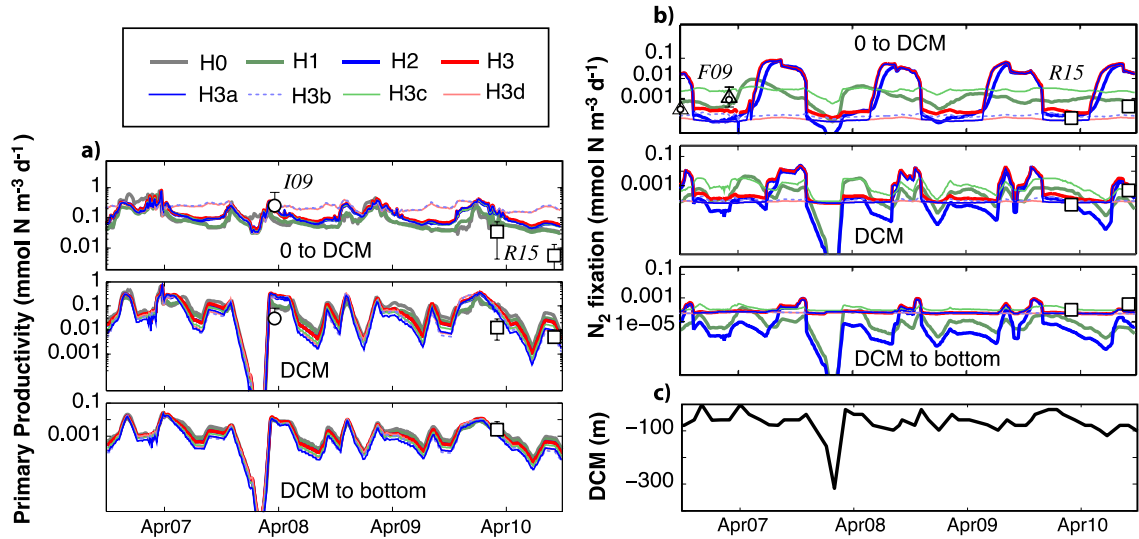


Figure 5.12: Comparison of previously reported in situ measurements and model results of primary production (a) and  $N_2$  fixation rates (b), averaged at three depth levels. Depth levels are from the surface to the Deep Chlorophyll Maximum, at the DCM and below it. (c) DCM estimated from observed Chl-a profiles at station A. I09, F09 and R15 refer to Iluz et al., (2009), Foster et al., (2009), and Rahav et al., (2015), respectively.

I report simulated  $N_2$  fixation rates in a similar fashion as the primary production rates (Figure 5.11b). Above the DCM, models H1, H2, H3 and H3a show a well-defined  $N_2$  fixation peak during summer months (i.e., after the peak in primary production). Maximum rates in these models range between 0.001 to 0.1  $\text{mmol N m}^{-3} \text{d}^{-1}$ . The lowest maximum values are obtained with model H2, whereas the highest values are from models H3 and H3a. Model version H3c only presents peaks in 2007 and 2008, being earlier and of smaller magnitude than the rest of the models. Simulated  $N_2$  fixation rates are low during winter and spring months. The lowest minimum is obtained with model H1 followed by models H3a, H2 and H3. Model versions where autotrophic diazotrophs contribution was minimal or neglected (i.e., H3b and H3d) have nearly constant rates in time. The winter minimum  $N_2$  fixation rates of H3 and H3b have the same magnitude as

the nearly constant rates obtained by model H3b. Similar temporal patterns and differences between model versions occur at the DCM and below it. Peaks in N<sub>2</sub> fixation at these depth levels are delayed from the surface peak, and have a shorter duration and smaller amplitude.

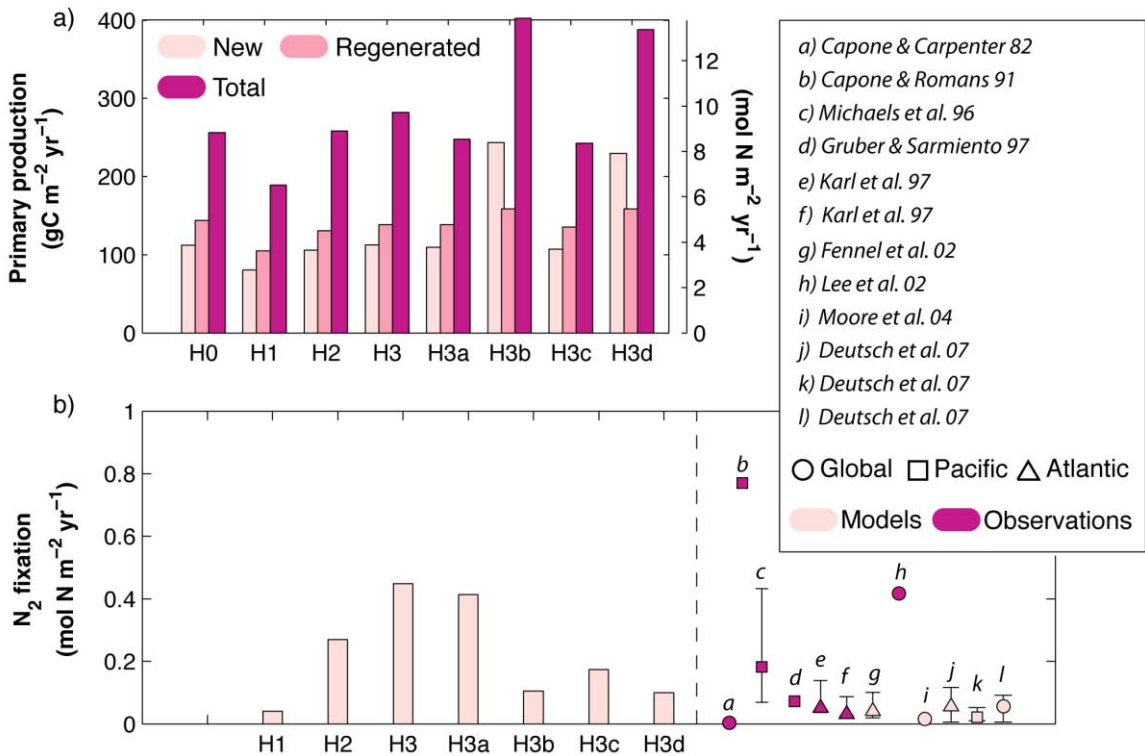


Figure 5.13: Simulated new, regenerated, and total primary production (a) and N<sub>2</sub> fixation rates (b). A summary of previous estimates of N<sub>2</sub> rates in observational and model studies is included in (b).

## 5.5 DISCUSSION

### 5.5.1 IS N<sub>2</sub> FIXATION RELEVANT IN THE GULF OF AQABA?

In this study I tested models with different assumptions about N<sub>2</sub> fixation in the Gulf of Aqaba, ranging from neglecting the process to assuming that heterotrophic N<sub>2</sub>

fixation can occur in the entire water column (i.e., independent of light availability). Despite the fact that the models I tested had very similar abilities to replicate chlorophyll-a, phosphate and oxygen observations, I found significant differences in their success to reproduce the observed pattern of deep-nitrate accumulation. The models' level of performance at replicating vertical nitrate distributions also affected their performance measured against the N\* metric. When I neglect N<sub>2</sub> fixation, excess phosphate tends to dominate the whole water column because nitrate is underestimated. Explicitly accounting for N<sub>2</sub> fixation (H1, H2, H3) improves the model's ability to replicate N\* variability and vertical structure. The best model performance was obtained with two groups of autotrophic organisms and a group of heterotrophic organisms (H3). A model without explicit N<sub>2</sub> fixation, but in the absence of bottom denitrification, also increases the accumulation of deep NO<sub>3</sub> in a similar fashion as version H2. This suggests that N<sub>2</sub> fixation rates at least as high as in H2 are necessary to compensate the effects of bottom denitrification. In my results, the average realized denitrification flux at the bottom is  $0.25 \pm 0.46 \text{ mmol N m}^{-2} \text{ d}^{-1}$ , with a maximum value of  $3.01 \text{ mmol N m}^{-2} \text{ d}^{-1}$ . These values are the lower end of sediment denitrification rates in the literature, which have a mean of  $2.2 \text{ mmol N m}^{-2} \text{ d}^{-1}$  and maximum values exceeding  $10 \text{ mmol N m}^{-2} \text{ d}^{-1}$  (Fennel et al., 2009).

The excess nitrogen observed in the Gulf of Aqaba appears to contrast exterior waters from the Arabian Sea and Indian Ocean, which are considered low oxygen, net nitrogen sink regions (Gruber and Sarmiento, 1997). It has been hypothesized that limited deep-water exchange at Bab-el-Mandeb allows waters of the Red Sea outside of the Gulf of Aqaba to acquire characteristics different from the Arabian Sea inflowing waters

(Naqvi et al 1986). My model results support this hypothesis and suggest that  $N_2$  fixation is key for the formation of the distinct chemical characteristics of Gulf of Aqaba waters, which retain only a negligible resemblance to the reported patterns of the exterior waters.

There are only few reported dissolved inorganic nitrogen-to-phosphorus ratios for the Red Sea region from Bab-el-Mandeb to the Strait of Tiran to provide a complete idea of the spatial distribution of  $N^*$ ; however the available information supports my conclusions. Naqvi et al. (1986) data shows excess nitrogen in the order of  $N^* = +2.5 \text{ mmol m}^{-3}$  in sub-surface waters outflowing at the Bab-el-Mandeb towards the Arabian Sea (reported as N:P ratios of  $\sim 20$ ). These studies posited that  $N_2$  fixation is a process required to account for the anomalies in the nitrogen budget between incoming and outgoing waters at Bab-el-Mandeb. The Red Sea  $N^*$  values are significantly higher than those of the Arabian Sea and Indian Ocean, where a strong deficit of nitrogen develops as losses due to denitrification exceed the input of newly fixed nitrogen (Gruber and Sarmiento, 1997; Morrison et al 1998, 1999; Naqvi, 1994; Burkill et al., 1993). Close to the entrance of the Persian Gulf,  $N^*$  values are below  $-5 \text{ mmol m}^{-3}$  at all depths and seasons reported, with minimum excess phosphate values in the order of  $N^* = -8 \text{ mmol m}^{-3}$  (Gruber and Sarmiento, 1997).

The lowest negative  $N^*$  values observed in surface waters in the Gulf of Aqaba during summer are not fully captured by any of my model versions; however this is not a source of large data-model discrepancies. In the context of a one-dimensional framework, I cannot reject the possibility that these minimum  $N^*$  values are a remnant signal of denitrification in the distant Arabian Sea. During their passage through the Red Sea,  $N_2$  fixation may be responsible of transforming waters with significant excess phosphorus

into these summer surface waters with small negative  $N^*$  deviations. If we consider the global average correction to  $N^*$  values of  $+2.89 \mu\text{mol kg}^{-1}$  used by Gruber and Sarmiento (1997),  $N^*$  values in the Gulf of Aqaba hold a permanent excess of nitrate with respect to other geographical regions. Similarly, the overestimation of surface  $\text{NO}_3$  obtained with the model that performs the best for deep  $\text{NO}_3$  suggests that the Gulf has potential to export newly fixed nitrogen to the outside waters through horizontal advection in the surface to mid-water layers. This was not tested within our one-dimensional model. Based on my model results in the context of the regional characteristics, I consider that  $\text{N}_2$  fixation is a necessary input of new nitrogen to explain positive  $N^*$  values in the Gulf of Aqaba, and the interannual accumulation of deep nitrate during years with weak convection.

#### 5.5.2 HOW DOES $\text{N}_2$ FIXATION CONTRIBUTE TO PRIMARY PRODUCTION?

In this section I discuss the contribution of  $\text{N}_2$  fixation to primary production in the Gulf of Aqaba, and my quantitative estimates of  $\text{N}_2$  fixation with respect to previously published global rates (Figures 5.12 and 5.13). My estimates of surface primary productivity agree with those reported by Iluz et al. (2009) for March-April of 2008. However, my models overestimate surface primary productivity values in 2010, compared to those reported by Rahav et al. (2015). On average, model versions that perform the best in terms of nutrient distributions estimated annual primary production rates of  $304 \pm 56.9 \text{ g C m}^{-2} \text{ yr}^{-1}$  (H3) and  $277 \pm 82.5 \text{ g C m}^{-2} \text{ yr}^{-1}$  (H3a). These rates are higher than previously published observational annual averages, which range from  $80 \text{ g C m}^{-2} \text{ yr}^{-1}$  (Levanon-Spanier et al. 1979; Iluz 1991) to  $170 \text{ g C m}^{-2} \text{ yr}^{-1}$  (Lazar et al. 2008).

The proportion of new production to total primary production (i.e., the f-ratio) in my experiments suggests that new production contributes from 15% to 80% of total production. Maximum f-ratios are estimated for winter months of January and February due to significant contributions from deep  $\text{NO}_3$ , whereas minimum f-ratios occurred during stratified conditions (June – August). My best performing model version, H3, estimates a summer minimum f-ratio 0.22. That is, about 22% of the primary production during summer is sustained by external sources of nitrogen. On average for all scenarios, I estimate that new production represents about 47% of the total annual production in the Gulf of Aqaba. This agrees with published estimates for the Gulf, which report that during the stratified period new production contributes about 50% of total production, as determined from a nitrate-diffusion model yielding an f-ratio of 0.5 (Badran et al. 2005).

Annual  $\text{N}_2$  fixation rate estimates from my best performing model versions (H3 and H3a) are skewed towards the highest estimates reported in the literature (Capone and Carpenter, 1982; Michaels et al., 1996; Lee et al., 2002), while those obtained by the rest of experiments agree with the complete range of values reported. Based on the best performing model version (H3) I estimate that 10% to 14% of the total primary production is related to  $\text{N}_2$  fixation.

### 5.5.3 ARE DIFFERENT DIAZOTROPHIC GROUPS IMPORTANT?

Colonial diazotroph blooms are responsible for the highest  $\text{N}_2$  fixation rates in my models, and thus are an important aspect of the model behaviour necessary to achieve resemblance with the observed  $\text{N}^*$  patterns. This result agrees with the conclusion that extensive blooms of *Trichodesmium spp.* are dominantly responsible for the high  $\text{N}_2$

fixation rates observed in the Arabian Sea and Red Sea (Capone et al., 1998; Post et al., 2002; Foster et al., 2009). Blooms of *T. erythraeum* and *T. thiebautii* have also been documented specifically in the Gulf of Aqaba, near the coast of Eilat (Kimor and Golandsky, 1977; Gordon et al., 1994; Post et al., 2002). At a global scale, it has been estimated that the latitudinal pattern of N<sub>2</sub> fixation overall coincides with the observed biogeography of *Trichodesmium spp.* (Deutsch et al., 2007).

My results, thus, agree with previous conclusions that *Trichodesmium* is one of the main contributors to global marine N<sub>2</sub> fixation. Surface N<sub>2</sub> fixation rates during the simulated colonial diazotrophs blooms are as high as 0.1 mmol N m<sup>-3</sup> d<sup>-1</sup>, which exceeds the maximum documented rates in the Gulf of Aqaba. Within my study period, studies using the <sup>15</sup>N<sub>2</sub> assimilation technique reported rates ranging from undetectable to a maximum of 1.9 nmol N L<sup>-1</sup> d<sup>-1</sup> (1.9 x 10<sup>-3</sup> mmol N m<sup>-3</sup> d<sup>-1</sup>; Foster et al., 2009; Rahav et al., 2013b). My models also estimate transient N<sub>2</sub> fixation rates higher than 1x10<sup>-3</sup> mmol N m<sup>-3</sup> d<sup>-1</sup> at 100 m, associated with the surface blooms. This agrees with reports of abundance of puff-shaped colonies and free trichomes up to 100 m (Post et al., 2002).

Here, the generic diazotroph group (introduced in H2) also exhibits blooming behaviour; however, N<sub>2</sub> fixation increases earlier in the year, and the maximum magnitudes are lower than those of the colonial group. Differences between H2 and H3 are related to resource competition of colonial and unicellular diazotrophs in the latter as well as to different assumptions about mortality pathways (see Appendix II). Minimum N<sub>2</sub> fixation rates are also the lowest among all models when only a generic diazotroph group is considered. In model version H2, unicellular diazotrophs set the minimum N<sub>2</sub> fixation rates. Grazers rapidly match unicellular growth, causing the low biomass of this

group; consequently, this group does not account for large contributions to the total N<sub>2</sub> fixation rates in my simulations.

In my approach, I assigned the same growth parameters to both the colonial and unicellular autotrophic diazotroph groups. This was decided to test mechanistic assumptions, rather than obtaining differences between groups due to parameter selection. It is possible that changes in the parameters of unicellular organisms may render a higher contribution of this group to total fixed nitrogen. *In situ* measurements of N<sub>2</sub> fixation by the small planktonic size fraction (<10 μm) in the Pacific Ocean range from measurable but low (Dore et al., 2002; Falcón et al., 2004) to high rates comparable to those of *Trichodesmium spp.* (Montoya et al., 2004). Unicellular diazotrophic organisms have different thermal ranges than those of *Trichodesmium spp.* (Moisander et al., 2010), and thus including both of these autotrophic groups or calibrating the generic autotrophic group in such a way that represents unicellular and colonial cyanobacteria simultaneously should be considered at global scale.

My model version H3 relaxes the assumption of light dependency for diazotrophy, through the inclusion of heterotrophic diazotrophs in addition to two groups of autotrophic diazotrophs. This model simulates the closest estimates of dissolved inorganic nutrients and oxygen compared to the observations. A good estimate can also be obtained in the absence of unicellular organisms (H3a). All model versions with heterotrophic organisms (H3a – H3d) are also able to match the order of magnitude of observational estimates of N<sub>2</sub> fixation in deep waters of the Gulf of Aqaba. Without heterotrophic N<sub>2</sub> fixation, N<sub>2</sub> fixation rates below the DCM are underestimated. Light independence contrasts with assumptions previously followed by models including diazotrophic

organisms (e.g., Hood et al., 2001; Fennel et al., 2002; Monteiro et al., 2010; Moore et al., 2004). This has been generally based on culture experiments showing that marine diazotrophs have high light requirements, and inhibited activity at low light level, therefore suggesting an adaptation to high light environments (Carpenter and Roenneberg 1995, Masotti et al 2007; Goebel et al 2008). Heterotrophic N<sub>2</sub> fixation previously remained elusive because measurements of N<sub>2</sub> fixation activity in the small plankton fraction cannot differentiate the contributions of unicellular autotrophs and bacterioplankton (Zehr et al. 2001; Montoya et al. 2004). Nevertheless, nocturnal N<sub>2</sub> fixation has been reported for this small plankton fraction (Montoya, 2004). Diazotrophy independence from light has also been suggested to explain the similarity of <sup>15</sup>N<sub>2</sub> fixation rates measured in parallel light and dark in situ incubations, as well as N<sub>2</sub> fixation rates in the absence of detectable chlorophyll in the South Pacific Gyre (Halm et al 2011). My results also agree with genetic evidence from the Gulf of Aqaba reporting the existence of heterotrophic proteobacteria  $\alpha$  and  $\gamma$  (Rahav et al., 2013; 2015), and the correlation of bacterial productivity rates with N<sub>2</sub> fixation rates (Rahav et al., 2013).

My different model versions provide insights in the effect of competition among diazotrophic organisms, although results are not completely intuitive. For instance, when there are fewer competitors for the phosphorus resources, N\* becomes skewed towards excess of nitrogen, but neither NO<sub>3</sub> nor PO<sub>4</sub> reach their maximum concentrations (Figure 5.9). This is a result of abundant nitrate and ammonium in mid-waters, and depleted phosphate throughout the whole water column. In general, my results suggest that including at least one autotrophic and one heterotrophic diazotroph group is necessary to

allow for sufficient model flexibility to capture surface and deep-water biochemical variations.

#### 5.5.4 LIMITATIONS AND UNCERTAINTIES

The one-dimensional nature of my physical setting, which neglects horizontal advection contributions to the vertical structure of simulated tracers, can be considered a limitation of this study. This simplification is, however, necessary to perform model calibration and testing multiple model structures at low computational expense. One-dimensional models are frequently used for plankton models, as it is assumed that the temporal scale of biological processes is faster than that of horizontal advection. As I applied temperature and salinity nudging to improve the representation of the density structure, I support my results by analyzing such structure with and without nudging. Results of this experiment show that correcting the temperature and salinity fields has negligible effect on deep waters, where the effect of  $N_2$  is the most relevant. This result agrees with the literature about circulation of the Gulf of Aqaba. As mentioned in the description of the study region, geomorphology and bathymetry limit water flux exchange between the Gulf of Aqaba and the Red Sea to the upper 300 m. Wolf-Vect et al., (1992) explains that the inflow at the Strait of Tiran has minimal effect on the thermal structure, possibly warming the upper layer a few weeks earlier in the summer. It this, therefore, unlikely that horizontal transport could explain the observed accumulation in deep  $NO_3$ . Nitrogen inputs from run-off are also unlikely, as evaporation rates are high (Ben-Sasson et al 2009).

In terms of the biological models themselves, an intrinsic limitation of all functional type numerical models is the uncertainty associated with parameter values (Denman et al., 2003). In my approach, I reduced this uncertainty with the use of parameter optimization. My methodology allowed for a more systematic selection of model parameter values and more objective comparison of different model structures, thus being preferable to subjective tuning. Nonetheless, parameters related to diazotrophic organisms are unconstrained by the observations. I followed observational and laboratory literature to assign these parameter values. It has to be highlighted that specific growth rates and other parameters estimated for individual species in isolation, or at selected locations and/or seasons, will not necessarily apply to in situ communities or to the aggregated functional groups that model simulate. Model assumptions about diazotrophs limitations and their parameter values likely influence the resulting behaviour of each group. Given these uncertainties, I opted for teasing apart the effects of mechanistic assumptions rather than modifying diazotrophs behaviour through the parameter values. The latter can certainly affect the contribution of each group to total  $N_2$  fixation rates; however it does not affect my conclusions with respect to the amount of  $N_2$  fixation necessary to better replicate chemical characteristics of deep waters at Station A. For example, as *Trichodesmium* spp. dominated  $N_2$  fixation in the euphotic zone, its parameters could be changed to decrease maximum surface values closer to the observational estimates. After this modification, an increase in the model  $N_2$  fixation rates by heterotrophic organisms may be required in order to match the deep dissolved inorganic nutrients. Depth-resolved, high temporal resolution in situ  $N_2$  fixation and primary production rates are necessary to better validate the behaviour of these different diazotrophic groups, by providing information to differentiate patterns of photic and

aphotic  $N_2$  fixation. Contributions of other complex symbiosis to  $N_2$  fixation remain uncertain, including diatom-diazotrophs associations, and aphotic  $N_2$  fixation by bacteria living on and inside of organisms such as copepods and benthic invertebrates (Braun et al., 1999; Harris, 1993; Zehr et al., 2000, 1998; Zehr and Capone, 1996). Pico- and nanophytoplankton dominate the Gulf of Aqaba primary producers throughout the year (Post et al., 2002; Foster et al., 2009), thus I did not test diatom-diazotrophs associations.

## **5.6 CONCLUSIONS**

My model results demonstrate the importance of  $N_2$  fixation in determining deep  $NO_3$  inventories. In the Gulf of Aqaba,  $N_2$  fixation allows its waters to develop a signature deep excess of nitrate. A model without a  $N_2$  fixation flux is challenged to replicate the observed vertical structure of inorganic nitrogen and phosphorus. Models that include diazotrophic organisms have the ability to significantly modify these variables. New nitrogen inputs from  $N_2$  fixation increase the fraction of remineralized nitrogen from organic matter decomposition, and are thus a plausible mechanism to explain biochemical characteristics at this location, and their contrast with exterior waters that show excess phosphate.

The simulated amount of  $N_2$  fixation required to replicate the observations in the Gulf of Aqaba is in line with the highest observational estimates of this flux. While aphotic  $N_2$  fixation rates are low, considering heterotrophic organisms allows more flexibility in replicating rates observed at depth, without an unrealistic increase in light-dependent  $N_2$  fixation. Overall, my results add to the body of evidence suggesting that the importance of  $N_2$  fixation may be globally underestimated (Karl et al., 2002).

The scarcity of measurements hinders model validation abilities, in particular to differentiate the contributions of autotrophic and heterotrophic diazotrophs. It is possible that observations have overlooked many diazotrophs as a result of the methodological and technical limitations of detecting low-abundance organisms and complex symbioses in oligotrophic waters (Zehr et al., 2000). Given the present observational and modelling limitations, the interpretation of these models results should be refined as new observational information becomes available.

## CHAPTER 6:

### CONCLUSIONS

My thesis was motivated by the need to revise key ecological paradigms that impact the estimates of marine primary production, taking into account the uncertainties related to observational and modelling data. Primary production estimates have important implications for short- and long-term predictions of higher trophic level production affecting commercial fisheries, as well as species of ecological and conservational interest. Moreover, the effects of marine primary production on long-term climate feedbacks are still under scrutiny. I carried out three case studies aimed at gaining insights about ecosystem processes that remain uncertain, mainly due to paucity of observational data. In particular, I investigated drivers of phytoplankton phenology in the North Atlantic Ocean, the effect of model complexity on regional estimates of primary production in northwest North Atlantic shelf seas, and the importance of different planktonic diazotroph traits in determining seawater chemical characteristics and sustaining primary production in the Gulf of Aqaba. In the context of these research topics, I outlined different approaches to use optimized biogeochemical models as hypothesis-testing tools aimed at improving our understanding of ecosystem functioning. My work included the development, calibration, and analysis of multiple marine biogeochemical models of low and intermediate complexity, in 1D and 3D ocean applications. I performed systematic model calibrations using an evolutionary algorithm with cost functions tailored to data availability and scientific objectives of each research topic. I also designed and tested idealized model experiments, model geographical portability experiments, and parameter sensitivity analyses. In the analysis of observations, optimized parameters and optimized model results, I used statistical techniques including correlation analysis, principal component analysis, Taylor series expansions, hierarchical clustering, and common statistical error metrics.

The outcomes of this work fall in three categories: i) model development, ii) insights into ecosystem modelling philosophy, and iii) insights into marine ecology. The model development category refers to the most basic outcome, which is the refinement of biogeochemical models to better fit available observations from the Subpolar North Atlantic Ocean, the coastal northwest North Atlantic, and the Gulf of Aqaba. The other two outcomes categories directly concern the results presented in chapters 2 to 5. I expand on the conclusions from these studies in the followings sub-sections.

## **6.1 INSIGHTS INTO ECOSYSTEM MODELLING PHILOSOPHY**

Throughout this thesis, I illustrated how parameter optimization methods offer a systematic approach for reducing subjective model tuning. This approach allows for testing of hypotheses about ecosystem functioning by quantitatively comparing ecosystem models under different assumptions (i.e., idealized experiments and/or additional levels of complexity). My results highlight that subjectivity is involved in parameter optimization, and demonstrate that the design of the optimization cost function, the selection of parameters to be optimized, the degree of preliminary calibration of a model, and the forcing environmental conditions all affect the conclusions about a model's accuracy and geographical portability.

I followed two main approaches in using parameter optimization for ecological hypothesis testing. The first approach is the comparison of an optimized model against un-optimized experimental tests. This type of approach implicitly assumes that the optimized model is an accurate representation of the natural environment, and behaves like it under perturbed conditions. This is the approach used when performing post-optimization sensitivity analyses, idealized experiments and geographical portability experiments (Chapter 2, Chapter 3 and Chapter 5). This approach is useful for determining whether or not the simulated system is

sensitive to certain parameters, variables and/or additional processes introducing changes to the model dynamics. However, it does not provide information about whether a different and/or improved model solution, with respect to the observations, could be reached under such perturbed conditions or new model dynamics.

The second approach attempts to perform objective comparisons between models with different structures, by applying the same optimization procedures to reduce model-observation misfits (Chapter 3 and Chapter 4). This approach is useful for identifying processes that are strongly influenced by differences in model structures, or model aspects that are unconstrained during the optimization. Finally, I used a combination of both of these approaches in Chapter 5, by optimizing a large number of parameters in the simplest of the model structures tested, and recalibrating only a few highly sensitive and well-constrained parameters after adding additional processes to the model. This combined approach provides insight into how well a simple model can replicate observations, and tests how far model performance can be improved when adding complexity.

My results highlight that a guided selection of the parameters to be optimized is essential, especially when little or no prior model tuning has been performed. This is particularly important for models with a high number of variables and with parameters that are unconstrained by the observations, as demonstrated in Chapters 3 and 4. Attempting to optimize an unfortunate selection of parameters can result in the extinction of certain plankton groups, thus generating unintended prey-predator relationships in models with high trophic complexity. The novel use of satellite-derived estimates of size-fractionated surface chlorophyll, as observational counterparts of the simulated chlorophyll concentrations in a model with multiple phytoplankton groups, was not sufficient to obtain traditionally known patterns of phytoplankton community seasonal succession. In fact, the optimization estimated similar phytoplankton growth parameter values for

the two autotrophic planktonic groups in this model, and differences among groups were mostly determined by their predefined interactions with grazers.

My use of satellite-derived models of size-fractionated surface chlorophyll for the optimization also impacted conclusions about the multiple preys and predators model's geographical portability. When calibrated for multiple geographical locations, this model was the best performing model when compared against assimilated and unassimilated observations, but it was prone to becoming overspecialized when calibrated for specific locations. This occurred because the parameters optimized at some locations tended to favor either small or large phytoplankton. This result is consistent with early theoretical notions about the expected behavior of complex models, however opposed to portability experiments previously performed in other ocean regions. Therefore, my results suggest that in order to benefit from the improved ecosystem representation that an optimized complex model provides, such model needs to be trained with observations from diverse geographical locations, and include theoretical *a priori* considerations to scale the parameters of multiple plankton groups. My results also show that the spatial representations of surface chlorophyll in regional models can benefit from simple additional mechanistic relationships, such as configuring all biological fluxes to depend on temperature. Based on this result, and taking into account parsimony principles, I suggest that improving the mechanistic relationships, rather than adding unconstrained diversity, can lead to more robust globally applicable models. These mechanistic relationships may include relationships between environmental variables and plankton growth, dynamic parameterizations of grazing, as well as allometric relationships. Nevertheless, in the absence of such improved relationships, certain regional models require additional processes in order to fully capture the observed biogeochemical variability. This was illustrated in Chapters 3 and 4, where a model with multiple planktonic prey and predator groups provided the best chlorophyll concentrations and annual primary production estimates in the oceanographically complex northwest North Atlantic. It was

also the case in Chapter 5, where specialized planktonic groups were needed to replicate deep inorganic nitrogen in the Gulf of Aqaba.

I also documented that there are common characteristics of model behavior that are independent from the model's ecological complexity and physical dimensionality. For example, phytoplankton growth parameters are involved in determining the timing of the spring bloom peak. This was reiterated in the results from the simple NPZD model used in the Subpolar North Atlantic case study, as well as in the intermediate complexity models used in the coastal northwest North Atlantic case study. In the latter, this behavior was evidenced in both the 1D and 3D model applications. Principal component analyses of the parameters optimized at specific geographical locations for these two North Atlantic case studies also revealed multi-dimensional correlations between the parameters selected for certain locations. In the Subpolar North Atlantic case, the spatial patterns show a clear differentiation between northern and southern areas. Spatial patterns in optimized parameters are not as clear in the coastal northwest North Atlantic, but a number of locations tended to select either high or low grazing values consistently, and independently of model complexity.

## **6.2 INSIGHTS INTO MARINE ECOLOGY**

My optimized and experimental results demonstrate that phytoplankton phenology in mid-latitude regions, such as the North Atlantic Ocean, is a continuum of bottom-up and top-down process dominating during different periods of the annual cycle. When contrasting a bottom-up and a top-down hypothesis for the spring bloom initiation (i.e., the critical-depth and the dilution-recoupling hypotheses, respectively), my results demonstrated that the conceptual basis of each is an ecological truism that cannot be considered in absolute isolation under realistic simulations. Idealized experiments with a simple model, and the comparison of models with

different trophic complexity show that the development, peak and early stages of the termination of the phytoplankton spring bloom are dominantly driven by bottom-up factors.

My results also show that a model's trophic complexity can strongly affect simulated biogeochemical fluxes during summer and fall. In a model with multiple prey and predator groups, the flexibility of the phytoplankton natural mortality and predation rates plays a role in modifying the velocity and time phase of nitrogen return from the organic to the inorganic pool. My results suggest that the pathways of zooplankton losses act as an important dynamic driver during low phytoplankton biomass periods. These periods coincide with elevated sea temperatures in summer; therefore the effect of thermal dependency on phytoplankton losses becomes important in defining chlorophyll spatial patterns. Nevertheless, temperature-dependent phytoplankton losses have only a limited effect on plankton standing stocks and primary production estimates.

Therefore, bottom-up and top-down ecological drivers control the imbalances between phytoplankton growth and its loss rates, which lead to the phenological characteristics observed in a given geographical region. My experimental results highlight that the variability in what triggers the spring bloom initiation depends on the system's baseline conditions at the end of the preceding year. In different regions or years, bloom development may closely track the last of any necessary conditions for bloom initiation that remains unsatisfied, including appropriate levels of nutrient or light availability and of grazing pressure. In the case of the North Atlantic, nutrients are abundant and predators' biomass is low at the end of winter. Hence, seasonal changes in the light environment are the main driver of the spring bloom initiation in this area. Spatial differences in winter vertical stratification can be associated with differences in spring bloom timing, as demonstrated by the areas of early spring blooms and shallow mixed layer depths in the northwest North Atlantic. This spatial pattern agrees with the canonical bottom-up effect of a

shallowing mixed layer on light conditions that phytoplankton experience, by concentrating them in well-lighted zones of the ocean.

Adequate representations of temperature, vertical stratification and deep-water nutrient concentrations are essential to avoid using the optimization to compensate for physical deficiencies in the model. In the North Atlantic case studies, deep nutrient concentrations were configured based on global climatologies. Due to the geomorphological and bathymetric characteristics of the Gulf of Aqaba, which limit deep-water exchange with the exterior, this location offered unique conditions for evaluating the importance of microbially mediated nitrogen fixation in the determination of deep-water nutrients.

My results suggest that nitrogen fixation allows waters of this northern extension of the Red Sea to develop a signature of nitrogen excess at depth, which contrasts with the exterior excess phosphate waters. Models that include diazotrophic organisms have the ability to significantly modify the vertical distribution of inorganic nitrogen, but it is important to highlight that a model without nitrogen fixation still can replicate chlorophyll variability with similar accuracy as the models with nitrogen fixation.

Nitrogen fixation activity increases the fraction of remineralized nitrogen from organic matter decomposition, and is thus a plausible mechanism to explain biochemical characteristics in the Gulf of Aqaba. I estimated that nitrogen fixation rates required to replicate the deep-water nitrate observations at this location are relatively high compared to previous observational estimates. My results agree with studies suggesting that the importance of  $N_2$  fixation may be globally underestimated. I also estimated that considering aphotic nitrogen fixation was important to increase the flexibility of a model, and allow it to replicate nitrogen fixation rates observed at depth, without unrealistically increasing light-dependent surface nitrogen fixation.

## 6.3 SUMMARY

The main findings of this thesis can be summarized as follows:

- The selection of an appropriate level of ecosystem model complexity and design of the model calibration is tied to the research questions to be addressed.
- Components of the ecosystem dynamics that are well constrained by the observations during model calibration can be similarly replicated by models with different complexities.
- Simplified trophic dynamics can be as suitable as more complex models for diagnosing some biogeochemical cycles at single locations, at seasonal scales or in areas with homogenous environmental conditions.
- Bottom-up drivers, such as light and nutrient availability, control the onset, peak and early stages of the phytoplankton spring bloom. The variability of vertical stratification is important to set light and nutrient conditions both at temporal and spatial scales. Top-down drivers control summer and fall phytoplankton concentrations, and impact nutrient cycling and export production.
- The inclusion of planktonic diversity and/or specific planktonic traits is necessary to explain biogeochemical characteristics at certain geographical locations. This is the case in the oceanographically complex northwest North Atlantic, where observed summer to fall chlorophyll concentrations and annual primary production is replicated the best by a model with multiple phytoplankton and zooplankton groups. It is also the case in the Gulf of Aqaba, where nitrogen fixation throughout the entire water column is important in determining deep-water nitrate concentrations.
- There is a significant gap of knowledge with respect to phytoplankton metabolism, natural mortality and predation. This hinders the understanding of

feedback effects from predator-prey relationships over biogeochemical interannual variability and regime changes, as well as definitive conclusions about the importance of complexity in ecosystem models.

- There is also a significant gap of knowledge about the contributions of autotrophic and heterotrophic diazotrophs to total rates of nitrogen fixation, both locally and globally.

- Due to data limitations, un-guided parameter optimization is not an infallible method for identifying the best parameters in the high-dimensional parameter space of complex models.

Despite the regional scope of the case studies I carried out, my conclusions provide insights that can be extrapolated to large-scale applications. My work also suggests potential future research directions, including the assessment of efficient sampling methodologies for calibrating global model surrogates, the evaluation of twin experiments assimilating all state variables using synthetic model data, and the use of optimization experiments to replicate controlled laboratory and mesocosm experiments. Finding common patterns of behavior in simple and complex models, which can reach similar conclusions about the ecosystem dynamics, is fundamental to reduce the uncertainties of future predictions.

## BIBLIOGRAPHY

- Aita, M.N., Yamanaka, Y., Kishi, M., 2007. Interdecadal variation of the lower trophic ecosystem in the northern Pacific between 1948 and 2002, in a 3-D implementation of the NEMURO model. *Ecol. Model.* 202, 81–94.
- Anderson, Thomas R. 2005. “Plankton Functional Type Modelling: Running before We Can Walk?” *Journal of Plankton Research* 27 (11): 1073–81.
- Anderson, T.R., Gentleman, W.C., Sinha, B., 2010. Influence of grazing formulations on the emergent properties of a complex ecosystem model in a global ocean general circulation model. *Prog. Oceanogr.* 87, 201–213.
- Arhonditsis, George B., and Michael T. Brett. 2004. “Evaluation of the Current State of Mechanistic Aquatic Biogeochemical Modelling.” *Mar. Ecol. Prog. Ser.* 271: 13–26.
- Armstrong, R.A., Lee, C., Hedges, J.I., Honjo, S., Wakeham, S.G., 2001. A new, mechanistic model for organic carbon fluxes in the ocean based on the quantitative association of POC with ballast minerals. *Deep Sea Res. Part II Top. Stud. Oceanogr.* 49, 219–236.
- Backhaus, J.O., Hegseth, E.N., Wehde, H., Irigoien, X., Hattern, K., Logemann, K., 2003. Convection and primary production in winter. *Mar. Ecol. Prog. Ser.* 251, 1–14.
- Badran, M.I., Rasheed, M., Manasrah, R., Al-Najjar, T., 2005. Nutrient flux fuels the summer primary productivity in the oligotrophic waters of the Gulf of Aqaba, Red Sea. *Oceanologia* 47.
- Bagniewski, W., Fennel, K., Perry, M.J., D’Asaro, E., 2011. Optimizing models of the North Atlantic spring bloom using physical, chemical and bio-optical observations from a Lagrangian float. *Biogeosciences* 8, 1291–1307. doi:10.5194/bg-8-1291-2011
- Banse, K., 1994. Grazing and zooplankton production as key controls of phytoplankton production in the open ocean. *Oceanography* 7, 13–20.
- Behrenfeld, M.J., Falkowski, P.G., 1997. Photosynthetic rates derived from satellite-based chlorophyll concentration. *Limnol. Oceanogr.* 42, 1–20.
- Behrenfeld, M.J., Boss, E., Siegel, D.A., Shea, D.M., 2005. Carbon-based ocean productivity and phytoplankton physiology from space. *Glob. Biogeochem. Cycles* 19.
- Behrenfeld, M.J., 2010. Abandoning Sverdrup’s critical depth hypothesis on phytoplankton blooms. *Ecology* 91, 977–989.

- Behrenfeld, M.J., Doney, S.C., Lima, I., Boss, E., Siegel, D.A., 2013. Annual cycles of ecological disturbance and recovery underlying the subarctic Atlantic spring plankton bloom. *Glob. Biogeochem. Cycles* 27, 526–540. doi:10.1002/gbc.20050.
- Ben-Sasson, M., Brenner, S., Paldor, N., 2009. Estimating air–sea heat fluxes in semienclosed basins: The case of the Gulf of Elat (Aqaba). *J. Phys. Oceanogr.* 39, 185–202.
- Berman-Frank, I., Cullen, J.T., Shaked, Y., Sherrell, R.M., Falkowski, P.G., 2001. Iron availability, cellular iron quotas, and nitrogen fixation in *Trichodesmium*. *Limnol. Oceanogr.* 46, 1249–1260.
- Berman, T., Paldor, N., Brenner, S., 2003. The seasonality of tidal circulation in the Gulf of Elat. *Isr. J. Earth Sci.* 52.
- Berman, T., Paldor, N., Brenner, S., 2000. Simulation of wind-driven circulation in the Gulf of Elat (Aqaba). *J. Mar. Syst.* 26, 349–365. doi:10.1016/S0924-7963(00)00045-2
- Bianucci, L., Fennel, K., Chabot, D., Shackell, N., Lavoie, N., 2015. Ocean biogeochemical models as management tools: a case study for Atlantic wolfish and declining oxygen. *ICES J. Mar. Sci.* 73, 263–274. doi:10.1093/icesjms/fsv220
- Bisset, W.P., Walsh, J.J., Dieterle, D.A., Carder, K.L., 1999. Carbon cycling in the upper waters of the Sargasso Sea: I. Numerical simulation of differential carbon and nitrogen fluxes. *Deep-Sea Res. I* 46, 205–269.
- Biton, E., Silverman, J., Gildor, H., 2008. Observations and modeling of a pulsating density current. *Geophys. Res. Lett.* 35.
- Boyd, P.W., Strzepek, R., Fu, F., Hutchins, D.A., others, 2010. Environmental control of open-ocean phytoplankton groups: Now and in the future. *Limnol. Oceanogr.* 55, 1353.
- Bopp, L., Aumont, O., Cadule, P., Alvain, S., Gehlen, M., 2005. Response of diatoms distribution to global warming and potential implications: A global model study. *Geophys. Res. Lett.* 32, 1–4.
- Bopp, Laurent, L. Resplandy, James C. Orr, Scott C. Doney, John P. Dunne, M. Gehlen, P. Halloran, et al. 2013. “Multiple Stressors of Ocean Ecosystems in the 21st Century: Projections with CMIP5 Models.” *Biogeosciences* 10: 6225–6245.
- Boss, E., Behrenfeld, M.J., 2010. In situ evaluation of the initiation of the North Atlantic phytoplankton bloom. *Geophys. Res. Lett.* 37.
- Brainerd, K.E., Gregg, M.C., 1995. Surface mixed and mixing layer depths. *Deep-Sea Res. I* 42, 1521–1543.
- Bratbak, G., Egge, J.K., Heldal, M., 1993. Viral mortality of the marine alga *Emiliania huxleyi* (Haptophyceae) and termination of algal blooms. *Mar. Ecol. Prog. Ser.*

- Braun, S.T., Proctor, L.M., Zani, S., Mellon, M.T., Zehr, J.P., 1999. Molecular evidence for zooplankton associated nitrogen-fixing anaerobes based on amplification of *nifH* gene. *FEMS Microbiol. Ecol.* 28, 273–279.
- Breitbarth, E., Oschlies, A., LaRoche, J., 2007. Physiological constraints on the global distribution of *Trichodesmium* - effect of temperature on diazotrophy. *Biogeosciences* 4, 53–61.
- Brennan, C., Bianucci, L., Fennel, K., 2016. Sensitivity of Northwest North Atlantic Shelf circulation to surface and boundary forcing: a regional model assessment. *Atmosphere-Ocean*. doi:10.1080/07055900.2016.1147416
- Brock, T.D., 1981. Calculating solar radiation for ecological studies. *Ecol. Model.* 14, 1–19.
- Brody, S.R., Lozier, M.S., Dunne, J.P., 2013. A comparison of methods to determine phytoplankton bloom initiation. *J. Geophys. Res. Oceans* 118, 1–13.
- Burchard, H., Bolding, K., Villarreal, M., 1999. GOTM- a general ocean turbulence model. Theory, applications and test cases (Technical Report No. EUR 18745 EN). European Commission.
- Burkill, P.H., Mantoura, R.F.C., Owens, N.J.P., 1993. Biogeochemical cycling in the northwestern Indian Ocean: a brief overview. *Deep Sea Res. Part II Top. Stud. Oceanogr.* 40, 643–649.
- Capone, D.G., Burns, J.A., Montoya, J.P., Subramaniam, A., Mahaffey, C., Gunderson, T., Michaels, A.F., Carpenter, E.J., 2005. Nitrogen fixation by *Trichodesmium* spp.: An important source of new nitrogen to the tropical and subtropical North Atlantic Ocean. *Glob. Biogeochem. Cycles* 19.
- Capone, D.G., Carpenter, E.J., 1982. Nitrogen fixation in the marine environment. *Science* 217, 1140–1142.
- Capone, D.G., Subramaniam, A., Montoya, J.P., Voss, M., Humborg, C., Johansen, A.M., Siefert, R.L., Carpenter, E.J., 1998. An extensive bloom of the N<sub>2</sub>-fixing cyanobacterium *Trichodesmium erythraeum* in the central Arabian Sea. *Mar. Ecol. Prog. Ser.* 172, 281–292.
- Capone, D.G., Zehr, J.P., Paerl, H.W., Bergman, B., Carpenter, E.J., 1997. *Trichodesmium*, a globally significant marine cyanobacterium. *Science* 276, 1221–1229
- Carlson, D.F., Fredj, E., Gildor, H., 2014. The annual cycle of vertical mixing and restratification in the Northern Gulf of Eilat/Aqaba (Red Sea) based on high temporal and vertical resolution observations. *Deep Sea Res. Part Oceanogr. Res. Pap.* 84, 1–17.

- Carlson, D.F., Fredj, E., Gildor, H., Biton, E., Steinbuck, J.V., Monismith, S.G., Genin, A., 2012. Observations of tidal currents in the northern Gulf of Eilat/Aqaba (Red Sea). *J. Mar. Syst.* 102, 14–28.
- Carozza, D.A., Bianchi, D., Galbraith, E.D., 2017. Formulation, general features and global calibration of a bioenergetically-constrained fishery model. *PloS One* 12, e0169763.
- Carpenter, E.J., McCarthy, J.J., 1975. Nitrogen fixation and uptake of combined nitrogenous nutrients by *Oscillatoria* (*Trichodesmium*) *thiebautii* in the western Sargasso Sea. *Limnol. Oceanogr.* 20, 389–401.
- Carpenter, E.J., Montoya, J.P., Burns, J.A., Mulholland, M.R., Subramaniam, A., Capone, D.G., 1999. Extensive bloom of a N<sub>2</sub>-fixing diatom/cyanobacterial association in the tropical Atlantic Ocean. *Mar. Ecol. Prog. Ser.* 185, 273–283.
- Carpenter, E.J., Roenneberg, T., 1995. The marine planktonic cyanobacteria *Trichodesmium* spp.: photosynthetic rate measurements in the SW Atlantic Ocean. *Mar. Ecol. Prog. Ser.* 267–273.
- Chapman, D.C., Beardsley, R., 1989. On the origin of shelf water in the Middle Atlantic Bight. *J. Phys. Oceanogr.* 19, 384–391.
- Chase, Z., Paytan, A., Johnson, K.S., Street, J., Chen, Y., 2006. Input and cycling of iron in the Gulf of Aqaba, Red Sea. *Glob. Biogeochem. Cycles* 20.
- Chen, Y., Mills, S., Street, J., Golan, D., Post, A., Jacobson, M., Paytan, A., 2007. Estimates of atmospheric dry deposition and associated input of nutrients to Gulf of Aqaba seawater. *J. Geophys. Res. Atmospheres* 112.
- Chiswell, S.M., 2011. Annual cycles and spring blooms in phytoplankton: don't abandon Sverdrup completely. *Mar. Ecol. Prog. Ser.* 443, 39–50. doi:10.3354/meps09453
- Christina, L., Passow, U., 2007. Factors influencing the sinking of POC and the efficiency of the biological carbon pump. *Deep Sea Res. Part II Top. Stud. Oceanogr.* 54, 639–658.
- Ciavatta, S., Kay, S., Saux-Picart, S., Butenschön, M., Allen, J.I., 2016. Decadal reanalysis of biogeochemical indicators and fluxes in the North West European shelf-sea ecosystem. *J. Geophys. Res. Oceans*.
- Colebrook, J.M., 1979. Continuous plankton records: seasonal cycles of phytoplankton and copepods in the North Atlantic Ocean and the North Sea. *Mar. Biol.* 51, 23–32.
- Colman, R.A., Power, S.B., McAvaney, B.J., 1997. Non-linear climate feedback analysis in an atmospheric general circulation model. *Clim. Dyn.* 13, 717–731.

- Conley, D.J., Malone, T.C., 1992. Annual cycle of dissolved silicate in Chesapeake Bay: implications for the production and fate of phytoplankton biomass. *Mar. Ecol. Prog. Ser.* Oldendorf 81, 121–128.
- Conversi, A., Piontkovski, S., Hameed, S., 2001. Seasonal and interannual dynamics of *Calanus finmarchinus* in the Gulf of Maine (Northeastern US shelf) with reference to the North Atlantic Oscillation. *Deep-Sea Res. II* 48, 519–530.
- Cota, Glenn F., Jian Wang, and Josefino Comiso. 2004. “Transformation of Global Satellite Chlorophyll Retrievals with a Regionally Tuned Algorithm.” *Remote Sensing of Environment* 90: 373–77.
- Cropp, R., Norbury, J., 2009. Parameterizing plankton functional type models: insights from a dynamical systems perspective. *J. Plankton Res.* 31, 939–963.
- Cropp, R., Norbury, J., 2010. Parameterising competing zooplankton for survival in plankton functional type models. *Ecol. Model.* 221, 1852–1864.
- Csanady, G.T., Hamilton, P., 1988. Circulation of slope water. *Cont. Shelf Res.* 8, 565–624.
- Dadou, I., Evans, G., Garçon, V., 2004. Using JGOFS in situ and ocean color data to compare biogeochemical models and estimate their parameters in the subtropical North Atlantic Ocean. *J. Mar. Res.* 565–594.
- Dee, D.P., Uppala, S.M., Simmons, A.J., Berrisford, P., Poli, P., Kobayashi, S., Andrae, U., Balsameda, M.A., Balsamo, G., Bauer, P., Bechtold, P., 2011. The ERA-Interim reanalysis: Configuration and performance of the data assimilation system. *Quarterly J. R. Meteorol. Soc.* 137, 553–597.
- Denman, K.L., 2003. Modelling planktonic ecosystems: parameterizing complexity. *Prog. Oceanogr.* 57, 429–452.
- Deutsch, C., Sigman, D.M., Gruber, N., Dunne, J.P., 2007. Spatial coupling of nitrogen inputs and losses in the ocean. *Nature* 445, 163–168. doi:10.1038/nature05392
- Doney, S., Glover, D., Najjar, R., 1996. A new coupled, one-dimensional biological-physical model for the upper ocean: Applications to the JGOFS Bermuda Atlantic Time series Study (BATS) site. *Deep-Sea Res. II* 4, 591–624.
- Doney, S., Lima, I., Moore, J.K., Lindsay, K., Behrenfeld, M.J., Westberry, T.K., Mahowald, N., Glover, D., Takahashi, T., 2009. Skill metrics for confronting global upper ocean ecosystem-biogeochemistry models against field and remote sensing data. *J. Mar. Syst.* 76, 95–112.
- Dore, J.E., Brum, J.R., Tupas, L.M., Karl, D.M., 2002. Seasonal and interannual variability in sources of nitrogen supporting export in the oligotrophic subtropical North Pacific Ocean. *Limnol. Oceanogr.* 47, 1595–1607.

- Dowd, Michael, Emlyn Jones, and John Parslow. 2014. "A Statistical Overview and Perspectives on Data Assimilation for Marine Biogeochemical Models." *Environmetrics*. doi:10.1002/env.2264.
- Dutkiewicz, S., Ward, B.A., Monteiro, F.M., Follows, M., 2012. Interconnection nitrogen fixers and iron in the Pacific Ocean: Theory and numerical simulations. *Glob. Biogeochem. Cycles* 26.
- Edwards, A.M., Yool, A., 2000. The role of higher predation in plankton population models. *J. Plankton Res.* 22, 1085–1112.
- Eppley, R.W., 1972. Temperature and phytoplankton growth in the sea. *Fish. Bull.* 70, 1063–1085.
- Eppley, R.W., Peterson, B.J., 1979. Particulate organic matter flux and planktonic new production in the deep ocean. *Nature* 282, 677.
- Evans, G., Parslow, J.S., 1985. A model of annual plankton cycles. *Biol. Oceanogr.* 3, 327–347.
- Fennel, K., Brady, D., DiToro, D., Fulwiler, R.W., Gardner, W.S., Giblin, A., McCarthy, M.J., Rao, A., Seitzinger, S., Thouvenot-Korppoo, M., Tobias, C., 2009. Modeling denitrification in aquatic sediments. *Biogeochemistry* 93, 159–178.
- Fahnenstiel, G.L., McCormick, M.J., Lang, G.A., Redalje, D.G., Lohrenz, S.E., Markowitz, M., Wagoner, B., Carrick, H., 1995. Taxon-specific growth and loss rates for dominant phytoplankton population from the northern Gulf of Mexico. *Mar. Ecol. Prog. Ser.* 117, 229–239.
- Falcón, L.I., Carpenter, E.J., Cipriano, F., Bergman, B., Capone, D.G., 2004. N<sub>2</sub> fixation by unicellular bacterioplankton from the Atlantic and Pacific Oceans: Phylogeny and in situ rates. *Appl. Environ. Microbiol.* 70, 765–770.
- Falkowski, P.G., 1997. Evolution of the nitrogen cycle and its influence on the biological sequestration of CO<sub>2</sub> in the ocean. *Nature* 387, 272–274.
- Falkowski, P.G., Barber, R.T., Smetacek, V., 1998. Biogeochemical controls and feedbacks on ocean primary production. *Science* 281, 200–206.
- Fasham, M.J.R., Ducklow, H.W., McKelvie, S.M., 1990. A nitrogen based model of plankton dynamics in the oceanic mixed layer. *J. Mar. Res.* 48, 591–639. Fasham, M.J.R., Sarmiento, J.L., Slater, R.D., Ducklow, H., Williams, R., 1993. Ecosystem behavior at Bermuda Station "S" and ocean weather station "India": A general circulation model and observational analysis. *Glob. Biogeochem. Cycles* 7, 379–415. doi:10.1029/92GB02784

- Fasham, M.J.R., Sarmiento, J.L., Slater, R.D., Ducklow, H., Williams, R., 1993. Ecosystem behavior at Bermuda Station “S” and ocean weather station “India”: A general circulation model and observational analysis. *Glob. Biogeochem. Cycles* 7, 379–415. doi:10.1029/92GB02784
- Fennel, K., 1999. Convection and the timing of phytoplankton spring blooms in the Western Baltic Sea. *Estuar. Coast. Shelf Sci.* 49, 113–128.
- Fennel, K., Losch, M., Schröter, J., Wenzel, M., 2001. Testing a marine ecosystem model: sensitivity analysis and parameter optimization. *J. Mar. Syst.* 28, 45–63.
- Fennel, K., Wilkin, J., Levin, J., Moisan, J., O’Reilly, J.E., Haidvogel, D., 2006. Nitrogen cycling in the Middle Atlantic Bight: Results from a three-dimensional model and implications for the North Atlantic nitrogen budget. *Glob. Biogeochem. Cycles* 20, 14. doi:10.1029/2005GB002456
- Fennel, K., Brady, D., DiToro, D., Fulwiler, R.W., Gardner, W.S., Giblin, A., McCarthy, M.J., Rao, A., Seitzinger, S., Thouvenot-Korppoo, M., Tobias, C., 2009. Modeling denitrification in aquatic sediments. *Biogeochemistry* 93, 159–178.
- Fennel, K., Hu, J., Laurent, A., Marta-Almeida, M., Hetland, R., 2013. Sensitivity of hypoxia predictions for the northern Gulf of Mexico to sediment oxygen consumption and model nesting. *J. Geophys. Res. Oceans* 118, 990–1002.
- Fennel, K., Spitz, Y.H., Letelier, R., Abbott, M.R., 2002. A deterministic model for N<sub>2</sub> fixation at stn. ALOHA in the subtropical North Pacific Ocean. *Deep-Sea Res. II* 49, 149–174.
- Flynn, K.J., 2005. Castles built on sand: dysfunctionality in plankton models and the inadequacy of dialogue between biologists and modellers. *J. Plankton Res.* 27, 1205–1210.
- Follows, M., Dutkiewicz, S., 2011. Modeling diverse communities of marine microbes. *Annu. Rev. Mar. Sci.* 3, 427–451.
- Foster, R.A., Paytan, A., Zehr, J.P., 2009. Seasonality of N<sub>2</sub> fixation and nifH gene diversity in the Gulf of Aqaba (Red Sea). *Limnol. Oceanogr.* 54, 219–233.
- Fournier, R.O., 1978. Biological aspects of the Nova Scotian shelfbreak fronts, in: *Oceanic Fronts in Coastal Processes*. Springer Berlin Heidelberg, pp. 69–77.
- Fournier, R.O., Marra, J., Bohrer, R., Det, M.V., 1977. Plankton dynamics and nutrient enrichment of the Scotian Shelf. *J. Fish. Board Can.* 34, 1004–1018.
- Franks, P.J., Di Lorenzo, E., Goebel, N.L., Chenillat, F., Riviere, P., Edwards, C.A., Miller, A.J., 2013. Modelling physical-biological responses to climate change in the California Current System. *Oceanography* 3, 26–33.

- Franks, Peter J. 2009. "Planktonic Ecosystem Models: Perplexing Parametrizations and a Failure to Fail." *Journal of Plankton Research* 31 (11): 1299–1309.
- Franks, P.J., Wroblewski, J.S., Flierl, G.R., 1986. Behavior of a simple plankton model with food-level acclimation by herbivores. *Mar. Biol.* 91, 121–129.
- Frantantoni, P.S., Pickart, R.S., Torres, D.J., Scotti, A., 2000. Mean structure and dynamics of the shelfbreak jet in the Middle Atlantic Bight during fall and winter. *J. Phys. Oceanogr.* 31, 2135–2156.
- Friedrichs, M.A.M., Hofmann, E.E., 2001. Physical control of biological processes in the central equatorial Pacific Ocean. *Deep Sea Res. Part Oceanogr. Res. Pap.* 48, 1023–1069.
- Friedrichs, M.A.M., Hood, R., Wiggert, J., 2006. Ecosystem model complexity versus physical forcing: Quantification of their relative impact with assimilated Arabian Sea data. *Deep-Sea Res. II Top. Stud. Oceanogr.* 53, 576–600.
- Friedrichs, M.A.M., Dusenberry, J.A., Anderson, L.A., Armstrong, R.A., Chai, F., Christian, J.R., Doney, S., Dunne, J.P., Fujii, M., Hood, R., McGillicuddy, D.J., Moore, K., Schartau, M., Spitz, Y.H., Wiggert, J., 2007. Assessment of skill and portability in regional marine biogeochemical models: Role of multiple planktonic groups. *J. Geophys. Res.* 112, 1–22.
- Fujii, M., Yamanaka, Y., Nojiri, Y., Kishi, M., Chai, F., 2007. Comparison of seasonal characteristics in biogeochemistry among the subarctic North Pacific stations described with a NEMURO-based marine ecosystem model. *Ecol. Model.* 52–67.
- Fuller, N.J., West, N.J., Marie, D., Yallop, M., Rivlin, T., Post, A.F., Scanlan, D.J., 2005. Dynamics of community structure and phosphate status of picocyanobacterial populations in the Gulf of Aqaba, Red Sea. *Limnol. Oceanogr.* 50, 363–375.
- García, H.E., Locarnini, R.A., Boyer, T.P., Antonov, J.I., Zweng, M.M., Baranova, O.K., Johnson, D.R., 2010. Nutrients (phosphate, nitrate, and silicate), in: *World Ocean Atlas 2009*, NOAA Atlas NESDIS 71. U.S. Government Printing Office, Washington, D.C., p. 398.
- Garver, S.A., Siegel, D.A., 1997. Inherent optical property inversion of ocean color spectra and its biogeochemical interpretation 1. Time series from the Sargasso Sea. *J. Geophys. Res.* 102, 18607–18625.
- Gatien, M.G., 1976. A study in the Slope Water region south of Halifax. *J. Fish. Res. Board Can.* 33, 2213–2217.
- Geider, R.J., MacIntyre, H.L., Kana, T.M., 1997. Dynamic model of phytoplankton growth and acclimation: responses of the balanced growth rate and the chlorophyll a: carbon ratio to light, nutrient-limitation and temperature. *Mar. Ecol. Prog. Ser.* 148, 187–200.

- Geider, R.J., MacIntyre, H.L., Kana, T.M., 1998. A dynamic regulatory model of phytoplanktonic acclimation to light, nutrients, and temperature. *Limnol. Oceanogr.* 43:4, 679-694.
- Genin, A., Paldor, N., 1998. Changes in the circulation and current spectrum near the tip of the narrow, seasonally mixed Gulf of Elat. *Isr J Earth Sci* 47, 87–92.
- Geshelin, Y., Sheng, J., Greatbatch, R., 1999. Monthly mean climatologies of temperature and salinity in the western North Atlantic. *Can Data Rep Hydrogr Ocean Sci Rapp Stat Can Hydrogr Sci Ocean.*
- Goebel, N.L., Edwards, C.A., Carter, B.J., Achilles, K.M., Zehr, J.P., 2008. Growth and carbon content of three different-sized diazotrophic cyanobacteria observed in the subtropical North Pacific. *J. Phycol.* 44, 1212–1220.
- Gordon, N., Angel, D.L., Neori, A., Kress, N., Kimor, B., 1994. Heterotrophic dinoflagellates with symbiotic cyanobacteria and nitrogen limitation in the Gulf of Aqaba. *Mar. Ecol. Prog. Ser.* 83–88.
- Greene, C.H., Pershing, A.J., 2003. The flip-side of the North Atlantic Oscillation and model shifts in slope-water circulation patterns. *Limnol. Oceanogr.* 48, 319–322.
- Gregg, W.W., 2008. Assimilation of SeaWiFS ocean chlorophyll data into a three-dimensional global ocean model. *J. Mar. Syst.* 69, 205–225.
- Gruber, N., Galloway, J.N., 2008. An Earth-system perspective of the global nitrogen cycle. *Nature* 451, 293–296.
- Gruber, N., Sarmiento, J.L., 1997. Global patterns of marine nitrogen fixation and denitrification. *Glob. Biogeochem. Cycles* 11, 235–266.
- Halm, H., Lam, P., Ferdelman, T.G., Lavik, G., Dittmar, T., LaRoche, J., D'hondt, S., Kuypers, M.M., 2012. Heterotrophic organisms dominate nitrogen fixation in the South Pacific Gyre. *ISME J.* 6, 1238–1249.
- Haidvogel, D., Arango, H.G., Budgell, W.P., Cornuelle, B.D., Curchistser, E., Di Lorenzo, E., Fennel, K., Geyer, W.R., Hermann, A.J., Lanerolle, L., Shchepetkin, A.F., Sherwood, C.R., Signell, R.P., Warner, J.C., Wilkin, J., 2008. Ocean forecasting in terrain-following coordinates: Formulation and skill assessment of the Regional Ocean Modeling System. *J. Comput. Phys.* 227, 3595–3624.
- Harris, J., 1993. The presence, nature, and role of gut microflora in aquatic invertebrates: a synthesis. *Microb. Ecol.* 25, 195–231.
- Haug, G.H., Pedersen, T.F., Sigman, D.M., Calvert, Nielsen, B., Peterson, L.C., 1998. Glacial/interglacial variations in production in nitrogen fixation in the Cariaco Basin during the last 580 kyr. *Paleoceanography* 13, 427–432.

- Hemmings, J.C.P., Challenor, P.G., 2012. Addressing the impact of environmental uncertainty in plankton model calibration with a dedicated software system: the Marine Model Optimization Testbed (MarMOT 1.1 alpha). *Geosci. Model Dev.* 471–498.
- Hemmings, J.C.P., Challenor, P.G., Yool, A., 2015. Mechanistic site-based emulation of a global ocean biogeochemical model (MEDUSA 1.0) for parametric analysis and calibration: an application of the Marine Model Optimization Testbed (MarMOT 1.1). *Geosci. Model Dev.* 697–731.
- Henson, S.A., Robinson, I., Allen, J.T., Waniek, J.J., 2006. Effect of meteorological conditions on interannual variability in timing and magnitude of the spring bloom in the Irminger Basin, North Atlantic. *Deep-Sea Res. I* 53, 1601–1615.
- Henson, S.A., Dunne, J.P., Sarmiento, J.L., 2009. Decadal variability in North Atlantic phytoplankton blooms. *J. Geophys. Res.* 114, 1–11.
- Hood, R., Bates, N.R., Capone, D.G., Olson, D.B., 2001. Modeling the effect of nitrogen fixation on carbon and nitrogen fluxes BATS. *Deep-Sea Res. II* 48, 1609–1648.
- Howell, T.E., Hashioka, T., Noguchi-Aita, M., Yamanaka, Y., 2011. Synoptic relationships between surface Chlorophyll-a and diagnostic pigments to phytoplankton functional types. *Biogeosciences* 8, 311–327.
- Hooten, M., Leeds, W.B., Fiechter, J., Wikle, C.K., 2011. Assessing first-order emulator interference for physical parameters in nonlinear mechanistic models. *J. Agric. Biol. Environ. Stat.* 16, 475–494.
- Houck, C.R., Joines, J.A., Kay, M.G., 1995. A genetic algorithm for function optimization: A Matlab implementation (Technical Report No. NCSU-IE-TR-95-09). North Carolina State University, Raleigh, NC.
- Huisman, J., Arrayas, M., Ebert, U., Sommeijer, B., 2002. How do sinking phytoplankton species manage to persist? *Am. Nat.* 159, 245–254.
- Huisman, J., van Oostveen, P., Weissing, F.J., 1999a. Species dynamics in phytoplankton blooms: Incomplete mixing and competition for light. *Am. Nat.* 154, 46–68.
- Huisman, J., van Oostveen, P., Weissing, F.J., 1999b. Critical depth and critical turbulence: Two different mechanisms for the development of phytoplankton blooms. *Limnol. Oceanogr.* 44, 1781–1787.
- Hurtt, G.C., Armstrong, R.A., 1996. A pelagic ecosystem model calibrated with BATS data. *Deep Sea Res. Part II Top. Stud. Oceanogr.* 43, 653–683.
- Hutchins, D.A., Fu, F.-X., Zhang, Y., Warner, M.E., Feng, Y., Portune, K., Bernhardt, P., Mullholland, M.R., 2007. CO<sub>2</sub> control of *Trichodesmium* N<sub>2</sub> fixation, photosynthesis, growth rates, and elemental ratios: Implications for past, present, and future ocean biogeochemistry. *Limnol. Oceanogr.* 52, 1293–1304.

- Iluz, D., 1991. Primary production of phytoplankton in the northern Gulf of Eilat, Red Sea. MSc thesis, Bar-Ilan University, Ramat-Gan (in Hebrew with English abstract).
- Iluz, D., Dishon, G., Capuzzo, E., Meeder, E., Astoreca, R., Montecino, V., Znachor, P., Ediger, D., Marra, J., 2009. Short-term variability in primary productivity during a wind-driven diatom bloom in the Gulf of Eilat (Aqaba). *Aquat. Microb. Ecol.* 56, 205–215.
- Joint, I., and Groom S., 2000. “Estimation of Phytoplankton Production from Space: Current Status and Future Potential of Satellite Remote Sensing.” *Journal of Experimental Marine Biology and Ecology* 250: 233–55.
- Joos, F., Plattner, G.-K., Stocker, T., Marchal, O., Schmittner, A., 1999. Global warming and marine carbon cycle feedbacks on future atmospheric CO<sub>2</sub>. *Science* 284, 464–467.
- Ji, R., Chen, C., Franks, P.J., Townsend, D.W., Durbin, E.G., Beardsley, R., Lough, R.G., Houghton, R.W., 2006. Spring phytoplankton bloom and associated lower trophic level food web dynamics on Georges Bank: 1-D and 2-D model studies. *Deep-Sea Res. II* 53, 2656–2683.
- Ji, R., Edwards, M., Mackas, D.L., Runge, J., Thomas, A., 2010. Marine plankton phenology and life history in a changing climate: current research and future directions. *J. Plankton Res.* 32, 1355–1368.
- Jossie, J.W., Goulet, J.R., 1993. Zooplankton trends: US north-east shelf ecosystem and adjacent regions differ from northeast Atlantic and North Sea. *ICES J. Mar. Sci.* 50, 303–313.
- Kane, A., Moulin, C., Thiria, S., Bopp, L., Berrada, M., Tagliabue, A., Crépon, M., Aumont, O., Badran, F., 2011. Improving the parameters of a global ocean biogeochemical model via variational assimilation of in situ data at five time series stations. *J. Geophys. Res. Oceans* 116. doi:10.1029/2009JC006005
- Karl, D., 2002. Nutrient dynamics in the deep blue sea. *TRENDS Microbiol.* 10, 410–418.
- Kimor, B., Golandsky, B., 1977. Microplankton of the Gulf of Elat: aspects of seasonal and bathymetric distribution. *Mar. Biol.* 42, 55–67.
- Kishi, M., Kashiwai, M., Ware, D.M., Megrey, B.A., Eslinger, D.L., Werner, F.E., Noguchi-Aita, M., Azumay, T., Fujii, M., Hashimoto, S., Huang, D., Iizumi, H., Ishida, Y., Kang, S., Kantakov, G.A., Kim, H., Komatsu, K., Navrotsky, V.V., Smith, S.L., Tadokoro, K., Tsuda, A., Yamamura, O., Yamanaka, Y., Yokouchi, K., Yoshie, N., Zhang, J., Zuenko, Y.I., Zvalinsky, V., 2007. NEMURO - a lower trophic level model for the North Pacific marine ecosystem. *Ecol. Model.* 202, 12–25.

- Klaas, C., Archer, D.E., 2002. Association of sinking organic matter with various types of mineral ballast in the deep sea: Implications for the rain ratio. *Glob. Biogeochem. Cycles* 16.
- Klinker, J., Reiss, Z., Kropach, C., Levanon, I., Harpaz, H., Halicz, E., Assaf, G., 1976. Observations on the circulation pattern in the Gulf of Elat (Aqaba), Red Sea. *Isr J Earth Sci* 25, 85–103.
- Kriest, I., Khatiwala, S., Oschlies, A., 2010. Towards an assessment of simple global marine biogeochemical models of different complexity. *Prog. Oceanogr.* 86, 337–360.
- Kuhn, A.M., Fennel, K., Mattern, J.P., 2015. Model investigations of the North Atlantic spring bloom initiation. *Prog. Oceanogr.* 176–193.
- Labiosa, R.G., Arrigo, K.R., Genin, A., Monismith, S.G., van Dijken, G., 2003. The interplay between upwelling and deep convective mixing in determining the seasonal phytoplankton dynamics in the Gulf of Aqaba: Evidence from SeaWiFS and MODIS. *Limnol. Oceanogr.* 48, 2355–2368.
- Lagman, K., Fennel, K., Thompson, K., 2014. Assessing the utility of frequency dependent nudging for reducing biases in biogeochemical models. *Ocean Model.* 25–35.
- Lampitt, R.S., Noji, T., Bodungen, B. von, 1990. What happens to zooplankton faecal pellets? Implications for material flux. *Mar. Biol.* 104, 15–23. doi:10.1007/BF01313152
- Lande, R., Wood, M., 1987. Suspension times of particles in the upper ocean. *Deep Sea Res. Part Oceanogr. Res. Pap.* 1, 61–72.
- Landry, M.R., 1993. Estimating rates of growth and grazing mortality of phytoplankton by the dilution method., in: *Handbook of Methods in Aquatic Microbial Ecology*. Lewis Publishers, Boca Raton, pp. 715–721.
- Landry, M.R., Hassett, R.P., 1982. Estimating the grazing impact of marine micro-zooplankton. *Mar. Biol.* 67, 283–288.
- Lazar, B., Erez, J., Silverman, J., Rivlin, T., Rivlin, A., Dray, M., Meeder, E., Iluz, D., 2008. Recent environmental changes in the chemical-biological oceanography of the Gulf of Aqaba (Eilat). *Aqaba-Eilat Improbable Gulf Environ. Biodivers. Preserv.* Magnes Press Jerus. 49–62.
- Lee, K., Karl, D.M., Wanninkhof, R., Zhang, J.-Z., 2002. Global estimates of net carbon production in the nitrate-depleted tropical and subtropical oceans. *Geophys. Res. Lett.* 29.
- Leeds, W.B., C.K. Wikle, J. Fiechter, J. Brown, and R.F. Milliff. 2012. “Modeling 3-D Spatio-Temporal Biogeochemical Processes with a Forest of 1-D Statistical Emulators.” *Environmetrics*. doi:10.1002/env.2187.

- Le Quéré, Corinne, Sandy P. Harrison, I. Colin Prentice, Erik T. Buitenhuis, Olivier Aumont, Laurent Bopp, Herve Claustre, et al. 2005. "Ecosystem Dynamics Based on Plankton Functional Types for Global Ocean Biogeochemistry Models" 11: 2016–40. doi:doi: 10.1111/j.1365-2486.2005.01004.x. Le Quéré, C., 2006. Reply to Horizons Article "Plankton functional type modelling: running before we can walk" Anderson (2005): I. Abrupt changes in marine ecosystems? *Journal of Plankton Research*. 28, 871–872.
- Lenz, J., Morales, alvaro, Gunkel, J., 1993. Mesozooplankton standing stock during the North Atlantic spring bloom in 1989 and its potential grazing pressure on phytoplankton: a comparison between low, medium and high latitudes. *Deep-Sea Res. II Top. Stud. Oceanogr.* 40, 559–572.
- Levanon-Spanier, I., Padan, E., Reiss, Z., 1979. Primary production in a desert-enclosed sea—the Gulf of Elat (Aqaba), Red Sea. *Deep Sea Res. Part Oceanogr. Res. Pap.* 26, 673–685.
- Levitan, O., Rosenberg, G., Setlik, I., Setloкова, E., Grigel, J., Klepetar, J., Prasil, O., Berman-Frank, I., 2007. Elevated CO<sub>2</sub> enhances nitrogen fixation and growth in the marine cyanobacterium *Trichodesmium*. *Glob. Change Biol.* 13, 531–538.
- Lewis, K., Allen, J.I., Richardson, A.J., Holt, J.T., 2006. Error quantification of a high resolution coupled hydrodynamic ecosystem coastal-ocean model: Part 3, validation with Continuous Plankton Recorder data. *J. Mar. Syst.* 63, 209–224.
- Li, W.K.W., 2002. Macroecological patterns of phytoplankton in the northwestern North Atlantic Ocean. *Nature* 419, 154–157.
- Linder, C.A., Gawarkiewicz, G., 1998. A climatology of the shelfbreak front in the Middle Atlantic Bight. *J. Geophys. Res. Oceans* 103, 18405–18423.
- Litchman, E., Klausmeier, C., 2008. Trait-based community ecology of phytoplankton. *Annu. Rev. Ecol. Evol. Syst.* 39, 615–639.
- Litchman, E., Klausmeier, C.A., Schofield, O.M., Falkowski, P.G., 2007. The role of functional traits and trade-offs in structuring phytoplankton communities: scaling from cellular to ecosystem level. *Ecol. Lett.* 10, 1170–1181.
- Loder, J.W., Greenberg, D.A., 1986. Predicted positions of tidal fronts in the Gulf of Maine. *Cont. Shelf Res.* 6, 397–414.
- Loder, J.W., Petrie, B., Gawarkiewicz, G., 1998. The coastal ocean off northwestern North America: A large-scale view, in: *The Sea*. John Wiley and Sons, pp. 105–133.

- Losa, S., Kivman, G.A., Ryanbchenko, V.A., 2004. Weak constraint parameter estimation for a simple ocean ecosystem model: what can we learn about the model and data? *J. Mar. Syst.* 1–20.
- Lozier, M.S., Gawarkiewicz, G., 2001. Cross-frontal exchange in the Middel Atlantic Bight as evidenced by surfae drifters. *J. Phys. Oceanogr.* 31, 2498–2510.
- MacIntyre, H.L., Kana, T.M., Anning, T., Geider, R.J., 2002. Photoacclimation of photosynthesis irradiance response curves and photosynthetic pigments in microalgae and cyanobacteria1. *J. Phycol.* 38, 17–38.
- Mackey, K.R., Rivlin, T., Grossman, A.R., Post, A.F., Paytan, A., 2009. Picophytoplankton responses to changing nutrient and light regimes during a bloom. *Mar. Biol.* 156, 1531–1546.
- Mahadevan, A., D’Asaro, E., Lee, C., Perry, M.J., 2012. Eddy-driven stratification initiates North Atlantic spring phytoplankton blooms. *Science* 337. doi:10.1126/science.1218740
- Maier-Reimer, E., Mikolajewicz, U., Winguth, A., 1996. Future ocean uptake of CO<sub>2</sub>: interaction between ocean circulation and biology. *Clim. Dyn.* 12, 711–721.
- Malone, T.C., Hopkins, T.S., Falkowski, P.G., Whittedge, T.E., 1983. Production and transport of phytoplankton biomass over the continental shelf of the New York Bight. *Cont. Shelf Res.* 1, 305–337.
- Manasrah, R., Raheed, M., Badran, M.I., 2006. Relationships between water temperature, nutrients and dissolved oxygen in the northern Gulf of Aqaba, Red Sea. *Oceanologia* 48.
- Marañón, E., Cermeño, P., Huete-Ortega, M., López-Sandoval, D.C., Mouriño-Carballido, B., Rodríguez-Ramos, T., 2014. Resource supply overrides temperature as a controlling factor of marine phytoplankton growth. *PLOS ONE* 9, e99312.
- Mariani, P., Andersen, K.H., Visser, A.W., Barton, A.D., Kiørboe, T., 2013. Control of plankton seasonal succession by adaptive grazing. *Limnol. Oceanogr.* 58, 173–184.
- Maritorena, S., Siegel, D.A., Peterson, A.R., 2002. Optimization of a semianalytical ocean color model for global-scale applications. *Appl. Opt.* 41, 2705–2714.
- Marra, J., Houghton, R.W., Garside, C., 1990. Phytoplankton growth at the shelf-break front in the Middle Atlantic Bight. *J. Mar. Res.* 48, 851–868.
- Margalef, R., 1978. Life-forms of phytoplankton as survival alternatives in an unstable environment. *Oceanol. Acta* 1, 493–509.

- Mariani, P., Andersen, K.H., Visser, A.W., Barton, A.D., Kiørboe, T., 2013. Control of plankton seasonal succession by adaptive grazing. *Limnol. Oceanogr.* 58, 173–184.
- Masotti, I., Ruiz-Pino, D., Le Bouteiller, A., 2007. Photosynthetic characteristics of *Trichodesmium* in the southwest Pacific Ocean: importance and significance. *Mar. Ecol. Prog. Ser.* 338, 47–59.
- Matear, R.J., 1995. Parameter optimization and analysis of ecosystem models using simulated annealing: A case study at Station P. *J. Mar. Res.* 53, 571–607.
- Mattern, J.P., Fennel, K., Dowd, M., 2012. Estimating time-dependent parameters for a biological ocean model using an emulator approach 32–47.
- McDonald, C.P., Bennington, V., Urban, N.R., McKinley, G.A., 2012. 1-D test-bed calibration of a 3-D Lake Superior biogeochemical model. *Ecol. Model.* 225, 115–126.
- Meeder, E., Mackey, K.R., Paytan, A., Shaked, Y., Iluz, D., Stambler, N., Rivlin, T., Post, A.F., Lazar, B., 2012. Nitrite dynamics in the open ocean-clues from seasonal and diurnal variations. *Mar. Ecol. Prog. Ser.* 453.
- Michaels, A.F., Olson, D., Sarmiento, J.L., Ammerman, J.W., Fanning, K., Jahnke, R., Knap, A.H., Lipschultz, F., Prospero, J.M., 1996. Inputs, losses and transformations of nitrogen and phosphorus in the pelagic North Atlantic Ocean, in: *Nitrogen Cycling in the North Atlantic Ocean and Its Watersheds*. Springer, pp. 181–226.
- Mills, E.L., Fournier, R.O., 1979. Fish production and the marine ecosystems of the Scotian Shelf, eastern Canada. *Mar. Biol.* 54, 101–108.
- Mitchell, M.R., Harrison, G., Pauley, K., Gagné, A., Maillet, G., Strain, P., 2002. Atlantic Zonal Monitoring Program Sampling Protocol, Can. Tech. Rep. Hydrogr. Ocean. Sci.
- Moisander, P., Beinart, R.A., Hewson, I., White, A.E., Johnson, K.S., Carlson, C.A., Montoya, J.P., Zehr, J.P., 2010. Unicellular Cyanobacterial Distribution Broadens the Oceanic N<sub>2</sub> Fixation Domain. *Science* 327, 1512–1514.
- Monismith, S.G., Genin, A., 2004. Tides and sea level in the Gulf of Aqaba (Eilat). *J. Geophys. Res. Oceans* 109.
- Montoya, J.P., Holl, C.M., Zehr, J.P., Hansen, A., Villareal, T.A., Capone, D.G., 2004. High rates of N<sub>2</sub> fixation by unicellular diazotrophs in the oligotrophic Pacific Ocean. *Nature* 430, 1027–1032.
- Moore, J.K., Doney, S., Lindsay, K., 2004. Upper ocean ecosystem dynamics and iron cycling in a global three-dimensional model. *Glob. Biogeochem. Cycles* 18.

- Morrison, J.M., Codispoti, L.A., Gaurin, S., Jones, B., Manghnani, V., Zheng, Z., 1998. Seasonal variation of hydrographic and nutrient fields during the US JGOFS Arabian Sea Process Study. *Deep Sea Res. Part II Top. Stud. Oceanogr.* 45, 2053–2101.
- Morrison, J.M., Codispoti, L.A., Smith, S.L., Wishner, K., Flagg, C., Gardner, W.D., Gaurin, S., Naqvi, S.W.A., Manghnani, V., Prosperie, L., others, 1999. The oxygen minimum zone in the Arabian Sea during 1995. *Deep Sea Res. Part II Top. Stud. Oceanogr.* 46, 1903–1931.
- Mosseau, L., Fortier, L., Legendre, L., 1998. Annual production of fish larvae and their prey in relation to size-fractionated primary production (Scotial Shelf, NW Atlantic). *ICES J. Mar. Sci.* 55, 44–57.
- Naqvi, S.W.A., 1994. Denitrification processes in the Arabian Sea. *Proc. Indian Acad. Sci.-Earth Planet. Sci.* 103, 279–300.
- Naqvi, S.W.A., Hansen, H.P., Kureishy, T.W., 1986. Nutrient-uptake and regeneration ratios in the red-sea with reference to the nutrient budgets. *Oceanol. Acta* 9, 271–275.
- Neumann, T., 2000. Towards a 3D-ecosystem model of the Baltic Sea. *J. Mar. Syst.* 23, 405–419.
- Nielsen, S.L., 2006. Size-dependent growth rates in eukaryotic and prokaryotic algae exemplified by green algae and cyanobacteria: comparisons between unicells and colonial growth forms. *J. Plankton Res.* 28, 489–498.
- O’Neil, J.M., Roman, M.R., 1994. Ingestion of the cyanobacterium *Trichodesmium* spp. by pelagic harpacticoid copepods *Macrosetella*, *Miracia* and *Oculosetella*, in: *Ecology and Morphology of Copepods*. Springer, pp. 235–240.
- O’Reilly, John E., Stephane Maritorena, B. Greg Mitchell, David A. Siegel, Kendall L. Carder, Sara A. Garver, Mati Kahru, and Charles McClain. 1998. “Ocean Color Chlorophyll Algorithms for SeaWiFS.” *Journal of Geophysical Research* 103 (C11): 24937–53.
- O’Reilly, John E., Stephane Maritorena, David A. Siegel, M.C. O’Brien, D. Toole, B. Greg Mitchell, M. Kahru, et al. 2001. “Ocean Color Chlorophyll a Algorithms for SeaWiFS, OC2 and OC4: Version 4.” NASA Tech. Memo. 2000–206892. SeaWiFS Postlaunch Calibration and Validation Analyses: Part 3. Greenbelt, MD: NASA Goddard Space Flight Center.
- Orr, James C., Victoria J. Fabry, Olivier Aumont, Laurent Bopp, S.C. Doney, Richard A. Feely, Anand Gnanadesikan, et al. 2005. “Anthropogenic Ocean Acidification over the Twenty-First Century and Its Impact on Calcifying Organisms.” *Nature* 437: 681–86.

- Oschlies, A., Schartau, M., 2005. Basin-scale performance of a locally optimized marine ecosystem model 63, 335–358.
- Platt, T., Bird, D.F., Sathyendranath, S., 1991. Critical depth and marine primary production. *Proc. R. Soc. Lond. B* 246, 205–217.
- Platt, T., White III, G.N., Zhai, L., Sathyendranath, S., Roy, S., 2009. The phenology of phytoplankton blooms: Ecosystem indicators from remote sensing. *Ecol. Model.* 220, 3057–3069. doi:10.106/J.ECOLMODEL.2008.11.022
- Pomeroy, L.R., Wiebe, W.J., 2001. Temperature and substrates as interactive limiting factors for marine heterotrophic bacteria. *Aquat. Microb. Ecol.* 23, 187–204.
- Post, A.F., Dedej, Z., Gottlieb, R., Li, H., Thomas, D.N., 2002. Spatial and temporal distribution of *Trichodesmium* spp. in the stratified Gulf of Aqaba, Red Sea. *Mar. Ecol. Prog. Ser.* 239, 241–250.
- Prasad, K.S., Haedrich, R.L., 1993. Primary production estimates on the Grand Banks of Newfoundland, north-west Atlantic Ocean, derived from remotely-sensed chlorophyll. *Int. J. Remote Sens.* 14, 3299–3304.
- Previdi, M., Fennel, K., Wilkin, J., Haidvogel, D., 2009. Interannual variability in atmospheric CO<sub>2</sub> uptake on the northeast U.S. continental shelf. *J. Geophys. Res.* 114, 13.
- Prieß, M., S. Koziel, and T. Slawig. 2013. “Marine Ecosystem Model Calibration with Real Data Using Enhanced Surrogate-Based Optimization.” *Journal of Computational Science* 4: 423–37.
- Prieß, M., J. Piwonski, S. Koziel, Andreas Oschlies, and T. Slawig. 2013. “Accelerated Parameter Identification in a 3D Marine Biogeochemical Model Using Surrogate-Based Optimization.” *Ocean Modelling* 68: 22–36.
- Putland, J.N., 2000. Microzooplankton herbivory and bacterivory in Newfoundland coastal waters during spring, summer and winter. *J. Plankton Res.* 22, 253–277.
- Quine, W.V., 1975. On empirically equivalent systems of the world. *Erkenntnis* 9, 313–328.
- Rahav, E., Bar-Zeev, E., Ohayion, S., Elifantz, H., Belkin, N., Herut, B., Mulholland, M.R., Berman-Frank, I.R., 2013. Dinitrogen fixation in aphotic oxygenated marine environments. *Front. Microbiol.* 4, 227.
- Rahav, E., Herut, B., Mulholland, M.R., Belkin, N., Elifantz, H., Berman-Frank, I., 2015. Heterotrophic and autotrophic contribution to dinitrogen fixation in the Gulf of Aqaba. *Mar. Ecol. Prog. Ser.* 522, 67–77.

- Rhee, G.Y., Gotham, I.J., 1981. The effect of environmental factors on phytoplankton growth: light and the interactions of light with nitrate limitation. *Limnol. Oceanogr.* 26, 649–659.
- Riley, G.A., 1965. A Mathematical model. *Limnol. Oceanogr.* 10, 202 – 215.
- Ryan, J.P., Yoder, J.A., Cornillon, P.C., 1999. Enhanced chlorophyll at the shelfbreak of the Mid-Atlantic Bight and Georges Bank during the spring transition. *Limnol. Oceanogr.* 44, 1–11.
- Sailley, S.F., Vogt, M., Doney, S., Aita, M.N., Bopp, L., Buitenhuis, E.T., Hashioka, T., Lima, I., Le Quéré, C., Yamanaka, Y., 2013. Comparing food web structures and dynamics across a suite of global marine ecosystem models. *Ecol. Model.* 261-262, 43–57.
- Sarmiento, Jorge L., Tertia M. C. Hughes, Ronald J. Stouffer, and Syukuro Manabe. 1998. “Simulated Response of the Ocean Carbon Cycle to Anthropogenic Climate Warming.” *Nature* 393 (245–251).
- Sarmiento, J.L., Hughes, T.M.C., Stouffer, R.J., Manabe, S., 1998. Simulated response of the ocean carbon cycle to anthropogenic climate warming. *Nature* 393.
- Sarthou, G., Timmermans, K.R., Blain, S., Tréguer, P., 2005. Growth physiology and fate of diatoms in the ocean: a review. *J. Sea Res.* 53, 25–42.
- Sathyendranath, S., Longhurst, A., Caverhill, C.M., Platt, T., 1995. Regionally and seasonally differentiated primary production in the North Atlantic. *Deep Sea Res. Part Oceanogr. Res. Pap.* 42, 1773–1802.
- Schartau, M., Oschlies, A., Jürgen, W., 2001. Parameter estimates of a zero-dimensional ecosystem model applying the adjoint method. *Deep-Sea Res. II* 48, 1769–1800.
- Schartau, M., Oschlies, A., 2003a. Simultaneous data-based optimization of a 1D-ecosystem model at three locations in the North Atlantic: Part I - Method and parameter estimates. *J. Mar. Res.* 61, 765–793.
- Schartau, M., Oschlies, A., 2003b. Simultaneous data-based optimization of a 1D-ecosystem model at three locations in the North Atlantic: Part II - Standing stocks and nitrogen fluxes. *J. Mar. Res.* 795–821.
- Schartau, M., Wallhead, P., Hemmings, J.C.P., Loptien, U., Kriest, I., Krishna, S., Ward, B.A., Slawig, T., Oschlies, A., 2017. Review and syntheses: parameter identification in marine planktonic ecosystem modelling. *Biogeosciences* 14, 1647–1701.
- Siegel, D.A., Doney, S.C., Yoder, J.A., 2002. The North Atlantic spring phytoplankton bloom and Sverdrup’s critical depth hypothesis. *Science, Reports* 296, 730–733.

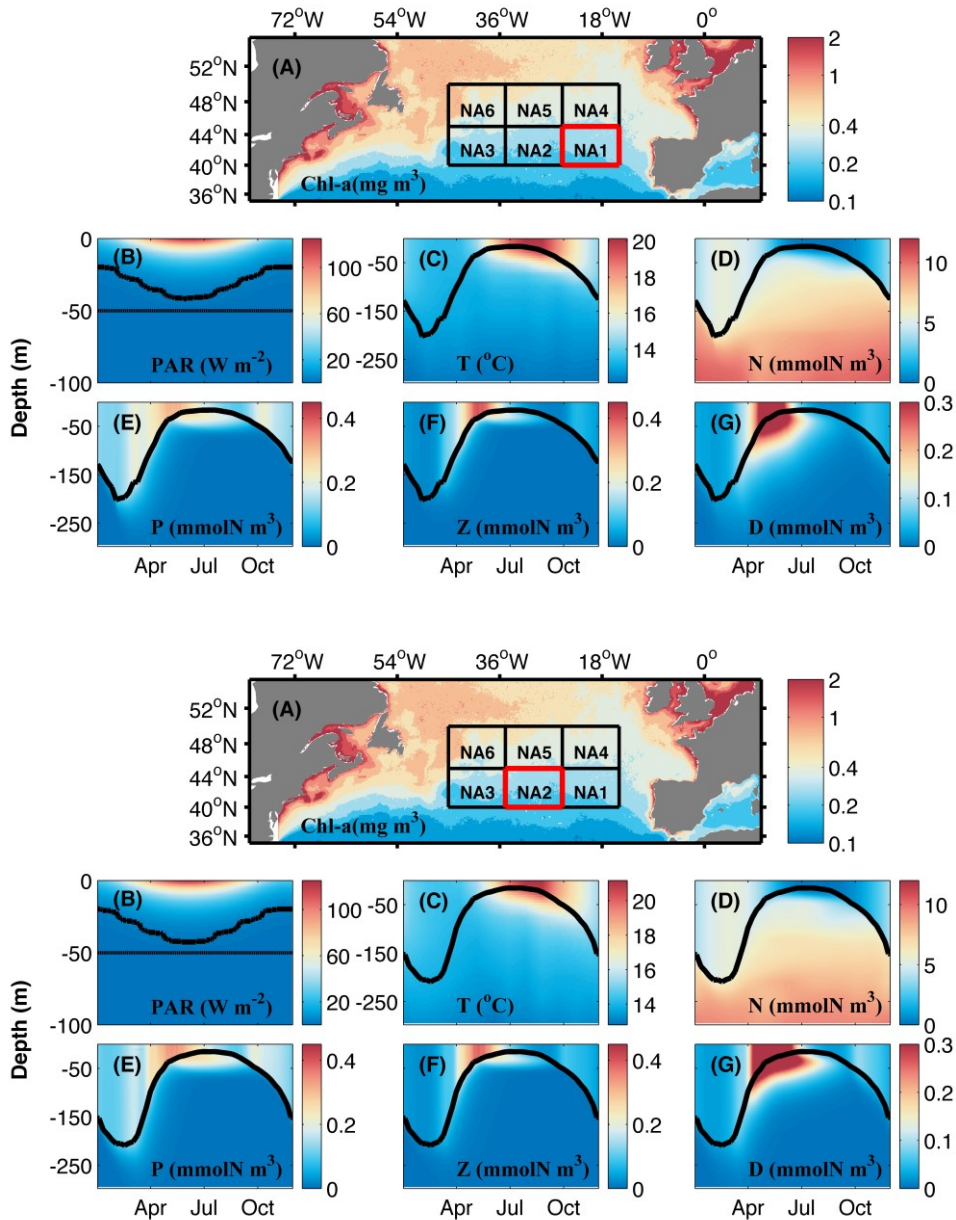
- Siegel, D.A., Maritorena, S., Nelson, N.B., Hansell, D.A., Lorenzi-Kayser, D., 2002b. Global distribution and dynamics of colored dissolved and detrital organic materials. *J. Geophys. Res.* 107, 3228.
- Silverman, J., Gildor, H., 2008. The residence time of an active versus a passive tracer in the Gulf of Aqaba: A box model approach. *J. Mar. Syst.* 71, 159–170.
- Smetacek, V., Passow, U., 1990. Spring bloom initiation and Sverdrup's critical depth model. *Limnol. Oceanogr.* 35, 228–234.
- Smith, E.L., 1936. Photosynthesis in relation to light and carbon dioxide. *Proc. Natl. Acad. Sci. U. S. A.* 22, 504 – 511.
- Song, H., Ji, R., Stock, C., Wang, Z., 2010. Phenology of phytoplankton blooms in the Nova Scotian Shelf - Gulf of Maine region: remote sensing and modeling analysis. *J. Plankton Res.* 32, 1485–1499.
- Steele, J.H., Henderson, E.W., 1992. The role of predation in plankton models. *J. Plankton Res.* 14, 157–172.
- Strom, S., 2002. Novel interactions between phytoplankton and microzooplankton: their influence on the coupling between growth and grazing rates in the sea. *Hydrobiologia* 480, 41–54.
- Strom, S.L., 2008. Microbial ecology of ocean biogeochemistry: a community perspective. *Science* 320, 1043–1045.
- Sverdrup, H.U., 1953. On conditions for vernal blooming of phytoplankton. *J. Cons.* 18, 287–295.
- Taylor, J.R., Ferrari, R., 2011a. Shutdown of turbulent convection as a new criterion for the onset of spring phytoplankton blooms. *Limnol. Oceanogr.* 56, 2293–2307.
- Taylor, J.R., Ferrari, R., 2011b. Ocean fronts trigger high latitude phytoplankton blooms. *Geophys. Res. Lett.* 38, 5. doi:10.1029/2011GL049312
- Thomas, M.K., Kremer, C.T., Klausmeier, C.A., Litchman, E. 2012. A global pattern of thermal adaptation in marine phytoplankton. *Science* 338 (6110):1085-1088. doi:10.1126/science.1224836
- Townsend, D.W., Keller, M.D., Sieracki, M.E., Ackleson, S.G., 1992. Spring phytoplankton blooms in the absence of vertical water column stratification. *Nature* 360, 59–62.
- Townsend, D.W., Thomas, A.C., Mayer, L.M., Thomas, M.A., Quinlan, J.A., 2004. Chapter 5: Oceanography of the Northwest Atlantic Continental Shelf (1,W), in: *The Sea: The Global Coastal Ocean: Interdisciplinary Regional Studies and Syntheses*. Harvard University Press.

- Urrego-Blanco, J., Sheng, J., 2012. Interannual variability of the circulation over the Eastern Canadian Shelf 50, 277–300. doi:10.1080/07055900.2012.680430
- Van Nes, E.H., Scheffer, M., 2005. A strategy to improve the contribution of complex simulation models to ecological theory. *Ecol. Model.* 185, 153–164.
- Verity, P.G., Smayda, T.J., 1989. Nutritional value of *Phaeocystis pouchetii* (Prymnesiophyceae) and other phytoplankton for *Acartia* spp.(Copepoda): ingestion, egg production, and growth of nauplii. *Mar. Biol.* 100, 161–171.
- Waite, A., Bienfang, P.K., Harrison, P.J., 1992. Spring bloom sedimentation in a subarctic ecosystem. *Mar. Biol.* 114, 119–129.
- Ward, B.A., Dutkiewicz, S., Moore, C.M., Follows, M., 2013. Iron, phosphorus, and nitrogen supply ratios define the biogeography of nitrogen fixation. *Limnol. Oceanogr.* 58, 2059–2075.
- Ward, B.A., Waniek, J.J., 2007. Phytoplankton growth conditions during autumn and winter in the Irminger Sea, North Atlantic. *Mar. Ecol. Prog. Ser.* 334, 47–61.
- Ward, B.A., Friedrichs, M.A.M., Anderson, T.R., Oschlies, A., 2010. Parameter optimization techniques and the problem of underdetermination in marine biogeochemical models. *J. Mar. Syst.* 81, 34–43.
- Ward, B.A., Schartau, M., Oschlies, A., Martin, A., Follows, M., Anderson, T.R., 2013. When is a biogeochemical model too complex? Objective model reduction and selection for North Atlantic time-series sites. *Prog. Oceanogr.* 49–65.
- Wasmund, N., Nausch, G., Matthaus, W., 1998. Phytoplankton spring blooms in the southern Baltic Sea: spatio-temporal development and long-term trends. *J. Plankton Res.* 20, 1099–1117.
- Westberry, T.K., Behrenfeld, M.J., Siegel, D.A., Boss, E., 2008. Carbon-based primary productivity modeling with vertical resolved photoacclimation. *Glob. Biogeochem. Cycles* 22.
- Wolf-Vecht, A., Paldor, N., Brenner, S., 1992. Hydrographic indications of advection/convection effects in the Gulf of Elat. *Deep Sea Res. Part Oceanogr. Res. Pap.* 39, 1393–1401.
- Yoshie, N., Yamanaka, Y., Rose, K.A., Eslinger, D.L., Ware, D.M., Kishi, M., 2007. Parameter sensitivity study of the NEMURO lower trophic level marine ecosystem model. *Ecol. Model.* 202, 26–37.
- Zehr, J.P., 2011. Nitrogen fixation by marine cyanobacteria 19, 162–173.

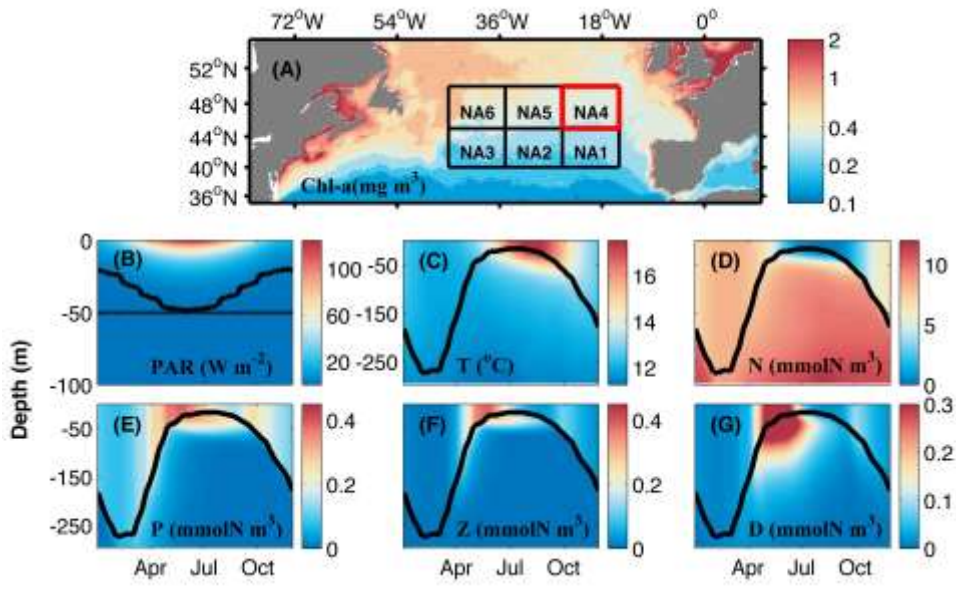
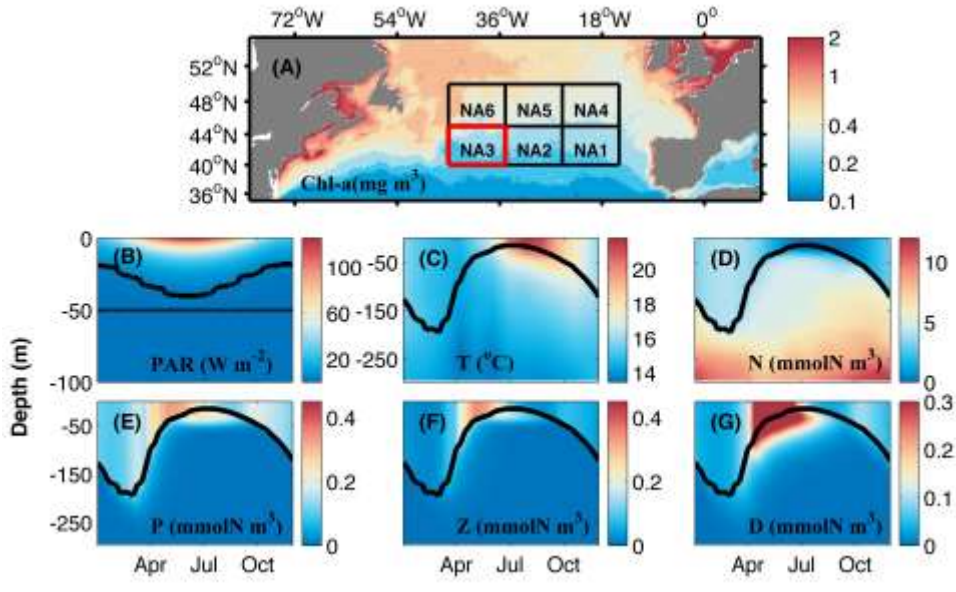
- Zehr, J.P., Bench, S.R., Carter, B.J., Hewson, I., Niazi, F., Shi, T., Tripp, H.J., Affourtit, J., 2008. Globally distributed uncultivated oceanic N<sub>2</sub>-fixing cyanobacteria lack oxygenic photosystem II. *Science* 322, 1110–1112.
- Zehr, J.P., Capone, D.G., 1996. Problems and promises of assaying the genetic potential for nitrogen fixation in the marine environment. *Microb. Ecol.* 32, 263–281.
- Zehr, J.P., Carpenter, E.J., Villareal, T.A., 2000. New perspectives on nitrogen-fixing microorganisms in tropical and subtropical oceans. *TRENDS Microbiol.* 8.
- Zehr, J.P., Mellon, M.T., Zani, S., 1998. New Nitrogen-Fixing Microorganisms Detected in Oligotrophic Oceans by Amplification of Nitrogenase (nifH) Genes. *Appl. Environ. Microbiol.* 64, 3444–3450.
- Zehr, J.P., Ward, B.B., 2002. Nitrogen cycling in the ocean: new perspectives on processes and paradigms. *Appl. Environ. Microbiol.* 68, 1015–1024.
- Zehr, J.P., Waterbury, J.B., Turner, P., Montoya, J.P., Omoregie, E., Steward, G.F., Hansen, A., Karl, D.M., 2001. Unicellular cyanobacteria fix N<sub>2</sub> in the subtropical North Pacific Ocean. *Nature* 412, 635–637.
- Zhai, L., Platt, T., Sathyendranath, S., Hernández Walls, R., 2011. Phytoplankton phenology on the Scotian Shelf. *ICES J. Mar. Sci.* 68, 781–791.
- Zwanenburg, K.C., Bowen, D., Bundy, A., Frank, K., Drinkwater, K., O’Boyle, R., Sameoto, D., Sinclair, M., 2002. 4 Decadal changes in the Scotian Shelf large marine ecosystem. *Large Mar. Ecosyst.* 10, 105–150.

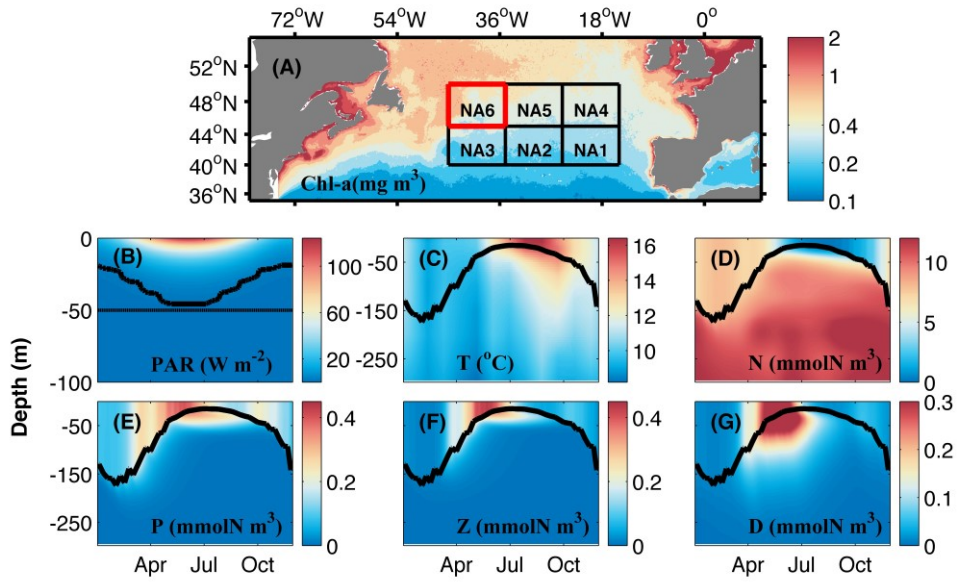
## APPENDIX A

### OPTIMIZED NPZD MODEL RESULTS FOR ALL SPATIALLY AVERAGED BINS IN THE SUBPOLAR NORTH ATLANTIC CASE STUDY<sup>1</sup>



<sup>1</sup> Bin NA5 is omitted, see Figure 2.1.

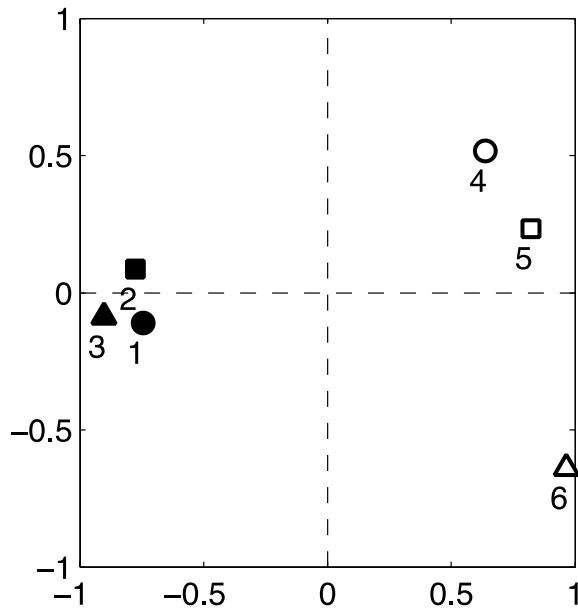




## APPENDIX B

### PRINCIPAL COMPONENT ANALYSIS OF THE MODEL INPUT VARIABLES IN THE SUBPOLAR NORTH ATLANTIC CASE STUDY

The analysis was performed using normalized forcing variables for all bins, which include: annual mean mixed layer depth, from the SODA & FNMOC mixed layer depth climatology, annual mean satellite-based phytoplankton biomass, annual mean WOA nitrate surface concentrations, WOA annual mean surface temperature, and annual mean surface photosynthetic radiation (PAR). Results of the principal component analysis of optimized parameters, showing the scaled arrangement of optimized parameter sets projected onto the first and second principal component (PC1, PC2). Solid black symbols represent the southern bins (NA1 to NA3), and the empty symbols are for the northern bins (NA4 to NA6). The distance between their symbols is representative of how different the bins are with respect to their averaged properties. The location of the variables symbols  $H_{MLD}$ ,  $P^{obs}$ ,  $N_{WOA}$ ,  $T$ ,  $PAR$  represents the scaled contribution of these variables to the variance among bins explained by PC1 and PC2.



APPENDIX C

NORTHWEST NORTH ATLANTIC MODELS (M1, M2 AND M3) EQUATIONS

235

M1 (base model, Fennel et al. 2006)	M2 (base model with temperature dependent biological rates)	M3 (model with increased trophic complexity based on Kishi et al. 2007)
<b>Phytoplankton</b>		
<b>P = growth - grazing - mortality - coagulation - sinking</b>	<b>Small P = growth - grazing (by small Z &amp; large Z) - mortality - sinking</b>	<b>Large P = growth - grazing (by large Z &amp; predatory Z) - mortality - coagulation - sinking</b>
$\frac{\partial P}{\partial t} = \mu P - gZ - m_P P - \tau(D_S + P)P$ $- w_P \frac{\partial P}{\partial Z}$	$\frac{\partial P}{\partial t} = \mu P - gZ - m_P P - \tau(D_S + P)P$ $- w_P \frac{\partial P}{\partial Z}$	$\frac{\partial P_S}{\partial t} = \mu_{P_S} P_S - g_{Z_S P_S} Z_S - g_{Z_L P_S} Z_L - m_{P_S} P_S$ $- w_{P_S} \frac{\partial P_S}{\partial Z}$ $\frac{\partial P_L}{\partial t} = \mu_{P_L} P_L - g_{Z_L P_L} Z_L - g_{Z_P P_L} Z_P - m_{P_L} P_L$ $- \tau(D_S + P_L)P_L - w_{P_L} \frac{\partial P_L}{\partial Z}$

M1 (base model, Fennel et al. 2006)	M2 (base model with temperature dependent biological rates)	M3 (model with increased trophic complexity based on Kishi et al. 2007)
Phytoplankton growth rate		
$\mu = \mu_{max} L_I(L_{NO3} + L_{NH4})$	$\mu = \mu_{max} L_I(L_{NO3} + L_{NH4})$	$\mu_{P_S} = \mu_{max}^{P_S} L_{I_{P_S}}(L_{NO3_{P_S}} + L_{NH4_{P_S}})$
		$\mu_{P_L} = \mu_{max}^{P_L} L_{I_{P_L}}(L_{NO3_{P_L}} + L_{NH4_{P_L}})$
Temperature dependent phytoplankton maximum growth rate		
$\mu_{max} = \mu_0 \phi^T$	$\mu_{max} = \mu_0 \phi^T$	$\mu_{max}^{P_S} = \mu_{0_{P_S}} \phi^T$
		$\mu_{max}^{P_L} = \mu_{0_{P_L}} \phi^T$
Light limitation for phytoplankton growth		
$L_I = \frac{\alpha I}{\sqrt{\mu_{max}^2 + \alpha^2 I^2}}$	$L_I = \frac{\alpha I}{\sqrt{\mu_{max}^2 + \alpha^2 I^2}}$	$L_{I_{P_S}} = \frac{\alpha_{P_S} I}{\sqrt{(\mu_{max}^{P_S})^2 + (\alpha_{P_S} I)^2}}$
		$L_{I_{P_L}} = \frac{\alpha_{P_L} I}{\sqrt{(\mu_{max}^{P_L})^2 + (\alpha_{P_L} I)^2}}$

M1 (base model, Fennel et al. 2006)	M2 (base model with temperature dependent biological rates)	M3 (model with increased trophic complexity based on Kishi et al. 2007)
Light attenuation with depth		
$I = I(z) = I_0 PAR_{frac} \exp \left\{ -z \left[ K_w + K_{chl} \int_z^0 Chl(\zeta) d\zeta \right] \right\}$	$I = I(z) = I_0 PAR_{frac} \exp \left\{ -z \left[ K_w + K_{chl} \int_z^0 Chl(\zeta) d\zeta \right] \right\}$	$I = I(z) = I_0 PAR_{frac} \exp \left\{ -z \left[ K_w + k_{chl} \int_z^0 (Chl_{P_S}(\zeta) + Chl_{P_L}(\zeta)) d\zeta \right] \right\}$
Nutrient limitation for phytoplankton growth		
$L_{NO3} = \frac{NO3}{k_{NO3} + NO3} \frac{1}{1 + NH4/k_{NH4}}$	$L_{NO3} = \frac{NO3}{k_{NO3} + NO3} \frac{1}{1 + NH4/k_{NH4}}$	$L_{NO3_{P_S}} = \frac{NO3}{k_{NO3_{P_S}} + NO3} \left[ \frac{1}{1 + NH4/k_{NH4_{P_S}}} \right]$ $L_{NO3_{P_L}} = \frac{NO3}{k_{P_L} + NO3} \left[ \frac{1}{1 + NH4/k_{NH4_{P_L}}} \right]$
$L_{NH4} = \frac{NH4}{k_{NH4} + NH4}$	$L_{NH4} = \frac{NH4}{k_{NH4} + NH4}$	$L_{NH4_{P_S}} = \frac{NH4}{k_{NH4_{P_S}} + NH4}$ $L_{NH4_{P_L}} = \frac{NH4}{k_{NH4_{P_L}} + NH4}$

M1 (base model, Fennel et al. 2006)	M2 (base model with temperature dependent biological rates)	M3 (model with increased trophic complexity based on Kishi et al. 2007)
Zooplankton grazing rates		
$g = g_{max} \frac{p^2}{k_p + p^2}$	$g = g_{max} \frac{p^2}{k_p + p^2}$	$g_{Z_S P_S} = g_{max}^{Z_S P_S} \frac{P_S^2}{k_{Z_S P_S} + P_S^2}$
		$g_{Z_L P_S} = g_{max}^{Z_L P_S} \frac{P_S^2}{k_{Z_L P_S} + P_S^2}$
		$g_{Z_L P_L} = g_{max}^{Z_L P_L} \frac{P_L^2}{k_{Z_L P_L} + P_L^2}$
		$g_{Z_L Z_S} = g_{max}^{Z_L Z_S} \frac{Z_S^2}{k_{Z_L Z_S} + Z_S^2}$
		$g_{Z_P P_L} = g_{max}^{Z_P P_L} \frac{P_L^2}{k_{Z_P P_L} + P_L^2} e^{-\psi_{P_L}(Z_S + Z_L)}$
		$g_{Z_P Z_S} = g_{max}^{Z_P Z_S} \frac{Z_S^2}{k_{Z_P Z_S} + Z_S^2} e^{-\psi_{Z_S}(Z_L)}$
		$g_{Z_P Z_L} = g_{max}^{Z_P Z_L} \frac{Z_L^2}{k_{Z_P Z_L} + Z_L^2}$

M1 (base model, Fennel et al. 2006)	M2 (base model with temperature dependent biological rates)	M3 (model with increased trophic complexity based on Kishi et al. 2007)
Temperature dependent maximum grazing rates		
-	$g_{max} = g_0 \phi^T$	$g_{max}^{Z_S P_S} = g_{0Z_S P_S} \phi^T$
		$g_{max}^{Z_L P_S} = g_{0Z_L P_S} \phi^T$
		$g_{max}^{Z_L P_L} = g_{0Z_L P_L} \phi^T$
		$g_{max}^{Z_L Z_S} = g_{0Z_L Z_S} \phi^T$
		$g_{max}^{Z_P P_L} = g_{0Z_P P_L} \phi^T$
		$g_{max}^{Z_P Z_S} = g_{0Z_P Z_S} \phi^T$
		$g_{max}^{Z_P Z_L} = g_{0Z_P Z_L} \phi^T$
Temperature dependent phytoplankton mortality rates		
-	$m_P = m_{0P} \phi^T$	$m_{P_S} = m_{0P_S} \phi^T$
		$m_{P_L} = m_{0P_L} \phi^T$

M1 (base model, Fennel et al. 2006)	M2 (base model with temperature dependent biological rates)	M3 (model with increased trophic complexity based on Kishi et al. 2007)
<b>Zooplankton</b>		
<b>Z = assimilated grazing - base metabolism - excretion - mortality</b>	<b>Small Z = assimilated grazing (on small P) - grazing (by large Z &amp; predatory Z) - base metabolism - excretion - mortality</b>	
	<b>Large Z = assimilated grazing (on small P, large P &amp; small Z) - grazing (by predatory Z) - base metabolism - excretion - mortality</b>	
	<b>Predatory Z = assimilated grazing (on large P, small Z &amp; large Z) - base metabolism - excretion - mortality</b>	
Zooplankton growth		
$\frac{\partial Z}{\partial t} = g\beta Z - l_{BM}Z - l_E \frac{P^2}{k_P + P^2} \beta Z - m_Z Z^2$	$\frac{\partial Z}{\partial t} = g\beta Z - l_{BM}Z - l_E \frac{P^2}{k_P + P^2} \beta Z - m_Z Z^2$	$\begin{aligned} \frac{\partial Z_S}{\partial t} = & g_{Z_S P_S} \beta_{Z_S} Z_S - g_{Z_L Z_S} Z_L \\ & - g_{Z_P Z_S} Z_P - l_{BM_{Z_S}} Z_S \\ & - l_{E_{Z_S}} \frac{g_{Z_S P_S}}{Z_S P_S} \beta_{Z_S} Z_S - m_{Z_S} Z_S^2 \end{aligned}$

M1 (base model, Fennel et al. 2006)	M2 (base model with temperature dependent biological rates)	M3 (model with increased trophic complexity based on Kishi et al. 2007)
		$\frac{\partial Z_L}{\partial t} = (g_{Z_L P_S} + g_{Z_L P_L} + g_{Z_L Z_S})\beta_{Z_L} Z_L - g_{Z_P Z_L} Z_P - l_{BM_{Z_L}} Z_L - l_{E_{Z_L}} \left( \frac{g_{Z_L P_S}}{g_{max}} + \frac{g_{Z_L P_L}}{g_{max}} + \frac{g_{Z_L Z_S}}{g_{max}} \right) \beta_{Z_L} Z_L - m_{Z_L} Z_L^2$ $\frac{\partial Z_P}{\partial t} = (g_{Z_P P_L} + g_{Z_P Z_S} + g_{Z_P Z_L})\beta_{Z_P} Z_P - l_{BM_{Z_P}} Z_P - l_{E_{Z_P}} \left( \frac{g_{Z_P P_L}}{g_{max}} + \frac{g_{Z_P Z_S}}{g_{max}} + \frac{g_{Z_P Z_L}}{g_{max}} \right) \beta_{Z_P} Z_P - m_{Z_P} Z_P^2$
Temperature dependent zooplankton base metabolic rates		
-	$l_{BM} = l_{BM0} \phi^T$	$l_{BM_{Z_S}} = l_{BM0_{Z_S}} \phi^T$
		$l_{BM_{Z_L}} = l_{BM0_{Z_L}} \phi^T$
		$l_{BM_{Z_P}} = l_{BM0_{Z_P}} \phi^T$

M1 (base model, Fennel et al. 2006)	M2 (base model with temperature dependent biological rates)	M3 (model with increased trophic complexity based on Kishi et al. 2007)
Temperature dependent zooplankton base metabolic rates		
-	$l_E = l_{E0}\phi^T$	$l_{EZ_S} = l_{E0Z_S}\phi^T$
		$l_{EZ_L} = l_{E0Z_L}\phi^T$
		$l_{EZ_P} = l_{E0Z_P}\phi^T$
Temperature dependent zooplankton mortality rates		
-	$m_Z = m_{0Z}\phi^T$	$m_{Z_S} = m_{0Z_S}\phi^T$
		$m_{Z_L} = m_{0Z_L}\phi^T$
		$m_{Z_P} = m_{0Z_P}\phi^T$
<b>Nutrient</b>		
<b>NO3 = - NO3 uptake + nitrification</b>		<b>NO3 = - NO3 uptake (by small P &amp; large P) + nitrification</b>
<b>NH4 = - NH4 uptake - nitrification + Z base metabolism + Z excretion + decomposition (of small D &amp; large D)</b>		<b>NH4 = - NH4 uptake (by small P &amp; large P) - nitrification + base metabolism (of small Z, large &amp; predatory Z) + excretion (of small Z, large Z and predatory Z) + decomposition (of small D &amp; large D)</b>

<b>M1 (base model, Fennel et al. 2006)</b>	<b>M2 (base model with temperature dependent biological rates)</b>	<b>M3 (model with increased trophic complexity based on Kishi et al. 2007)</b>
$\frac{\partial NO_3}{\partial t} = -\mu_{max} f(I)L_{NO_3}P + nNH_4$	$\frac{\partial NO_3}{\partial t} = -\mu_{max} f(I)L_{NO_3}P + nNH_4$	$\frac{\partial NO_3}{\partial t} = -\mu_{max}^{P_S} L_{I_{P_S}} L_{NO_3_{P_S}} - \mu_{max}^{P_L} L_{I_{P_L}} L_{NO_3_{P_L}} + nNH_4$

M1 (base model, Fennel et al. 2006)	M2 (base model with temperature dependent biological rates)	M3 (model with increased trophic complexity based on Kishi et al. 2007)
$\frac{\partial NH_4}{\partial t} = -\mu_{max} f(I) L_{NH_4} P - n NH_4 + l_{BM} Z + l_E \frac{p^2}{k_p + p^2} \beta Z + r_{D_S} D_S + r_{D_L} D_L$	$\frac{\partial NH_4}{\partial t} = -\mu_{max} f(I) L_{NH_4} P - n NH_4 + l_{BM} Z + l_E \frac{p^2}{k_p + p^2} \beta Z + r_{D_S} D_S + r_{D_L} D_L$	$\begin{aligned} \frac{\partial NH_4}{\partial t} = & -\mu_{max}^{P_S} L_{I_{P_S}} L_{NH_4 P_S} - \mu_{max}^{P_L} L_{I_{P_L}} L_{NH_4 P_L} - n NH_4 \\ & + r_{P_S} P_S + r_{P_L} P_L \\ & + \left[ l_{B_{M_{Z_S}}} + l_{E_{Z_S}} \frac{g_{Z_S P_S}}{g_{max}} \beta_{Z_S} \right] Z_S \\ & + \left[ l_{B_{M_{Z_L}}} + l_{E_{Z_L}} \left( \frac{g_{Z_L P_S}}{g_{max}} + \frac{g_{Z_L P_L}}{g_{max}} + \frac{g_{Z_L Z_S}}{g_{max}} \right) \beta_{Z_L} \right] Z_L \\ & + \left[ l_{B_{M_{Z_P}}} + l_{E_{Z_P}} \left( \frac{g_{Z_P P_L}}{g_{max}} + \frac{g_{Z_P Z_S}}{g_{max}} + \frac{g_{Z_P Z_L}}{g_{max}} \right) \beta_{Z_P} \right] Z_P + r_{D_S} D_S \\ & + r_{D_L} D_L \end{aligned}$

<b>M1 (base model, Fennel et al. 2006)</b>	<b>M2 (base model with temperature dependent biological rates)</b>	<b>M3 (model with increased trophic complexity based on Kishi et al. 2007)</b>
0Light inhibited nitrification rate		
$n = n_{max} \left( 1 - \max \left[ 0, \frac{I - I_0}{k_I + I - I_0} \right] \right)$	$n = n_{max} \left( 1 - \max \left[ 0, \frac{I - I_0}{k_I + I - I_0} \right] \right)$	$n = n_{max} \left( 1 - \max \left[ 0, \frac{I - I_0}{k_I + I - I_0} \right] \right)$
<b>Detritus</b>		
<p><b>Small D= Z egestion + Z mortality+ P mortality - Coagulation (Small D + P) - decomposition - sinking</b></p> <p><b>Large D= Coagulation - decomposition - sinking</b></p>		<p><b>Small D= mortality (of small P, large P, small Z, and large Z) + egestion (by small Z, and large Z) - coagulation (of small D and small P) - decomposition - sinking</b></p> <p><b>Large D= mortality (of predatory Z) + egestion (by predatory Z)+ coagulation - decomposition - sinking</b></p>
$\frac{\partial D_S}{\partial t} = g(1 - \beta)Z + m_Z Z^2 + m_P P$ $- \tau(D_S + P)D_S$ $- r_{D_S} D_S - w_{D_S} \frac{\partial D_S}{\partial Z}$	$\frac{\partial D_S}{\partial t} = g(1 - \beta)Z + m_Z Z^2 + m_P P^2$ $- \tau(D_S + P)D_S$ $- r_{D_S} D_S - w_{D_S} \frac{\partial D_S}{\partial Z}$	$\frac{\partial D_S}{\partial t} = \varepsilon_{Z_S} Z_S + \varepsilon_{Z_L} Z_L + m_{P_S} P_S^2 + m_{P_L} P_L^2$ $+ m_{Z_S} Z_S^2 + m_{Z_L} Z_L^2$ $- \tau(D_S + P_L)D_S$ $- r_{D_S} D_S - w_{D_S} \frac{\partial D_S}{\partial Z}$

M1 (base model, Fennel et al. 2006)	M2 (base model with temperature dependent biological rates)	M3 (model with increased trophic complexity based on Kishi et al. 2007)
$\frac{\partial D_L}{\partial t} = \tau(D_S + P)^2 - r_{D_L}D_L - w_{D_L} \frac{\partial D_L}{\partial Z}$	$\frac{\partial D_L}{\partial t} = \tau(D_S + P)^2 - r_{D_L}D_L - w_{D_L} \frac{\partial D_L}{\partial Z}$	$\frac{\partial D_L}{\partial t} = \varepsilon_{Z_P}Z_P + m_P Z_P^2 + \tau(D_S + P_L)^2 - r_{D_L}D_L - w_{D_L} \frac{\partial D_L}{\partial Z}$
<b>Chlorophyll</b>		
$\frac{\partial chl}{\partial t} = \rho_{chl}\mu P - gZ \frac{chl}{P} - m_P chl - \tau(D_S + P)chl$	$\frac{\partial chl}{\partial t} = \rho_{chl}\mu P - gZ \frac{chl}{P} - m_P chl - \tau(D_S + P)chl$	$\begin{aligned} \frac{\partial chl_S}{\partial t} &= \rho_{chl_S}\mu_{P_S}P_S - g_{Z_S P_S} \frac{chl_S}{P_S} Z_S \\ &\quad - g_{Z_L P_S} \frac{chl_S}{P_S} Z_L \\ &\quad - r_{P_S} chl_S - m_{P_S} chl_S^2 \end{aligned}$ $\begin{aligned} \frac{\partial chl_L}{\partial t} &= \rho_{chl_L}\mu_{P_L}P_L - g_{Z_L P_L} \frac{chl_L}{P_L} Z_L \\ &\quad - g_{Z_P P_L} \frac{chl_L}{P_L} Z_P \\ &\quad - r_{P_L} chl_L - m_{P_L} chl_L^2 \\ &\quad - \tau(D_S + P_L)chl_L \end{aligned}$
Chlorophyll to phytoplankton ratio		

M1 (base model, Fennel et al. 2006)	M2 (base model with temperature dependent biological rates)	M3 (model with increased trophic complexity based on Kishi et al. 2007)
$\rho_{chl} = \frac{\theta_{max}\mu P}{\alpha IChl}$	$\rho_{chl} = \frac{\theta_{max}\mu P}{\alpha IChl}$	$\rho_{chl_S} = \frac{\theta_{maxP_S}\mu_{P_S}P_S}{\alpha_{P_S}IChl_S}$
		$\rho_{chl_L} = \frac{\theta_{maxP_L}\mu_{P_L}P_L}{\alpha_{P_L}IChl_L}$

## APPENDIX D

### NORTHWEST NORTH ATLANTIC IN SITU VERSUS SATELLITE SURFACE CHLOROPHYLL REGRESSIONS

- *Standard AZMP* refers to Turner fluorometry chlorophyll measurements available on-line at <http://www.meds-sdmm.dfo-mpo.gc.ca/isdm-gdsi/azmp-pmza/hydro/index-eng.html>
- *High Performance Liquid Chromatography (HPLC)* measurements come from additional field studies, and ships of opportunity (C. Johnson & A. Cogswell, pers. comm.). The dataset does not include measurements inside the Gulf of St. Lawrence.
- *SeaWiFS*: Chl-a from Sea-Viewing Wide Field-of-View Sensor 1997-2010.
- *GlobCol GSM*: Chl-a from GlobColour merged with GSM model based on Maritorena and Siegel (2005, Remote Sensing of Environment).
- *GlobCol AVW*: Chl-a from GlobColour merged using weighted averaging method (AVW), with weightings based on the sensor/product characterisation

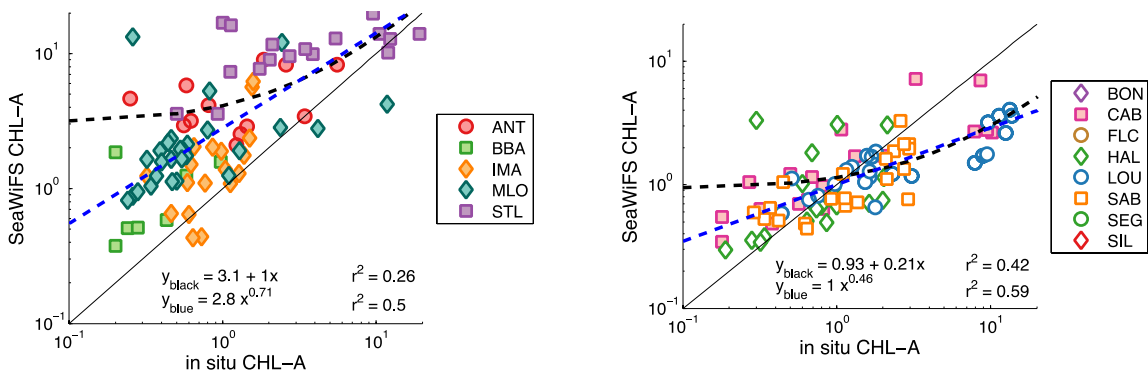


Figure C1: Standard AZMP chl-a vs. SeaWiFs, top 1 m in situ observations and daily (+- 1 day) satellite observations (0.1 x 0.1 degrees around in situ measurement). Left: Measurements inside the Gulf of St. Lawrence. Right: Measurements outside the Gulf of St. Lawrence.

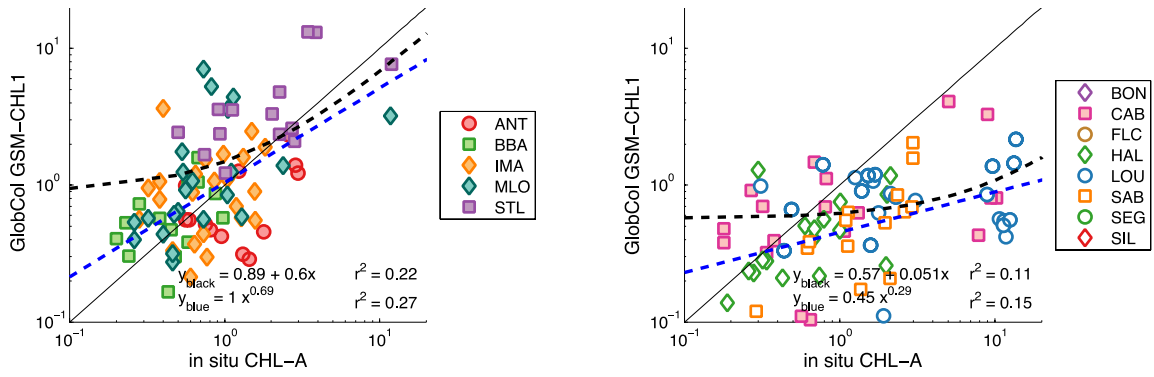


Figure C2: Standard AZMP chl-a vs. GlobCol GSM, details as in Figure C1.

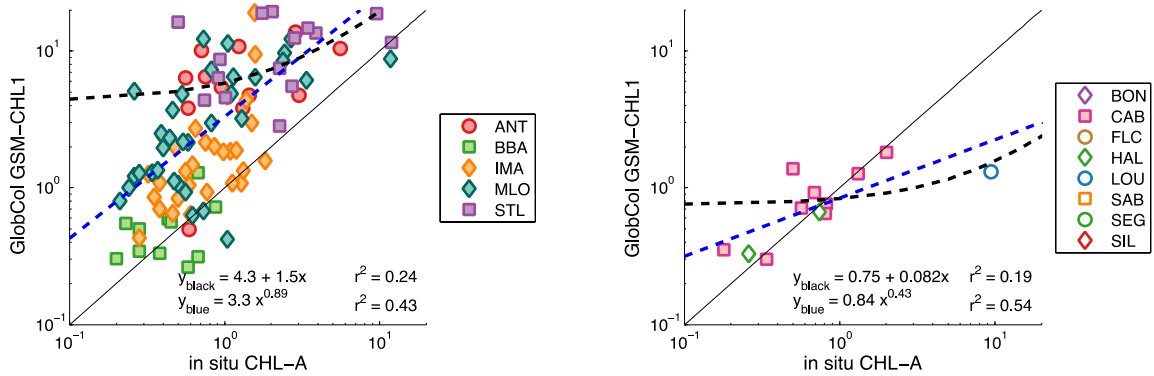


Figure C3: Standard AZMP chl-a vs. GlobCol AVW, details as in Figure C2.

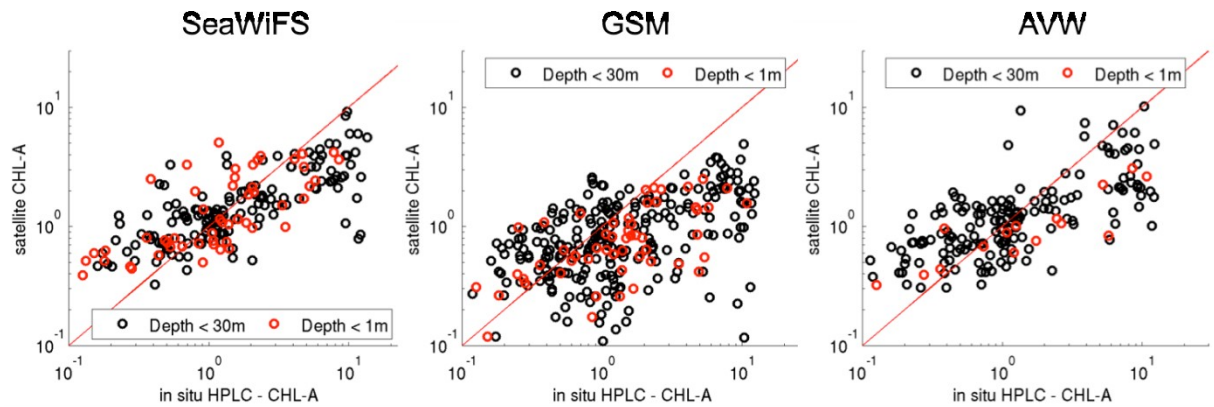


Figure C4: HPLC chl-a vs. SeaWiFs and GlobColour satellite chlorophyll 1999 – 2010. Notice similitude with results from Standard AZMP outside the Gulf of St. Lawrence, as the HPLC dataset does not include measurements inside the gulf.

**APPENDIX E**

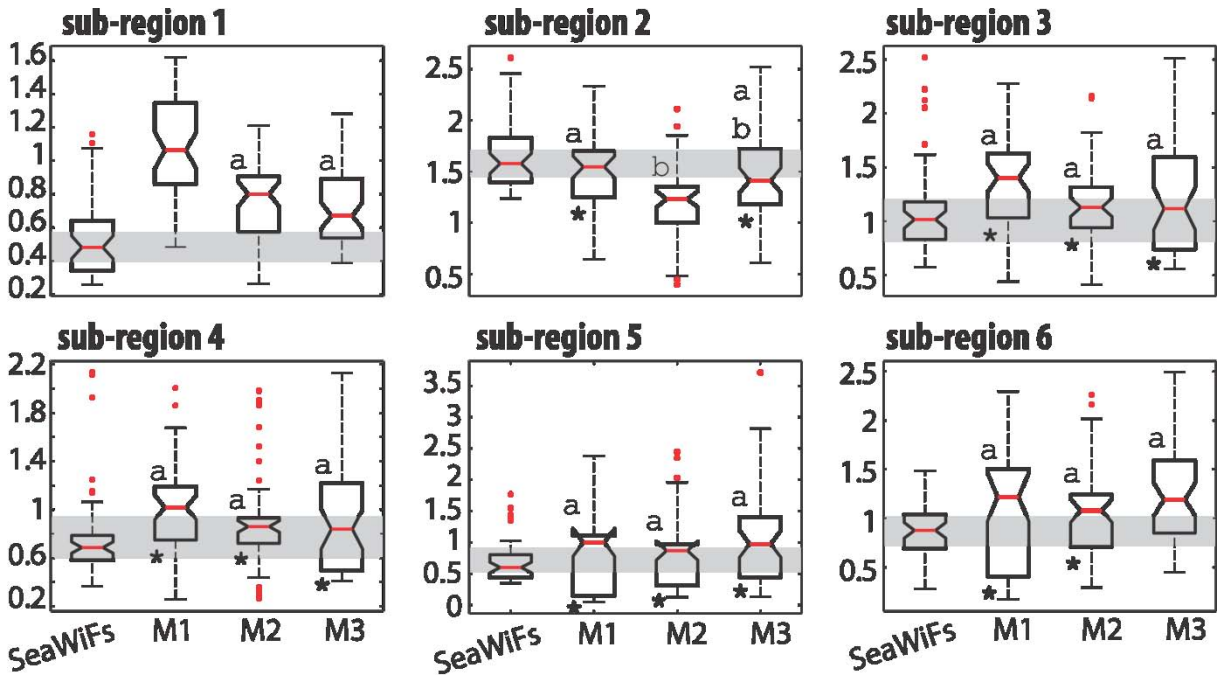
**CONTRIBUTION OF VARIABLES AND SURROGATE LOCATIONS TO THE TOTAL MODEL COST VALUES PRIOR TO OPTIMIZATION**

Location	M1			M2			M3			
	Sat. chl-a	in situ chl-a	in situ NO <sub>3</sub>	Sat. chl-a	in situ chl-a	in situ NO <sub>3</sub>	Sat. chl-a Pico-Nano	Sat. chl-a Micro	in situ chl-a	in situ NO <sub>3</sub>
1	72.37	9.74	5.85	68.92	10.93	7.30	41.94	30.32	4.70	4.87
2	255.35	5.59	23.07	607.53	4.32	28.98	380.61	997.97	43.41	4.33
3	88.97	7.54	10.51	66.56	7.51	8.87	187.58	17.62	1.68	1.98
4	69.90	6.34	8.43	59.74	6.52	7.03	194.57	24.12	2.46	2.35
5	54.64	5.91	8.12	37.39	6.00	8.11	228.32	13.21	5.55	1.72
6	94.17	9.11	10.03	88.15	7.53	8.19	92.15	10.76	0.79	0.72
7	165.82	2.96	5.49	290.80	3.16	4.90	180.62	150.69	1.51	1.14
8	115.73	7.87	13.51	111.47	8.32	11.22	209.70	23.27	2.08	1.82
9	88.90	3.46	6.28	152.46	3.73	4.66	148.31	81.14	1.83	1.54
10	52.72	4.15	21.34	54.70	4.38	25.83	115.81	30.36	29.32	0.87
11	114.39	5.24	22.15	154.98	4.86	24.23	118.82	69.10	26.04	1.79
12	73.76	2.33	13.30	77.69	2.06	15.06	66.97	19.51	8.00	0.47
13	62.04	0.92	6.58	75.08	0.91	6.64	88.53	26.89	1.98	0.82
14	137.88	7.25	6.43	197.06	6.26	6.16	148.91	54.33	1.46	2.34
15	84.79	8.89	6.18	98.21	7.27	5.92	81.95	21.71	1.23	2.06
16	89.10	6.97	6.96	77.01	5.13	6.46	64.22	7.18	0.65	0.85
17	47.17	2.82	9.03	70.82	2.39	11.97	72.88	34.55	10.34	0.84
18	55.43	4.04	10.59	67.66	3.42	13.22	58.88	10.90	6.98	0.72
19	56.67	3.72	6.60	66.01	3.06	8.94	62.06	10.52	4.97	0.47
20	69.58	21.25	8.15	69.76	19.88	8.50	90.79	20.27	2.57	7.20
21	96.97	14.72	10.66	89.51	11.71	9.95	108.95	22.03	1.95	4.19
22	109.21	17.68	8.52	139.84	14.47	7.19	161.94	33.14	1.69	4.62
F(p)	685.19	52.84	75.92	907.12	47.94	79.78	968.17	569.86	53.73	15.90
	813.95			1034.83			1607.67			

## APPENDIX F

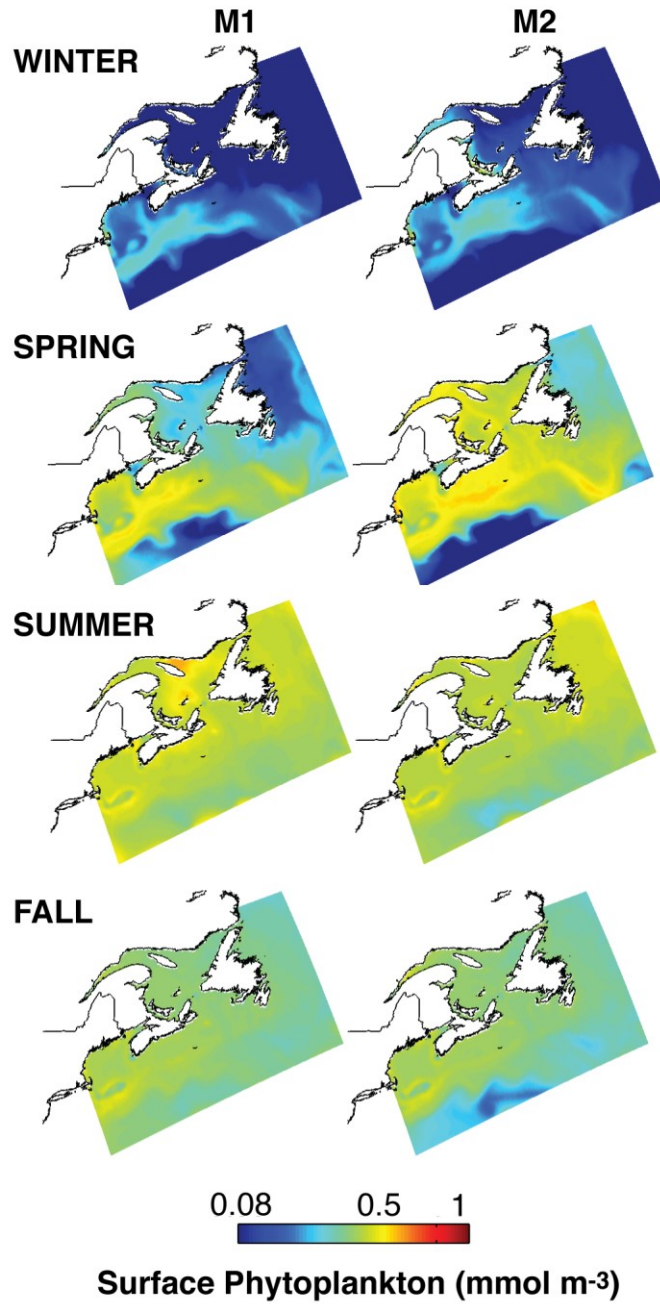
### ANALYSIS OF VARIANCE AMONG SATELLITE AND SIMULATED SURFACE CHLOROPHYLL ANNUAL CYCLES IN THE NORTHWEST NORTH ATLANTIC

Boxplots for each sub-region show the medians (red lines inside the boxes) of the observed and simulated chlorophyll annual cycles. Overlap between the median notches of each box shows the similitude/difference among medians at 95% confidence. The lower and upper edges of the boxes are the 25th and 75th percentiles. The whiskers extend to the most extreme data points that are not considered outliers. The outliers are plotted individually as red dots. Additionally, the grey shadow shows similitude/difference between the observed mean and the simulated values at a 99% confidence. Asterisks (\*) at the bottom of each box represent model means that are significantly similar to the observational mean. Letters at the top of each box represent the significance of similitudes among models. Models sharing equal letters are significantly similar to each other.



APPENDIX G

NORTHWEST NORTH ATLANTIC SEASONAL SURFACE PHYTOPLANKTON BIOMASS



## APPENDIX I

### GULF OF AQABA MODEL EQUATIONS

#### i. Hypothesis 0: Neglecting N<sub>2</sub> fixation

As a starting hypothesis, we test whether a model without nitrogen fixing can reproduce the observed distribution of inorganic nutrients. We test this model with and without allowing a sediment denitrification flux, denoted as H0 and H0', respectively. Therefore, H0 fully neglects N<sub>2</sub> fixation, while H0' implicitly assumes that N<sub>2</sub> fixation inputs and N<sub>2</sub> denitrification are balanced.

This model (H0) tracks the changes of 8 state-variables: nitrate (NO<sub>3</sub>), ammonium (NH<sub>4</sub>), dissolved inorganic phosphorus (DIP), non-fixing phytoplankton (Phy), zooplankton (Zoo), “small” detritus (D<sub>s</sub>), “large” detritus (D<sub>l</sub>), and oxygen (O<sub>2</sub>). Model equations correspond to those described in Fennel et al., 2006 and 2013. Changes in phytoplankton and zooplankton biomass are measured in nitrogen units only, which implies a constant N:P ratio for these functional groups. The stoichiometry of non-fixing phytoplankton and zooplankton is set to the Redfield ratio ( $R_{N:P}^{nf}=16$ ), and their biomass changes according to:

$$\frac{\partial Phy}{\partial t} = \mu_{Phy} Phy - gZoo - m_{Phy} Phy - w_{Phy} \frac{\partial Phy}{\partial z} \quad (1)$$

$$\frac{\partial Zoo}{\partial t} = g\beta Zoo - l_{BM} Zoo - l_E \frac{Phy^2}{k_{Phy} + Phy^2} \beta Zoo - m_{Zoo} Zoo^2 \quad (2)$$

Phytoplankton growth (equ. 1) depends on light and nutrient supply according to:  $\mu_{Phy} = \mu_{Phy}^{max} f(I) \min(L_{NO_3} + L_{NH_4}, L_{DIP})$ . This formulation assumes that growth is limited by light and nutrient availability using a multiplicative effect. In terms of nutrient limitation, it follows Liebig's Law of the minimum, as growth is limited by the scarcest nutrient resource of either nitrogen or phosphorus. The maximum non-fixing phytoplankton growth rate,  $\mu_{Phy}^{max}$ , varies with temperature using a Q<sub>10</sub> formulation according to  $\mu_{Phy}^{max}(T) = \mu_{Phy}^0 1.88^{T/10^\circ C}$  (Eppley, 1972), where  $\mu_{Phy}^0$  is the assumed maximum growth rate at T = 0°C. The light limitation function is equal to  $f(I) = \frac{\alpha_{Phy} I}{\sqrt{(\mu_{Phy}^{max})^2 + \alpha_{Phy}^2 I^2}}$  (Smith, 1936), where  $I$  is the depth varying photosynthetically active radiation, and  $\alpha_{Phy}$  is the initial slope of the photosynthetic reaction. The value of  $I$

decreases exponentially with depth ( $z$ ) according to  $I(z) = I_0(1 - \phi)e^{-z k_w - \int_0^z k_{chl} Chl_{Phy} dz}$ , where the coefficients  $\phi=0.62$  and  $k_w = 0.05 \text{ m}^{-1}$  are set for oceanic clear waters according to Jerlov's type IA (Paulson and Simpson, 1977), and the coefficient  $k_{chl} = 0.04 \text{ m}^{-1}$  represents light attenuation due to chlorophyll concentrations ( $Chl$ ).  $I_0$  is the surface solar radiation recorded at the IUI station.

Non-fixing phytoplankton is grazed by zooplankton at a density dependent rate  $g = g_{Phy}^{max} \frac{Phy^2}{k_{Zoo}^{Phy} + Phy^2}$ , with only a fraction  $\beta$  being assimilated into zooplankton growth. The last two terms in equation 1 represent non-fixing phytoplankton mortality and sinking, which occur at a rate of  $m_{Phy}$  and a speed of  $w_{Phy}$ , respectively. In equation 2,  $l_{BM}$ ,  $l_E$ , and  $m_Z$  represent the zooplankton base metabolic, excretion and mortality rates.

Changes in nutrient concentrations are defined by the following set of equations:

$$\frac{\partial NO_3}{\partial t} = -\mu_{Phy}^{max} f(I) L_{NO_3} Phy + nNH_4 \quad (3)$$

$$\frac{\partial NH_4}{\partial t} = -\mu_{Phy}^{max} f(I) L_{NH_4} Phy + l_{BM} Zoo + l_E \frac{Phy^2}{k_P + Phy^2} \beta Zoo + r_{D_S} D_{S(N)} + r_{D_L} D_{L(N)} - nNH_4 \quad (4)$$

$$\frac{\partial DIP}{\partial t} = \frac{1}{R_{N:P}^{nf}} \left( -\mu_{Phy}^{max} f(I) L_{DIP} Phy + l_{BM} Zoo + l_E \frac{Phy^2}{k_P + Phy^2} \beta Zoo \right) + r_{D_{S(P)}} D_{S(P)} + r_{D_L} D_{L(P)} \quad (5)$$

Equations 3, 4, and 5 represent the changes in nitrate, ammonium, and dissolved inorganic phosphorus, respectively. In these equations, nutrient uptake by non-fixing phytoplankton is modulated by the maximum non-fixing phytoplankton growth rate  $\mu_{Phy}^{max}$ , the light limitation function  $f(I)$ , and the corresponding nutrient limitation factor ( $L_{NO_3}$ ,  $L_{NH_4}$ , or  $L_{DIP}$ ). The nutrient limitation factors for ammonium and dissolved inorganic phosphorus in the form of phosphate are Michaelis-Menten (1913) functions:

$$L_{NH_4} = \frac{NH_4}{k_{Phy}^{NH_4} + NH_4} \quad (6)$$

$$L_{DIP} = \frac{DIP}{k_{Phy}^{DIP} + DIP} \quad (7)$$

The nitrate limitation factor is also a Michaelis – Menten (1913) function, but is modified by the availability of  $NH_4$ , which inhibits  $NO_3$  uptake:

$$L_{NO_3} = \frac{NO_3}{k_{Phy}^{NO_3} + NO_3} \frac{1}{\left(1 + NH_4/k_{Phy}^{NH_4}\right)} \quad (8)$$

Both  $NH_4$  and DIP receive contributions from zooplankton metabolic and excretion losses, and from the degradation of small and large detritus. The parameters  $l_{BM}$ ,  $l_E$  are the metabolic loss and mortality rates of zooplankton. Degradation rates for small and large detritus are represented by  $r_{D_S}$  and  $r_{D_L}$ , respectively. Both the nitrogen and phosphorus fractions of the two detritus groups are tracked, for which we use the subscripts “(N)” and “(P)” correspondingly. The last terms in equations 3 and 4 represent the transformation of  $NH_4$  into  $NO_3$  via nitrification at rate  $n$ .

The model also estimates non-fixing phytoplankton chlorophyll content ( $Chl_{Phy}$ ):

$$\frac{\partial Chl_{Phy}}{\partial t} = \rho_{Chl_{Phy}} \mu_{Phy} Phy - g_{Zoo} \frac{Chl_{Phy}}{Phy} - m_{Phy} Chl_{Phy} - w_{Phy} \frac{\partial Chl_{Phy}}{\partial z} \quad (9)$$

where the factor  $\rho_{Chl_{Phy}}$  represents a variable chlorophyll-to-biomass ratio. This factor accounts for the photoacclimation effect of increased chlorophyll production under low light conditions and is determined following Geider et al., (1997):

$$\rho_{Chl_{Phy}} = \frac{\theta_{Phy}^{max} \mu_{Phy} Phy}{\alpha_{Phy} I Chl_{Phy}} \quad (10)$$

The two fractions of detritus aim to represent small-suspended particles of non-living organic matter ( $D_S$ ) that can aggregate to form larger sinking particles ( $D_L$ ). “Small” detritus (eq. 11) is formed from the unassimilated fraction of zooplankton grazing (i.e., sloppy feeding), and from dead phytoplankton and zooplankton. The small detritus pool suffers losses from coagulation and degradation. “Large” detritus (eq. 12) is produced through the coagulation  $D_S$ , and is removed by degradation and sinking at a  $w_{D_L}$  speed. The sinking speed of large detritus is assumed to be faster than for non-fixing phytoplankton ( $w_{Phy}$ ).

$$\frac{\partial D_S}{\partial t} = g(1 - \beta)Zoo + m_Z Zoo^2 + m_{Phy}Phy - r_{D_S}D_S \quad (11)$$

$$\frac{\partial D_L}{\partial t} = \tau D_S^2 - r_{D_L}D_L - w_{D_L} \frac{\partial D_L}{\partial Z} \quad (12)$$

Oxygen (eq. 13) is produced during photosynthesis and consumed by zooplankton metabolism, and the degradation of dissolved organic matter and detritus, as in Fennel et al. (2013):

$$\begin{aligned} \frac{\partial O_2}{\partial t} = & \mu_{Phy}^{max} f(I)(L_{NO_3}R_{O_2:NO_3} + L_{NH_4}R_{O_2:NH_4})Phy - 2 nNH_4 \\ & - R_{O_2:NH_4}(l_{BM}Zoo + r_{D_S}D_S - r_{D_L}D_L) \end{aligned} \quad (13)$$

where  $R_{O_2:NO_3} = \frac{138 \text{ mol } O_2}{16 \text{ mol } NO_3}$  and  $R_{O_2:NH_3} = \frac{106 \text{ mol } O_2}{16 \text{ mol } NH_3}$  represent stoichiometric ratios corresponding to the oxygen produced during photosynthesis per mole of nitrate and ammonium consumed.

At the ocean surface, oxygen concentrations are modified by the air-sea gas exchange  $F_{air-sea}$ :

$$F_{air-sea} = \frac{vk_{O_2}}{\Delta z} (O_{sat} - O_2) \quad (14)$$

such that a flux of oxygen into the top layer of thickness  $\Delta z$  occurs when its oxygen concentration is lower than the oxygen saturation value ( $O_{sat}$ ), and a flux into the atmosphere occurs if it is higher. The formulation of  $O_{sat}$  is based on García and Gordon (1992), and the gas exchange coefficient for oxygen,  $vk_{O_2}$ , is parameterized following Wanninkhof et al., (2011) as:

$$vk_{O_2} = 0.28 u_{10}^2 \sqrt{\frac{660}{S_{CO_2}}}, \quad (15)$$

where  $u_{10}$  is the wind speed 10 m above the sea surface, and  $S_{CO_2}$  is the Schmidt number.

We assume that organic matter reaching the bottom is instantaneously remineralized into ammonium. Sediment oxygen consumption is represented as in Fennel et al. (2013). This model was tested with and without allowing a denitrification flux (H0 and H0', respectively). When present, the denitrification flux follows Fennel et al. (2013) with a loss fraction 6 mol  $N_2$  per mol of organic matter remineralized.

**ii. Hypothesis 1: Generic autotrophic N<sub>2</sub> fixers**

In model version H1, we introduce the state variable  $G_F$ , which represents a group of generic autotrophic N<sub>2</sub> fixers:

$$\frac{\partial G_F}{\partial t} = \mu_F G_F - m_F G_F - l_F G_F - \tau(D_S + G_F)G_F \quad (16)$$

The growth of the fixing organisms is limited by light and DIP only (i.e., an obligate autotrophic diazotroph). The parameters  $m_F$ ,  $l_F$ ,  $\tau$  represent a mortality rate, an excretion rate, and the coagulation rate, respectively. An accompanying chlorophyll equation is also introduced, and total chlorophyll becomes the sum of the non-fixing and fixing autotrophic organisms:  $Chl = Chl_{Phy} + Chl_{G_F}$ . All other state variable equations are modified accordingly. That is, uptake of DIP by  $G_F$  is included as a sink in the DIP equation (Eq. 5),  $G_F$  excretion becomes an additional source of ammonium in Eq. 4,  $G_F$  mortality becomes a source of  $D_S$  in Eq. 11, and  $G_F$  coagulated aggregates become a source of  $D_L$  in Eq. 12. The stoichiometry of diazotrophs is set to  $R_{N:P}^f = 45$  (Fennel et al., 2002; Letelier and Karl, 1996).

**iii. Hypothesis 2: Unicellular and colonial N<sub>2</sub> fixers**

In model version H2, we replace the generic autotrophic diazotroph group with two different groups that represent colonial and unicellular cyanobacteria:

$$\frac{\partial U_F}{\partial t} = \mu_{U_F} U_F - m_{U_F} U_F - l_{U_F} U_F - g_{U_F} Zoo \quad (17)$$

$$\frac{\partial C_F}{\partial t} = \mu_{C_F} C_F - m_{C_F} C_F - l_{C_F} C_F - \tau(D_S + C_F)C_F \quad (18)$$

The group of colonial N<sub>2</sub> fixers,  $C_F$ , represents *Trichodesmium* spp. A minimum temperature limit for the growth of *Trichodesmium* spp. is imposed by setting the maximum growth rate to 0 when temperature is below 20°C, based on the inability to culture this type of organism below this temperature (Breitbarth et al., 2007). The unicellular cyanobacteria group,  $U_F$ , overall follows the same formulation as the generic diazotroph, except that no coagulation term is included in this equation as they represent picoplanktonic free-living cells that do not form large colonies. Instead, this group is grazed by zooplankton similar to grazing on non-fixing phytoplankton. This is based on evidence that *Trichodesmium* spp. colonies may be less palatable and harder to digest due to toxins and that grazing is not a major fate of this group (O'Neil and Roman, 1994). Moreover, it

has been suggested that colonies represent an evolutionary adaptation that allows a decreased grazing pressure (Nielsen 2006). As in the previous model version, other equations are modified where necessary.

**iv. Hypothesis 3: Heterotrophic N<sub>2</sub> fixers**

In model version H3 we introduce an additional heterotrophic diazotroph group  $H_F$ , so that this ecosystem model includes three types of N<sub>2</sub> fixers. The formulation of  $H_F$  follows:

$$\frac{\partial H_F}{\partial t} = \mu_{H_F} H_F - m_{H_F} H_F - l_{H_F} H_F \quad (18)$$

These organisms are not limited by light availability and grow by consuming both dissolved inorganic and organic phosphorus from  $D_S$ , following  $\mu_{H_F} = \psi_{DIP} \frac{DIP}{k_{H_F}^{DIP} + DIP} + \psi_{D_S} \frac{D_{S(P)}}{k_{H_F}^{D_S} + D_{S(P)}}$ . The coefficients  $\psi_{DIP}$  and  $\psi_{D_S}$  represent preferences, which are set as equal ( $\psi_{DIP} = \psi_{D_S} = 0.5$ ).

## APPENDIX J

### COPYRIGHT

An edited version of Chapter 2 was published by Elsevier Ltd. Copyright © 2015 Elsevier Ltd. It is reproduced here by permission of Elsevier Ltd:

7/25/2017

RightsLink Printable License

#### ELSEVIER LICENSE TERMS AND CONDITIONS

Jul 25, 2017

---

This Agreement between Angela M Kuhn ("You") and Elsevier ("Elsevier") consists of your license details and the terms and conditions provided by Elsevier and Copyright Clearance Center.

License Number	4156081363460
License date	Jul 25, 2017
Licensed Content Publisher	Elsevier
Licensed Content Publication	Progress in Oceanography
Licensed Content Title	Model investigations of the North Atlantic spring bloom initiation
Licensed Content Author	Angela M. Kuhn,Katja Fennel,Jann Paul Mattern
Licensed Content Date	Nov 1, 2015
Licensed Content Volume	138
Licensed Content Issue	n/a
Licensed Content Pages	18
Start Page	176
End Page	193
Type of Use	reuse in a thesis/dissertation
Portion	full article
Format	both print and electronic
Are you the author of this Elsevier article?	No
Will you be translating?	No
Title of your thesis/dissertation	INTEGRATION OF OBSERVATIONS AND MODELS FOR AN IMPROVED UNDERSTANDING OF MARINE ECOSYSTEM DYNAMICS
Expected completion date	Sep 2017
Estimated size (number of pages)	260
Requestor Location	Angela M. Kuhn 1355 Oxford Street Department of Oceanography Dalhousie University Halifax, NS B3H 4R2 Canada Attn: Angela M. Kuhn
Total	0.00 USD
Terms and Conditions	

#### INTRODUCTION

1. The publisher for this copyrighted material is Elsevier. By clicking "accept" in connection with completing this licensing transaction, you agree that the following terms and conditions apply to this transaction (along with the Billing and Payment terms and conditions established by Copyright Clearance Center, Inc. ("CCC"), at the time that you opened your Rightslink account and that are available at any time at <http://myaccount.copyright.com>).

<https://s100.copyright.com/CustomAdmin/PLF.jsp?ref=c7890e64-d718-4931-9643-4455d4a3d139>

1/6

**GENERAL TERMS**

2. Elsevier hereby grants you permission to reproduce the aforementioned material subject to the terms and conditions indicated.
3. Acknowledgement: If any part of the material to be used (for example, figures) has appeared in our publication with credit or acknowledgement to another source, permission must also be sought from that source. If such permission is not obtained then that material may not be included in your publication/copies. Suitable acknowledgement to the source must be made, either as a footnote or in a reference list at the end of your publication, as follows:  
"Reprinted from Publication title, Vol /edition number, Author(s), Title of article / title of chapter, Pages No., Copyright (Year), with permission from Elsevier [OR APPLICABLE SOCIETY COPYRIGHT OWNER]." Also Lancet special credit - "Reprinted from The Lancet, Vol. number, Author(s), Title of article, Pages No., Copyright (Year), with permission from Elsevier."
4. Reproduction of this material is confined to the purpose and/or media for which permission is hereby given.
5. Altering/Modifying Material: Not Permitted. However figures and illustrations may be altered/adapted minimally to serve your work. Any other abbreviations, additions, deletions and/or any other alterations shall be made only with prior written authorization of Elsevier Ltd. (Please contact Elsevier at [permissions@elsevier.com](mailto:permissions@elsevier.com)). No modifications can be made to any Lancet figures/tables and they must be reproduced in full.
6. If the permission fee for the requested use of our material is waived in this instance, please be advised that your future requests for Elsevier materials may attract a fee.
7. Reservation of Rights: Publisher reserves all rights not specifically granted in the combination of (i) the license details provided by you and accepted in the course of this licensing transaction, (ii) these terms and conditions and (iii) CCC's Billing and Payment terms and conditions.
8. License Contingent Upon Payment: While you may exercise the rights licensed immediately upon issuance of the license at the end of the licensing process for the transaction, provided that you have disclosed complete and accurate details of your proposed use, no license is finally effective unless and until full payment is received from you (either by publisher or by CCC) as provided in CCC's Billing and Payment terms and conditions. If full payment is not received on a timely basis, then any license preliminarily granted shall be deemed automatically revoked and shall be void as if never granted. Further, in the event that you breach any of these terms and conditions or any of CCC's Billing and Payment terms and conditions, the license is automatically revoked and shall be void as if never granted. Use of materials as described in a revoked license, as well as any use of the materials beyond the scope of an unrevoked license, may constitute copyright infringement and publisher reserves the right to take any and all action to protect its copyright in the materials.
9. Warranties: Publisher makes no representations or warranties with respect to the licensed material.
10. Indemnity: You hereby indemnify and agree to hold harmless publisher and CCC, and their respective officers, directors, employees and agents, from and against any and all claims arising out of your use of the licensed material other than as specifically authorized pursuant to this license.
11. No Transfer of License: This license is personal to you and may not be sublicensed, assigned, or transferred by you to any other person without publisher's written permission.
12. No Amendment Except in Writing: This license may not be amended except in a writing signed by both parties (or, in the case of publisher, by CCC on publisher's behalf).
13. Objection to Contrary Terms: Publisher hereby objects to any terms contained in any purchase order, acknowledgment, check endorsement or other writing prepared by you, which terms are inconsistent with these terms and conditions or CCC's Billing and Payment terms and conditions. These terms and conditions, together with CCC's Billing and Payment

terms and conditions (which are incorporated herein), comprise the entire agreement between you and publisher (and CCC) concerning this licensing transaction. In the event of any conflict between your obligations established by these terms and conditions and those established by CCC's Billing and Payment terms and conditions, these terms and conditions shall control.

14. **Revocation:** Elsevier or Copyright Clearance Center may deny the permissions described in this License at their sole discretion, for any reason or no reason, with a full refund payable to you. Notice of such denial will be made using the contact information provided by you. Failure to receive such notice will not alter or invalidate the denial. In no event will Elsevier or Copyright Clearance Center be responsible or liable for any costs, expenses or damage incurred by you as a result of a denial of your permission request, other than a refund of the amount(s) paid by you to Elsevier and/or Copyright Clearance Center for denied permissions.

#### LIMITED LICENSE

The following terms and conditions apply only to specific license types:

15. **Translation:** This permission is granted for non-exclusive world **English** rights only unless your license was granted for translation rights. If you licensed translation rights you may only translate this content into the languages you requested. A professional translator must perform all translations and reproduce the content word for word preserving the integrity of the article.

16. **Posting licensed content on any Website:** The following terms and conditions apply as follows: Licensing material from an Elsevier journal: All content posted to the web site must maintain the copyright information line on the bottom of each image; A hyper-text must be included to the Homepage of the journal from which you are licensing at <http://www.sciencedirect.com/science/journal/xxxx> or the Elsevier homepage for books at <http://www.elsevier.com>; Central Storage: This license does not include permission for a scanned version of the material to be stored in a central repository such as that provided by Heron/XanEdu.

Licensing material from an Elsevier book: A hyper-text link must be included to the Elsevier homepage at <http://www.elsevier.com>. All content posted to the web site must maintain the copyright information line on the bottom of each image.

**Posting licensed content on Electronic reserve:** In addition to the above the following clauses are applicable: The web site must be password-protected and made available only to bona fide students registered on a relevant course. This permission is granted for 1 year only. You may obtain a new license for future website posting.

17. **For journal authors:** the following clauses are applicable in addition to the above:

#### Preprints:

A preprint is an author's own write-up of research results and analysis, it has not been peer-reviewed, nor has it had any other value added to it by a publisher (such as formatting, copyright, technical enhancement etc.).

Authors can share their preprints anywhere at any time. Preprints should not be added to or enhanced in any way in order to appear more like, or to substitute for, the final versions of articles however authors can update their preprints on arXiv or RePEc with their Accepted Author Manuscript (see below).

If accepted for publication, we encourage authors to link from the preprint to their formal publication via its DOI. Millions of researchers have access to the formal publications on ScienceDirect, and so links will help users to find, access, cite and use the best available version. Please note that Cell Press, The Lancet and some society-owned have different preprint policies. Information on these policies is available on the journal homepage.

**Accepted Author Manuscripts:** An accepted author manuscript is the manuscript of an article that has been accepted for publication and which typically includes author-incorporated changes suggested during submission, peer review and editor-author communications.

Authors can share their accepted author manuscript:

- immediately
  - via their non-commercial person homepage or blog
  - by updating a preprint in arXiv or RePEc with the accepted manuscript
  - via their research institute or institutional repository for internal institutional uses or as part of an invitation-only research collaboration work-group
  - directly by providing copies to their students or to research collaborators for their personal use
  - for private scholarly sharing as part of an invitation-only work group on commercial sites with which Elsevier has an agreement
- After the embargo period
  - via non-commercial hosting platforms such as their institutional repository
  - via commercial sites with which Elsevier has an agreement

In all cases accepted manuscripts should:

- link to the formal publication via its DOI
- bear a CC-BY-NC-ND license - this is easy to do
- if aggregated with other manuscripts, for example in a repository or other site, be shared in alignment with our hosting policy not be added to or enhanced in any way to appear more like, or to substitute for, the published journal article.

**Published journal article (JPA):** A published journal article (PJA) is the definitive final record of published research that appears or will appear in the journal and embodies all value-adding publishing activities including peer review co-ordination, copy-editing, formatting, (if relevant) pagination and online enrichment.

Policies for sharing publishing journal articles differ for subscription and gold open access articles:

**Subscription Articles:** If you are an author, please share a link to your article rather than the full-text. Millions of researchers have access to the formal publications on ScienceDirect, and so links will help your users to find, access, cite, and use the best available version. Theses and dissertations which contain embedded PJAs as part of the formal submission can be posted publicly by the awarding institution with DOI links back to the formal publications on ScienceDirect.

If you are affiliated with a library that subscribes to ScienceDirect you have additional private sharing rights for others' research accessed under that agreement. This includes use for classroom teaching and internal training at the institution (including use in course packs and courseware programs), and inclusion of the article for grant funding purposes.

**Gold Open Access Articles:** May be shared according to the author-selected end-user license and should contain a [CrossMark logo](#), the end user license, and a DOI link to the formal publication on ScienceDirect.

Please refer to Elsevier's [posting policy](#) for further information.

18. **For book authors** the following clauses are applicable in addition to the above:

Authors are permitted to place a brief summary of their work online only. You are not allowed to download and post the published electronic version of your chapter, nor may you scan the printed edition to create an electronic version. **Posting to a repository:** Authors are permitted to post a summary of their chapter only in their institution's repository.

19. **Thesis/Dissertation:** If your license is for use in a thesis/dissertation your thesis may be submitted to your institution in either print or electronic form. Should your thesis be published commercially, please reapply for permission. These requirements include permission for the Library and Archives of Canada to supply single copies, on demand, of the complete thesis and include permission for Proquest/UMI to supply single copies, on demand, of the complete thesis. Should your thesis be published commercially, please

reapply for permission. Theses and dissertations which contain embedded PJAs as part of the formal submission can be posted publicly by the awarding institution with DOI links back to the formal publications on ScienceDirect.

#### **Elsevier Open Access Terms and Conditions**

You can publish open access with Elsevier in hundreds of open access journals or in nearly 2000 established subscription journals that support open access publishing. Permitted third party re-use of these open access articles is defined by the author's choice of Creative Commons user license. See our [open access license policy](#) for more information.

#### **Terms & Conditions applicable to all Open Access articles published with Elsevier:**

Any reuse of the article must not represent the author as endorsing the adaptation of the article nor should the article be modified in such a way as to damage the author's honour or reputation. If any changes have been made, such changes must be clearly indicated.

The author(s) must be appropriately credited and we ask that you include the end user license and a DOI link to the formal publication on ScienceDirect.

If any part of the material to be used (for example, figures) has appeared in our publication with credit or acknowledgement to another source it is the responsibility of the user to ensure their reuse complies with the terms and conditions determined by the rights holder.

#### **Additional Terms & Conditions applicable to each Creative Commons user license:**

**CC BY:** The CC-BY license allows users to copy, to create extracts, abstracts and new works from the Article, to alter and revise the Article and to make commercial use of the Article (including reuse and/or resale of the Article by commercial entities), provided the user gives appropriate credit (with a link to the formal publication through the relevant DOI), provides a link to the license, indicates if changes were made and the licensor is not represented as endorsing the use made of the work. The full details of the license are available at <http://creativecommons.org/licenses/by/4.0>.

**CC BY NC SA:** The CC BY-NC-SA license allows users to copy, to create extracts, abstracts and new works from the Article, to alter and revise the Article, provided this is not done for commercial purposes, and that the user gives appropriate credit (with a link to the formal publication through the relevant DOI), provides a link to the license, indicates if changes were made and the licensor is not represented as endorsing the use made of the work. Further, any new works must be made available on the same conditions. The full details of the license are available at <http://creativecommons.org/licenses/by-nc-sa/4.0>.

**CC BY NC ND:** The CC BY-NC-ND license allows users to copy and distribute the Article, provided this is not done for commercial purposes and further does not permit distribution of the Article if it is changed or edited in any way, and provided the user gives appropriate credit (with a link to the formal publication through the relevant DOI), provides a link to the license, and that the licensor is not represented as endorsing the use made of the work. The full details of the license are available at <http://creativecommons.org/licenses/by-nc-nd/4.0>.

Any commercial reuse of Open Access articles published with a CC BY NC SA or CC BY NC ND license requires permission from Elsevier and will be subject to a fee.

Commercial reuse includes:

- Associating advertising with the full text of the Article
- Charging fees for document delivery or access
- Article aggregation
- Systematic distribution via e-mail lists or share buttons

Posting or linking by commercial companies for use by customers of those companies.

#### **20. Other Conditions:**

v1.9

Questions? [customercare@copyright.com](mailto:customercare@copyright.com) or +1-855-239-3415 (toll free in the US) or

<https://s100.copyright.com/CustomAdmin/PLF.jsp?ref=c7890e64-d718-4931-9643-f455d4a3d139>

5/6

7/25/2017

RightsLink Printable License

+1-978-646-2777.

---